The Dissertation Committee for Shaina Alysa Kelly certifies that this is the approved version of the following dissertation:

USING NANOFLUIDICS AND MICROSCOPY TO STUDY UNCONVENTIONAL PORE-SCALE TRANSPORT PHENOMENA

Committee:

Matthew T. Balhoff, Co-Supervisor

Carlos Torres-Verdín, Co-Supervisor

Hugh C. Daigle

David DiCarlo

Thomas M. Truskett

USING NANOFLUIDICS AND MICROSCOPY TO STUDY UNCONVENTIONAL PORE-SCALE TRANSPORT PHENOMENA

by

Shaina Alysa Kelly, B.S.E.E.; M.S.E.

Dissertation

Presented to the Faculty of the Graduate School of

The University of Texas at Austin

in Partial Fulfillment

of the Requirements

for the Degree of

Doctor of Philosophy

The University of Texas at Austin

December 2015

Dedication

To my mother and father, Judy and Ken,

for their unconditional love and support.

To my brother and sister, Max and Naomi,

for making childhood a lot more interesting.

To my grandparents, Gertrude and Albert,

whose memory I cherish always.

&

To Ayaz

for making these graduate school years so memorable

from late nights at the library to early mornings at the running trails.

Acknowledgements

This dissertation was possible due to the guidance, encouragement, and support of my research advisors, Carlos Torres-Verdín and Matthew Balhoff, who formulated a very stimulating project idea for me that empowered my development as a researcher. I am extremely grateful to my other dissertation committee members, Hugh Daigle, David DiCarlo, and Thomas Truskett, for their time and guidance. I would also like to acknowledge my summer internship mentors at ConocoPhillips, Rich Ostermeier and Hesham El-Sobky, for broadening my knowledge base in the field of geoscience. I thank Mark Shannon, the manager of ConocoPhillips Petrophysical Technology during my internships, for the opportunity to work in his group and for his guidance and continued interest in my research and career.

Use of the University of Texas at Austin's Center for Nano- and Molecular Science cleanroom was vital to this work and I thank the Welch Foundation for their support of those facilities. A special acknowledgement is given to Damon Smith, Josh Bolinger, and Mark Andrews for help and patience with cleanroom instrument training. I also thank the University of Texas at Austin's Institute for Cellular and Molecular Biology and the Electron Microbeam Laboratories (Jackson School of Geosciences, The University of Texas at Austin) for the use of their microscopy equipment. I acknowledge NIL Technology and Niklas Hansson for their assistance in nanofluidic chip fabrication.

I am grateful to Donggao Zhao for his detailed instruction of electron microscopy methods, Julie Hayes for instruction in fluorescent microscopy, Dwight Romanovicz for acquisition of agarose SEM images, Kitty Milliken of the Bureau of Economic Geology for assistance in procuring shale samples, and my Statoil fellowship contacts Daniel

Ebrom and Beatriz Garcia-Fresca for project guidance and sample acquisition. I thank Rafael Longoria and George Shubieta for their introduction to and help with reflected differential interference contrast microscopy and access to the Nikon Eclipse Ti. I am also very grateful to Yashar Mehmani for helpful conversations on techniques to analytically solve the advection diffusion equation discussed in Chapter 4.

Furthermore, I would like to recognize Reynaldo Casanova and Heather Felauer for their help with administrative matters; Roger Terzain for his assistance with computer and software matters; Daryl Nygaard, Glen Baum, and Gary Miscoe for their assistance with machining and experimental setups; Rod Russel for his help with x-ray fluorescence; Vahid Shabro for fruitful research collaborations; David Medellin Salas for stimulating conversations and experimental guidance; Robert Starr, Behzad Eftekhari, and their research advisor Michael Marder for exciting molecular dynamics simulations collaborations; and all of the UT PGE staff for making the department a pleasurable environment to work in.

I am privileged to say that the list of wonderful and helpful officemates, classmates, and friends I have had here at UT and in Austin in general is too long to transcribe (in addition, I do not want to accidently leave anyone out!). Indeed, it was my peers and friends that made late nights of studying and working, necessary components of the graduate school experience, manageable and even enjoyable at times. In particular, I want to thank Ayaz Mehmani and Yashar Mehmani for motivating me to always try my best, hours of intriguing intellectual conversations, and the many fond memories I have of our adventures in Austin, TX.

I would like to acknowledge the undergraduate interns I had the pleasure of working with during my Ph.D.: Marisa Jasso, Virginia Bolivar-Baez, Alberto Tardio, and Yasmeen Farra. These talented individuals taught me about leadership in a research

setting and their help with research tasks was greatly appreciated. Speaking of pedagogical leadership, the education I have received here at UT is valuable beyond measure due to the thorough lesson plans and challenging assignments of the various professors I have taken courses with. I thank all of my course professors for effectively conveying their passion for the subject matter and skill sets to their students. Outside of the classroom, I would like to thank Maša Prodanović, who went above and beyond her professorial duties to organize enriching activities that I partook in, including the Team Energy running club and Explore UT.

ConocoPhillips is gratefully acknowledged for providing the FIB-SEM and SEM images and corresponding core data discussed in this dissertation and for access to the ConocoPhillips cluster computing facility. The FIB-SEM images and complementary core data analyzed or referred to in this dissertation (Chapter 7) were acquired by ConocoPhillips and Sandia National Laboratories (Albuquerque, NM). In addition, I recognize Tom Dewers and Hongkyu Yoon from Sandia National Labs for helpful conversations on digital rock physics and the lattice Boltzmann method.

This research was partially supported by the donors of the American Chemical Society Petroleum Research Fund (Grant #: 52817-ND9) and the Statoil Fellows Program at The University of Texas at Austin. The work is also supported by the University of Texas at Austin's Formation Evaluation Research Consortium, jointly sponsored by Anadarko, Aramco, Baker-Hughes, BG, BHP Billiton, BP, Chevron, COSL, ConocoPhillips, DEA Deutsche Erdoel AG, Det Norske, ENI, ExxonMobil, Halliburton, Hess, Maersk Oil, Paradigm, Petrobras, PTTEP, Repsol, Southwest Energy, Schlumberger, Shell, Statoil, Total, Weatherford, Wintershall and Woodside Petroleum Limited.

USING NANOFLUIDICS AND MICROSCOPY TO STUDY UNCONVENTIONAL PORE-SCALE TRANSPORT PHENOMENA

Shaina Alysa Kelly, Ph.D.

The University of Texas at Austin, 2015

Co-Supervisors: Carlos Torres-Verdín and Matthew Balhoff

Shales are unconventional geologic media primarily composed of nanopores. Once considered impermeable by conventional reservoir descriptions, these media have received attention in recent years due to their vast energy and sequestration potential. Actuating and quantifying fluid flow through shale matrix remains a formidable challenge. Nanofluidics (nanoscale lab-on-a-chip devices) are a promising approach to studying fluid transport anomalies in tight porous media, including shale, because they allow visualization of fluid phenomena and control of synthetic nanoscale geometry. Readily fabricated nanoscale "reservoir-on-a-chip" devices enable testing of geometry- and nanoconfinement-related hypotheses alongside core data. This dissertation discusses nanofluidic studies in different-sized nanochannels and nano-networks and the fabrication of these devices, including first of their kind "shale-on-a-chip" nanomodels. Most experiments documented herein were performed within two-dimensional (2D) silica nanochannels as small as 30 nm × 60 nm in cross-section; foundational results for other geometries are presented as well. Anomalous fluid transport trends were revealed through nanoscale imbibition experiments.

Liquid imbibition was captured with fluorescent microscopy and reflected differential interference contrast microscopy; dynamic flow data are rare in geometries that are nanoscale in two dimensions due to the limited resolution of optical microscopy. Imbibition of various wetting liquids in the arrays of horizontal, 2D silica nanochannels consistently demonstrated substantial divergence from the imbibition speeds predicted by the continuum Washburn equation for capillary flow as a function of hydraulic diameter and liquid type. Non-Washburn or non-diffusive front length-versus-time dynamics were also observed. These findings and other atypical imbibition data presented herein are explained by the enhanced influence the following phenomena at the nanoscale: surface forces at fluid-solid boundaries, the presence of quasi-crystalline thin films or boundary regions, and potential solid surface or boundary layer deformation due to meniscus-induced negative pressures (suction). This dissertation presents an experimental method and corresponding image and data analysis scheme that enable identification of the origin of imbibition irregularities in terms of transport variables: independent effective values of nanoscale capillary pressure, liquid viscosity, diffusivity, and interfacial gas partitioning coefficients were determined from imbibition within the tested nanochannels. The method can also be used in nano-networks and nanoporous materials. Phenomenological models were derived to match the nanofluidics data and include descriptions of effective diameter, effective capillary pressure, and effective liquid viscosity. The scalable implications of these findings and models for tight rocks and nanoporous materials are discussed in the context of fluid transport in shale.

A complementary study was conducted into the utility of digital rock physics in three dimensional models of nanoscale resolution rendered from focused ion beam scanning electron microscopy (FIB-SEM) images. Results indicate that FIB-SEM images below ~5000 μm^3 volume (the largest volume analyzed) are not a suitable volume for

extracting representative shale pore-scale networks, permeability, and other fluid transport properties. These findings strengthen the usefulness of nanofluidics in the study of unconventional rocks: nanofluidics fills the gap in quantifying pore-scale transport mechanisms where digital rock physics and indirect core analysis methods have limited scope and/or resolution.

Table of Contents

List of Tables

List of Figures

Figure 6.4: *Solid curves*: effective contact angles for the experimental fluids along the range of applicable nanochannel hydraulic diameters using the result of Eq. (6.18) (2D case). *Dashed curves*: effective contact angles using the result of Eq. (6.19) (3D case). θ_{eff} gradually approaches bulk contact angle θ_0 (mainly zero) as hydraulic diameter increases and rises steeply as hydraulic diameter decreases below 10 nm. For example, at D_H = 1 μm, θ_{eff} (3D case) = 14° and θ_{eff} (2D case) = 3° for isopropanol; cos(14°) = 0.970 and cos(3°) = 0.997. Recall that θ_{eff} is not representing an actual contact angle, but a correction due to surface force influences. The right plot is a close up of the region to the left of the leftmost dotted gray line in the left plot. The rightmost dotted gray line indicates the etched depth of the nanochannels.....167

CHAPTER 1: Introduction

If a problem is clearly stated, it has no further interest to the physicist.

Peter Debye, Nobel laureate in Chemistry

To begin with, the keywords of this dissertation's title are defined as they pertain to the work. **Nanofluidics** refers to the study or utilization of fluid flow in nanoconfinements. High resolution **microscopy** techniques are used to capture nanofluidics as well as characterize synthetic and geologic samples. **Unconventional** in the geoscience community refers to the properties of low permeability porous media/rock and **pore-scale** refers to the interstitial void spaces in a rock. **Transport phenomena** includes the subjects of momentum, energy, and mass transport and is studied at the macroscopic, microscopic, and molecular levels [1]; in this work, I discuss momentum and mass transfer at the microscopic and molecular levels. The following subsections introduce to the reader how these concepts relate to one another.

1.1 "WHY ARE WE MOTIVATED TO STUDY TRANSPORT IN NANOPOROUS MEDIA?"

Geologic porous media with a predominance of nanopores (often among micro-pores) include: shales, siltstones, slates, clays [2], mudstone, tight sandstones, low permeability carbonates, and carbonaceous materials (soots, coals/coalbed methane, kerogen) [3]. These low permeability or "tight" rocks are of interest to a number of earth science disciplines including petrophysics, geology, hydrology, and subsurface engineering due to their positions as unconventional hydrocarbon resources, caprocks (seemingly impermeable formations which trap underlying fluids), and potential

repositories for carbon dioxide and hazardous waste storage. In particular, shales and other mudrocks, once considered virtually impermeable, have received considerable attention in recent years because of their vast (but not easily accessible) hydrocarbon content generated in situ. If strategically produced, the world's currently identified shale formations have the capacity to provide energy security over at least the next few decades. However, hydrocarbon recovery from shales has raised concerns regarding the leakage of injected fluids to nearby aquifers [4] [5]. In addition, large amounts of injected water are lost to these low permeability formations during the hydraulic fracturing process [6]. The long-term integrity of these repositories for sequestration is another active research subject [7].

Natural and induced fractures are believed to be the key pathways by which water, fracture fluids, hydrocarbons, and sequestered fluids and contaminants can travel in shale and other tight media [8]. The characterization and importance of fluid transport within the nanoporous matrix between the hydraulically conductive fracture pathways is a challenging and debated subject. Figure 1.1 displays three scanning electron microscope (SEM) images of the local nanoporous matrix in an Eagle Ford shale sample. Knowledge of the permeability and imbibition/drainage interactions in shale matrices are vital in understanding long term production in shale reservoirs and the fate of injected fluids.

Actuating, understanding, and predicting fluid flow through unconventional media remains a formidable challenge. Macro- and mesoscopic measurements of shale samples will not necessarily reveal governing pore-scale interactions and transport phenomena, but will most likely be affected by them. Micro- and nanofluidics are a promising approach to studying transport anomalies in porous media, including shale,

because they allow control and visualization of fluid phenomena. Readily fabricated lab-on-a-chip devices with nanofluidic channels and/or networks enable testing of geometry- and nanoconfinement-related hypotheses alongside tight core data.

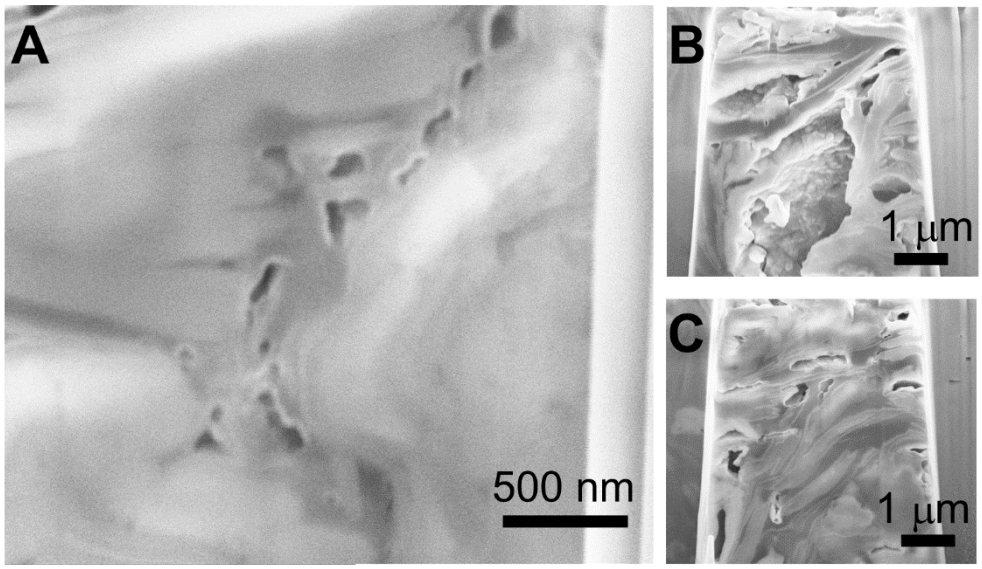

Figure 1.1: Focused ion beam - scanning electron microscope (FIB-SEM) images of an oil window Eagle Ford shale sample. (A) Close-up of sub-500 nm pores in the kerogen between clay-sized grains; (B) A relatively larger pore that appears to be an inter-particle pore and displays noticeable surface roughness; (C) A medley of inter-particle and organic matter associated pores with some evident clays.

This work utilizes fabricated nanofluidic chips to conduct controlled experimental study of imbibition, spontaneous displacement of a non-wetting fluid by a wetting fluid, and other transport processes in arrays of different-sized nanochannels (or nanocapillaries) and nanoscale networks. The fluidic patterns on previous lab-on-a-chip devices which simulate porous media (discussed subsequently) are microscale and/or homogenous. This work presents a simple and cost efficient fabrication scheme (Chapter

3) that results in dual-scale (nanoscale and microscale features), heterogeneous networks that resemble the perceived pore topology of shale. Quantification of disparities between the macroscopic equations used in conventional porous media and those applicable for nanopores can be assessed by experimentation in such fundamental and observable nanoscale geometries.

Interest in liquid behavior and the applicability of bulk transport solutions and physical property values within nanoconfinements spans beyond the geosciences. For instance, nano-membranes are actively studied for filtration, adsorption, and chemical separation purposes [9]. In addition, within the field of biomedical engineering, information on liquid transport in nanoconfinements is necessary for targeted drug delivery systems in nanoporous organs such cell membranes and the human brain where approximately 20 nm pores are filled with interstitial liquid [10].

1.2 PRESENT APPROACHES TO STUDYING TRANSPORT IN NANOPOROUS ROCKS

The majority of nanoscale pores in shale range greatly in connectivity, shape, and pore wall composition (varying clays, grains, or organic matter) [11]. This topology and textural complexity poses challenges in consistent core analysis methods, the application of classic thermodynamic and fluid flow models, pore-network and reservoir scale modeling, well log interpretation, and representative sample imaging.

1.2.1 Shale core analysis challenges

Core analysis is a key step in determining the porosity and permeability of a reservoir among other petrophysical attributes. Though estimates of these properties are also retrieved from well logs, the core data is regarded as the more accurate of the two.

There are currently no industry standards for shale core analysis. In fact, results are often inconsistent; Sondergeld et al. reported that when *identical* sample sets were sent to different laboratories permeability estimates reported differed an order of magnitude [12].

Well-practiced core analysis techniques for obtaining capillary pressure curves (indicating pore size distribution) from conventional media include mercury injection capillary pressure (MICP), the porous plate method, and the centrifuge method. A common conventional method for porosity is the Boyle's Law pressure chamber method and conventional measurements of Darcy permeability are performed by controlling pressure and monitoring flow rate (via Micro-CT scans, effluent, etc.). For shale these techniques must be retrofitted or changed altogether to account for smaller pores, much higher injection pressures, and the still undetermined nature of the nanopore connectivity. Furthermore, nanopores are beneath the resolution of most imaging instruments (e.g. Micro-CT) and require electron microscopy for visualization.

Core analysis techniques commonly applied to shales include pressure pulse decay testing of cores with helium (pressure transient analysis), MICP at much greater pressure thresholds, and crushing of the sample to allow greater access to pores (destructive method). Some creative analysis techniques such as nitrogen adsorption measurements based on capillary condensation and analyzing resident tracer concentrations via vaporizing micron-size holes in the sample [13] have also been employed on shale samples. In a departure from macro-scale experimental setups, Fadaei et al. developed a microfluidic device that encapsulated bitumen pieces to enable the study of fluid diffusivity in the bitumen [14].

However, all of these methods have uncertainties; for example, in pulse decay experiments induced microcracking cannot be eliminated consistently [15] and the use of

helium molecules may lead to an overestimation of gas permeability. Capillary condensation measurements are only indicative of pore size distribution to the extent the vapor-liquid interface (meniscus) adheres to Kelvin's equation. Retrofitting conventional core analysis techniques to honor the nanopores in shale is a valid effort assuming that the dominant physics at the macro- and micro-scale still govern at the nanoscale. An example of such retrofitting is the application of MICP to shale cores, where samples are subjected to pressures up to 60,000 psi (414 MPa) to enable entrance of non-wetting mercury into nanopores. The Young-Laplace equation for capillary pressure stipulates that at this high pressure limit pore throats of 3.8 nm diameter should be accessible to mercury [12], but the applicability of the Young-Laplace equation in a sub-5 nm confinement has not been clearly addressed by the petrophysics community.

1.2.2 Shale digital rock physics

Digital rock physics is the process of constructing three dimensional (3D) pore morphologies from image data and using those morphologies as a means of conducting virtual experiments (simulations). These simulations should be performed in a representative elementary volume (REV) or area (REA), which is defined as the smallest sample volume or area over which a measured attribute of a media renders a value representative of the bulk media itself [16]. Simulation results of conventional (microporous) rocks in Micro-CT-informed domains often match well against experimental measurements [17] and aid in assessing the sensitivity of petrophysical properties to changes in boundary conditions and transport parameters. Blunt et al. overview and discuss the overall outlook for digital rock physics and include challenges associated with imaging and simulating flow in shale [18].

Advancements in focused ion beam-scanning electron microscopy (FIB-SEM) imaging technology allow researchers to view consecutive slices of shale media in a microscale domain with a resolution generally as small as ~5 nm/pixel. The FIB-SEM image acquisition process is well documented; an overview of the process is included in Appendix D and Figure 1.2 displays an image of a FIB-SEM site. FIB-SEM shale

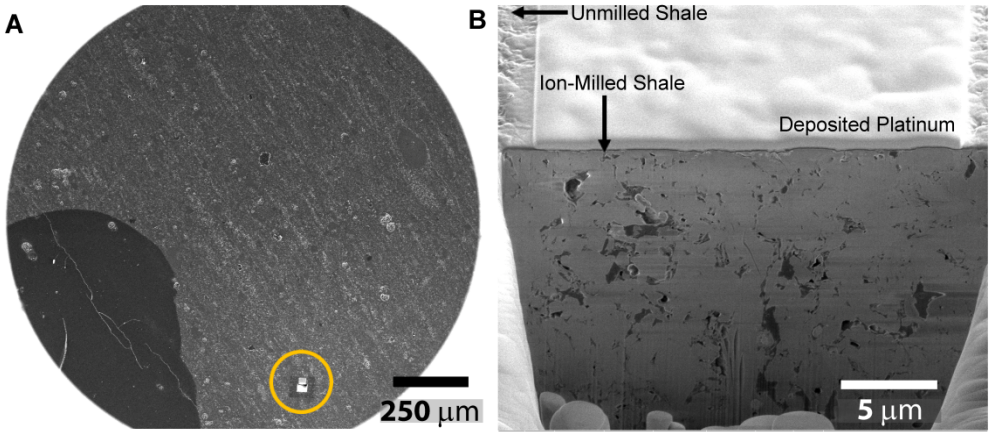

Figure 1.2: (A) Low magnification SEM image of an example of a mechanically milled/smoothed shale sample surface and the selection of a FIB-SEM site (within the circled region). (B) High magnification SEM image of the FIB-SEM site. Platinum is deposited onto the FIB-SEM site with the FIB-SEM instrument's (FEI Company) material deposition system. The platinum helps reduce the accumulation of impinging electrons or "charging". Images were provided by ConocoPhillips and Sandia National Labs (Albuquerque, NM).

image stacks are qualitatively informative, but their utility for quantitative analysis remains a subject of debate. Figure 1.3 displays images of a shale sample at different scales. The difficulty in finding an REV for shale may be due to the topologically heterogeneous nature of the media itself or the disparity between the length scale of the nanopores and the length scale of multiple connected pathways (high resolution imaging techniques such as FIB-SEM are limited in field of view). An important question

addressed in Chapter 7 is whether the microscale domain size inherent to FIB-SEM can capture representative network models of shale's nano- and micropores as well as macroscopic shale petrophysical properties such as porosity, mineralogy, and permeability. Furthermore, the practical utility of the extracted 3D models in the upscaling process is another open question. Acquisition of FIB-SEM images is currently an expensive task costing upward of several thousand dollars. Additionally, FIB-SEM image processing and subsequent flow simulations are typically very computationally intensive.

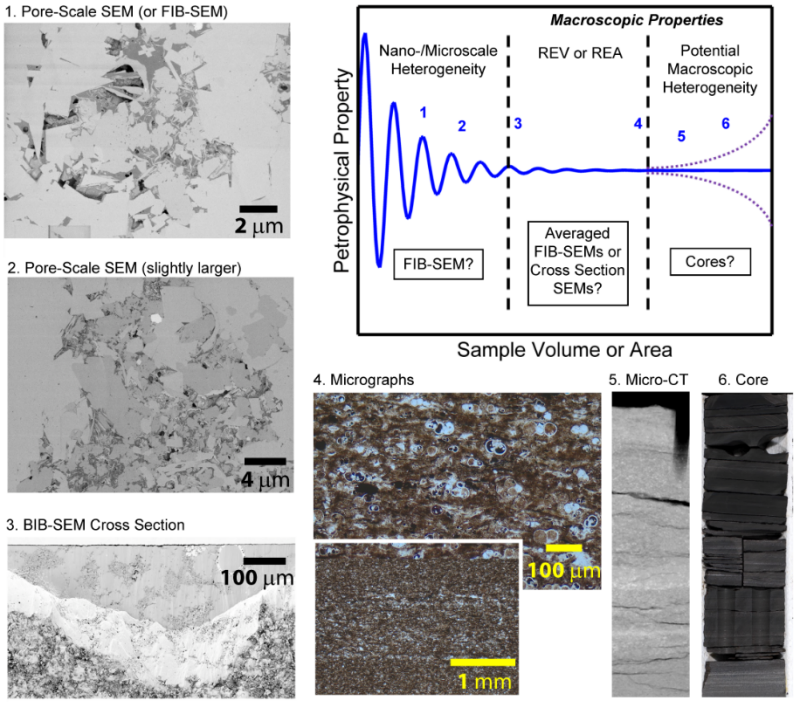

Figure 1.3: Example of scales of view, all from the same shale core sample, and how this analysis suggests they relate to REV. The REV diagram is adapted from Bear [19] and VandanBygaart [20]. Micro-CT images are 11 µm/voxel and the width of the presented image is approximately 11 mm. The core sample is on the order of centimeters, though most measurements were taken on crushed sample. Images were provided by ConocoPhillips.

1.3 NANOFLUIDICS AND LAB-ON-A-CHIP DEVICES

The use of nanofluidic devices in petroleum engineering is a nascent approach to can help answer nanopore-scale transport questions where core measurements, imaging, and simulations are insufficient.

Nanoporous materials such as zeolites and Vycor glass (Corning Inc.) have been used for years for mesoscopic nanofluidic studies of the response of a bulk material. Wafer-scale nanofabrication is rapidly progressing field that enables the controlled construction of nanoscale features on the surface of a substrate. Advancements include the creation of nanochannels of sizes less than 50 nm in one or two dimensions as well as complex features such as integrated electrodes. Micro-sized features are often incorporated to help interface nano-structures with the outside world. Common materials used in cleanroom nanofabrication include glass, silicon dioxide (silica), and silicon. Silicon, the second most abundant element on earth, is found in most rocks and minerals, including quartz, and thus is a suitable, hydrophilic material as a proxy for rock mineral surfaces. Polymers such as polydimethylsiloxane (PDMS) are often used to produce replicas of nanofabricated features in a more cost and timely manner by casting and curing the polymer on the fabricated master substrate. PDMS is hydrophobic and allows diffusion of gas through its matrix, two features which render this material similar to organic matter found in shale. Various bonding techniques, ranging from anodic bonding to oxygen plasma induced surface activation of certain substrates allow for the fabricated systems to be hermetically enclosed. The resultant miniscule systems or lab-on-a-chip devices are used primarily as either a platform for controlled study of phenomena of interest or to perform very specific tasks such as DNA separation; in this work I develop

and utilize lab-on-a-chip devices for the former purpose. Figure 1.4 displays some images of lab-on-a-chip devices from this work.

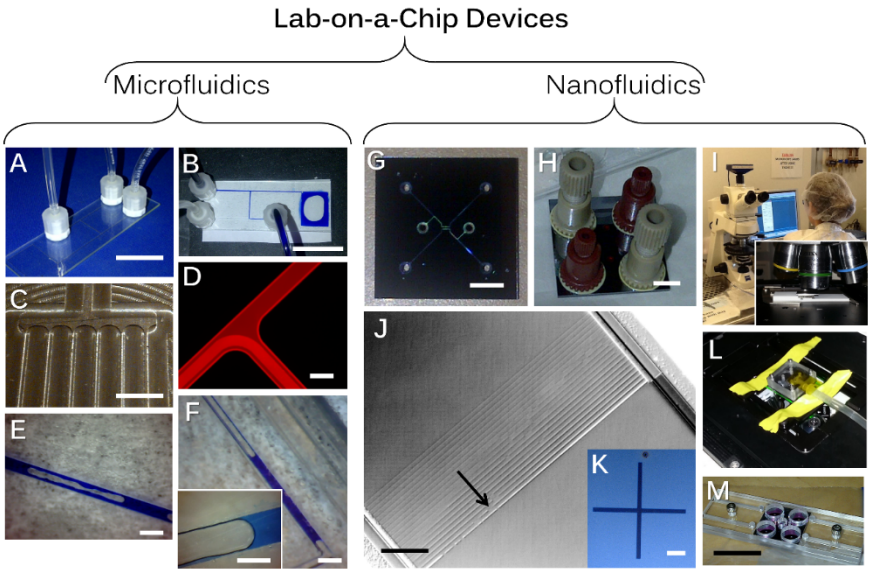

Figure 1.4: Images depicting examples of lab-on-a-chip efforts during the course of this work. Microfluidics was explored before transitioning to nanofluidics. (A)-(B) Glass microfluidic chips where water with blue dye in injected by means of a syringe pump (Q = 1 μL/min) and tubing (scale = 25 mm). (G)-(H) Silicon wafer-based nanofluidic chips with connection ports (Upchurch Scientific) for tubing connection (scale = 5 mm). (E)-(F) Visualization of menisci and prewetting films in microchannels is achieved with a standard optical microscopes (scale = 200 μm). In contrast, (I) high resolution research-grade microscopes such as the Zeiss Axioskop 2 MAT are required for detecting 2D nanochannels. (J) Liquid plugs (the black arrow points to one of these) are detectible in 2D nanochannels (scale = 40 μm), but far more challenging to characterize than those of microchannels; image displayed is the average of 130 consecutive images. In addition, (L)-(M) delicate chips often require chip holders for interfacing with equipment and microscope stages (scale = 25 mm). (D) Another useful type of imaging is fluorescent microscopy (scale = 80 μm). (K) A crosshair made for calibration purposes in a PMMA mask with electron beam lithography, a common method for generating nanostructures (scale = 60 μm). (C) A positive stamp with a microfluidic pattern made in steel with a CNC mill used for polymer casting (scale = 3 mm).

1.3.1 Utility of imbibition studies in nanoconfinements

Despite advances in nanofabrication, most nanofluidic investigations are either net measurements in nanoporous materials or studies of partially nanoconfined liquids in thin films and nano-slits. This experimental work is differentiated from many other nanoscale transport investigations by its use of observable two-dimensional (2D) nanochannels: 2D nanochannels are nanoscale in both cross-sectional height and depth, as opposed to one dimensional (1D) nanochannels or slits which are nanoscale in only one dimension (typically depth). The general underutilization of 2D nanochannels is often because researchers are presented with a number of challenges when performing experiments in observable and fully sub-micron nanoconfinements. Construction of functional nanofluidic devices requires a considerable amount of delicate fabrication steps and trial and error with cleanroom tool parameters. Once a nanofluidic device is successfully built, problematic tasks include interfacing the nanochannels with external detection apparatuses and fluid pumps, visualizing fluid flow in the channels or implementing other flow detection techniques, and keeping the nanofluidic devices from fouling.

Due to these technical challenges associated with nanofluidic experiments, the majority of the experimental work investigating liquid transport in nanoconfinements observes imbibition, the wicking of a wetting liquid into a dry medium, within 1D nanochannels. Because imbibition is driven by capillary pressure, liquid is drawn into the nanochannels naturally without implementation of an external pressure difference. Furthermore, interfaces between a dry and wet medium can be visualized with various optical microscopy techniques, especially when the width of the channels is on the order of microns (the case with 1D nanochannels). Researchers compare their length-versus-

time data to the Washburn equation [21] for imbibition in the viscous regime, assuming negligible changes in external pressure. Thus, liquid imbibition provides a mechanism for studying the effects of solid-liquid and solid-liquid-gas interfaces on nanoscale transport.

Atypical nanochannel imbibition results invoke several fundamental questions: Is deviation from the macroscopic imbibition solution amplified as the confinement size decreases? Which local phenomena are most responsible for atypical flow? In this work imbibition was also used as the method of liquid actuation, but experiments were performed in 2D nanochannels as small as 30 nm × 60 nm in cross-section. To my knowledge, this is the smallest nanochannel cross-sectional area directly observed and reported in a nanofluidic chip imbibition experiment to date.

1.4 EMERGENT NANOSCALE PHENOMENA

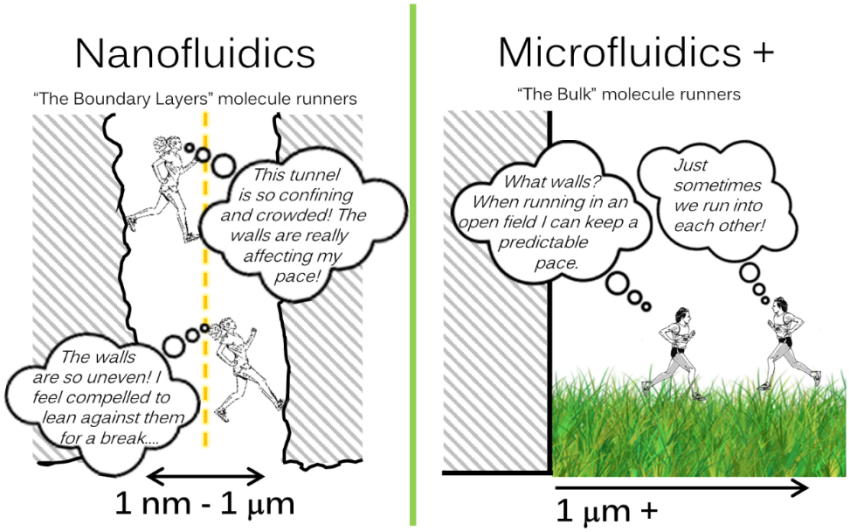

Figure 1.5: Cartoon of the effect of confinement on fluid molecules, which are analogously depicted as runners in a narrow tunnel versus and open-field.

There is a host of surface-related phenomena that are negligible at the microscale, but may affect hydrodynamic and diffusive flow at the nanoscale (see the cartoon in Figure 1.5 and the diagram in Figure 1.6). Nanofluidics gives researchers an opportunity to probe these emergent physics. This subsection details some of these potential phenomena for liquid and two-phase flow.

Due to the extremely small radii of curvature of nanoscale menisci, capillary pressure is considered to be the dominant force behind flow actuation or imbibition in nanoscale two-phase flow systems [22]. The Young-Laplace equation is the continuum description of capillary pressure and is commonly invoked in analysis of two-phase flow within porous media and microscale conduits. van der Waals forces, also known as long-range intermolecular forces, and other surface forces (electrical double layer, structural forces, etc.) prevail in thin films of fluid [23]. These thin films are of sub-micron thickness and bounded between other fluids and/or solid materials. The concurrent existence of capillary or bulk surface tension forces and local surface force phenomena in the vicinity of a solid-fluids boundary is accounted for in the augmented Young-Laplace equation [24] [25] [26]. However, in nanoscale conduits surface-force-dominated and transition regions occupy a significant portion of a conduit's volume and can even feel the influence of opposing channel walls [27], intensifying their effects.

While capillary pressure is the dominant flow actuation force at the nanoscale, viscous forces provide substantial resistance to flow. Liquid viscosity is often found to increase from its bulk value at this scale. One explanation for this divergence is the spatial prominence of structured boundary layers, which exhibit increased viscosity on account of surface force-induced ordering. The reported extents of these boundary layers varies greatly in the literature; for example, various experiments with water on

hydrophilic surfaces have found a range of boundary layer extents from 0.5 - 150 nm and beyond [28] [29] [30].

In addition, nanoscale pore or conduit diameters can be highly vulnerable to environmental conditions. The mechanical distortion of confining walls under the influence of stresses provided by capillary forces is known as elastocapillary deformation. This phenomena explains the coalescence of fibrous materials during imbibition [31] as well as the deformation or collapse of parallel plates and nano-and microstructures in the presence of small menisci [32] [33]. Elastocapillarity is highly relevant at the nanoscale due to both large capillary pressures and large specific surface areas, the ratio of a pore-space's surface area to volume. Imbibition/drainage, capillary condensation, and liquid evaporation all result in menisci and liquid plugs and may lead to a contraction of pores in nanoporous materials.

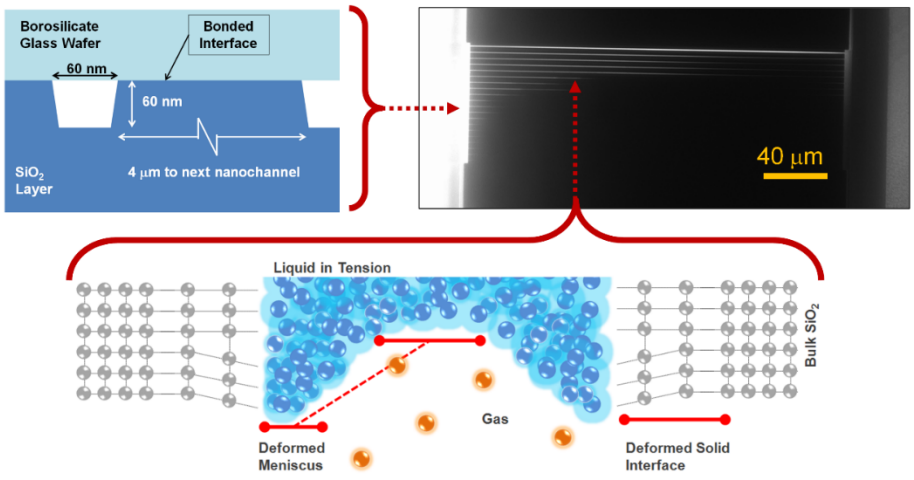

Figure 1.6: Phenomenological models for deformation of nanoscale menisci and solid interfaces are required to explain stymied imbibition (upper right fluorescent microscopy image) of various liquids into 2D lyophilic silica nanochannels (see Chapters 5 and 6 for details) and potentially other nanoporous domains.

Consequently, an important nanofluidics question arises: how influential are interfacial interactions and deformations on nanoscale menisci and hydrodynamics, and as a result, fluid imbibition and two-phase flow?

1.5 RESEARCH OBJECTIVES AND DISSERTATION ROADMAP

This dissertation addresses how nanofluidics can be used to investigate a fluid transport-related hypothesis for tight porous media. The prime hypothesis explored herein was that the properties of interfaces between confining walls and confined fluids need to be accounted for in transport equations describing flow through nanoscale domains. Specifically, long range intermolecular forces, the electrical double layer, resultant disjoining pressures, precursor films and corner flow, nanoscopic surface roughness, etc. highly influence liquid and multi-phase flow in nanopores. The organization of this dissertation is as follows:

Chapter 1 familiarized readers with the importance of understanding transport through a particular tight media, shale, and current challenges associated with studying shale. The chapter also introduced the field of nanofluidics and why it is likely that observed transport at this scale will differ from macro- and microfluidic studies.

Chapter 2 provides greater details on the aforementioned surface forces as well as background information on shale topology, relevant transport equations, and a literature review of complementary experimental work performed on the subject.

Chapter 3 discusses the developed methods for fabrication of nanochannel and nano-network fluidic chips and experimentation/observation in these constructed chips. Several relatively inexpensive and repeatable methods were arrived at through iterations

of the fabrication approach. These detailed methods can be used by others wishing to employ a nanofluidics approach to porous media studies.

Chapter 4 details an implemented experimental approach that allows the estimation of independent values of effective capillary pressures, P_c, viscosity, μ, diffusivity, D, and interfacial gas partitioning coefficients, k_H, in single 2D nanochannels.

Chapter 5 examines the nanofluidic results for various fluids in the chips and the disparities between these results and continuum or macroscopic predictions used in conventional transport models. Results include the decreased effective capillary pressure values, increased effective viscosity values, and non-diffusive trends. The nanochannels were studied more comprehensively than the nano-networks, of which only preliminary results are shown (the Future Work section details many uses for these chips). Imbibition was the most frequently studied transport mechanism.

Chapter 6 presents phenomenological models and semi-analytical descriptions of the physical interfacial mechanisms that control liquid and interfacial flow at the nanoscale. These models are based on the nanofluidic results and differ from some popular conceptions of nanoscale transport (e.g. enhanced flow rates by slip). In fact, the models describe the non-negligible role of fluid and solid interfacial deformations in these miniscule confinements. Descriptions of effective channel diameter, effective viscosity, effective capillary pressure, and scaling parameters, all useful values in petrophysical studies, are introduced. These values are informed by available macroscopic fluid and solid properties.

Chapter 7 addresses an investigation into the utility of another nanoscale approach to studying shale, FIB-SEM imaging and digital rock physics. These topics were introduced earlier in this chapter and are discussed in greater detail in Chapter 2. The

investigation detailed in Chapter 7 demonstrates that shale FIB-SEM images, used for shale digital rock physics, are useful mainly for qualitative purposes. This finding further strengthens the necessity of nanofluidic approaches for studying shale and retrofitting shale sample investigation approaches.

Finally, Chapter 8 discusses the major conclusions of the work and the practical implications and applications stemming from the findings. A substantial portion of the chapter is dedicated to recommendations for future research on the approach set forth in this dissertation.

CHAPTER 2: Background and Literature Review

What I want to talk about is the problem of manipulating and controlling things on a small scale…

I leave to your imagination the improvement of the design to take full advantage of the properties of things on a small scale…

Richard Feynman, Nobel laureate in Physics
Challenging others to explore nanotechnology.
From his lecture *Plenty of Room at the Bottom* (1959)

2.1 SHALE MICROFABRIC AND PORE-NETWORK TOPOLOGY

The nanopores in shale are generally classified into the following categories: organic matter pores, intergranular pores, and intercrystalline pores [34]. Visualizations of shale pores and pore-networks with an SEM reveal a locally ill-connected medium [35] [36]. Correlations between total organic carbon (TOC), porosity, and organic matter maturity in shales have been identified with laboratory measurements and advanced imaging techniques such as SEM. However, using field emission scanning electron microscopy (FE-SEM), Milliken et al. found an unexpected negative correlation between TOC and SEM-visible pores in Marcellus shale samples, even though they observed that the majority of pores visually detected were associated with organic matter inclusions [37]. Loucks et al. used argon ion beam milling and FE-SEM to identify organic nanopores mainly ranging between 5 nm and 750 nm in Barnett shale samples [11]. They found that porosity extracted from images greatly underestimated helium derived porosity. These authors suggested that many of the pores in the system are not visible

under SEM resolution, and are perhaps of Angstrom scale. Another possibility is that some pores captured with advanced imaging techniques are not present in situ at formation pressures and are generated when the core/sample is exposed to atmospheric pressure upon which it expands and expels gas. An additional viable contention is that the SEM-imaged domain may not *appear* connected because the sample has undergone severe nanostructural changes during its transport from the subsurface to ambient conditions and upon drying.

Notwithstanding poor local connectivity, several researchers have performed image analysis and fluid flow simulations on FIB-SEM image stacks of shale and other tight media with varying results. Yoon and Dewers carried out image analysis and permeability simulations with the lattice-Boltzmann method in FIB-SEM images from a Cretaceous chalk sample and found that around 2400 μm^3 of FIB-SEM images is a suitable REV for chalk [38]. Curtis et al. reconstructed 3D pore-networks and extracted geometric properties from the FIB-SEM image stacks of nine different shale formations; the volume of each 3D image was approximately 125 μm^3 [39]. The researchers examined only one reconstructed image per formation and found, overall, low pore connectivity and that extracted porosity was less than Helium-derived porosity. Bai et al. constructed a single 2500 μm^3 pore network from FIB-SEM images of Fayetteville shale and used the 3D structure to describe the sample's pore sizes and structure. Permeability was estimated with the adjusted Kozeny equation. However, the only macroscopic data comparison presented by the authors was a comparison with laboratory TOC values, which were in good agreement with the 3D model [40]. Finally, Shabro et al. used a very local shale FIB-SEM of 4.4 μm^3 in volume from the Eagle Ford shale to verify the application of several digital rock physics assessments including electrical resistivity for

different water saturations, slip flow and Knudsen diffusion, and Langmuir desorption and diffusion in kerogen (all investigated via finite difference methods) [41]. The authors did not claim that the 3D shale network was representative of bulk shale properties.

Transmission Electron Microscopy (TEM) and Helium Ion Microscopy (HIM) [42] are imaging methods that offer even higher resolution than FE-SEM. While TEM can provide a view of the interior of a thin sample (where "thin" equates to sub-micron sample thickness), sample preparation is challenging and the field of view is limited. HIM has higher resolution and less imaging artifacts than FE-SEM, but to my knowledge does not currently operate in tandem with a FIB and, thus, provides a 2D view. However, a comprehensive study conducted by the company Ingrain found that HIM imaging did not reveal any significant differences in sample pore volume (i.e. smaller pores) from that of FE-SEM [43]. Additionally, atomic force microscopy (AFM) is sometimes used to examine shale nanopores at high resolution and provides textural information, albeit also only a 2D view [44]. The most viable microscopy alternative to FIB-SEM for capturing a REV or REA is currently the broad ion beam SEM images (BIB-SEM) technique, which provides large sections of ion beam smoothed shale upon which a series of high resolution 2D "cross-section" images are taken [45].

Amidst the uncertainties with relevant pore morphology and pore-network topology, it is clear that the specific surface area (ratio of pore surface area to pore volume) of shale is much larger than conventional media. Consequently, fluid flow in the nanopore space is hypothesized to be dominated by interfacial physical and chemical phenomena. It is posited and confirmed herein that nanofluidic devices are more useful for investigations into these nanoscale phenomena than image-based digital rock physics.

2.2 RESERVOIR-ON-A-CHIP DEVICES

Disciplines such as mechanical, chemical, and biomedical engineering have primarily been at the forefront of utilizing micro- and nanofluidics. In recent years porous media researchers have utilized "micromodels", microfluidic devices with network patterns that resemble porous media, to improve understanding of pore-scale transport mechanisms in conventional reservoirs, especially focusing on enhanced oil recovery techniques. Gunda et al. constructed a microscale "reservoir-on-a-chip" that emulated the pore structure of natural rock and verified waterflooding in these networks [46]. Wu et al. performed single phase and multi-phase experiments in a microfluidic chip whose micro-network resembled a Voronoi tessellation [47]. Oostrom et al. benchmarked various numerical simulators against solute experiments performed in idealized and symmetrical micromodels composed of arrays of disc-shaped "grains" (posts) [48]. The literature abounds with examples of such micromodels; specifically, Karadimitriou and Hassanizadeh review the utilization of micromodels for two-phase flow studies [49].

Yet, to my knowledge, no successful nanomodels or "reservoir-on-a-chip" versions of shale ("shale-on-a-chip") have been reported prior to this work. Lab-on-a-chip or nanofluidic works pertaining to shale or nanoscale multi-phase flow have mainly investigated arrays of non-connected nanochannels [50] [51] [52], though most of these channels are only nanoscale in one dimension. Some works in non-geoscience fields have explored the diffusion of nanoparticles in uniform arrays of nanoposts [53], which are too homogenous and porous to accurately represent shale. Presumably, the inherent challenges and expenses associated with nanofabrication explain the current underdevelopment of porous media nanomodels; the construction of detailed nanoscale patterns is typically approached with lengthy, expensive, and relatively difficult methods

such as electron beam lithography and focused-ion beam milling. These challenges are circumvented with the use of appropriate widespread shadow masks, as detailed in Chapter 3.

2.3 RELEVANT IMBIBITION TRANSPORT EQUATIONS

The proceeding sections provide some background information on the physics and equations relevant to liquid imbibition, the type of nanofluidic experiment performed most frequently in this work. Additional details and equations for other relevant phenomena arise as needed within the proceeding chapters.

2.2.1 Capillary pressure

Capillary pressure is a phenomenon that occurs due to molecules at an interface seeking to minimize interfacial energy by assuming the lowest energy position at a three phase boundary (in petroleum systems this is usually a boundary of two immiscible fluids and a grain surface). High energy, polar molecules such as water will orient themselves towards the more polar phase at interfaces; silica and glass surfaces have significant polar and hydrogen bonding forces and thus are hydrophilic. Low energy, non-polar molecules such as hydrocarbons and air will prefer to adhere to low energy, non-polar hydrophobic surfaces such as silicones or organic matter. To maintain a stable, low energy system the bulk of the fluid will orient itself into a convex (hydrophobic) or concave (hydrophilic) spherical region called a meniscus. The Young-Laplace equation is ubiquitously used to describe this thermodynamic occurrence.

The Young-Laplace equation stipulates that the curvature, κ, at any point of a conventional, static liquid-gas meniscus is constant and governed by the point's

corresponding radii of curvature, R_1 and R_2. Specifically, two perpendicular planes intersect along the surface normal, $\vec{n}$, of the chosen point and the intersection of the planes with the meniscus interface produces two space curves with principal radii of curvature and centers of curvature lying on the surface normal vector. The product of the curvature and surface tension, γ, renders the macroscopic capillary pressure, P_c^m, between two fluids, namely,

$$P_c^m = \gamma\left(\nabla \cdot \vec{n}\right) = \gamma\kappa = \gamma\left(\frac{1}{R_1} + \frac{1}{R_2}\right). \tag{2.1}$$

Solid-liquid-gas contact angles are approximated by Young's equation, given by

$$\gamma_{sg} = \gamma_{ls} + \gamma_{gl}\cos\theta\ , \tag{2.2}$$

where γ_{sg}, γ_{ls}, and γ_{gl}, are, respectively, the solid-gas, liquid-solid, and gas-liquid interfacial tensions and θ is the "fixed contact angle" boundary condition for the Young-Laplace equation [54]. γ_{gl} is typically referred to as just γ as seen in Eq. (2.1). For lyophilic ("liquid loving") surfaces such as silica, liquid is the wetting fluid and gas is the non-wetting fluid. The simplest and most common form of the Young-Laplace equation is for a cylindrical capillary tube,

$$P_c = \gamma\frac{2\cos\theta}{r}\ . \tag{2.3}$$

Bulk capillary pressure in a rectangular conduit of dimensions $h \times w$, a firsthand approximation for the geometry of the nanochannels in this work, is then defined as [55] [56] follows:

$$P_c^m = 2\gamma\cos\left(\theta\right)\left(\frac{1}{h} + \frac{1}{w}\right). \tag{2.4}$$

At equilibrium, capillary pressure is equal to the difference in pressure between non-wetting and wetting fluids,

$$P_c\big|_{eq} = P_w - P_{nw} = -\gamma\kappa\,. \tag{2.5}$$

2.2.2 Viscous losses and the Washburn equation

Imbibition is the process where a wetting fluid invades a conduit or pore space occupied by a non-wetting fluid. This process is driven by capillary pressure, slowed down by viscous forces, and affected by any external body forces. The motion of the bulk or continuum portion of a fluid is described by analytical and numerical solutions to the Navier-Stokes equation for momentum transport:

$$\rho \frac{D\vec{u}}{Dt} = -\nabla P + \mu \nabla^2 \vec{u} + g_{ext} \ , \tag{2.6}$$

where ρ is fluid density, t is time, P is pressure, μ is fluid viscosity, $\vec{u}$ is velocity vector, and g_{ext} is the term that comprises external forces. If an imbibing liquid is considered to be the control volume, from the integral form of the conservation of momentum equation,

$$\sum F_x = \int_V \left[\frac{\partial (\rho u_x)}{\partial t} \right] dV + \int_S u_x (\rho \vec{u}) \cdot \vec{n} dS \ , \tag{2.7}$$

where x is the position along a channel, F are forces acting on the control volume, and the right hand side of the equation represents, respectively, the change in momentum of mass inside the control volume, V, and change in momentum flux across the surface of the control volume, S. For the case of imbibition in a horizontal channel (for a vertical channel there will be a gravity body force term), Eq. (2.7) simplifies to

$$\sum F_x = F_{capillary} + F_{viscous} = m \frac{d^2 x}{dt^2} + A \frac{1}{2} \rho \left(\frac{dx}{dt} \right)^2 \ , \tag{2.8}$$

where m is the mass of the fluid and A is the cross-sectional area of the channel. In the viscous regime, the right hand side of Eq. (2.8) or inertial effects becomes negligible, and imbibition can be described by Eq. (2.9), a quasi-equilibrium expression. Specifically, at the imbibition length, l, capillary pressure, P_c, is in equilibrium with the pressures of the nonwetting and wetting fluids, P_{nw} and P_w, taking into account viscous losses (Poiseuille flow) due to imbibition velocity, fluid viscosity, conduit permeability or hydraulic

conductivity, k, and imbibition length, l, and neglecting the viscous resistance of air, the non-wetting fluid such that

$$P_{nw} = P_l - P_c \tag{2.9}$$

and

$$P_l = P_w - \frac{u\mu l}{k} \ . \tag{2.10}$$

Thus, a decrease in capillary pressure and/or increase in viscosity results in decreased values of imbibition length and velocity. Setting $u = dl/dt$ in Eq. (2.10) and solving the resulting differential equation results in the Washburn equation (1921) [57], which gives the length of capillary imbibition as a function of time, where P_{ext} is any external pressures acting on the system:

$$l = \sqrt{\frac{2k(P_c + P_{ext})}{\mu} t} \ . \tag{2.11}$$

Eq. (2.11) is given in a general form, in terms of permeability, k. Capillary pressure is incorporated into Eq. (2.11) in the term which represents the sum of the pressures acting on the fluid. The analytical solution (from the Navier Stokes equation) for the permeability of a rectangular conduit is

$$k = \frac{h^2}{12}\left[1 - \sum_{n,odd}^{\infty} \frac{1}{n^5}\frac{192}{\pi^5}\frac{h}{w}\tanh\left(n\pi\frac{w}{2h}\right)\right] \ . \tag{2.12}$$

When the ratio of channel dimensions, w/h is >> 1 or << 1 (slit-like channels) the permeability approaches a parallel plate solution; i.e., simply

$$k = \frac{h^2}{12} \ , \tag{2.13}$$

or a bit less simplified [58],

$$k = \frac{h^2}{12}\left[1 - 0.630\frac{h}{w}\right] \ . \tag{2.14}$$

Per the format of Eq.'s (2.11) and (2.12), in the laminar flow regime, imbibition is expected to proceed faster in larger conduits. Note that intermolecular interactions between channel solid and fluid and are not considered in the above equations. Also note that gas mobility during imbibition is usually assumed infinite compared to liquid mobility.

2.2.3 Molecular theory of viscosity

Viscosity, μ, can be summarized as a resistance to flow when a stress or shear is applied that is due to the strength of intermolecular forces between liquid molecules. Liquid viscosity can be estimated with Eyring's theory [59],

$$\mu = \left(\frac{\delta}{a}\right)^2 \frac{\tilde{N}h_p}{\tilde{V}} \exp\left(\Delta\tilde{G}_0 / RT\right) , \tag{2.15}$$

where δ is the distance between molecular layers, a is length of jump a molecule must make to get to a vacant space, $\tilde{N}$ is Avogadro's number, h_p is the Planck constant, $\tilde{V}$ is liquid molar volume, R is the gas constant, T is temperature, and $\Delta\tilde{G}_0$ is the molar free energy of activation for a molecule to escape from a "cage" of neighbor molecules.

Liu and Li performed molecular dynamics simulations for pressure driven liquid flow between parallel plates with nanoscale apertures. They confirm that liquid flow rate, which is dependent on viscosity, can show notable variance from the macroscopic value in channels of $D < 50$ nm with increases in fluid-wall binding energy and particularly diverges when $D < 5$ nm [60].

2.2.5 Knudsen number

The Knudsen number (Kn) is a dimensionless number used to estimate whether fluid transport is in the continuum ($Kn < 0.001$), slip ($0.001 < Kn < 0.1$), transition ($0.1 < Kn < 10$), or free molecular diffusion ($Kn > 10$) regimes. It is defined by the ratio of the

mean free path of the fluid molecules, λ, divided by the confinement's length scale, L, namely,

$$Kn = \frac{\lambda}{L} \ . \tag{2.16}$$

For liquids, the transition from the continuum regime occurs around a channel diameter of 3 nm, per Eq. (2.16) [58]. Note that molecular dynamics simulations of nano-jets show that in the absence of pore walls nanoscale liquid transport follows continuum mechanics with jet dimensions as small as 10 molecules in each spatial direction [61]. However, the aforementioned simulations of Liu and Li [60] show a divergence from the Navier-Stokes equation at apertures of ~50 nm (150 molecular diameters) and lower [60]; the hydraulic diameter of the smallest conduits explored in this work is 40 nm. *Kn* values for gases are much larger than those of liquids, but highly pressure dependent, and are discussed in Chapter 7.

2.3 SURFACE FORCES

Fluid molecules experience attractive or repulsive forces within the local region where a fluid contacts a solid. Such forces are well known in the field of surface chemistry and are categorized as long-range intermolecular or van der Waals forces, osmotic or electrical double layer (or electrostatic) forces, and steric and structural forces [62]. Long-range intermolecular forces or van der Waals forces are the sum of the dipole forces between molecules, including London (dispersion interactions), Keesom (orientation or dipole-dipole interactions), and Debye (induction or dipole-induced dipole interactions) forces; thus, van der Waals forces are composed of both electrostatic (polar)

and dispersion (nonpolar) effects. Thus, there is a net force or pressure present within thin films or interfacial zones; this net force acts perpendicularly to the interface surface [63].

Local repulsion at surfaces with low affinity for liquids (lyophobic) is believed to be the molecular basis for hydrodynamic slip, evidenced by flow in carbon nanotubes where flow rates of water are reported to be several orders of magnitude higher than expected [64]. Regions affected by surface forces are given the term "boundary layers" and are defined to span on the order of a few nanometers from the solid interface when only long-range intermolecular forces are considered [65]. The effect of interfacial boundary layers on fluid transport is often negligible for conduits on the order of micro-scale and larger and is typically not considered in respective fluid flow calculations. However, in nanoconfinements, an increased pore surface area to volume ratio (specific surface area) increases the influence of boundary layers on fluid transport.

When two surfaces approach each other such that the distance between them is on the order of even tens of nanometers, their boundary layers near or overlap each other and an additional attractive or repulsive force is produced, depending on the properties of the surfaces and the fluids and the distance between the interfaces. This force manifests itself in the form of an additional pressure term, Π, called the disjoining (positive value; repulsive force) or conjoining pressure (negative value; attractive force). In a static system, the disjoining pressure is the difference between the pressure in the confinement and the bulk pressure at the inlet and outlet. Disjoining pressure was comprehensively introduced by Derjaguin in 1936 to describe thin films and is thermodynamically described as the Gibbs free energy per distance per unit area, or interface forces per unit area [63]. Disjoining pressure can be described by the superposition of the aforementioned surface forces, i.e. van der Waals, electrical double layer, and structural:

$$\Pi = \Pi_{vdW} + \Pi_{EDL} + \Pi_{s} \ . \tag{2.17}$$

Derjaguin's thin films are currently one of the more well understood nanofluidic systems, but that the disjoining pressure terms are derived for *static* conditions and films which are nanoscale in only one direction. In this work these surfaces forces are considered during *dynamic* capillary filling in nanochannels, nanoscale in two dimensions.

2.3.1 van der Waals forces

The theoretical extent of van der Waals forces from a surface is generally reported as several tens nanometers (hundreds of Angstroms) and this extent is typically divided into non-retarded and retarded zones. Retarded forces are also referred to as Casimir forces and decay faster than non-retarded forces [66] [67]. Retardation effects occur when confined molecules are relatively far enough apart that their dipole moments become out of phase faster than the electric field interactions between the molecules, which are limited by the finite speed of light [68]. Thus, retardation effects occur in only certain aperture or pore sizes. Theoretically, retardation effects occur at separation distances greater than 10 nm, but decay rapidly [69]; hence, retarded forces are not felt in confinements smaller than this threshold and become negligible beyond the nanoscale. However, experimentally, Israelachvili and Tabor observed that retarded forces are found in planar apertures above 50 nm [68], while Boström et al. found non-retarded forces in apertures as small as 3 nm [70].

An important variable in the description of van der Waals forces is the Hamaker constant, A_H, an interaction constant (with units of Joules) that is unique for each thin film system and that takes into account molecular interactions and the number density of

molecules in the solids/fluids surrounding the film [71]. For an aperture of distance d, the van der Walls component of disjoining pressure is

$$\Pi_{vdW} = \frac{A_H}{6\pi d^3} \ . \tag{2.18}$$

Specifically, calculations of A_H account for induction, orientation, and dispersion van der Waals forces, dependent on fluid and material properties, and allow these intermolecular interactions to be considered from a continuum perspective. The macroscopic approximation for A_H with by Lifshitz mean field theory [69] is

$$A_H \approx \frac{3}{4} k_B T \left(\frac{\varepsilon_1 - \varepsilon_3}{\varepsilon_1 + \varepsilon_3} \right) \left(\frac{\varepsilon_2 - \varepsilon_3}{\varepsilon_2 + \varepsilon_3} \right) + \frac{3 h_p \nu_e}{8\sqrt{2}} \frac{(n_1^2 - n_3^2)(n_2^2 - n_3^2)}{\sqrt{n_1^2 + n_3^2}\sqrt{n_2^2 + n_3^2}\left(\sqrt{n_1^2 + n_3^2} + \sqrt{n_2^2 + n_3^2} \right)} , \tag{2.19}$$

where k_B is the Boltzmann constant, ν_e is the main electronic adsorption frequency (~ 3.0 × 10^{15} Hz for most organic liquids [72]), and ε_i and n_i are the dielectric and refractive constants of a respective phase i. The non-retarded van der Waals force per unit area decays as $1/d^3$, while the retarded van der Waals force per unit area decays as $1/d^4$; A_H values differ between these regimes [68].

Derjaguin performed calculations for polymolecular adsorption and condensed menisci shapes as a result of the influence of van der Walls forces in narrow pores [73]. "Narrow" is defined as the spacing between parallel plates that results in a complete overlap of long range intermolecular force fields (several nanometers, smaller than the nanochannel widths and heights studied in this work).

2.3.2 Electrical double layer forces

Many materials, such as silica, clay, kerogen, and even PDMS [74], gain an accumulated charge at their surface when in contact with ionic liquids due to the interaction of ions with the immobilized charge of the wall material itself. The electrical

double layer (EDL) is the term used for the ionic environment in the vicinity of this charged surface, which consists of a bound layer of ions called the Stern layer as well as a diffuse layer of ions. The thickness, λ_D, of the EDL is, among other factors, inversely proportional to the ionic concentration of a solution and can range in size from 0.1 – 100 nm [58]. An approximation of λ_D can be made for a monovalent electrolyte,

$$\lambda_D = \frac{1}{e}\sqrt{\frac{\varepsilon k_B T}{\sum_{i=1}^{2} z_i^2 \, n_i^0}} \ , \tag{2.20}$$

where z_i is the valence number of the ionic species of the system, e is the elementary charge, and n_i^0 is the bulk concentration of the said ionic species. Furthermore, the electric potential distribution, Ψ, which comprises the EDL is analytically described by the Poisson-Boltzmann distribution,

$$\nabla^2 \Psi = -\frac{e}{\varepsilon}\sum_i z_i n_i^0 \exp\left(-\frac{z_i e \Psi}{k_B T}\right) \ . \tag{2.21}$$

Solutions for Ψ in various geometries of interest, including parallel plates and cylindrical and rectangular conduits can be found in the literature. There are several equations derived from the Poisson-Boltzmann distribution which describe the contribution of the electrical double layer to disjoining pressure. For example, Eq. (2.22) is popularly used and assumes relatively low zeta potentials between identical surfaces with a slight EDL overlap:

$$\Pi_{EDL} = \frac{2\varepsilon\varepsilon_0}{\lambda_D^2}\Psi_0^2 \exp\left[\frac{-d}{\lambda_D}\right] , \tag{2.22}$$

where Ψ_0 is the surface potential of the solid. Solutions for binary ionic systems, high zeta potentials, and non-identically charged planes exist as well.

The electrostatic pressure contribution is always repulsive, but only relevant when ions are present. Electrostatic forces are prevalent in aqueous solutions (note that the

majority of the liquids tested herein are nonaqueous). The EDL is present in bound water films and "conductive clays" in shale and greatly affects electrical resistivity measurements. Research in the field of colloid science has even suggested the formation of very large double layers (almost an order of magnitude higher than that that of aqueous fluids) in non-polar fluids, such as oils, in the presence of an ampholytic electrolyte due to a greatly reduced screening layer [75].

While only incorporated as a boundary condition in microchannels, the relative size of the EDL (and possible overlap in some pores) may have a substantial effect on liquid flow in nanopores. An example of such is the electric field caused by a natural streaming potential (moving ions) which can counter menisci or pressure driven flow, decreasing permeability. In some applications the EDL can be used to create a "nanofluidic diode" where the overlap of regions of high counter-ion concentration allows for selective sieving of particular ions or molecules via electrostatic repulsion; this occurrence is described in greater detail in Chapter 8. Revil and Pessel [76] discuss that electroosomotic flow can be used to move liquids through shale in cases where mechanical pumping is insufficient due to low permeability and can even, without a fluid pressure gradient, be used for precise permeability estimates of these low permeability rocks.

2.3.3 Structural forces

Liquids undergo molecular ordering and adhesion in the proximity of a hydrophilic surface and this effect is amplified in confinements whose size approaches the order of several molecular diameters leading to structural forces [77]. Denser packing of molecules equates to a liquid density increase in the associated region. Short-range

solvation forces are prominent only within approximately a nanometer from an interface and decay rapidly, while long range solvation forces remain a controversial topic [77].

2.4 EXPERIMENTS PROBING BOUNDARY LAYER EXTENTS

There is a division in the literature with regard to boundary layer influence on liquid transport. Numerous surface-force balance (SFB) and atomic force microscopy (AFM) experiments on thin films have reported boundary layers of around several nanometers or less [78] [79]. Specifically, SFB experiments indicate that the effective viscosity of films of deionized (DI) water increases no more than three times its bulk value even when confined to approximately 1 nm thickness [78], but that the effective viscosity of films of organic solvents (such as isopropanol) diverge greatly when several nanometers thick [80]. On the other hand, interfacial force microscopy (IFM) experiments report that the effective viscosity of a DI water meniscus between a carboxyl terminated hydrophilic tip and surface within 1 nm of interfacial separation is seven orders of magnitude higher than that of bulk water [81]. This viscosity is similar to that of structured, quasi-crystalline fluid. The development and nature of boundary layers is extremely sensitive to material and fluid properties; in fact, IFM tests on silicon surfaces have found viscous water films to completely disappear when the surface is treated to become more hydrophobic [81].

Experiments performed with water in glass membranes of a 3-4 nm average pore diameter have indirectly observed increases in apparent viscosity of around 1.6 times higher than water's bulk value, evidencing thin boundary layers of several molecular diameters. Additionally, increases in viscosity from 1.5 times to zero were observed in cylindrical quartz capillaries on the order of 30 nm to 1 μm in diameter through a

thermostatted bath with a horizontal comparator and the use of external pressure assemblies [65]. These increases in effective viscosity support theories that viscosity increases most significantly within only several molecular diameters from hydrophilic interfaces.

On the other hand, another body of experiments report vastly different findings in regard to the extent of boundary layers. Those works describe a region of structured layers of liquid molecules near hydrophilic or charged surfaces that are inherently more viscous than the bulk fluid and extend on the order of microns. Such regions are often termed *exclusion zones* because they exclude other molecules or impurities in the local system, thus suggesting a different molecular structure or ordering in the zone. The most commonly studied liquid for the exclusion zone phenomenon is water. Some authors theorize that exclusion zones are actually quasi-crystalline in structure, composed of layers of hexagonal units which have some fluidity due to slip between layers [82]. The hypothesis behind liquid crystal boundary layer growth is that liquid molecules align themselves in multiple layers along a surface, nucleating until disrupted by shearing or thermal motion effects (Brownian motion) [83]. Evidence for the existence of exclusion zones includes numerous microscopy experiments that observe micro-beads, biological materials, and tracer molecules in aqueous solutions and clearly capture a void zone on the order of microns thick at water-solid surfaces [84] [85] [86]. Further exclusion zone evidence is found in experiments which show that less hydrophilic surfaces generate smaller void zones, and data of destruction of these void zones with an increase in temperature (higher thermal motion) [85] [86]. Recently, experiments in Nafion tubes have suggested that exclusion zones can also form near hydrophilic surfaces in polar

liquids other than water; one of the polar fluids this phenomenon was seen in was isopropanol [87], a fluid used frequently in this work.

While boundary layers on the order of several molecular layers, the more popular of the boundary layer views presented herein, are too thin to explain anomalous increases in nanochannel hydrodynamic resistance detailed later in Chapter 5 of this work, the exclusion zone argument typically discussed in the literature describes zones extending at least several microns from free surfaces. This size is, of course, not applicable in the scope of nanoconfinements. It is logical that the extent of boundary zones decreases considerably for non-quiescent fluids and non-ideal surfaces. That is, in addition to viscous shearing and thermal motion, boundary zone growth can be tapered by surface roughness because the formation of multiple planes of growth can create destructive interference. Additionally, experiments have shown that impurities in solutions actually limit exclusion zone growth [82].

Looking at polymeric fluids, 15-20 nm boundary layers have been reported for experiments of polydimethylsiloxane flows on steel [88] and experiments with nitrobenzene on lyophilic surfaces have found boundary layers spanning 40-60 nm thick at room temperature [65]. Pashley and Kitchener found evidence of structured multilayers on the order of 150 nm thick for quiescent water on clean quartz using ellipsometric techniques [89].

2.5 NANOFLUIDICS IMBIBITION AND MENISCI EXPERIMENTS

Microchannel imbibition experiments in rectangular glass and polymer microchannels both show very close agreement with the Washburn equation [90]. Conversely, nanochannel imbibition experiments in rectangular nanochannels report

considerable negative deviations from the Washburn equation, but vary in the choice of channel material and size, fluids used, extent of deviation from the analytical solution, and explanation of the results [91] [92] [93] [94]. Possible explanations for irregular imbibition in nanochannels proposed in the literature include increased boundary layer viscosity and deformed dynamic menisci due to the influence of long-range intermolecular forces [91] [92] [93], channel roughness [95] [22], capillary condensation and thin films [96] [24], bubble entrainment behind an advancing meniscus [97], and even cavitation and nanochannel deformation [98] [91].

From length-versus-time data alone it cannot be discerned whether discrepancies between nanochannel imbibition and bulk behavior lie with the value of viscosity used, Laplace's definition of the liquid-gas interface shape, Young's definition of the solid-liquid-gas contact angle, or a combination of effects, since these terms are all multiplied by one another in the Washburn equation. For example, Haneveld et al. [91] used narrow slit channels of dimensions 20 μm × 5 nm composed of silicon dioxide on three sides and borosilicate glass on one side and found that the imbibition rate for DI water was less than predicted by the Washburn equation by a factor of 2.6. They systematically discounted channel deformation as the cause of decreased imbibition and, assuming the macroscopic values of capillary pressure, attributed the inability to meet the Washburn equation to an increase in boundary layer viscosity. Phan et al. [92] observed that the effective viscosity of isopropanol was almost two times its bulk value from early time data in closed-end 10 μm × 45 nm planar silicon nanochannels also assuming the macroscopic definition of capillary pressure. The consensus from these works is that within 1D nanochannels liquid imbibes slower than predicted by the Washburn equation, but roughly follows the expected $t^{0.5}$ trend [91] [92].

Fluid flow experiments in 2D nanochannels are rare due to difficulty in nanochannel visualization, but can be found in the work of Han et al. [93] They performed experiments in channels ranging from 27 nm × 500 nm to 50 nm × 900 nm in size and composed of silicon dioxide on three sides and silicon nitride on one side. Han et al. explain their slower imbibition results in terms of large dynamic contact angles; they back-calculated dynamic contact angles for DI water on silica as high as 68°.

Experimental evidence of irregular menisci and breakdown of the Young-Laplace equation have been documented in the literature. For low viscosity polymer flow in 2D nanochannels, Kim et al. observed hindered imbibition and additional menisci curvatures near the solid-liquid-gas interface with reduction in channel cross-sectional area [99]. The authors solidified the polymer during imbibition with UV-activated cross-linking and extracted the cured fluid strips from the nanofluidic chip for inspection with an SEM. Near plug-like menisci were observed in channels 50 nm in width due to overlap of the aforementioned curvature regions. Although the experiments were not performed in silica nanochannels, the channel sizes were similar to the ones used in this work. Those irregularities in the vicinity of the fluid-solid interface were attributed to long range intermolecular forces, but rigorous models for this effect were not derived. Honschoten et al. captured an image of a nanoscale water meniscus bridging a surface and an incident probe with an environmental scanning electron microscopy (ESEM); for the given chamber humidity, the radius of the meniscus was much larger than predicted by the macroscopic Kelvin equation (which includes the Laplace pressure assumption in its definition) [100]. Another study utilizing an ESEM captured unconventional menisci curvatures and slow filling of water in sub-200 nm carbon nanotubes with disordered walls [101].

In regard to single phase liquid flow, non-microscopy experiments performed by Tamaki et al. in 380 nm x 240 nm silica nanochannels reported velocities were slower than Poiseuille flow such that the apparent viscosity for water was 2.5 cP (as opposed to 1 cP) [102]. Meanwhile, experimental work in carbon nanotubes has reported water velocities on the order of thousands of times higher than those predicted by Poiseuille flow [103]. However, these carbon nanotubes are essentially frictionless, which is not the case in shale pores (as displayed by some of the exposed inner pore surfaces in Figure 1.1) or glass/silica nanochannels. It is clear that surface roughness, more pronounced in smaller pores and channels, may also play a significant role on nanoscale transport anomalies.

On the computational front, molecular dynamics (MD) simulations of nanoscale imbibition or liquid-gas interfaces have primarily focused on water uptake in graphene and carbon nanotubes [104], menisci between a surface and AFM tip [105], and thin films on nanostructured surfaces [106]. The extensive computational times and memory-intensive nature of MD simulations restrict these models to localized (nanoscale) studies and simulation times on the order of several pico-seconds; "snapshots" of menisci situations are required to simulate a longer process such as imbibition. Another approach, the lattice Boltzmann Method (LBM), a mesoscopic modeling method, allows for the incorporation of body and interparticle forces between meso-"particles" representing molecule distributions by a probability density function, $f(\mathbf{r},\mathbf{p},t)$. LBM is discussed further in Chapter 7.

CHAPTER 3: Nanofabrication Methods and Experimental Techniques

Now comes the interesting question: How do I make such a tiny mechanism? I leave that to you.

Richard Feynman, Nobel laureate in Physics
Challenging others to explore nanotechnology.
From his lecture *Plenty of Room at the Bottom* (1959)

Experimentation with a variety of liquids in a range of nanoconfinements enables a comparison of imbibition anomalies on the basis of fluid and geometric properties. Experiments were conducted at room temperature and ambient conditions.

Unlike shale, fluid interfaces and tracers in the transparent nanochannels and nano-networks of nanofluidic devices are directly visible with optical microscopy techniques. This approach allows direct control or quantification of each device's channel sizes or network topology and other geometrical properties, including pore size distribution and connectivity. In actual shale samples, such properties are only inferred and are uncertain due to the limitations of common petrophysical analytical techniques and sample imaging methods (for a review of those limitations see Section 1.2.1).

3.1 DEVICES WITH A PORE-SIZE DISTRIBUTION OF 2D NANOCHANNELS

Nanofluidic chips that contain an array of twenty parallel nearly rectangular 2D nanochannels were constructed to mimic the types of cross-sectional areas seen in shale pores; Figure 3.1 shows an example of the likeness of the synthetic cross-sections to SEM-imaged shale pores. This simple channel geometry enables comparison against bulk

analytical transport solutions. Three sides of the channels are silicon dioxide, SiO_2, and one side is borosilicate glass. The nanochannels are all 60 nm in depth and range in width from 30-500 nm. Specifically, the widths of the 20 nanochannels are (triplicates and duplicates of certain channel widths are indicated in parenthesis): 30, 40, 50 (3), 60, 70, 80, 90, 100 (2), 120, 150 (3), 175, 200 (2), 250, and 500 nm. For reference, the established diameter of a water molecule is around 2.8 Å, which means that the width of the chip's smallest channel equals around 100 water molecules stacked on top of one another. The channels are 250 µm long, L, which, combined with a nanoscale cross-section, results in extremely high hydraulic resistivity. Still, the liquid capillary pressure in these channels is theoretically, per the Young-Laplace equation, strong enough to traverse the entire 250 µm length in less than a second, even with substantial viscous drag. The length of the nanochannels was necessary to facilitate observation of the interface position during the relatively short timescale of the imbibition experiments.

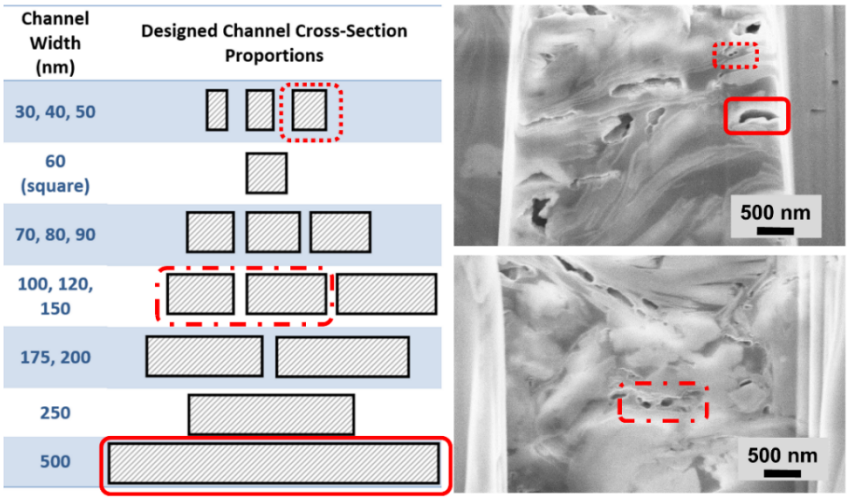

Figure 3.1: Illustration of the distribution of approximate channel cross sections and their spatial similarity to shale pores revealed with FIB-SEM (Eagle Ford shale sample).

3.1.1 Fabrication materials and methods

These nanofluidic chips were constructed through a series of fabrication steps. The fluidic patterns were constructed on a 100 mm diameter, 500 μm thick silicon wafer with a 1 μm thick layer of silicon dioxide. These patterns were written with electron beam lithography on a spin-coated layer of polymethyl methacrylate (PMMA). After the application of a developer solution to create a mask in the PMMA, reactive ion etch (RIE) was used to transfer these pattern a depth of 60 nm into the silica. The PMMA mask was subsequently dissolved. Note that there is approximately a $\pm$ 10 nm vertical tolerance associated with this etching method [107]. Next, 80 μm wide microchannels were patterned into the silicon dioxide on opposite ends of the nanochannel array with the same procedure and etched to a depth of 1 μm with reactive ion etch. Thin layers of chromium (Cr) and then platinum (Pt) were sputtered onto portions of the low aspect ratio microchannels by means of a masking procedure. The purpose of the metal films and the unusual configuration of the microchannels (see Figure 3.3) were for the creation of electrodes that spanned from the entrances of the nanochannels to electrical connection points on the chip; measurements utilizing these electrodes are not explored in the work presented in this dissertation.

Through-holes 1 mm in diameter were made in the silicon wafer for fluid inlet and outlet ports. After cleaning both substrates with a piranha solution, an anodic bonder was used to bond the oxidized silicon wafer to a 200 μm thick borosilicate glass wafer. Piranha solution (4:1 H_2SO_4/H_2O_2) is a strong oxidizing agent that is especially useful for removing organic contaminants from surfaces. In addition, oxidizing agents add hydroxyl groups to a substrate's surface (silanol groups in the case of glasses/silica). Clean and hydroxylated surfaces correspond to hydrophilic or lyophilic wetting conditions. Finally,

the bonded wafers were diced into a batch of approximately 20 mm-wide square nanofluidic chips.

Figures 3.2 and 3.3 display, respectively, SEM images of some of the nanochannels and optical microcopy mages of the fluidic network of a chip, as well as schematics of the fluidic cross-sections. The two low aspect ratio (one cross-sectional dimension is significantly larger than the other) microchannel/nano-slit pathways serve as conduits to the adjoining array of 2D nanochannels of different sizes.

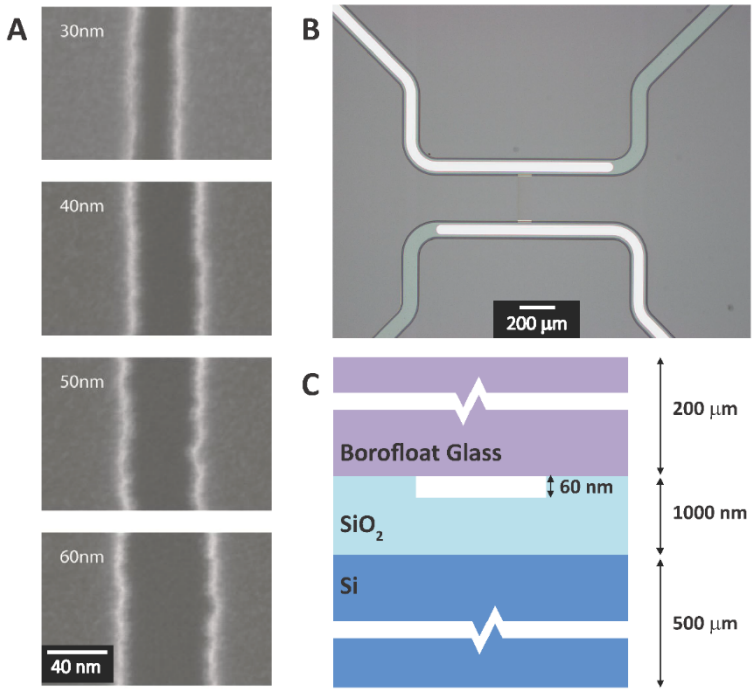

Figure 3.2: (A) Secondary electron SEM images of a selection of the smaller nanochannels. (B) A brightly illuminated reflected microscopy image of the main fluidic pathways in the nanofluidic chips: an array of nanochannels (center and barely visible) bridging between two microchannels, each of which has a respective inlet and outlet. (C) Schematic (not to scale) of a local cross-section of the nanofluidic chip materials where a nanochannel is the 60 nm deep aperture.

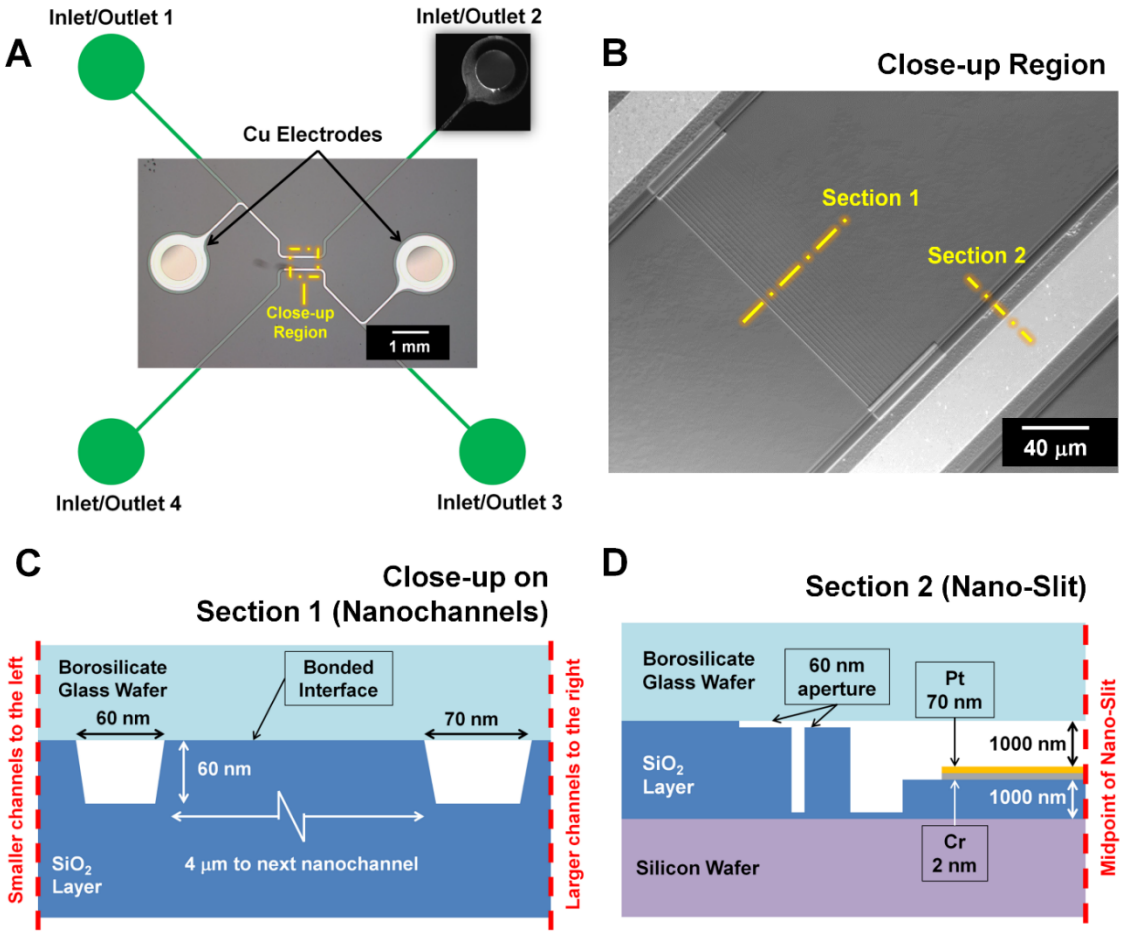

Figure 3.3: (A) Schematic of the nanofluidic chip design with an inset brightfield microscopy image of the fluidic network of two low aspect ratio microchannels/nano-slits with an array of nanochannels connecting them. The copper electrodes flanking the nano-slits were not utilized in this dissertation. (B) Reflected differential interference contrast microscopy images of a nanochannel array and adjoining low aspect ratio microchannels (nano-slits) in one of the nanofluidic chips. (C) Schematic cross-sections (not to scale) of two of the nanochannels. (D) Schematic cross-sections (not to scale) of half of a nano-slit. Thin layers of chromium (Cr) and then platinum (Pt) were sputtered onto portions of the low aspect ratio nano-slits. The original purpose of the metal films and the unusual configuration of the nano-slits were for the creation of the aforementioned electrical connections; again, measurements with these electrodes were not explored in this dissertation.

The nanochannels exhibit surface roughness characteristic of reactive ion etch (RIE) and 85˚ sidewall tapering, which renders them slightly trapezoidal in cross-section; both of these artifacts are typical to dry etching processes such as RIE. Mannion et al. reported nanochannel floor roughness (hillocks) of 10-20 nm as a result of RIE [108]. Figure 3.4 depicts an example of the 2D nanochannel cross-section. Most natural nano-confinements exhibit surface texture similar to such nanochannel surface roughness; this is especially true in geological nano-confinements (see Figure 1.1.B of shale pores).

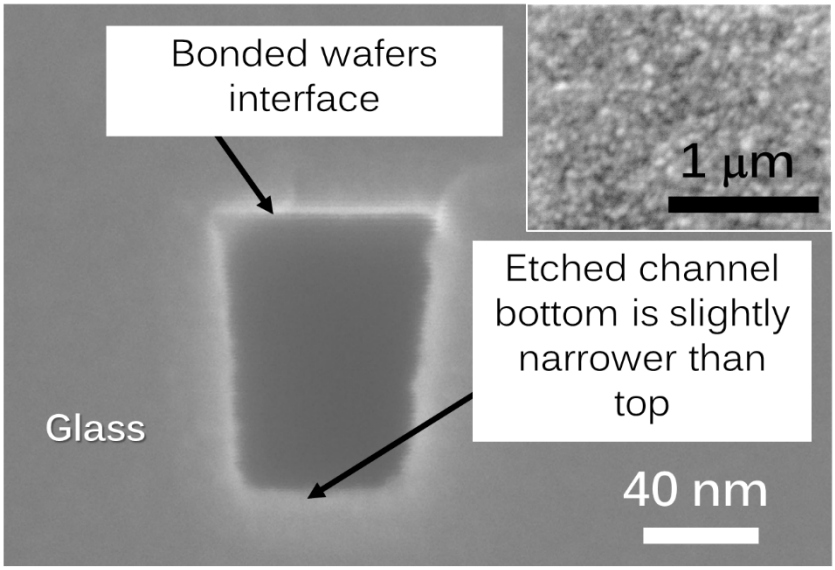

Figure 3.4: An SEM image (accelerating voltage: 15 kV, detector: in-lens secondary electron [SE], working distance: 2.1 mm) of the cross-section of an approximately 60 nm trial nanochannel etched in a glass wafer displays the channel's slight trapezoidal geometry. The nanochannel bottom and right walls (etched regions) are not atomically smooth. Image provided by contracted NIL Technology using the MC2 Chalmers nanofabrication laboratory. *Inset:* top-view SEM image (accelerating voltage: 15 kV, detector: SE, working distance: 9.9 mm) of the surface roughness produced on a silicon wafer as a result of RIE etching with CF_4.

3.1.2 Limitations and obstacles

The greatest limitation of the nanofluidic experiments in the 2D nanochannel array chips as well as in general was fluid control and chip fouling. Because the region of fluid entrance is a microchannel only 1 μm high the creation of a small air bubble at the entrance or the presence of some particulate matter from the ambient atmosphere can make fluid entry very difficult (this is especially so for fluids with higher surface tensions such as water). Successful methods for entry of high surface tension liquids include reducing the pressure at the outlet by inducing a vacuum at those ports, mixing a wetting agent (i.e. an alcohol) with the fluid of interest at a specific ratio, or cleaning the chip inlets with compressed air or oxygen plasma. Proper storage of chips if another factor to consider. It is recommended to fill the chips with DI water while they are not being used since surfaces easily foul in air environments. Storage in a desiccator to limit relative humidity is another option. Additionally, inlet/outlets of chips stored in air can be protected with non-residual tape (wafer dicing tape is a suitable option).

Potential non-ideal experimental conditions include excessive surface roughness in the nanochannels induced by the RIE process, possible inconsistencies in channel width along the channel lengths (inconsistencies are caused by electron beam "drift," but should not exceed several nanometers), any impurities in the IPA, and the formation and influence of a monolayer or thin film of liquid bound to the glass or silica surfaces. Such a monolayer may be present even when experiments are performed in new chips that fluid has never been injected into, due to condensation from water vapor in air. In regard to fluid purity, trace impurities are often unavoidable, especially if the impurities are ions and silica leached from the borosilicate glass side of the channel itself [109] [110]. Evaporation of fluid from the meniscus interface during open-ended channel imbibition is

another concern. If evaporation does occur during the imbibition experiments it takes place only across the meniscus interface and, as such, its effect should remain approximately constant with time and will not affect the expected $t^{0.5}$ power law imbibition trend. In the trapped bubble experiments, detailed in Chapters 4 and 5, evaporation is not a concern. An additional non-ideal possibility is that of gas diffusion (leakage) across the anodic bonding interface, although experimental work on this subject shows the possibility of notable diffusion at such interfaces occurs only at temperatures higher than 300°C [111]. It is also assumed that the fluorine-based RIE and anodic bonding processes have not compromised the surface charge or wetting properties of the oxidized silicon surface or created channel distortions [112]. As shown in Figure 3.5 some surface defects are visible with differential interference microscopy techniques; such chips were not used for data acquisition.

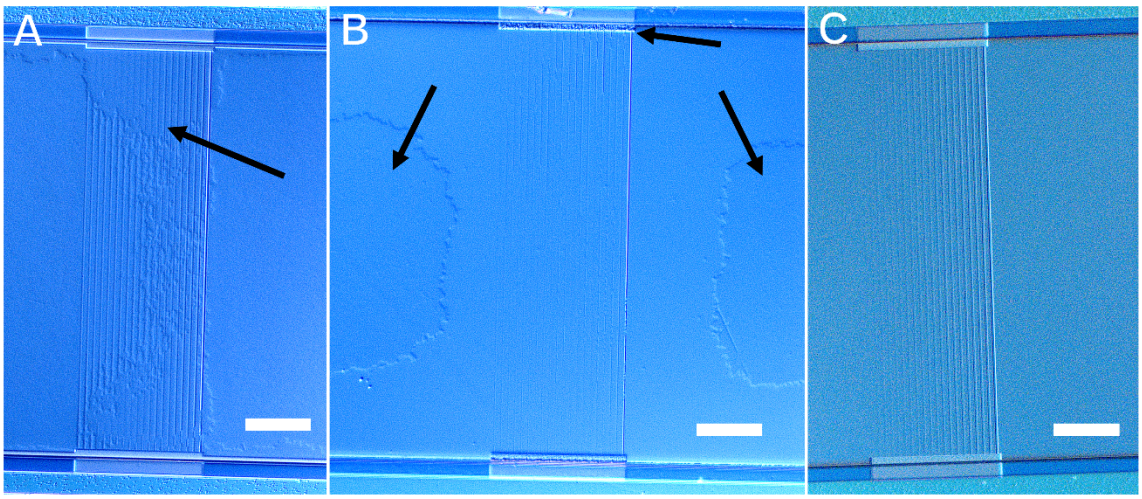

Figure 3.5: Images of array style nanofluidic chips with and without surface defects. Scale bar is 40 μm for all images. (A) Arrow points to apparent wafer unevenness. (B) Random defects (left and right arrows) that do not affect the nanochannels; however, these channels are clogged with Rhodamine B residue (top arrow displays example of such). (C) Pristine chip with a clear and smooth distribution of nanochannels.

3.2 "SHALE-ON-A-CHIP" NANO-NETWORK DEVICES

First of their kind synthetic representations of shale matrix pore-networks in nanofluidic devices were constructed using standard facile and replicable cleanroom nanofabrication methods. The reported two-dimensional network geometries are mostly nanoscale, irregular, and composed of hydraulically resistive paths (throats) meeting at junctures (pores) to mimic the perceived low topological connectivity of shale. The geometry also includes microscale grid patterns that border the nanoscale networks and represent microfracture pathways of greater hydraulic conductivity (dual-porosity). The main techniques used in the development of the nano-network master patterns include the use of transmission electron microscopy (TEM) grids with lacey carbon support film as shadow masks, thermal evaporation/deposition, and reactive ion etch (RIE). Master patterns were successfully replicated with polymer materials. The hydrophilicity, strength of hermetic sealing/compression, diffusivity, and swelling nature of the solid network patterns can all be adjusted with the fabrication process reported herein.

3.2.1 Fabrication materials and methods

A master pattern is a pristine version of a chip design that is later replicated with a double casting [113] soft lithography process [114]. The fabrication of the nanomodel master pattern is simple because it principally requires the use of only two instruments, a thermal evaporator and a reactive ion etch plasma system. These instruments are common fixtures in a cleanroom facility. If access to these tools and/or a cleanroom facility are not available, then the construction of these master patterns can be commissioned by a nanofabrication foundry or similar entity. Subsequent replication of master patterns with double casting is inexpensive and can be repeated multiple times with various polymer materials to produce batches of identical nanomodels of various surface chemistries.

Alternatively, those wishing to have the nanofluidic networks set in quartz (or a similar master pattern material such as silicon or polysilicon) for experimentation can use the master patterns themselves as lab-on-a-chip(s). Figure 3.7 depicts the reservoir/shale-on-a-chip fabrication scheme. Figure A.1 of Appendix A provides photos of the process.

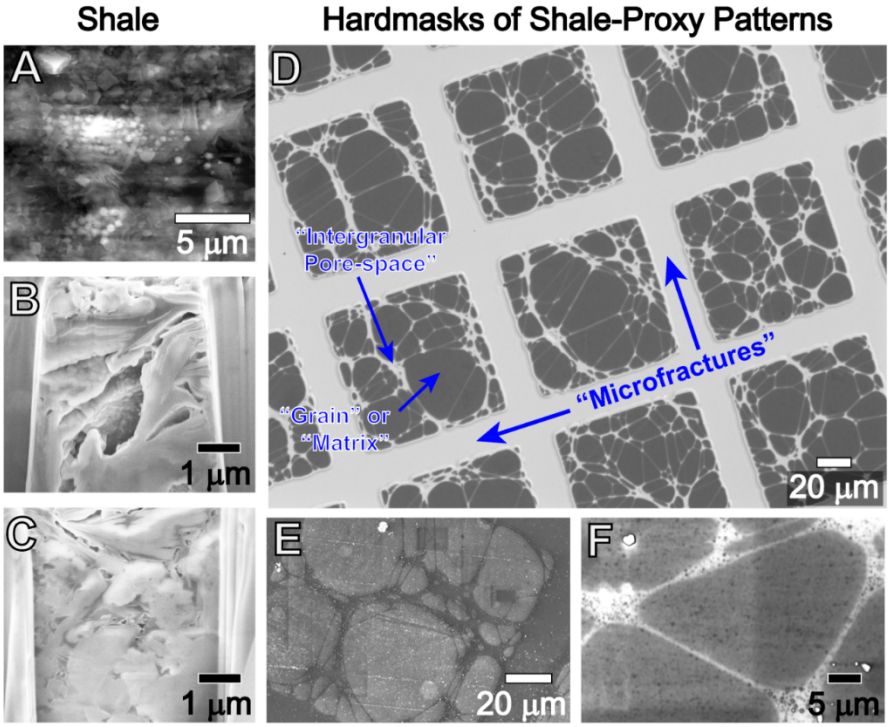

Figure 3.6: (A) SEM image of a mechanically-milled surface of an oil-window Eagle Ford shale sample (accelerating voltage (AV): 20 kV, detector: gaseous secondary electron (SE), working distance (WD): 9.5 mm); 3D grains, clays, and pyrite framboids are clearly visible. (B)-(C) High magnification focused ion beam-smoothed SEM images from the same Eagle Ford shale sample (AV: 5 kV, detector: in-lens SE, WD: 5 mm); the upper image features a relatively large matrix pore while the lower image displays compacted grains and clays with intermixed kerogen (darker gray sections) and pores (darkest regions). (D) DIC image of a section of the synthetic shale network geometry after RIE, but prior to removal of the Cu hardmask (dark sections). (E)-(F) Close-up SEM images of the synthetic network pattern in the Cu hardmask display local connectivity and channel smoothness (AV: 10 kV, detector: SE, WD: 9 mm).

3.2.1.1 Master pattern fabrication

Nano-network masters were fabricated in a class 100 cleanroom via the following steps, materials, and instruments. First, TEM grids with lacey carbon support films (Pacific Grid-Tech and SPI Supplies) were secured (lacey carbon side facing down) with Scotch tape to a clean 25 mm × 25 mm quartz substrate (1 mm thick, AdValue Technology). The quartz substrate cleaning procedure was sonication in acetone followed by rinsing with isopropanol and immediate drying with a nitrogen spray gun. The TEM grids are made of thin copper (Cu), are 3.05 mm in diameter, and typically feature 25 μm wide Cu mesh which can be spaced to contain 50-600 square cell regions. Single-hole or slot pattern grids are also obtainable. A film of lacey carbon networks comes adhered to the grid and appears within the grid square or aperture regions. The carbon networks are non-uniform and around 20-30 nm thick [115]. Lacey carbon films were selected for their heterogeneous patterns, which, serendipitously, resemble an inverse arrangement of unconventional pore spaces between compacted grains (the holes in the carbon film); in fact, the holes in lacey carbon range from < 0.25 μm (the size of clay grains) to 10 μm (the size of fine silt grains). The Cu grid mesh is reminiscent of a grid-like microfracture network. Two types of grids were procured for fabrication: mesh grids with 200 square regions, each spanning ~ 97 μm across (Pacific Grid-Tech) and single-hole grids, each with a 1 mm diameter hole (SPI Supplies). The former design is widely available while the latter required a custom order. Respectively, the designs represent a dual-scale (dual-porosity) media of microfractures and shale matrix [116] and a relatively widespread region (1 mm diameter circle) of entirely shale matrix. Regions masked by the Scotch tape used to secure the TEM grid against the substrate masks later serve as fluid reservoirs. If more complex fluidic pathways/reservoirs (i.e. microchannels and multiple

inlets) are desired, those features can be incorporated in a separate fabrication process or in the masking process by way of a secondary hard shadow mask which holds the TEM grid in place by compression.

Next, a thin film ($\leq$ 10 nm) of 99.999% Cu (Ted Pella, Inc.) was isotropically deposited onto the quartz (the Cu atoms travel in a "line of sight" fashion) with a Denton thermal evaporation and material deposition system; the TEM grids with lacey carbon film act as shadow masks [117] or stencils [118] and do not need to be directly adhered ("bonded") to the substrate. In our setup, Cu bead(s) of 1-3 mm in diameter sat in a dimpled tungsten boat (Ted Pella, Inc.) and were heated to their melting point within a vacuum chamber, upon which they evaporated and subsequently condensed/deposited on the substrate, forming a thin film. The rate of deposition and thickness of the films were monitored with quartz crystal microbalances. The Cu was deposited everywhere but the grid pattern mask, resulting in the network patterns shown in Figures 3.5-3.7. Thermal evaporation was performed at a pressure of $1\text{-}5\times10^{-5}$ torr, the sample was not rotated, and the deposition rate was ~ 1 Å/s. Cu was selected as the deposition metal because it does not react with the etching gases used in the subsequent step (chlorine gas is needed to perform Cu etching) [119], and, therefore, the deposited Cu acts as a hardmask. Additionally, the adhesion of Cu to glass or quartz is weak and the Cu was easily removed after etching with tape and/or by letting the substrate sit in water for several days.

Reactive ion etching (RIE) of the master substrate was performed with fluorinated gases in a March Plasma CS170IF system; etching success is a formula-dependent process. Etch rates of approximately 100 nm/min and lower for quartz and glasses have been reported in the literature [120]. The smoothness of the etched substrate is highly

influenced by the uniformity of the crystal structure [121]; due to the impurities in glass, it was found that quartz substrates are superior to glass ones for etching purposes. Diced silicon wafers are another substrate alternative which etch easily with fluorinated gases. Figure 3.9.A-D display the difference in etching quality between CF_4 and SF_6 plasmas on glass. Tapering of the nanochannel sidewalls and hardmask erosion are artifacts of the anisotropic RIE process. Figure 3.9.A-D also show that tapering and redeposition of material are more apparent in the samples etched with SF_6 plasmas; it was concluded that CF_4 produced an overall cleaner etching result. The following etching parameters were used for fabrication: radio frequency (RF) power of 250 W, base pressure of 80 millitorr, and CF_4 flow of 10.5 sccm and achieved a fairly linear etching rate of ~ 200 nm/min in quartz, as indicated by a Dektak 6M Stylus Profilometer. Figure A.2 of Appendix A displays images of the results for variations in etching recipe. The networks displayed in Figure 3.6.D and Figure 3.6.C are etched ~ 200 nm deep.

Lengthy and expensive techniques such as electron beam lithography and direct focused ion beam milling as well as extensive fabrication workflows and multiple material layers are avoided with this two-step master pattern fabrication method. Note that optimal nanofabrication parameters which can vary from lab to lab depending on the instruments used; sample characterization at each step and parameter iteration are encouraged for successful implementation of the fabrication workflow.

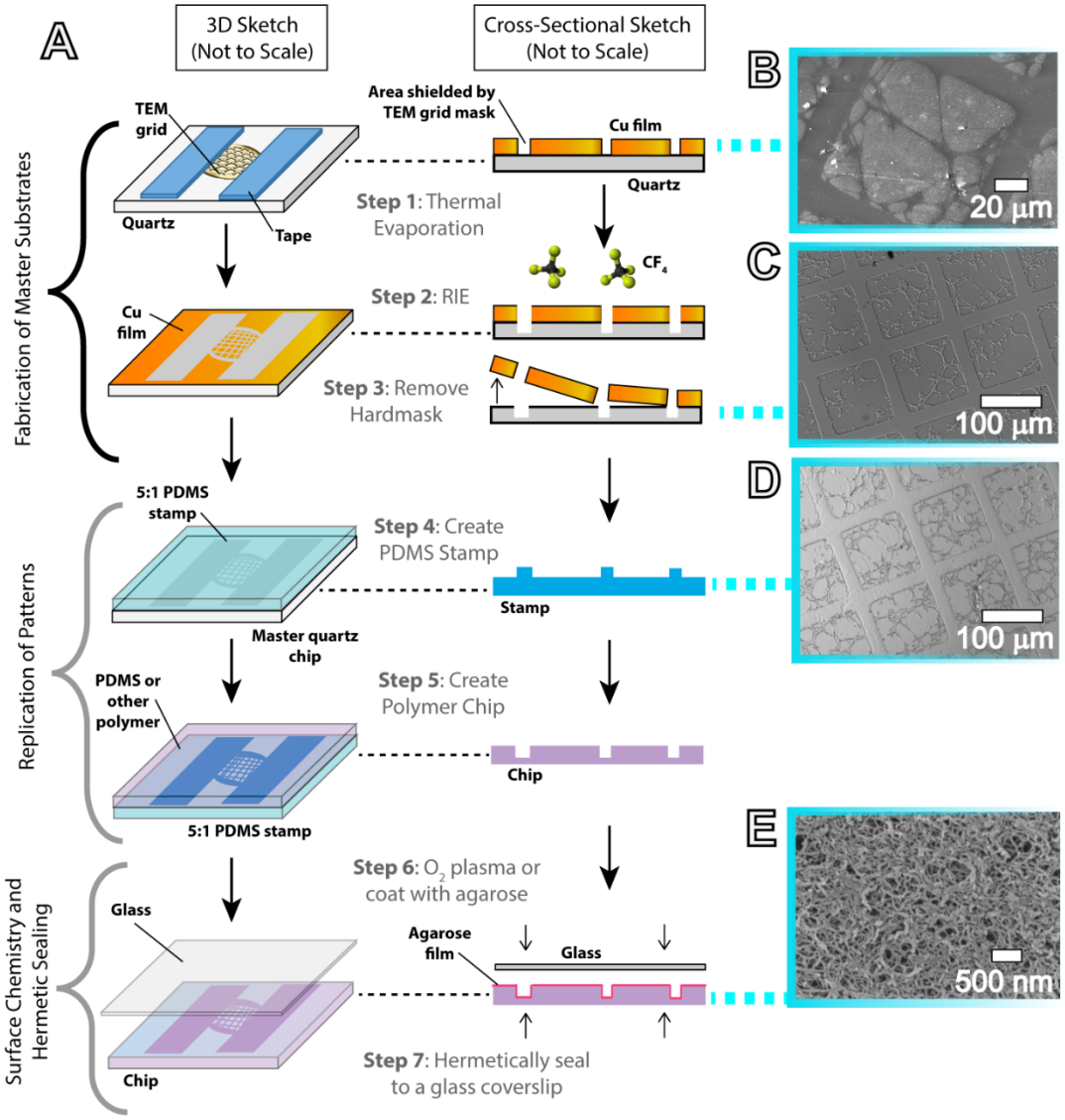

Figure 3.7: (A) Schematic workflow diagram of the fabrication scheme. Fabrication of the master substrates is a two-step process. Subsequent steps depict pattern replication and chip sealing/bonding. Cross-sectional sketches are local to a few network channels for illustration purposes. (B)-(E) show images associated with each step: respectively, an SEM image of the hardmask pattern (AV: 10 kV, detector: SE, WD: 9 mm); a DIC image of the pattern transferred into quartz after RIE; a DIC image of the pattern replicated in a PDMS stamp; and a field emission-SEM image of agarose (AV: 5 kV, detector: SE, WD: 9.3 mm), a possible surface coating for the pattern. Note that pattern details are well-preserved from image (C) to (D) during soft lithography.

3.2.1.2 Double casting pattern replication

Once the master pattern was successfully transferred into the quartz substrate, this patterned substrate was used as a mold to reproduce the pattern on multiple polymeric chips. Because the nano-network pattern is inset or "negative" on the quartz master a double stamping method is required. A "positive" or embossed version of the master pattern was generated by casting polydimethylsiloxane (PDMS) (Sylgard 184, Dow Corning) with an elastomer to curing agent ratio of 5:1 on the master pattern. PDMS with an elastomer to curing agent ratio of 10:1 was later cast on the cured positive 5:1 PDMS stamp and this step was repeated to manufacture multiple replicas of the original inset master pattern; note that another polymer can be used instead of PDMS for this step. A 5:1 elastomer to curing agent ratio was used for the positive stamp to produce a stiffer replica than the standard 10:1 ratio. The positive stamp was coated with a release agent composed of standard dishwashing detergent mixed and 75% ethanol in a 1:10 ratio [122]. Other techniques for successful release during double casting of PDMS include application of hydroxypropyl methylcellulose (HPMC) as a release agent [113], corona discharge treatment [123], and thermal aging of the positive stamp [124]. During each casting step of this procedure, Scotch tape was firmly adhered around the edges of the surface onto which PDMS was poured, effectively creating a casting "trough" or "boat" to prevent PDMS leakage. Note that PDMS replicas of ~1 mm thick or less were optimal for subsequent bonding and microscopy steps.

3.2.1.3 Chip bonding

After pattern fabrication and replication, enclosure of the nanofluidic networks was achieved using two methods. In the first method, a PDMS replica containing the inset nano-network pattern was bonded to a clean glass coverslip (Fisherfinest cover glass

#1, Fisher Scientific). Oxygen plasma bonding was implemented with a March Plasma CS170IF system and the following dry etching recipe: RF power of 125 W, base pressure of 300 mTorr, O_2 flow of 60 sccm, and run time of 60 s. Substrates were immediately pressed together after plasma exposure. Perforations to facilitate fluid flow were made with a biopsy punch prior to bonding. In the second enclosure method, hermetic sealing of a PDMS replica to a glass coverslip was accomplished using an in-house machined compression holder with a circular 18 mm in diameter beveled viewport for subsequent microcopy. A rubber gasket, glass coverslip, and < 1 mm thick PDMS substrate were, in that order, sandwiched between two 25×75 mm, 3 mm thick polycarbonate sheets, and secured in compression with an array of eight hexagonal socket cap bolts and nuts. The compressed PDMS substrate acts as a secondary gasket due to its flexibility.

If the master patterns are to be used as chips themselves, quartz-glass bonding through a hydrolyzed layer is recommended [125], though fusion bonding and anodic bonding (if the master is made of silicon) are viable options as well [126].

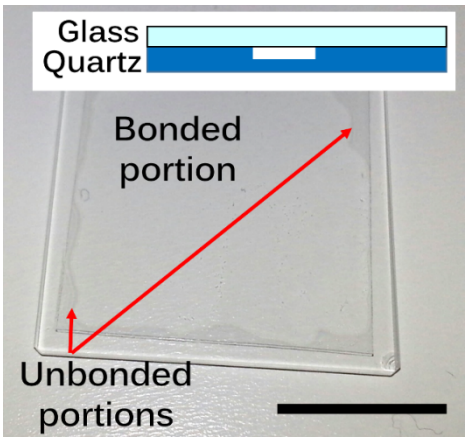

Figure 3.8: Quartz shale-on-a-chip master (pattern not visible with regular photography) bonded to a glass cover slip using the room temperature bonding method of Jia et al. [125]. Interference fringes indicate areas that are not bonded. Scale bar is 12.5 mm.

3.2.1.4 Surface chemistry

The quartz master patterns are hydrophilic, while the PDMS replicas are, in their native state, hydrophobic. Two methods were used to alter the surface chemistry of the PDMS. The first method is one commonly used in the literature: the substrate was cleaned with O_2 plasma (using the same recipe as was used for plasma bonding), thus activating silanol groups, and then stored in water to preserve this activated surface [127]. If the PDMS substrate is left in air, methyl groups configure at the surface and the substrate quickly reverts to its hydrophobic state. The second method implemented was vertical dip-coating of the substrate in 3% agarose, a hydrophilic nanoporous hydrogel with a uniform concentration-controlled pore size distribution, to form a thin film of agarose on top of the PDMS, other chip polymer of choice, or quartz [128]. The thin layer of agarose adds another porosity scale to the nanofluidic devices, but chips with agarose treatment must be stored in a hydrated or moist environment.

3.2.1.5 Cost-effectiveness

The construction cost of a single master pastern, as of the year 2015 and including capital costs of all necessary supplies and costs of renting the thermal evaporation and RIE instruments at a user-facility cleanroom, was calculated to be ~$175. Subsequent master pattern creation is ~$35-$50 per chip and the price decreases dramatically when a batch of masters are fabricated in parallel. Replication of the master patterns is essentially only as expensive as the cost of the polymers selected as casting materials.

3.2.2 Pattern success and characterization

The nano-network masters were characterized with both reflected and transmission optical light microscopy and SEM. The former was helpful in capturing large-scale fields of view of the networks, while the latter was helpful in establishing the

quality of the nano-network patterns below the resolution of optical light microscopy. Optical microscopes used were a Zeiss Axiovert 200M and a Zeiss Axioskop 2 MAT. With these instruments, patterns features are successfully visualized in brightfield, phase contrast, and differential interference contrast (DIC) modes; DIC mode is recommended for improved capture of the sub-micron fluidic pathways and for enhanced contrast when introducing fluids into the chips during experiments. The SEMs used were a JEOL JSM-6490 SEM and a FEI XL30 Environmental-SEM; both of these microscopes had tungsten electron guns. Further details on SEM imaging parameters are found in the figure captions and Appendix A. Figure 3.9 displays images from the pattern characterization process. Image analysis revealed that the width of individual nanochannel pathways (throats) created with the lacey carbon shadow masks ranges from approximately 200 nm to 5 μm. Pattern nodes, representing pores or junctures where the nanochannels meet, are on the order of 10 μm or less along their widest point. The nanoscale depths of the networks are user-controlled with RIE. Figure 3.10 displays typical "grain" and "pore" size distributions for the nanofluidic chips. The quartz master structures are extremely robust; during development of the fabrication scheme, these nano-networks were subjected to repeated PDMS casting and cleaning and still retained their pattern.

Inspection of the PDMS positive and negative replicas revealed high pattern fidelity from master to stamp to chip. Figure 3.9.I displays an example of pattern transfer success to a PDMS stamp upon casting. When PDMS is selected as the chip material, determination of a successful release agent or technique is crucial or the PDMS stamp and chip (second replica) will not separate. In addition to PDMS, other potential polymer materials for the chips include Polymethyl methacrylate (PMMA), NOA 63 [129], cyclic olefin copolymer (COC) [130], and OrmoStamp (MicroResist Technology GmbH) [131].

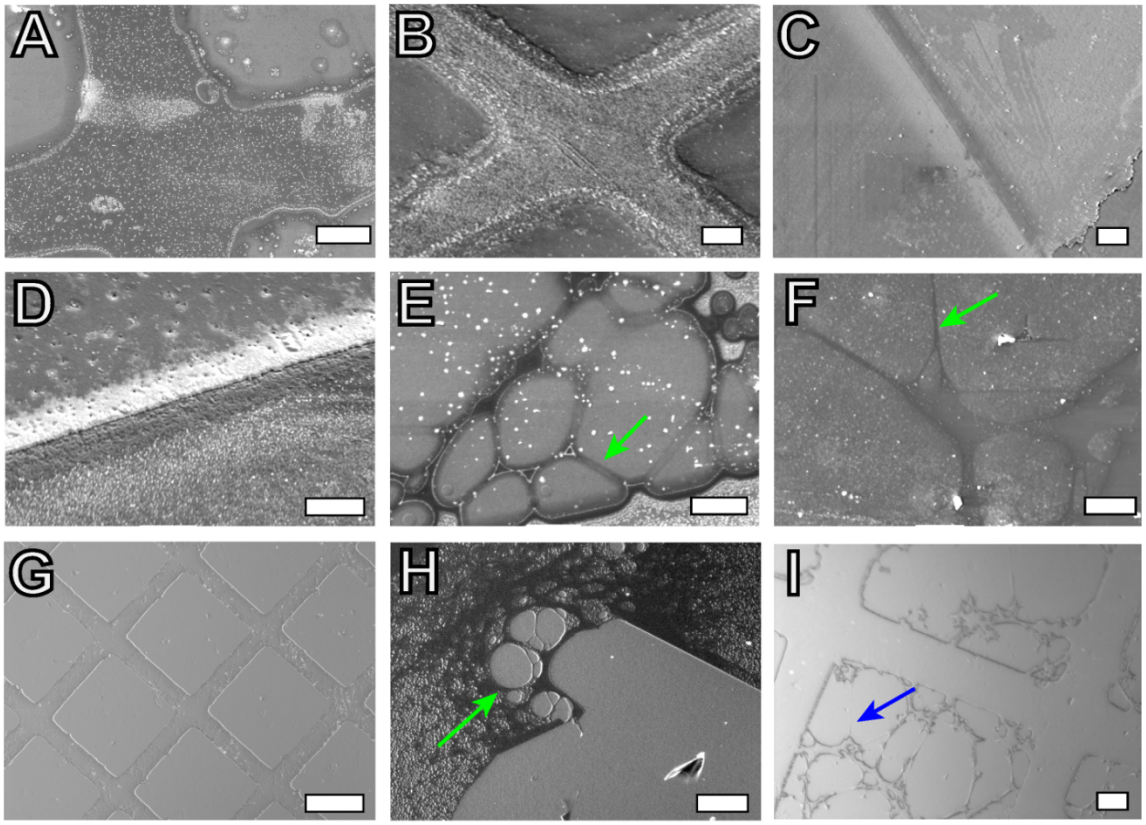

Figure 3.9: SEM and DIC images that characterize challenges in different steps of the fabrication process. All scale bars are 10 μm with the exception of Panel G where the scale bar is 50 μm. SEM images (A) and (C) display the result of etching glass with CF_4 at pattern edges/steps (AV: 15 kV, detector: SE, WD: 9 mm, sample tilt: 20˚) and SEM images (B) and (D) analogously correspond to etching glass with SF_6 (AV: 20 kV, detector: SE, WD: 18 mm, sample tilt: 45˚); the latter is rougher and more prone to etching byproducts and sidewall tapering than etching with CF_4. (E) and (F) compare SEM images of a Cu hardmask with (AV: 8 kV, detector: SE, WD: 9 mm) and without (AV: 10 kV, detector: SE, WD: 9 mm) etching byproducts; the etching byproducts clog the narrow channels (compare channels at the arrow positions). (G) DIC image of unsuccessful transfer of the minor networks with RIE due to etching byproducts. The major grid patterns (microfracture replicas) always transferred successfully. (H) DIC image of unsuccessful shadow masking with the single-hole TEM grids; due to film sag, only isolated regions of the Cu hardmask, such as those identified with the arrow, replicated the widespread lacey carbon pattern. (I) DIC image of pattern fidelity upon positive replication with PDMS; the arrow points out the location of a well reproduced narrow nanochannel.

3.2.3 Pattern resemblance to shale media

The fabricated fluidic patterns are a dual-porosity or dual-permeability medium. Shale exhibits dual-porosity at multiple scales: the natural microfractures and intergranular (crystalline) pore space, the hydraulic fractures and intergranular pore space, and the intergranular pore space and organic matter/kerogen matrix. The nanofluidic device's fluidic patterns represent: (a.) microfractures (major pattern), which are typically on the order of ~10 μm thick and found in mainly horizontal orientation with periodic ~90˚ vertical intersections [132], and (b.) intergranular nanopore space (minor pattern), which have been characterized as locally heterogeneous with pore-scale electron beam microscopy [35] [36] [34]. When PDMS or a similar polymer is used as the chip material, the chip exhibits a third transport medium because PDMS, similar to organic matter, is diffusive to gases and vapors [133] and some liquids [127]. In fact, the reported diffusivity, D, of methane in water saturated shale, $\sim 2\times10^{-6}$ cm^2/s [134], is similar in magnitude to the values of D for methane in PDMS, $\sim 22\times10^{-6}$ cm^2/s [133]; gas diffusivity values for materials greatly range and others have reported the diffusion of methane in amorphous kerogen at far lower values: $D \sim 10^{-16}$ cm^2/s [135]. Note that the diffusivity of PDMS (and possibly other polymers) can be adjusted with surface plasma treatments [136]. Some organic, nonpolar liquids diffuse into PDMS leading to swelling and successive deformation of the network structure; PDMS does not swell with water, but hydrocarbons such as pentane can lead to a change in PDMS dimensions of ×1.44 [127]. Likewise, nanostructural changes of clay minerals [137] and kerogen [138] are prominent during shale production. Yet another porosity scale is attained if the chip surface is coated with a thin film of agarose. Agarose is negatively charged and adsorbs water, reminiscent of hydrated clays. The quartz masters also exhibit a strong negative

surface charge, similar to shale. A third option is to allow agarose in its melt form to imbibe into an enclosed chip and crosslink, thus filling the majority of the pore space with this clay or hydrophilic-state kerogen surrogate.

The nano-network pattern pore size distribution reported in Figure 3.10 was calculated by dividing the topology into pore body and pore throat regions using a watershed segmentation algorithm [139] and finding the maximum inscribed circle in each of those regions. Reports of shale throat and pore size distributions vary among formations and experimental methods applied (mainly nitrogen adsorption, mercury intrusion capillary pressure (MICP), and SEM imaging), but, in general, exhibit lognormal and/or non-unimodal distributions with pores falling into the following three International Union of Pure and Applied Chemistry (IUPAC) pore classifications: micropores (< 2 nm), mesopores (2-50 nm), and macropores (>50 nm). Using a combination of gas adsorption and MICP tests, Bustin et al. reported bimodal pore size distributions for Barnett and Antrim shale samples with modes around 10 nm and 10 μm [140]. The range of this pore size distribution coincides with the range of the distribution produced by the lacey carbon support films (Figure 3.10); IUPAC-defined mesopores and micropores as well as bimodality are added when secondary porosity provided by an agarose film or the polymer substrate itself are taken into account. In addition, the hole sizes and the width of connections between nodes in lacey carbon support films varies between manufacturers. In characterizing lacey carbon films from several manufactures (namely, Oken Shoji, Pelco, Agar Scientific, and Quantifoil), Karlsson reported a TEM image of a typical lacey carbon film where the majority of the connections between nodes were much less than 500 nm wide [115]; such films may provide a distribution of smaller pore throat values than the films featured in this work. The equivalent 2D grain size

diameters displayed in Figure 3.10 fall within the grain sizes for clays/muds (< 3.9 μm in diameter) and siltstones (< 63 μm in diameter) per the Udden-Wentworth grain size classification scheme. Equivalent grain diameter is the diameter of a circle whose area is equal to that of the irregularly shaped synthetic grain. The areas of the 2D synthetic grains are found by binarizing an image of the networks with fuzzy c-means segmentation and extracting the isolated connected regions ("grains") with MATLAB's *bwconncomp* function.

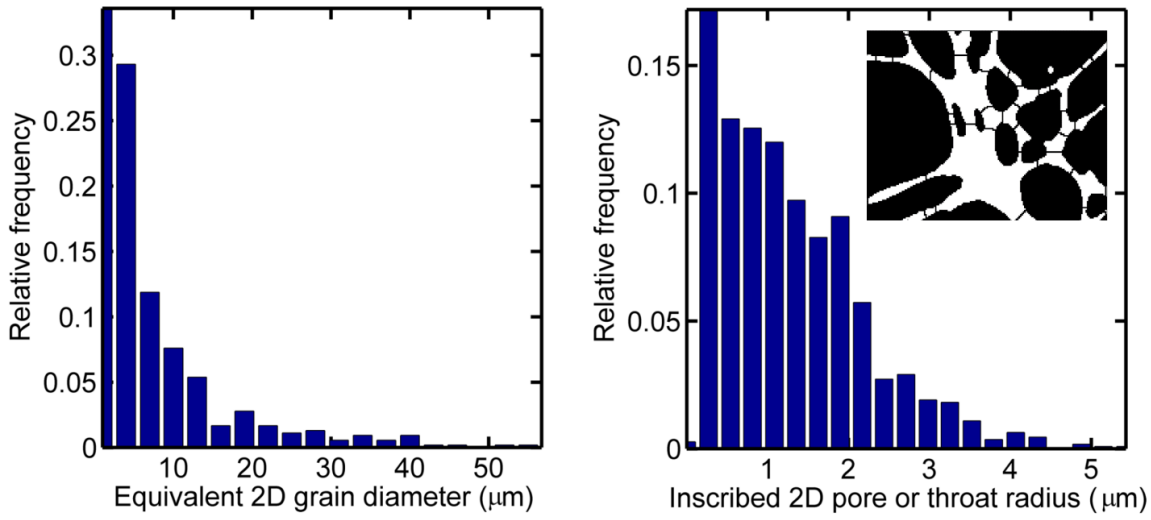

Figure 3.10: Relative frequency distributions of synthetic 2D grain sizes and synthetic 2D pore body and throat sizes in the nanofluidic patterns. The third dimension (depth) is controlled by reactive ion etch. Displayed distributions were extracted from Figure 3.6.D and the microfracture-like conduits were excluded from the calculation of pore-size distribution. Inscribed pore or throat radius is the radius of the maximum inscribed circle in a defined pore space region (see the inset close-up image of a section of the pore space divided into pore and throat regions via a watershed segmentation image analysis method [139]). Throats occupy the lower part of the histogram, but the exact threshold between pore bodies and throats is user-defined.

3.3.4 Ancillary support film nanopatterns

Lacey support films can also be prepared in a standard research laboratory to produce even larger-scale versions of the patterns straight onto a desired substrate, bypassing the use and purchase of premade TEM grids and the necessity of carbon as the film material. Such preparation requires relatively inexpensive supplies: formvar, a film-forming polymer, in ethylene dichloride and a steam chamber or sonicator; lacey film preparation protocols are commonly available on the internet, but do vary among labs. There is no need to carbon coat these lacey films because the purpose of the film is to serve as a mask in thermal evaporation.

In addition to lacey carbon, there are other patterned TEM grid support films available that may suit additional reservoir/lab-on-a-chip applications. These support films include holey carbon, which features sparse and randomly distributed holes of desired size(s), and a variety of uniformly distributed patterns manufactured by Quantifoil, which feature defined hole sizes and pitches. The smallest versions of these Quantifoil films currently available are a rectangular mesh lattice of ~ 1μm bars ("pore size") spaced ~7 μm apart ("grain size"), or a lattice of circles 1-2 μm in diameter ("grain size") spaced ~1 μm apart ("pore size"). Use of such regular lattices in the fabrication scheme presented herein are ideal for scaling down the common micromodel pattern composed of arrays of disc-shaped posts/grains [48] to nanoscale features.

3.3.5 Limitations and obstacles

Success of the TEM grid and lacey support film as a shadow mask during thermal evaporation is critical for this fabrication scheme. Variables in the thermal evaporation process include whether or not the sample is rotated during deposition, the rate of metal deposition (1 Å/s is generally considered an optimal rate), the height of the film

deposited, and the degree of vacuum in the deposition chamber (a vacuum of 10^{-6} torr is optimal; our system took approximately 45 minutes to pump down to this vacuum). It was found that the generation of successful Cu hardmasks with lacey films mounted on mesh TEM grids was extremely robust to these thermal evaporation parameters. However, the Cu hardmasks generated with lacey films mounted across the 1 mm single-hole grids were extremely sensitive to those parameters and resulted in blurred patterns (see Figure 3.9.H for an example) even when higher vacuums, slower deposition rates, and thinner Cu films (~ 5 nm thick) were implemented. "Sag" of the lacey carbon film occurs between grid bars/mesh or holes and is most likely the cause of the difficulties with the single-hole grids. Film sag is logically more likely to occur across larger grid apertures, but is challenging to control or measure.

While the generation of Cu hardmasks with lacey films on mesh TEM grid shadow masks is robust for deposited Cu films as thick as 30 nm (the thickest film attempted), the subsequent quartz etching process is very sensitive to the thickness of the Cu film. As displayed in Figures 3.7.E and 3.7.G, the RIE etching step was unsuccessful if the Cu film thickness exceeded ~10 nm; in that case, smaller nano-network apertures were filled in with nonvolatile etching byproducts as a result of Cu oxidation [141] or material redeposition. Alternatively, implementers of this fabrication method are encouraged to try other deposition metals such as aluminum.

Channel pairing and collapse are concerns associated with narrow features in soft, flexible materials such as PDMS upon bonding [142]. Collapse of the low aspect ratio (25 μm × 200 nm) microfracture-like channels was frequent with PDMS chips; note that such collapse can potentially result in the generation of nanofluidic pathways at collapsed channel edges [143]. Overall, compression bonding was found to be favorable to O_2

bonding because, in addition to facilitating easier cleaning, PDMS channel collapse was reversible with the former. Furthermore, harder polymer materials such as PMMA and NOA 63 are recommended as chip materials to avoid structure collapse and pairing.

3.3 LARGE-SCALE PATCHWORKS OF NANOCHANNELS AND PSEUDO-SHALE FEATURES

In the early stages of this research conventional nanofabrication protocols were followed and resulted in the precise chips featured in Section 3.1. Undoubtedly, these chips allow excellent user control over geometry (via electron beam lithography), but are not easily accessible for many researchers wishing to explore nanofluidics for shale studies, are expensive, and require diligent cleaning. As the research presented in this dissertation progressed, I sought techniques for the creation of facile, inexpensive, and disposable nanofluidic chips. In Section 3.2 a simple and effective technique for shale-like network-style patterns was introduced. This section details an even simpler fabrication method that renders large-scale (extensive) arrays of nanochannels on the order of millimeters (or even centimeters if desired). Patchworks of shale-like features such as pseudo-fractures, pseudo-fossils, and pseudo-kerogen clusters can be heterogeneously incorporated into these arrays with the very things that most nanofabrication processes strive to avoid: dust, particulates, fibers, tears and scratches. The following technique does not require a cleanroom facility, though, if accessible, the use of one is recommended for the creation of nanochannel arrays only.

3.3.1 Fabrication materials and methods

Diffraction gratings were used as a master stamp to create arrays of nanochannels in cast polymers. Diffraction gratings are transparent (transmission) or reflective

(mirrored) substrates that feature a periodic and large-scale pattern of nanoscale or single-digit microscale grooves (near the wavelength of the visible light spectrum) that are used in optics to split incoming light into separate wavelengths. These miniscule grating features are typically fabricated in blazed (sawtooth), sinusoidal, or rectangular configurations, and, though intended for optics, resemble arrays of open fluidic channels. Compact discs (CDs), digital video/versatile discs (DVDs) or Blu-ray discs (BRDs) are easily accessible rectangular diffraction gratings; a rainbow or blue spectrum appears on these discs when they are held up to white light. Unwritten (blank) CDs, DVDs, and BRDs contain a spiral of concentric tracks (which are rows of channels up-close) molded in polycarbonate in their interior with pitches (distance between the center of one track/channel to another) of, respectively, 1.6 μm, 740 nm, and 320 nm; the actual width of a CD track, for instance, is ~ 600 nm. Pits are etched into these channels with laser wavelengths, λ, of, respectively, 780 nm, 650 nm, and 405 nm to create written (encoded) discs. For the case of a CD each pit is ~ 160 nm deep and has a minimum width of 600 nm and variable length; pits get progressively smaller for DVDs and BRDs. The depth of the track grooves is 0.25λ; e.g. 195 nm for a CD.

A professional glass-mounted transmission diffraction grating with 300 lines/mm (3.3 μm width channels) made to resolve the sodium lines (3B Scientific, model U19512), CDs (Sony), BRDs (Sony), and PDMS were used to prototype this facile fabrication scheme. Using the diffraction gratings as masters, PDMS was cast directly on them as is described in Section 3.2.1.2 and as is displayed in Figure 3.13.A. CDs and BRDs were prepared by first cutting a sector of the disc with scissors and carefully separating the foil and plastic base of the cut section with a blade and/or similar manipulation tools. The revealed interior of the separated foil or the plastic can be used as

a master pattern (the diffraction of light will indicate the correct side is facing up); a resultant replica is shown in Figure 3.12. For the writable disc gratings, some channel surface complexity or texture can be incorporated with the abovementioned sub-micron pits. Connected and isolated channels were created in the arrays by adding various imperfections to the gratings. In this work, scratches were found to replicate fractures and add inter-channel connections. Dust and debris resulted in heterogeneous inclusions. Figure 3.13 displays some examples of these imperfections. Peeling a PDMS chip off of its corresponding stamp in a double replication process before the former was before completely cured resulted in tears which propagated as: (a) larger and rougher fractures such as shown in Figure 3.13.B or (b) dendrite structures such as shown in Figure 3.13.G. Crushing/destroying sections of the grating, which are characteristically treated with upmost delicately, resulted in the isolated patterns featured in Figure 3.11; compression of the chips during bonded caused further growth of these pseudo-organic matter regions. Again, all micron sized and above artificial heterogeneities introduced can be optically characterized. Surface chemistry can be adjusted as is described in Section 3.2.1.4 and is displayed with agarose incorporation in Figure 3.13.C-E.

3.3.2 Limitations and obstacles

A shortcoming of the diffraction grating-based patchwork nanofluidic devices is that the geometry of the patterns is limited by the gratings available. Implementers of this straightforward fabrication technique are restricted in the variation of groove pitch or pattern density; this is not a limitation of direct write methods such as EBL and FIB. The size of the grooves/nanochannels are also often set by either the resolution of etching lasers (as opposed to an electron beam) or the pattern desired for the original diffraction or encoding purpose of the grating; pitches less than the lower λ limit of optical light, 400

nm, are not expected. Furthermore, these devices are not interconnected pore-networks such as those of Section 3.2; though the entire medium is connected in terms of diffusive transport. As opposed to silica structures, when soft polymers such as PDMS are used in the fabrication of these devices, the shallow channels are extremely sensitive to structural (see Figure 3.12) and elastocapillary deformation.

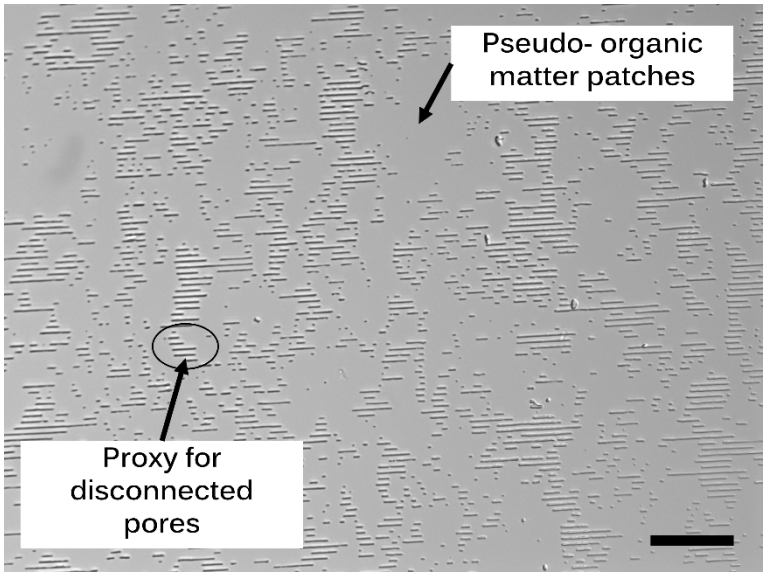

Figure 3.11: Patchwork 10:1 PDMS-glass nanofluidic device made with an optical-grade diffraction grating generated pattern subject to crushing and collapse. Channels are akin to pore pathways for [trapped] fluid flow and collapsed regions are akin to matrix regions that mainly only allow diffusion of gas molecules. Scale bar is 45 μm and the image was taken with a Zeiss Axiovert 200M in DIC mode.

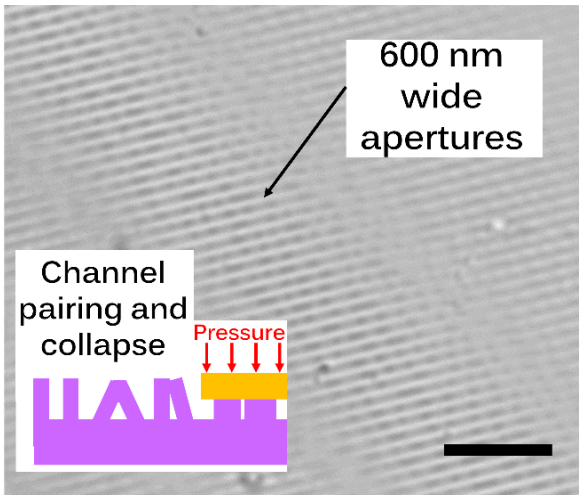

Figure 3.12: 10:1 PDMS-glass nanofluidic device made with the internal diffraction grating of an encoded CD. Dark holes are pits and diagonal white lines are track grooves. The inset cartoon illustrates deformation issues when the substrate is soft. Scale bar is 6 μm and the image was taken with a Zeiss Axiovert 200M in DIC mode.

Another obstacle with many optical-grade diffraction gratings and DVDs and BRDs is that the small and closely located parallel channels are often challenging to capture with optical miscopy; this difficulty is especially aggravated if these channels pair and deformed during chip bonding. Some applicable microscopy techniques are discussed in the proceeding section; other methods include the development of superlenses or use of microspheres to overcome the diffraction limit [144] [145]. Hence, the diffraction grating used for prototyping had relatively large groove widths of 3.3 μm (not nanoscale until channel collapse commenced), which enabled clear channel visualization with optical microscopy (see Figure 3.11).

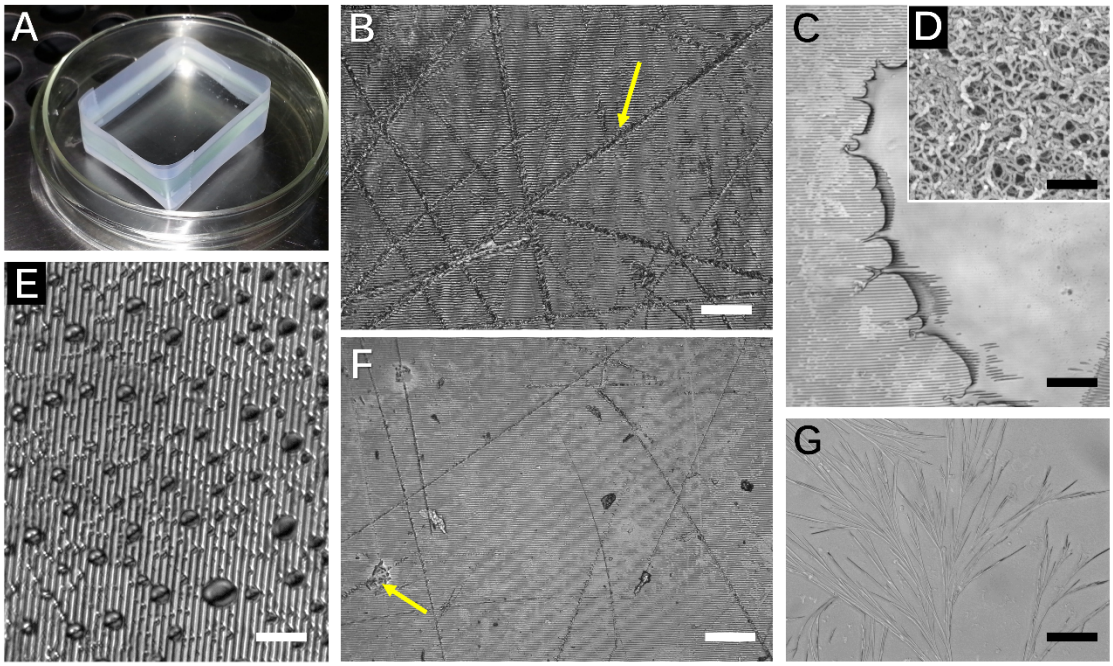

Figure 3.13: (A) Direct polymer casting on a glass-mounted diffraction grating; tape is set in place to prevent uncured polymer leakage. (B) Arrow points out tear-generated "microfractures"; scale bar is 40 μm. (F) Arrow points out dust-generated "fossil inclusions"; scale bar is 50 μm. (C) and (E) compare water on the surface of a PDMS chip, respectively, after and before treatment with a thin agarose film; scale bars are 30 and 20 μm. (D) displays an SEM image of critical point dried agarose; scale bar is 500 nm. (G) Tear-generated dendrite-like "fractures" on the surface of a pattern from a BRD (note that nanochannels are difficult to visualize); scale bar is 50 μm.

3.4 IMBIBITION AND MICROSCOPY TECHNIQUES

Custom chip holders were both machined and made with three-dimensional (3D) printing to secure the various nanofluidic chips into both types of microscope configurations, inverted (objective is below the sample and cover glass faces down) and upright (objective is above the sample and cover glass faces up), and allow interfacing with fluid. Figure 3.14 displays example of such custom holders. When using an inverted

microscope, liquids were introduced to nanofluidic chips by administering droplets (~ 2 μL in the case of the 2D nanochannel array style chips) to one of the inlet holes with a micropipette. When using an upright microscope, the chips were slightly elevated and a saturated glass cover slip was used to introduce a small volume of fluid into one or two of the chip ports (inlets) while leaving the other ports (outlets) open to the atmosphere. As displayed in Figure 3.3.A, the 2D nanochannel array nanofluidic chips have four inlet/outlet holes. Other chips featured less sophisticated entry mechanisms such as a biopsy punch simple hole in the PDMS substrate (large-scale patterns) or narrow reservoirs between glass substrates ("shale-on-a-chip" devices). Tested liquids naturally imbibed into the 1000 nm high nano-slits of the 2D nanochannel array style chips with the exception of water, which required a syringe pump and tubing connection system for fluid entry. The experimental difficulty with water, the tested liquid with the greatest surface tension, was *entering* the narrow chip inlets. The issue may have been exacerbated by the inevitable accumulation of particulates at the inlet apertures; water imbibition success was increased when inlets were sprayed with compressed air, sonicated, and/or subject to oxygen plasma cleaning. Water did spontaneously imbibe (though anomalously, as described in this work), once introduced into the array style nanofluidic chips. Other chips featured less sophisticated entry mechanisms such as a biopsy punch simple hole in the PDMS substrate (large-scale patterns) or narrow reservoirs between glass substrates ("shale-on-a-chip" devices).

Optical microscopy was used to observe the movement of liquid-gas interfaces of various liquids within the nanofluidic chips. Only the location of fluid interfaces in 2D nanochannels can be captured with optical microscopy; the widths of these nanochannels are near the resolution of an optical microscope (this resolution is limited by the

wavelength of light and numerical aperture of an objective), and menisci curvatures cannot be discerned from images. Again, all nanofluidic chips were open to the atmosphere and at room temperature. Most images featured in this dissertation were captured in monochromatic mode.

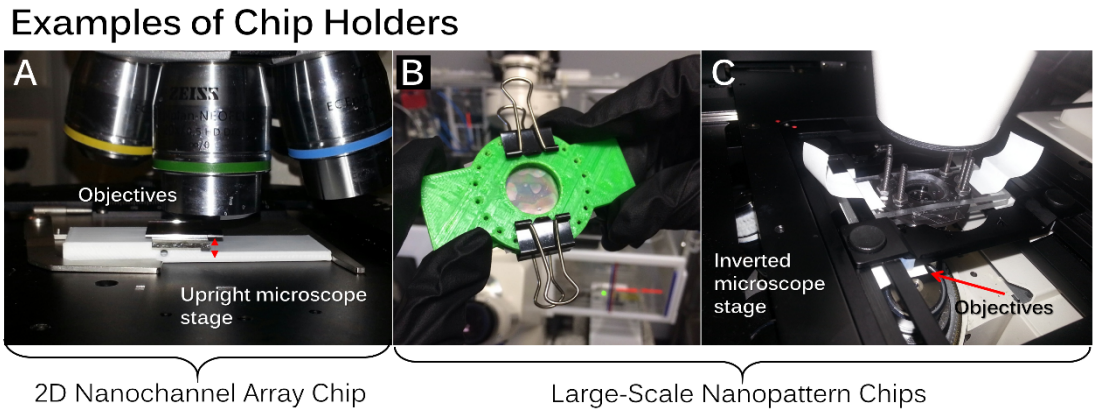

Figure 3.14: Images of simple chip holders used in the nanofluidic experiments. In (A) a non-residue gel pad is used to keep the chip still and a bit of vertical space (red arrow) is incorporated so that wetted glass slide can slip under the chip for fluid constant. In (B) and (C) a compression mechanism is used to bond the chips; some trapped air bubbles are encouraged and seen

It should be mentioned that a more complex pumping setup was first implemented for fluid control instead of spontaneous imbibition. Originally a syringe pump (Chemyx Fusion Touch 400) and tubing were interfaced with the nanofluidic chips. Tubing and connectors were selected from IDEX's Upchurch Scientific line. 6-32 Coned NanoPort Assemblies were attached to the selected inlet through holes via a cured adhesive and 10-32 Coned NanoPort Assemblies were similarly attached the selected outlets holes (as shown in Figure 1.4.H). Both 1/32" and 1/16" capillary polyether ether keytone (PEEK)

tubing with respective inner diameters of 25 μm and 90 μm were used with these connectors. PEEK tubing, an alternative to stainless steel, is chemically inert, can withstand high pressures, and is easily cut. Inline microfilters (also from Upchurch Scientific) were connected to the tubing connected so as to protect the chip (specifically, the nanochannels) from any large unwanted particulate matter in the fluids. However, this setup, did not offer as much control as predicted, as many of the conduits of connection pieces were bigger than the chip features; leakage through adhesives was a constant issue at higher flowrates, especially with water.

3.4.1 Fluorescent microscopy

When fluorescent microcopy was used as an observation technique, tested liquids were doped with Rhodamine B (Sigma-Aldridge), $C_{28}H_{31}ClN_2O_3$, a neutral fluorophore molecule, and captured with a Zeiss Axiovert 200M fluorescent light microscope (FLM). Specifically, powdered Rhodamine B was dissolved into the designated solvents to a solute concentration of ~100 μM and magnetically stirred. Note that Rhodamine B is most soluble in alcohols and water and exhibits low solubility in hydrocarbons. Rhodamine B is excited by ultraviolet light (UV) and a visible light wavelength peak of 540 nm and emits light (fluoresces) at a maximum wavelength peak of 625 nm with a full width at half maximum (FWHM) of approximately 10 nm. These peaks can shift slightly depending on the solvent the fluorophore is dissolved in. A UV-Longpass filter cube was used in the Zeiss Axiovert 200M to satisfy the excitation and emission criteria, given that the Longpass filter has a narrow 12 nm band of excitation light, which peaks at 365 nm (UV range) and is sensitive to all emission wavelengths above 397 nm. A TRITC filter cube, which has an excitation bandpass of around 530 - 550 nm and an emission bandpass capture of around 570 - 615 nm, was also used in the experiments.

The Zeiss Axiovert 200M is a widefield inverted fluorescent microscope, uses a 100 W mercury lamp as its light source, and captures images with a Zeiss CCD camera interfaced with a desktop computer; Figure 3.15 displays a schematic of this microscope. 20X (air) and 100X (oil immersion) objectives were used for large field of view and close-up perspectives, respectively. Image analysis of the locations of liquids in the nanofluidic chips was performed using ImageJ/Fiji (National Institutes of Health) and MATLAB. The location of the fluorescing fluid was distinct against the opaque background of the silicon wafer material (see Figures 5.3 for examples). Fluid was assumed to be wherever fluorescence was detected, even if the fluorescent intensity waned at the tip of the front (for example, see Figure 5.3.D); such regions may correspond to precursor films or flow along channel corners.

To help prevent chip fouling, nanofluidic chips were subject to solvent (isopropanol and acetone) "flushes" with a syringe pump between uses, sonication, and soaking in the aforementioned solvents for prolonged periods of time (diffusion-based cleaning). Despite these efforts, it was found that once a nanofluidic chip was exposed to Rhodamine B, complete removal of the fluorophore is problematic. Such residual Rhodamine B may lead to additional surface roughness and, as a result, lower hydraulic conductivity in the nanofluidic system and channels (see results of Figure 5.6). Most experiments from the presented data were performed on brand new chips; for the 2D nanochannel arrays these results are designated with an asterisk in Figure 5.4.

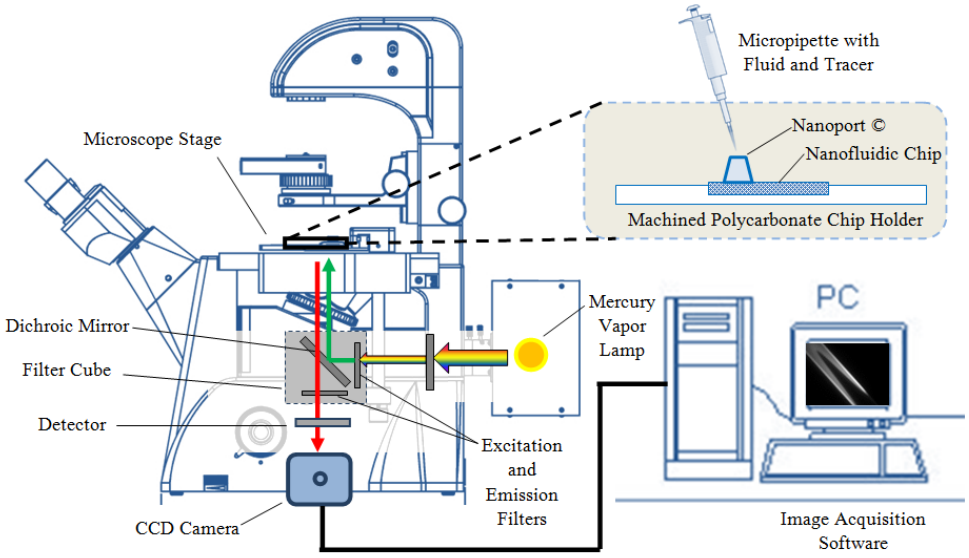

Figure 3.15: Diagram of the fluorescent microscope setup (Zeiss Axiovert 200M) used to capture data.

3.4.2 Differential interference contrast microscopy

Tracer-free (pure fluid) visualization of imbibition was achieved using transmission or reflected differential interference contrast (DIC) microscopy; the latter is required for opaque substrates such as the silicon wafer-based array style nanofluidic chips. In this work, I had access to two microscopes with reflected DIC capability, an upright Zeiss Axioskop 2 MAT and an inverted Nikon Eclipse Ti, and one microscope with transmission DIC capability, the inverted Zeiss Axiovert 200M. The majority of the DIC experiments on the array style chips were performed on the Axioskop with a Zeiss EC Epiplan-Neofluar 20X, 0.50 NA High Definition DIC objective due to availability and the enhanced contrast provided by the microscope's circular-DIC mode [146]. Monochromatic 1292 × 968 pixel TIFF images of the fluid progression in the nanochannels were captured with a Zeiss AxioCam MRc 5 CCD camera and Zeiss

AxioVision software's time-lapse module at a rate of approximately 5 frames per second (exposure dependent). The CCD camera connected to the Nikon Eclipse Ti system provided a superior frame rate (data in channels 80 nm in width and greater was obtained at up to 40 frames per second) and higher magnification and was used to achieve substantial data points on length-versus-time curves for power law analysis.

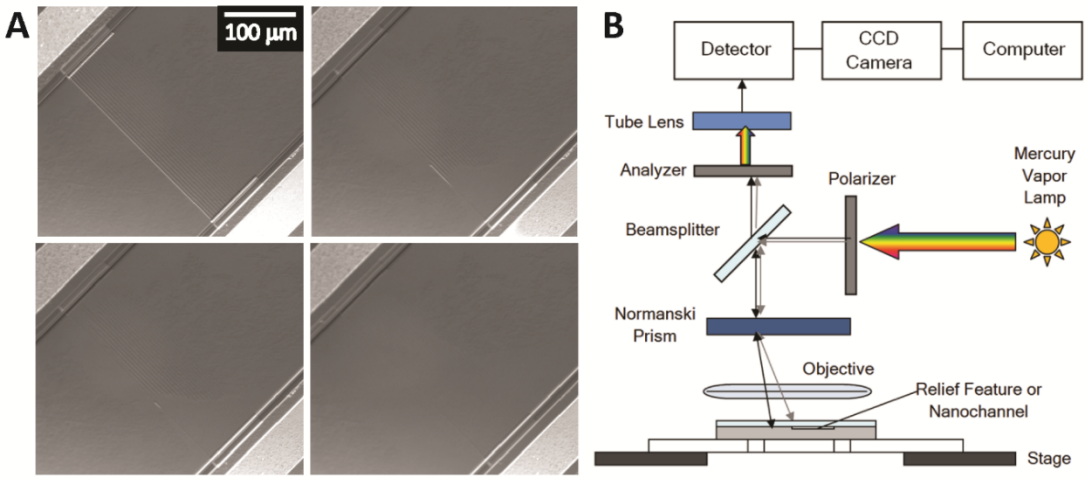

Figure 3.16: (A) Examples of reflected DIC images of a dry (top left) and then wetted nanochannel array spanning between two microchannels captured with a Zeiss Axioskop 2 MAT in monochromatic mode. Nanochannels visually disappear when filled with fluid. (B) Schematic of reflected DIC microscopy.

Dynamic image analysis is necessary to extract the position of liquid within the nanochannels from amidst noise in the DIC image stacks, especially in channels less than 100 nm wide. A signature of DIC microscopy is pairs of light and dark signals produced at feature edges, as displayed in Figure 3.17.C. When fluid invades nanochannel structures there is a contrast between the wetted and dry edge signals (Figures 3.16.A and 3.17.A-B).

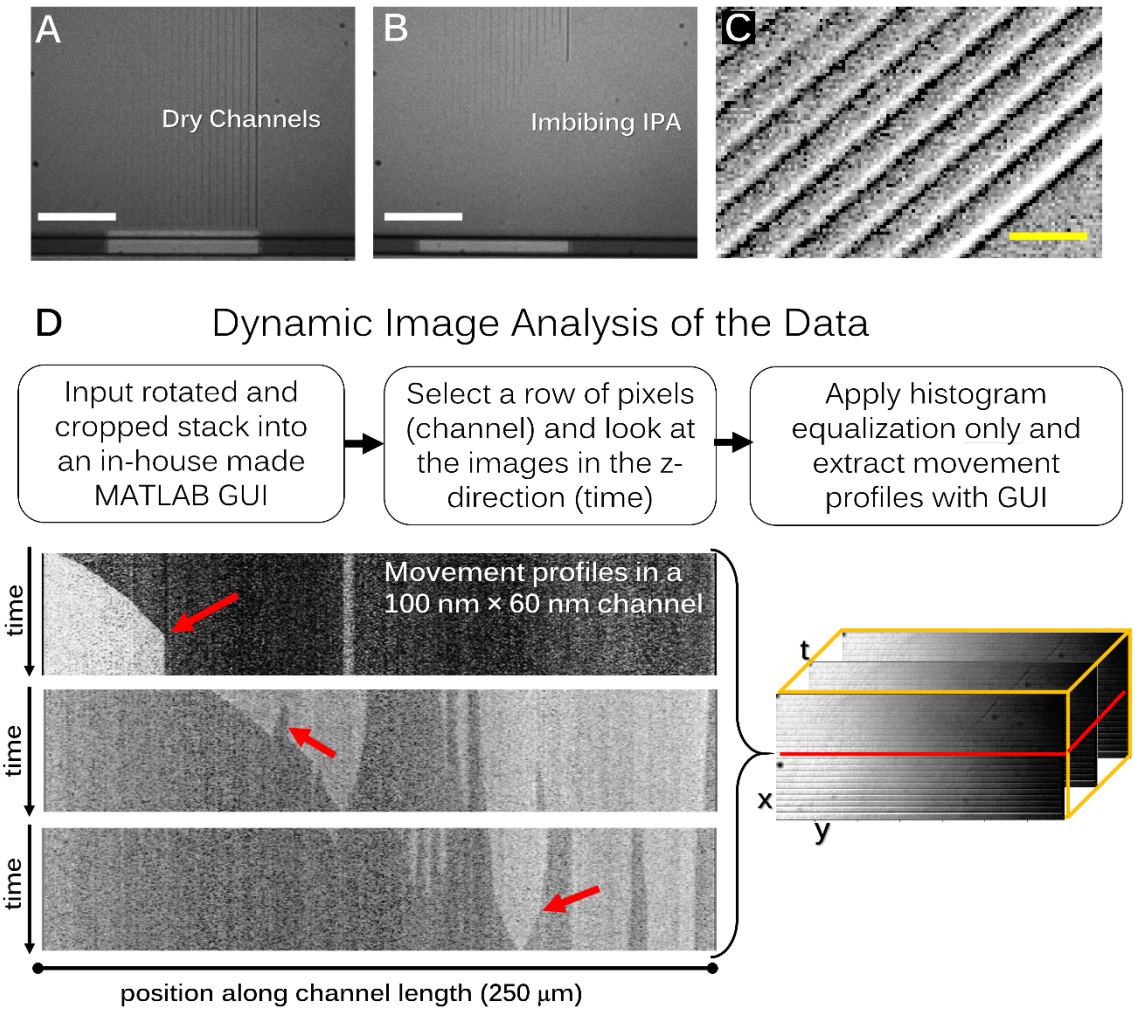

Figure 3.17: (A) and (B) display how isopropanol (IPA)-wetted and dry channels image in the silica array style nanochannels with reflected DIC (Nikon Eclipse Ti); scale bar is 40 μm. (C) Signature pair of light and dark signals at interfaces with a refractive index contrast allows the nanochannels to be visualized amidst noise; scale bar is 6 μm. (D) Dynamic image analysis workflow for extracting liquid and gas positions/profiles in the channels. Complex movement profiles are displayed as examples. The arrows point to, respectively from top to bottom, sudden imbibition stoppage (liquid is lighter-colored signal), spontaneous liquid plug formation (liquid is darker-colored signal), and swift dissolution of a gas plug when in contact with undersaturated imbibing liquid (gas is lighter-colored signal).

For arrays of parallel nanochannels, an image stack was oriented so that the channels were horizontal across the frame and 2D slices of selected rows of pixels across the stack in the direction of time were extracted. These slices revealed "profiles" of fluid movement in the nanochannel corresponding to the selected row of pixels. Figures 3.17, 5.9, 5.10, and 5.12 display examples of the profiles of fluid position within the channel (x-axis) versus experiment time (y-axis) extracted from channels as small as 30 nm in width (Figure 5.12). The only modification applied to the imbibition profile slices was histogram equalization to enhance contrast. Image analysis and profile extraction were also performed with an integration of ImageJ software and original MATLAB scripts. Contrasted areas of the nanochannels were assumed to be completely filled with liquid. The gas-liquid interface position is discernable within a few pixels, but any error introduced by this marginally smeared interface is negligible due to the extensive length of the nanochannels, approximately 400 pixels across.

3.5 CONCLUSIONS AND RECOMMENDATIONS

Nanofluidics, microscopy and image analysis techniques, and shale-inspired experimental methods for nanofabrication were presented in this chapter; the nanofabrication methods span from complex, precise, and expensive (Section 3.1) to facile, replicable, and economical (Sections 3.2 and 3.3). As shown in Chapter 5, the array-style silica nanofluidic chips, a product of an intensive nanofabrication scheme, were robust and versatile for experimentation purposes. However, because standard nanofabrication methods are often costly and of limited success rate to external or novice users, it is recommended to seek simplified methods when possible, so that research focus may be put on the experiments themselves.

This work reports the first construction of "reservoir-on-a-chip" versions of shale. Such synthetic representations of shale enable a novel branch of experimental investigations into nanopore-scale fluid transport physics (nanofluidics) that are intended to supplement conventional shale core analysis techniques. The documented two-step fabrication scheme is relatively simple, robust, and cost-effective; cleanroom tools are required for master pattern fabrication, but with subsequent soft lithography techniques, multiple batches of chips can be generated from a single master substrate. The key contribution of this fabrication scheme is the successful use of lacey carbon support films as shadow masks and the resemblance of the resulting copper hardmask to tight, dual-porosity, heterogeneous porous media such as shale.

Sag of the support films and redeposition of copper hardmask material during RIE are identified as limiting parameters of the shale-on-a-chip fabrication scheme. Investigations into the successful use of single-hole TEM grids with lacey carbon films as shadow masks are recommended in extensions of the work. The in-house preparation of widespread lacey patterns with formvar is also encouraged. Etching with CF_4 was found to be preferable to SF_6 for minimizing pattern roughness. Channel collapse and pairing, inherent to shallow and narrow PDMS structures, can be avoided with the use of alternative harder polymers such as PMMA or NOA 63 or use of the glass masters themselves as lab-on-a-chip devices.

In addition, using fouling mechanisms to the advantage of the researcher will render reservoir-on-a-chip construction processes of great ease. This approach was demonstrated with the patchwork nanochannel arrays created by imperfect diffraction gratings. The repurposing of consumer-grade discs is very simple and inexpensive, but

has only been employed for practical use in a few works such as that of Smith et al., who used BRDs for photon trapping applications [147].

In regard to tested fluids, nanochannel clogging is likely if the molecular diameter or particle size of injected surfactants, polymers, nanoparticles, or ferrofluids is on par with channel cross-sectional dimensions. It is recommended that future experimenters revisit the pumping scheme described in Section 3.4 to achieve greater fluid control. Due to the straightforward and flexible nature of their fabrication scheme, the documented shale-on-a-chip nanofluidic devices and patchwork nanochannel array devices can be readily constructed and integrated into unconventional reservoir rock research laboratories with access to research-grade optical microscopes.

Finally, these lab-on-a-chip devices eliminate the spatial uncertainty of the pore or pore network topology in an accompanying numerical model; thus, numerical and experimental comparisons can be clearer made on the basis of fluid physics.

> *Progress is made by trial and failure; the failures are generally a hundred times more numerous than the successes; yet they are usually left unchronicled.*
>
> William Ramsay, Nobel laureate in Chemistry

CHAPTER 4: Methodology for Finding Effective Nanoscale Viscosity, Capillary Pressure, Diffusivity, and Partitioning Coefficient*

Discovery consists of looking at the same thing as everyone else and thinking something different.

Albert Szent-Györgyi, Nobel laureate in Medicine

Two imbibition situations are discussed in this dissertation. One is the standard *open-ended imbibition* where liquid imbibes from one reservoir or microchannel into a nanoscale domain or nanochannels and the opposing reservoir or microchannel remains open to the atmosphere. The non-standard situation implemented herein is *trapped air bubble imbibition* where liquid imbibes into both of the opposing microchannels or reservoirs, entering the nanoscale domain or nanochannels from both sides and giving rise to a bubble of trapped air. As the liquid imbibes the size of the bubble shrinks and the rate of bubble compression competes with gas diffusion across the gas-liquid interface. This scenario enables a methodology, discussed in this chapter, for decoupling the following transport variables: capillary pressure, viscosity, diffusivity, and interfacial partitioning coefficient. Section 5.2 discusses the results when the methodology is implemented for the arrays of 2D silica nanochannels. The methodology is primarily devised for finding effective transport values in arrays of parallel nanochannels, but it can also be adapted and applied to nano-networks and bulk samples as is described in Section 4.4.

* The methodology presented in this chapter was published under the following reference, which was completed under the supervision of Matthew Balhoff and Carlos Torres-Verdín.

Kelly SA, Balhoff MT, Torres-Verdin C. Quantification of Bulk Solution Limits for Liquid and Interfacial Transport in Nano-Confinements. Langmuir 2015. doi:10.1021/la504742w.

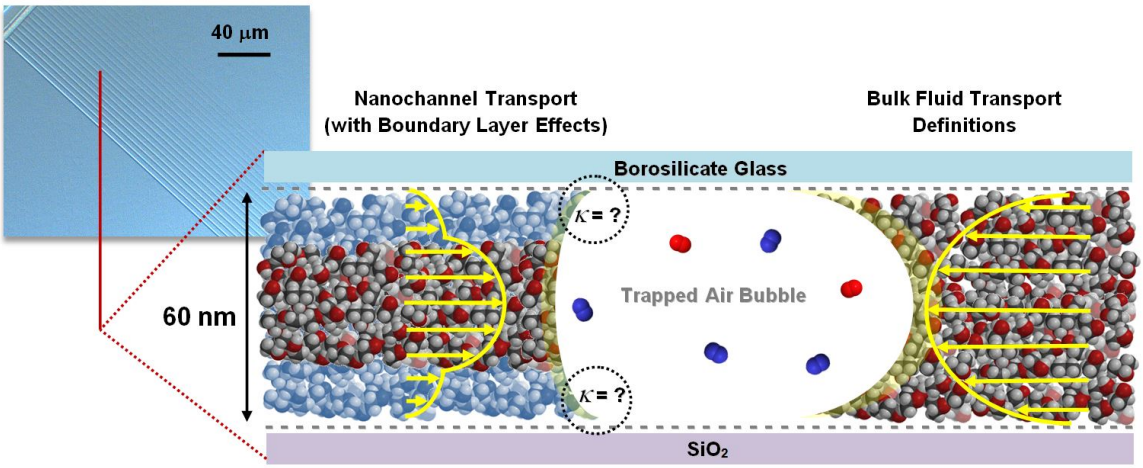

Figure 4.1: A trapped air bubble is introduced into the imbibition process to add an additional non-constant force such as gravity would add in a larger, vertical system. A subsequent analysis process enabled by the trapped bubble renders effective values of nanoscale capillary pressure and viscosity; these values are compared to the corresponding bulk values.

4.1 "HOW?": IMBIBITION WITH INTENTIONALLY TRAPPED BUBBLES

Recall that liquid imbibition is mathematically described by a conservation of momentum force balance, where the volume of liquid wicked into the channel is the control volume. At the onset of imbibition inertia dominates, negligible viscous terms are omitted from the force balance and, as a result, imbibed fluid length increases linearly with time for a short period of time. Poiseuille or viscous flow becomes established once inertia induced entrance effects have diminished. In a channel with radius R, and for a liquid of density ρ this transition occurs at a characteristic timescale of approximately [148]

$$t^* = \frac{2.1151\rho R}{\mu}, \tag{4.1}$$

which equates to times on the order of a mere 10^{-9} seconds in the 2D nanochannels due to their extremely high hydraulic resistivity. Thus, fluid inertia and entrance effects can be neglected and the analysis performed for the viscous regime. Extremely low dimensionless Reynolds numbers (*Re*) on the order of 10^{-7} in all of the nanochannels further confirm that the flow is viscous-dominated Stokes flow. In the viscous regime, inertial terms are neglected with a lubrication approximation, P_c is the driving force and increasing viscous losses, ΔP, cause the fluid to slow down with time. As a review of concepts introduced in Chapter 2, ΔP is described by Poiseuille's equation [1] for pressure driven flow which includes viscosity, μ, a geometric permeability term specific to the conduit shape, k, average velocity, u, and imbibed fluid length, l:

$$P_c = \Delta P = \frac{\mu}{k} u(t) l(t) \ . \tag{4.2}$$

The nanochannels are horizontally situated and hence the imbibition process is not affected by gravity. It is assumed that the dynamic meniscus maintains a roughly constant curvature, κ, throughout the imbibition process (quasi-static) and external pressures on opposite ends of the nanochannels are equal (atmospheric). The dimensionless capillary number (*Ca*) for the system is on the order of 10^{-6}, a range which indicates that surface tension and capillary forces dominate over viscous forces at menisci interfaces; these *Ca* numbers suggest that the meniscus shape is barely deformed by viscous forces. When u is expressed as $u=dl/dt$, the Washburn equation for imbibition [21], can be derived from Eq. (4.2):

$$l = \beta \sqrt{t} \tag{4.3}$$

where

$$\beta = \sqrt{2 P_c \frac{k}{\mu}} \ . \tag{4.4}$$

The macroscopic solutions for k and P_c in a rectangular geometry are given in Section 2.3. Note that in Eq. (4.3) P_c and μ^{-1} are multiplicative terms in a "wicking coefficient," β, such that the values of these variables for a given set of length-versus-time data are non-unique in the current form of the equation.

Section 3.4.2 explained how to extract length-versus-time nanochannel imbibition profiles from optical microscopy data. Each individual nanochannel's imbibition profile(s) are fit to the following functional form, where α and n are fitting parameters, and velocity is arrived at by the derivative of the function, i.e.,

$$l = \alpha t^n \tag{4.5}$$

and

$$u = \alpha n t^{n-1} \ . \tag{4.6}$$

This power law description is inspired by the Washburn equation, but n does not necessarily have to equal 0.5. Open-ended imbibition experiments merely require extracting the best-fit values of α and n from length-versus-time data.

The experiments key to the methodology for decoupling transport variables are designed so that a trapped air pocket occurs between two imbibing liquid interfaces. The purpose of this bubble is to directly introduce an additional time-dependent force term to the imbibition force balance [149] without relying on the accuracy or effectiveness of external apparatuses on the isolated nanochannels. The following equation reflects the addition of the bubble pressure, $P_b(t)$, to Eq. (4.2):

$$P_c - P_b(t) = \frac{\mu}{k} u(t) l(t) \tag{4.7}$$

and

$$P_b(t) = P_c - \frac{\mu}{k} \alpha^2 n t^{2n-1} \ . \tag{4.8}$$

A time-dependent function, Eq. (4.8), is produced by the introduction of the time-dependent pressure term. P_c and μ are now linearly independent coefficients, unlike in Eq. (4.2), and unique positive values of least-squares best-fit can be determined from a series of time-versus-bubble pressure data points.

4.2 CASES AND DESCRIPTIONS OF TRAPPED BUBBLE PRESSURES

The changing pressure of the trapped bubble must be described in order to determine P_c and μ from Eq. (4.8). The n-values fitted to imbibition data indicate whether trapped-bubble pressures remain constant with time (Case I), increase (Case II), or decrease (Case III). Table 4.1 explains this relationship and the utility of each case. In all cases the volume and number of moles of gas in the bubble decrease with time. Data sets from three independent trapped bubble experiments with isopropanol and air are analyzed in Section 5.2. The threshold for assigning data to Case I versus Cases II and III was $n = 0.5 \pm 0.025$; an error of 0.025 is approximately the standard deviation of the set of n-values that render a normal distribution around $n = 0.5$. The n-values vary from experiment to experiment even in the same channel because they are a product of the original size of the bubble and the formation of liquid plugs. When a liquid plug is present at one end of a channel the imbibition into the trapped bubble occurs primarily from the other side of the channel. Liquid plugs are detected in the data via unusual, slower, or static fluid profiles (see Figure 5.12 for examples of this occurrence). Diffusion of air across liquid plugs is assumed to be minimal because these plugs are quickly saturated with air molecules.

Trapped bubble data categories and significance

Case	*n*-value	Bubble Pressure	Notes
Case I	$n = 0.5$	Remains approx. constant with time	▪ Approximately constant molar volume in the bubble ▪ No appreciable external force variation ▪ Constant Dirichlet boundary condition for the advection-diffusion equation ▪ The number of molecules in the bubble and partitioned across the meniscus with time can be assessed ▪ Appropriate values of D, k_H, and N_i can be assessed
Case II	$n < 0.5$	Increases with time	▪ Bubble molar volume is not constant ▪ Transient Dirichlet boundary condition for the advection-diffusion equation ▪ Compression occurs faster than gas partitioning/diffusion ▪ Data can be used to estimate P_c and μ
Case III	$n > 0.5$	Decreases with time	▪ Bubble molar volume is not constant ▪ Transient Dirichlet boundary condition for the advection-diffusion equation ▪ Gas partitioning/diffusion occurs faster than compression ▪ Data can be used to estimate P_c and μ

Table 4.1: Trapped bubble data categories and significance.

Bubbles in the nanochannels are very unstable when the concentration of gas in the imbibing liquid is dilute; a trapped bubble disappears within less than a minute for a 30 nm × 60 nm channel and within seconds for a 500 nm × 60 nm channel. Thus, a determination of the bubble pressure must take into account the number of moles of air lost due to partitioning, $N_p(t)$, across one or both menisci interfaces. The pressure in the shrinking bubble is described with the ideal gas law, given by

$$P_b(t) = \frac{RT}{V_b(t)}\left(N_0 - \sum_{t_i=0}^{t} N_p(t_i) \right), \tag{4.9}$$

where the number of moles initially in the bubble, N_0, is determined by calculating the number of moles at atmospheric pressure in the initial volume of the bubble. R is the ideal gas constant, T is temperature and is assumed to remain constant, and $V_b(t)$ is the volume of the bubble with time from the microscopy data. The ideal gas equation of state is deemed appropriate because the pressures in the bubbles do not exceed a few bars due to the significant mass transfer of gas across the liquid menisci during compression. However, by using the ideal gas law to estimate the pressure of trapped air bubbles it is implicitly assumed that gas molecules are statistically numerous, partake in elastic molecular interactions, and are negligible in size compared to their confinement. Regarding the statistical ability to describe gases trapped in the nanochannels, the number of molecules present is far less than one mole, but still initially on the order of millions of molecules.

Interfacial partitioning and dissolved gas transport in liquid must be considered to determine $N_p(t)$. Specific analytical solutions to the 1D advection-diffusion equation (ADE) describe the concentration of air, c_a, within the imbibing liquid in time, t, and space, x, where D is the diffusivity of a gas in a liquid. The 1D ADE is a second-order, non-linear partial differential equation (PDE) for the imbibition situation because the velocity coefficient, u_x, is time-dependent, i.e.,

$$\frac{\partial c_a}{\partial t} + u_x(t)\frac{\partial c_a}{\partial x} = D\frac{\partial^2 c_a}{\partial x^2} \quad . \tag{4.10}$$

The first term of Eq. (4.10) is the transient term, the second term is the advection term, and the term on the right hand side of the equation is the diffusion term.

The variables in Eq. (4.10) are non-dimensionalized as follows:

$$\overline{c}_a = \frac{c_a}{C^*} \ , \tag{4.11}$$

$$\overline{x} = \frac{x}{L} \ , \tag{4.12}$$

$$\overline{t} = \frac{t}{\tau} \ , \tag{4.13}$$

and

$$\tau = \left(\frac{L}{\beta} \right)^2 \ , \tag{4.14}$$

where L is the length of half of a nanochannel, τ is the characteristic timescale of imbibition into the entire length L as calculated by Eq. (4.3), and C^* is the concentration of air originally in the trapped bubble. These variables render a non-dimensional form of the 1D ADE, given by

$$\left[\frac{L^2}{D\tau} \right] \frac{\partial \overline{c}_a}{\partial \overline{t}} + \left[\frac{u_x(\overline{t})L}{D} \right] \frac{\partial \overline{c}_a}{\partial \overline{x}} = \frac{\partial^2 \overline{c}_a}{\partial \overline{x}^2} \ . \tag{4.15}$$

The dimensionless numbers that arise are the bracketed terms in Eq. (4.15) and are, from left to right, the inverse of the Fourier number (*Fo*) and the Péclet number (*Pe*). Péclet numbers for the trapped bubble nanochannel case are calculated, using experimentally observed values of u_x, to be near unity. *Pe* values near unity signify that the rate of advective gas transport is on par with the rate of diffusive gas transport in the imbibing liquid; hence, neither phenomenon can be neglected. Fourier numbers calculated using the experimentally observed imbibition times also approach unity, indicating that the time for diffusing gas molecules to reach the beginning of one of the nanochannels (D/L^2), is comparable to the timescale of imbibition, τ. However, only when $Fo >> 1$ can the transient or unsteady-state term in Eq. (4.15) be neglected [150]. Specifically, a system can potentially be considered pseudo steady-state when $Fo > 10$

[151]. Thus, a semi-infinite boundary condition at the entrance of the 2D nanochannels described in Section 3.1 is appropriate for the problem at hand. The case of very high *Fo* numbers occurs for long imbibition times, short nanochannels, and liquids with high diffusivity. In the cases of very low or high *Pe* numbers the advection or diffusion terms, respectively, can be neglected and the problem is simplified. These cases may occur in other nanofluidic constructions and for different liquid-gas combinations.

Henry's Law for phase partitioning is used to relate the bubble pressures to the concentration of air dissolved in imbibing liquid at the gas-liquid boundary, namely,

$$c_{a0}(t) = \frac{P_b(t)}{k_H} = \frac{P_c - \frac{\mu}{k}\alpha^2 n t^{2n-1}}{k_H} \quad , \tag{4.16}$$

where k_H is a mass transfer coefficient and is, macroscopically, a constant value for a particular bulk liquid-gas interface. This relationship manifests itself as either a constant (Case I) or time-dependent (Cases II and III) Dirichlet boundary condition in the 1D ADE diffusion problem. Appropriate analytical solutions to the 1D ADE for the scenario presented herein are derived in detail in Section 4.3 [152] [153] [154]. The derivative of the solutions evaluated at $x = 0$, the meniscus, for $t > 0$ is necessary to determine the mass flux of air, J, at an interface, given by

$$J = -D\frac{dc_a}{dx}\bigg|_{x=0}^{t=t} = \frac{N_{p,i}^{ADE}}{wh\Delta t} \quad , \tag{4.17}$$

where Δt is the time between data points (image frames) and $N_{p,i}^{ADE}$ is the amount of air partitioned across a single meniscus, labeled i, according to the analytical solution to the 1D ADE. Partitioning often occurs at both sides of the bubble, whereby the total number of moles partitioned is dependent on the sum of the mass flux solved at each interface, i.e.,

$$N_p^{ADE}(t) = N_{p,left}^{ADE}(t) + N_{p,right}^{ADE}(t) \ . \tag{4.18}$$

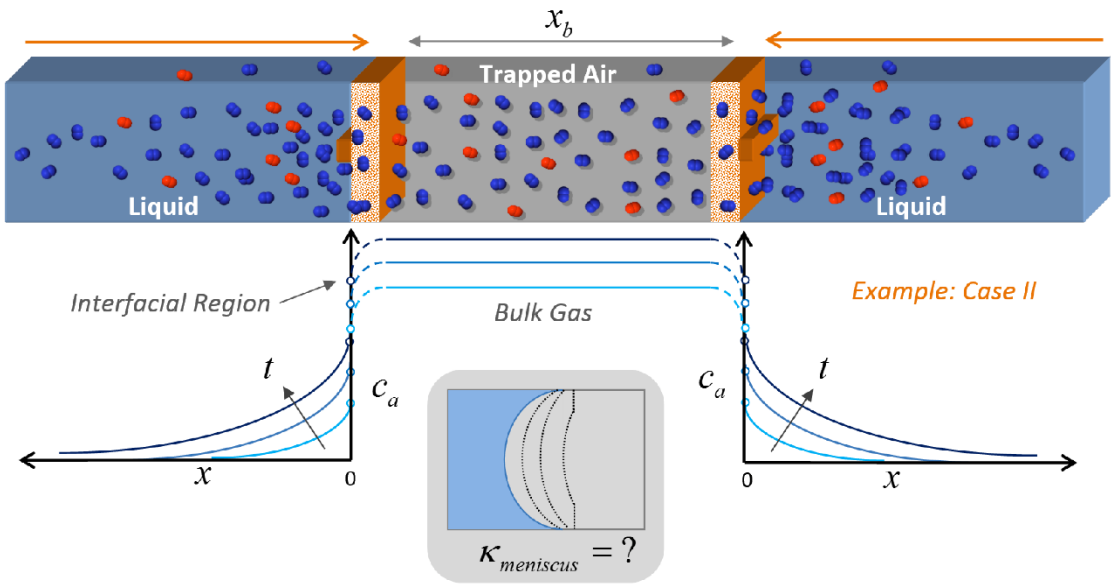

Figure 4.2: A conceptual cartoon of the trapped air bubble imbibition process. Menisci are depicted as and are akin to pistons with permeable membranes which compress the molecules of trapped air due to the driving force of capillary pressure. Air molecules partition across the interfaces and diffuse into the imbibing liquid as a function of position and time. The actual meniscus is curved, although the nature of κ is uncertain (an effective capillary pressure is found).

Thus far it has been assumed that the bulk concentration of air molecules in both the liquid and bubble regions extend right up to the interface. In actuality there is an *interfacial region* at partitioning surfaces in which there is a positive, negative, or even null "surface excess" amount of molecules depending on where an interfacial "Gibbs dividing surface" is assigned [155]. Notable interfacial resistance to mass transport across liquid-vapor menisci is observed in nanoporous membranes [96]. That is, significant

molecular reflection at the interface due to nano-confinement is possible. An additional term, N_i, accounting for the difference in air molecules between the interfacial region and the bulk is necessary, whereupon

$$N_p(t) = N_p^{ADE}(t) - N_i = wh\Delta t\left(-D\frac{dc_a}{dx}\bigg|_{x=0}^{t} \right) . \tag{4.19}$$

It is noted that fully air-saturated liquid can be used to prevent significant bubble diffusion and potentially simplify the problem by eliminating the N_p term. However, this method was not employed in the experiments presented herein due to issues with *in situ* bubble formation with aerated fluids and a desire to learn about liquid-gas mass transfer in nano-confinements.

4.2.1 Case I data: determination of diffusion values

Case I data is used to: (1) determine appropriate values of D, k_H, and N_i, and (2) validate the applicability of the 1D ADE to describe gas partitioning and diffusion in solution within the nanochannels. Unlike Case II and III data, the bubbles in Case I data have an approximately constant pressure, and, therefore, constant molar volume with time. Case I data renders the number of moles in a bubble with time and, consequently, the rate of gas partitioning across a nanochannel meniscus. To determine the former, $x_b(t)$, the bubble length with time, and then V_{b0}, the initial volume of the bubble, are obtained from an image stack, and the number of moles in the bubble, N_b, needed to satisfy constant molar volume at each time is calculated as

$$N_b(t) = \frac{N_0}{V_{b0}} whx_b(t) . \tag{4.20}$$

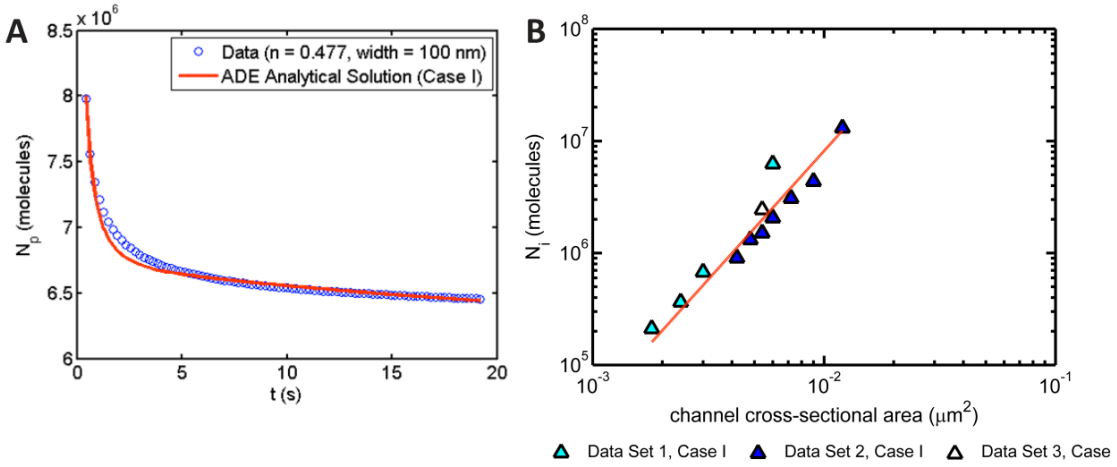

Figure 4.3: (A) Comparison between data of a selected case of Case I imbibition in a 100 nm × 60 nm channel and the corresponding 1D ADE analytical solution of the number of molecules partitioned with time across a meniscus interface (Eq. (4.37)). Equal partitioning across both imbibing menisci and no partitioning across liquid plugs are assumed when calculating $N_p(t)$. The parameters resulting in the above fit are D = 2150 μm^2/s, k_H = 8.15×10^{20} μm^3-Pa/mol, and N_i = ~6.3x10^6 molecules. (B) The trend of molecular reflection with interface area is later used to estimate the interfacial resistance in Case II/III data.

The number of moles partitioned across the interfaces at each time frame, $N_p(t)$, is simply the difference in N_b between a current and previous time frame. Validation of the applicability of the 1D ADE for nanoscale mass transport is made by comparing its solution (see Eq. (4.37)) to $N_p(t)$ curves calculated from sets of Case I data points. Appropriate values of D, k_H, and N_i are obtained by iterating to find the set of values that minimize the sum of squared residuals between the two curves. Figure 4.3 displays an example of a match between the curves. This fitting was performed across all instances of Case I nanochannel data and good fits were obtained when D remained very near to its bulk value (2200 μm^2/s) and k_H was on the order of 10^{20}-10^{21} μm^3-Pa/mol, a realistic value for gas-liquid interfaces. The value of N_i is ~2.1x10^5 molecules for a 30 nm × 60

nm channel and grows with increasing channel width, a logical trend since excess surface amount is a function of interface area. A log-linear function is fit to values of N_i versus channel cross-sectional area to enable estimates of molecular reflection with interface size.

4.2.2 Case II/III data: determination of P_c and μ

Case II and III data are used to estimate the values of P_c and μ in the 2D nanochannels. A combination of Eq.'s (4.8), (4.9), (4.17), and (4.18) results in an expanded version of the original pressure balance:

$$P_c - \frac{\mu}{k}\alpha^2 n t^{2n-1} = \frac{RT}{V_b(t)}\left(N_0 - \sum_{t_i=0}^{t} wh\Delta t\left(-D\right)\left(\left.\frac{dc_a}{dx}\right|_{x=0,left}^{t_i} + \left.\frac{dc_a}{dx}\right|_{x=0,right}^{t_i} \right) - N_i \right) , \quad (4.21)$$

where P_c and μ are linearly independent variables. The value of D used is 2200 $\mu m^2/s$; this value's appropriateness is verified by Case I data analysis. By insertion of Eq.'s (4.47)-(4.53), Eq. (4.21) can be represented as the following system of linear equations where each row of the matrix/vector system represents a data point from the imbibition process (to keep the equation succinct, N_i = 0 and diffusion through only one imbibing meniscus are assumed):

$$\left[A\right]\left[x\right] = \left[b\right] \quad (4.22)$$

$$[A] = \begin{bmatrix} \left(\frac{1}{RTwh\Delta tD} - \frac{1}{V_b(t)}\sum_{t=0}^{t_1}\left(\frac{1}{k_H}\frac{dA}{dx}\Big|_{x=0}^{t=t_1}\right)\right) & \left(\frac{-\alpha^2 nt^{2n-1}}{RTwh\Delta tDk} - \frac{1}{V_b(t)}\sum_{t=0}^{t_1}\left(-\frac{a_2}{kk_H}\frac{dB_{\lambda_1}}{dx}\Big|_{x=0}^{t=t_1} - \frac{b_2}{kk_H}\frac{dB_{\lambda_2}}{dx}\Big|_{x=0}^{t=t_1}\right)\right) \\ \vdots & \vdots \\ \vdots & \vdots \\ \left(\frac{1}{RTwh\Delta tD} - \frac{1}{V_b(t)}\sum_{t=0}^{t_f}\left(\frac{1}{k_H}\frac{dA}{dx}\Big|_{x=0}^{t=t_f}\right)\right) & \left(\frac{-\alpha^2 nt^{2n-1}}{RTwh\Delta tDk} - \frac{1}{V_b(t)}\sum_{t=0}^{t_f}\left(-\frac{a_2}{kk_H}\frac{dB_{\lambda_1}}{dx}\Big|_{x=0}^{t=t_f} - \frac{b_2}{kk_H}\frac{dB_{\lambda_2}}{dx}\Big|_{x=0}^{t=t_f}\right)\right) \end{bmatrix} \tag{4.23}$$

$$[x] = \begin{bmatrix} P_c \\ \mu \end{bmatrix} \tag{4.24}$$

$$[b] = \frac{N_0}{wh\Delta tD}\begin{bmatrix} \frac{1}{V_b(t_1)} \\ \vdots \\ \vdots \\ \frac{1}{V_b(t_f)} \end{bmatrix}. \tag{4.25}$$

A linear least-squares criterion (MATLAB's *mldivide* function) is applied to this overdetermined system of equations, to solve for the values of P_c and μ that correspond to the smallest residuals. No constraints are imposed on the least-squares algorithm and the matches between the $V_b(t)$ data and the bubble volumes calculated from Eq. (4.21) using best-fit values of P_c and μ are inspected for quality control. Iteration on the value of k_H for each trapped bubble case was necessary to achieve good fits; k_H shows up in the rightmost terms of Eq. (4.21). An example of goodness of fit between these curves is displayed in Figure 4.4. The extracted k_H values and implications of a non-constant partitioning coefficient result are addressed later in Chapter 5.

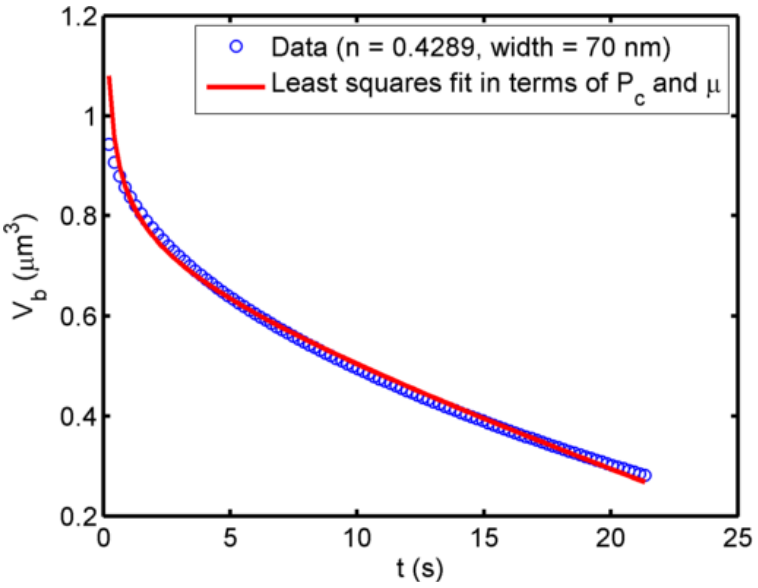

Figure 4.4: Example of a fit for a Case II set of data with isopropanol-air in a 70 nm × 60 nm channel obtained between bubble volume data and the volume obtained from Eq. (4.21) with the best-fit values of capillary pressure and viscosity. Early times are the most difficult to match with the least-squares fit because the liquid is swiftest at the beginning of the imbibition process, resulting in fewer data points. Additionally, imbibition at very early times may not be subject to the effects of the trapped bubble yet. For the data set shown above 21.26 seconds of imbibition were captured, $\alpha = 49.25$ μm/s^n, $n = 0.4289$ and the fit of the data to this $l=\alpha t^n$ functional form is $R^2 = 0.996$. From the least-squares analysis of Eq.'s (4.22)-(4.25), $\mu = 15.52\times10^{-3}$ Pa s (a factor of 7.9 times higher than the bulk value), $P_c = 235{,}686$ Pa (83% lower than the bulk value), and $k_H = 4\times10^{22}$ μm^3.Pa/mol.

The best-fit values of P_c and μ are always positive for Case II data analysis because Eq. (4.7) was derived assuming the force vector from the enclosed bubble acts against the capillary force. For Case III, the best-fit values of P_c and μ are both mathematically negative (per Eq. (4.7)), correctly indicating that the dropping pressure of the enclosed bubble aids in pulling the fluid forward (multiply both sides of Eq. (4.7) by -1 to put the equation in the correct from for Case III). In a few instances of Case III data

analysis the best-fit values of P_c and μ are, respectively, positive and negative. This outcome is unexpected and physically may correspond to net dewetting, where the nanoscale meniscus curvature becomes deformed such that capillary pressure acts against imbibition and the vacuum effect of the Case III bubble solely pulls the fluid forward.

4.3 DERIVATION OF ANALYTICAL SOLUTIONS FOR 1D GAS DIFFUSION WITHIN AN IMBIBING LIQUID

A closed-form 1D ADE solution to describe diffusion across a meniscus interface and within an imbibing liquid in a long conduit was necessary for the analysis detailed in Section 4.2. This solution enabled an assessment of the amount of moles partitioned across the meniscus interface with time, N_p, information that was required to determine for the pressure of the trapped bubble. For the physical case of gas diffusion within an imbibing liquid, the 1D ADE has a nonlinear term due to the time-dependent fluid velocity coefficient, $u_x(t)$. Nonlinear PDE's are typically challenging to solve and require the employment of various mathematical techniques to arrive at a closed form solution if one is possible. Shown and referenced herein are the techniques used to solve this nonlinear PDE.

A math-transferable summary of the physical problem of diffusion of air from a trapped bubble into an imbibing liquid within a long channel is as follows:

- Time dependent liquid velocity, $u_x(t)$
- Constant diffusivity, D
- Moving boundary (meniscus)
- One-dimensional diffusion and velocity (x-direction)
- The concentration of gas in the liquid is initially dilute or solute free

- The pressure of the bubble (hence the concentration of air molecules at the interface) can either remain constant, increase, or decrease with time

The mathematical conditions, techniques, and simplifications made were:

- Placement of the problem's coordinate system at the moving meniscus
- For simplicity, assumption that the meniscus is rigid and flat
- Assumption of a semi-infinite domain at the end of the long channel
- A Dirichlet concentration boundary condition (BC) of uniform, increasing, or decreasing nature (Cases I, II, and III, respectively) at the liquid meniscus

Thus, in terms of variables, the initial condition is written as

$$c_a(t=0)=0 \ , \tag{4.26}$$

while the Neumann boundary condition on the end of the channel where the fluid originates from is expressed as

$$\frac{dc_a}{dx}(x\to\infty)=0 \ . \tag{4.27}$$

The case of uniform concentration at the boundary translates to the following Dirichlet boundary condition:

$$c_a(x=0)=c_{a0} \ , \tag{4.28}$$

where

$$c_{a0}=\frac{P_b}{k_H}=\frac{P_c-\frac{\mu}{k}u_x l}{k_H}=\frac{P_c-\frac{\mu}{k}\alpha^2 n}{k_H} \ , \tag{4.29}$$

per Henry's Law for phase partitioning and the relationship between the bubble pressure and capillary pressure and viscous losses (Eq. (4.7)). The case of variable concentration at the boundary translates to the following Dirichlet boundary condition:

$$c_a(x=0)=f(t) \ , \tag{4.30}$$

where

$$f(t) = \frac{P_b}{k_H} = \frac{P_c - \frac{\mu}{k} u_x l}{k_H} = \frac{P_c - \frac{\mu}{k} \alpha^2 n t^{2n-1}}{k_H} \quad . \tag{4.31}$$

Note that Henry's Law assumes thermodynamic equilibrium at the interface; thus, in using Henry's Law local equilibrium is assumed at each time step (each image captured) in the dynamic imbibing system.

As alluded to in the problem summary, to account for the moving fluid boundary, the coordinate system ($x = 0$) is placed at the moving boundary (the meniscus), which is simplified to a flat interface for the problem description. From the perspective of the meniscus, the liquid in the nanochannel elongates with time such that the end of the channel is constantly growing farther away with time and can be approximated as a semi-infinite domain. The amount of air partitioning across the interface at $x = 0$ changes per the pressure of the bubble on the other side of the boundary. Convective resistance to the diffusion of air in solution changes with time because the velocity of imbibing liquid decreases with time.

Jaiswal et al. provide analytical solutions to the 1D ADE with time-dependent coefficients in a semi-infinite domain for several physical cases. They reduce the time-dependent coefficients of the equation to constant coefficients with a variable transformation and solve the resulting equation with Laplace transforms [152]. The authors' variable transform is written as follows:

$$X = \int f_2(mt) dx = x f_2(mt) \tag{4.32}$$

and

$$T = \int_0^t f_2^2(mt) dt \quad , \tag{4.33}$$

for, respectively, spatial and temporal variables. The method of Jaiswal et al. requires that

$$u_x(t) = u_0 f_2(mt) \ , \tag{4.34}$$

such that $f_2(mt) = 1$ when m or t is zero. This relation ensures that $T = 0$ at $t = 0$, so that the initial condition remains the same in the new time domain. To meet this criterion, imbibition velocity data were fitted to the following functional form:

$$u_x = c(a\exp(-bt) + 1 - a) \ . \tag{4.35}$$

When $c = u_0$ and $b = m$, Eq. (4.35) can be rewritten as

$$f_2(mt) = 1 + a[\exp(-mt) - 1] \ . \tag{4.36}$$

Note that u_0 is negative when the function is reinserted into the final solution since velocity is acting in a direction against that of the diffusion.

For a constant boundary condition (Case I) the appropriate analytical solution is derived by Jaiswal et al. (refer to their paper for derivation details) as [152]

$$c_a(X,T) = \frac{c_{a_0}}{2}\left[erfc\left(\frac{X - u_0 T}{2\sqrt{DT}}\right) + \exp\left(\frac{u_0}{D}X\right) erfc\left(\frac{X - u_0 T}{2\sqrt{DT}}\right)\right] \ . \tag{4.37}$$

For the case of a non-constant boundary condition (Case II and III), the variable transformation of Jaiswal et al. is again applied to deal with the time-dependent velocity function, i.e.,

$$\frac{\partial c_a}{\partial t} + u_x(t)\frac{\partial c_a}{\partial x} = D\frac{\partial^2 c_a}{\partial x^2} \rightarrow \frac{\partial c_a}{\partial T} + u_0\frac{\partial c_a}{\partial X} = D\frac{\partial^2 c_a}{\partial X^2} \ , \tag{4.38}$$

$$f(t) \rightarrow f(T) \ . \tag{4.39}$$

Note that implementation of this transformation does not change the form of the original boundary conditions, which are then written in terms of the new space and time variables, namely,

$$c_a(T = 0) = 0 \ , \text{(Initial condition)} \tag{4.40}$$

$$c_a(X = 0) = f(T) \ , \text{(Dirichlet BC)} \tag{4.41}$$

$$\frac{dc_a}{dX}(X \to \infty) = 0 \text{ . (Neumann BC)} \tag{4.42}$$

Next, I invoke the analytical solution of Marino, which solves the 1D ADE in a semi-infinite domain for a constant velocity coefficient and an exponentially changing boundary condition of the following form where the time coefficient λ can be a positive or negative value [153]:

$$c_a(x=0) = Ce^{-\lambda t} \ . \tag{4.43}$$

By way of Jaiswal et al.'s transformation, the PDE is now in the appropriate form to apply the Marino solution. Recall the description of *f(t)*, now described in terms of *T* as

$$f(T) = \frac{P_b}{k_H} = \frac{P_c - \frac{\mu}{k} u_x l}{k_H} \ . \tag{4.44}$$

Likewise, the time-dependent imbibition velocities, u_x, and imbibition lengths, l, must be described in terms of T. The product of u_x and l is described with a summation of exponentials, given by

$$u_x l = \alpha^2 n t^{2n-1} = a_2 e^{-\lambda_1 T(t)} + b_2 e^{-\lambda_2 T(t)} \ . \tag{4.45}$$

By combining Eq.'s (4.43) and (4.44), the boundary condition at the interface is then specified as

$$c_a(X=0) = C_1 + C_2 e^{-\lambda_1 T(t)} + C_3 e^{-\lambda_2 T(t)} \ , \tag{4.46}$$

where

$$C_1 = \frac{P_c}{k_H} \ , \tag{4.47}$$

$$C_2 = -\frac{a_2 \mu}{k k_H} \ , \tag{4.48}$$

and

$$C_3 = -\frac{b_2 \mu}{k k_H} \ . \tag{4.49}$$

The superposition principle can be applied due to the additive nature of the boundary condition of Eq. (4.45). Accordingly, the PDE of Eq.'s (4.38)-(4.42) is solved for each case of the time dependent (exponentially changing) boundary condition, $C_2 e^{-\lambda_1 T(t)}$ and $C_3 e^{-\lambda_2 T(t)}$, using the Marino solution. Those solutions, labeled $B(X,T)|_{\lambda=\lambda_1}$ and $B(X,T)|_{\lambda=\lambda_2}$, and the solution for a constant boundary condition (Eq. (4.37)), labeled $A(X,T)$, are superimposed to arrive at a complete analytical solution in terms of X and T, given by [154]

$$c_a(X,T) = C_1 A(X,T) + C_2 B(X,T)|_{\lambda=\lambda_1} + C_3 B(X,T)|_{\lambda=\lambda_2} , \tag{4.50}$$

$$A(X,T) = \frac{1}{2} erfc\left(\frac{X - u_0 T}{2\sqrt{DT}}\right) + \frac{1}{2}\exp\left(\frac{u_0 X}{D}\right) erfc\left(\frac{X + u_0 T}{2\sqrt{DT}}\right) , \tag{4.51}$$

$$B(X,T) = e^{-\lambda T}\left[\frac{1}{2}\exp\left(\frac{(u_0 - y)X}{2D}\right) erfc\left(\frac{X - yT}{2\sqrt{DT}}\right) + \frac{1}{2}\exp\left(\frac{(u_0 + y)X}{2D}\right) erfc\left(\frac{X + yT}{2\sqrt{DT}}\right)\right] , \tag{4.52}$$

and

$$y = u_0\left(1 - \frac{4\lambda D}{u_0^2}\right)^{1/2} . \tag{4.53}$$

The initial variable transform is reapplied to express the solution in terms of x and t again. For rare imbibition cases with constant velocity (possible, for example, in counter-current imbibition and nanochannels with non-constant geometry) this transform is simply $X=x$ and $T=t$.

4.4 USING THE METHODOLOGY FOR CHIPS AND SAMPLES WITH NANO-NETWORKS

The methodology described for parallel nanochannels can be used for both nano-network style chips and bulk nanoporous samples with slight modifications. For the case

of nano-networks nanofluidic devices, optical microscopy data will enable the size and locations of trapped bubbles to be captured with time. The liquid-gas interfacial area can also be determined with a combination of microscopy data and knowledge or characterization of the fabricated geometry. As was discussed in previous chapters, this visualization is a major advantage of nanofluidic studies. For bulk samples such as nanoporous materials and shale, visualization is a challenge and indirect data methods must be used; though, transparent mediums such as Vycor 7930 nanoporous glass and high resolution Micro-CT may provide the overall location of an imbibition front with time. In addition, for bulk samples the use of a trapped bubble or air mass to introduce an additional force may not induce an appreciable force on the fluid until late times (the size of the trapped air mass will depend on the size of the sample) and/or may not be feasible to capture (especially with opaque samples). Thus, another source of significant pressure, P_{ext}, can be implemented for bulk samples in place of the bubble pressure used in the nanofluidic devices, such that

$$P_c - P_{ext}(t) = \frac{\mu}{k} u(t) l(t) \ . \tag{4.54}$$

The P_{ext} term must be either time dependent or position dependent (i.e., a function of length imbibed x). An example of the latter, implemented in a decoupling scheme by Li and Horne (2001) for imbibition in conventional porous media [156], is hydrostatic pressure in a vertical system, $P_h = \rho g y$; albeit gravity effects are typically negligible in nanoscale systems. For the assumption of constant values of μ and P_c, a constant external pressure on the imbibing fluid will produce a linear relationship of the form $y=ax$; the form $y=ax+b$ is necessary to decouple μ and P_c.

Besides trapped gas bubbles, $P_{ext}(t)$ or $P_{ext}(x)$ variation can be implemented in various ways for nano-network devices or nanoporous media samples. Examples of $P_{ext}(t)$

include piston or syringe pumping in the liquid at the inlet and/or pulling a vacuum at the sample/chip outlet in addition to imbibition. The strength of the pump or vacuum (or both implemented simultaneously) will ramp with time. Technically, these methods equate to a hybrid of forced imbibition with spontaneous imbibition. A non-wetting fluid can be used in this method as well if the pump or vacuum is strong enough. Alternatively, the sample can be fully wetted and drainage, pulling a wetting liquid out of the pore-space or fluidic geometry, can be achieved using a ramped vacuum pump. Besides gravity, $P_{ext}(x)$ can be challenging to implement without rendering μ, k, or P_c non-constant by altering the pore space.

Data arrays of $u(t)$ and $l(t)$ are readily obtained from images of imbibition in nanofluidic chips with geometries that facilitate a piston-like front. For opaque porous media, $q_w(t)$ and $V_w(t)$, flow rate and volume imbibed, can instead be monitored. Handy presented the Washburn equation for imbibition in a form suitable for porous media [157],

$$V_w^2 = A^2 \frac{2P_c k_w \phi S_w}{\mu_w} t \ , \tag{4.55}$$

where the subscript w indicates wetting fluid, A is the sample area perpendicular to the direction of imbibition, ϕ is porosity, and S_w is saturation of the wetting fluid in the pore volume, V_p. Thus, in porous media Eq. (4.54) takes the form of

$$P_c - P_{ext}(t) = \frac{q_w \mu_w x}{A k_w} \ , \tag{4.56}$$

assuming a piston-like imbibition front, such as was imbibition in a single nanochannel. The volume of imbibed liquid is expressed as [156]

$$V_w = Ax\phi(S_{wf} - S_{wi}) \ , \tag{4.57}$$

where S_{wf} is the saturation of the wetting fluid at the imbibing front and S_{wi} is the initial (often irreducible) saturation of water in the sample. Before imbibition, S_{wi} can be estimated with methods such as nuclear magnetic resonance (NMR) using very short relaxation or T_2 times (I found a T_2 maximum around 2 ms to be appropriate for bound water in shales). Combining Eq.'s (4.56) and (4.57) results in

$$P_c - P_{ext}(t) = \frac{\mu_w}{k_w} \frac{q_w L}{A\left(S_{wf} - S_{w_i}\right)} \frac{V_w}{V_p} \ , \tag{4.58}$$

where L is the sample length. The effective μ (or k) and P_c values obtained are for wetting front saturation S_{wf} or maximum saturation, assumed constant during the imbibition process; thus, these values represent one crucial point on a capillary pressure (P_c vs. S_w) or relative permeability curve (k_w vs. S_w). Ideally, $S_{wf} = 1$ and $S_{wi} = 0$. S_{wf} can be readily obtained in the nano-network fluidic chips where an imbibition pressure balance of the form in Eq. (4.58) may be necessary for the heterogeneous nano-networks described in Section 3.2.

Next, assuming piston-like imbibition fronts, the 1D diffusion equation and its applicable solutions described in Section 4.3 will apply for nano-network samples and chips where liquid is injected from both ends of a sample; solutions to the radial form of the 1D ADE may need to be derived for some experimental configurations. The use of gas saturated liquid will mitigate diffusion effects and greatly simplify the calculation of the bubble pressure (Eq. (4.9)). However, methods that do not use the trapped and diffusing bubble as an additional force or do not use will not obtain nanoscale diffusion transport values D and k_H, such as was shown in the preceding sections.

4.5 CONCLUSIONS AND RECOMMENDATIONS

This chapter introduced a method that enables quantification of the effects of fully sub-micron nanoconfinement on imbibition, capillary pressure, viscosity, and interfacial mass transfer within a nanochannel geometry. Key parameters and recommendations concerning the presented methodology are as follows:

- The decoupling scheme is most accurate in data from nanofluidic devices, specifically arrays of nanochannels, due to the ability to observe flow and the knowledge of precise geometry.
- Values of effective viscosity increase/decrease can also be interpreted as a decrease/increase in effective diameter; i.e.; one can assume μ to be the bulk value and synonymously solve for permeability, k.
- The method detailed is applicable in the limit of sharp, piston-like fronts.
- If either μ, k, or P_c are a strong function of length imbibed, the linear relationship crucial to this method will no longer apply.
- The Fo and Pe numbers of a specific nanofluidic system should be assessed before corresponding data from the trapped air bubble method is analyzed. In the cases of very low or high Pe numbers the advection or diffusion terms, respectively, can be neglected. When $Fo>>1$ can the transient (unsteady-state) terms of the ADE can be neglected [150], and a system can potentially be considered pseudo steady-state when Fo >10 [151]. All of these scenarios simplify the solution to the ADE problem set up in this chapter; the solution to the most complex case, where no terms were neglected, was provided in this chapter.

- Fully air-saturated liquid can be used to prevent significant bubble diffusion and potentially simplify the problem by eliminating gas partitioning and diffusion from the trapped bubble.

Water films on fully hydroxylated quartz are much thicker than expected…

The only certainty is that a great deal more experimental and theoretical work is necessary before the mystery of this and similar systems is finally unravelled.

Gee, Healy, and White (1990) [158]
Journal of Colloid and Interface Science

CHAPTER 5: Nanofluidic Results and Observations

Experiment - where theory comes to die.

Sidney Nagel, physicist

Imbibition, the displacement of a non-wetting fluid by a wetting one through capillary forces, and relevant imbibition equations are introduced in Section 2.3. The Washburn equation for imbibition [57], derived from continuum hydrodynamic principles, is used as basis of comparison for the nanofluidic results. Figure 5.1 describes an overall workflow for the different types of nanofluidic experiments. The majority of experiments documented in this work were performed in the arrays of 2D nanochannels, detailed in Section 3.1. Experiments were performed at room temperature and pressure conditions.

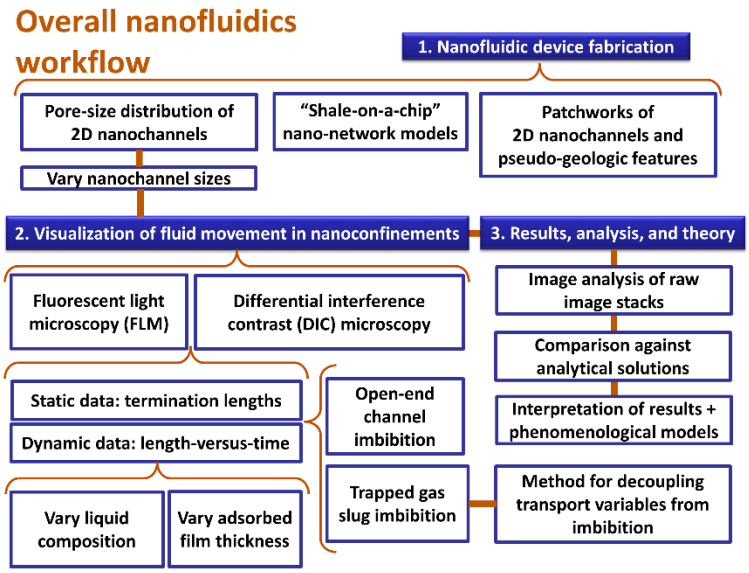

Figure 5.1: Overall nanofluidics workflow undertaken in this dissertation work.

As a refresher, the terminology *open-end imbibition* refers to the scenario where liquid imbibes from one reservoir (i.e., microchannel) into conduit(s) (i.e., nanochannels) and the opposing reservoir remains open to the atmosphere. *Trapped bubble imbibition* refers to the scenario where air slugs are trapped between imbibing fronts to introduce an additional force. Isopropanol (IPA), a perfect wetting liquid (θ = 0° on macroscopic surfaces), is the most frequently used fluid in the experiments. The data presented in this chapter are samples of repeated anomalous observations.

5.1 DISPARITIES BETWEEN IMBIBITION TRENDS IN 2D NANOCHANNELS AND THE WASHBURN EQUATION

The liquids observed in the arrays of 2D nanochannels ubiquitously display 1.) substantial divergence from the imbibition speeds predicted by the Washburn equation and/or 2.) non-Washburn or non-diffusive dynamics in terms of the power-law exponents fit to the imbibing fronts. These results are further explained in the proceeding subsections.

Imbibition speed is proportional to channel diameter. Per the Washburn equation, the theoretical times for a wetting liquid such as IPA to traverse the entire lengths of the largest (500 nm × 60 nm) and smallest (30 nm × 60 nm) nanochannels in the nanofluidic array, are, respectively, 0.28 s and 0.54 s; theoretical channel traverse times for other wetting liquids are the same order magnitude. The plots throughout this chapter display that imbibition times observed in the 2D nanochannel experiments are on the order of seconds, not microseconds. The magnitude of this divergence from the Washburn equation prediction is greater than deviations reported in 1D nanochannel experiments [91] [92] [93] [94].

5.1.1 Non-diffusive imbibition cessation at varied lengths

Upon imbibing at least an order of magnitude slower than predicted, various liquids were observed to come to a stop within some of the nanochannels. This stopping point persisted for the duration of the experiment. Figure 5.3 displays a depiction of such dynamics for heptane, where the liquid front comes to a stop at a distance of ~ 100 μm. Cessation of an imbibing liquid front in a horizontal channel is a non-diffusive trend.

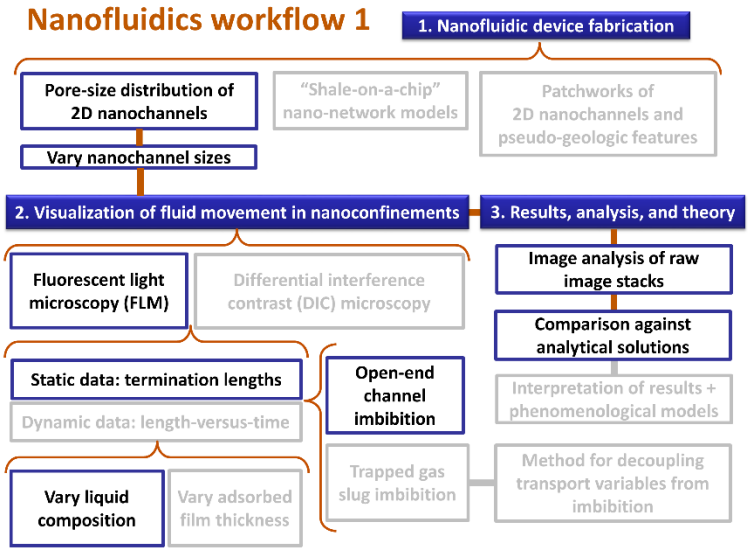

Figure 5.2: Workflow for the static FLM experiments detailed in Section 5.1.1.

All imbibing liquids discussed in this section were doped with ~100 μM of Rhodamine B (Sigma-Aldridge), $C_{28}H_{31}ClN_2O_3$, a neutral fluorescent tracer molecule, and captured with a Zeiss Axiovert 200M fluorescent light microscope (FLM). A restrictive frame rate of approximately one frame per second (fps) for these data sets rendered the capture of consistent velocity data in the nanochannels challenging. Thus, dynamic imbibition was not studied with the FLM experiments and the results are

presented in terms of anomalous front termination lengths, l_t (static data). Some dynamic data was successfully achieved with FLM, such as that displayed in Figure 5.3.

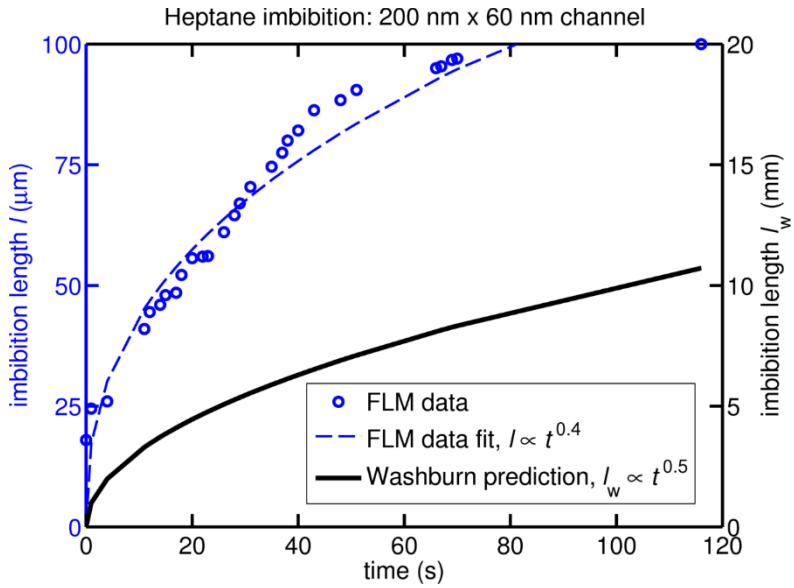

Figure 5.3: Example of heptane imbibition length with time in a 200 nm × 60 nm nanochannel captured with FLM. The the data severely diverges from the Washburn equation in terms of speed and reaches a termination length around 100 μm.

Termination lengths generally increased with nanochannel width, and in most of the array's smaller channels l_t was far shorter than 250 μm. Figure 5.4 shows visual examples of such termination lengths, while Figure 5.5 compares the termination lengths of the different fluids studied along the range of nanochannel hydraulic diameters, D_H, where $D_H = 4 \times A/P$ (A is cross-sectional area and P is perimeter). The wetting liquids tested were deionized (DI) water, brine (0.05 M NaCl mixed in a 50%:50% ratio with methanol), IPA, acetone, methanol, heptane, and decane. The resident non-wetting fluid was air. Results for the 0.05 M NaCl/methanol mixture are displayed and reveal that the mixture imbibes less than DI water; however, this liquid is not further analyzed due to its

compositional complexity. Figure 5.7 shows the sensitivity of imbibition termination lengths to channel end conditions (open or closed) and fouling for several liquids.

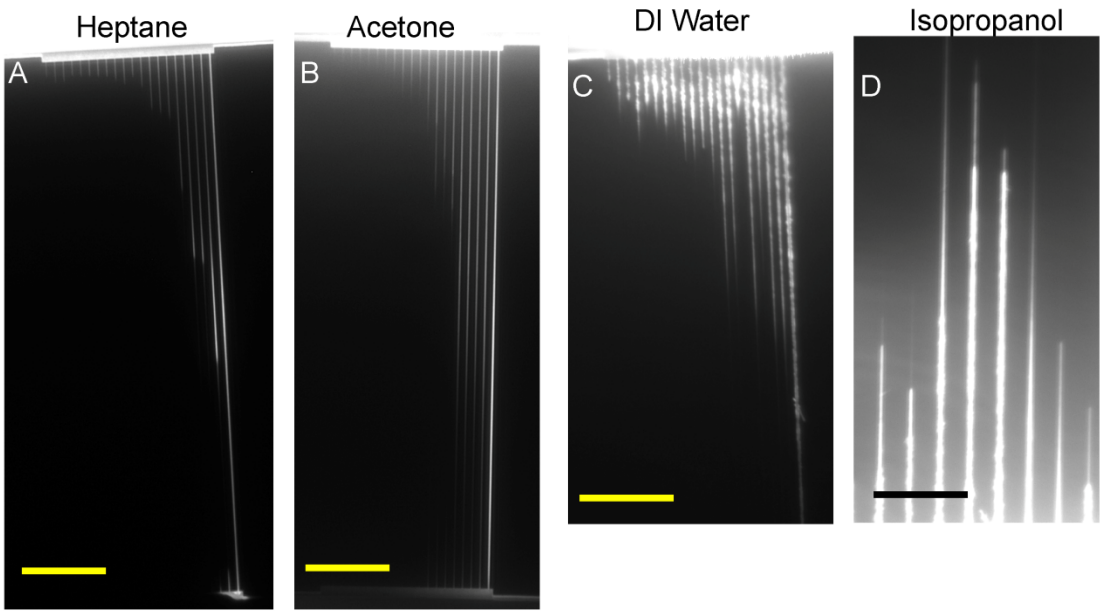

Figure 5.4: All fluids were doped with Rhodamine B and images are captured with a Zeiss Axiovert 200M FLM. The fluorescent signal makes the nanochannels appear larger than their actual size. (A) - (C) Imbibition termination lengths of labeled experimental fluids captured with a 20X objective. The scale bar is 40 μm for these images. Nanochannel sizes increase from left to right from 30 × 60 nm to 500 × 60 nm in cross-section. (D) Imbibition termination lengths of isopropanol within nanochannels in the middle of the array captured with a 100X objective; scale bar is 12 μm. This close-up image exhibits a change in fluorescent intensity at the tips of the imbibition fronts, an observation often seen in the experiments that may correspond to a prewetting film. Alternatively, channel buckling and opposite wall contact may be the cause of such areas of decreased fluorescent intensity. The imbibition front in the largest nanochannels frequently made it to the opposing nano-slit reservoir, and, as a result, some imbibition did occur from the opposing reservoir back into the smaller nanochannels. However, this front was typically small (due to limited liquid volume in the nano-slit reservoir) and primarily occurred after the imbibition fronts in the smaller nanochannels had reached their termination lengths.

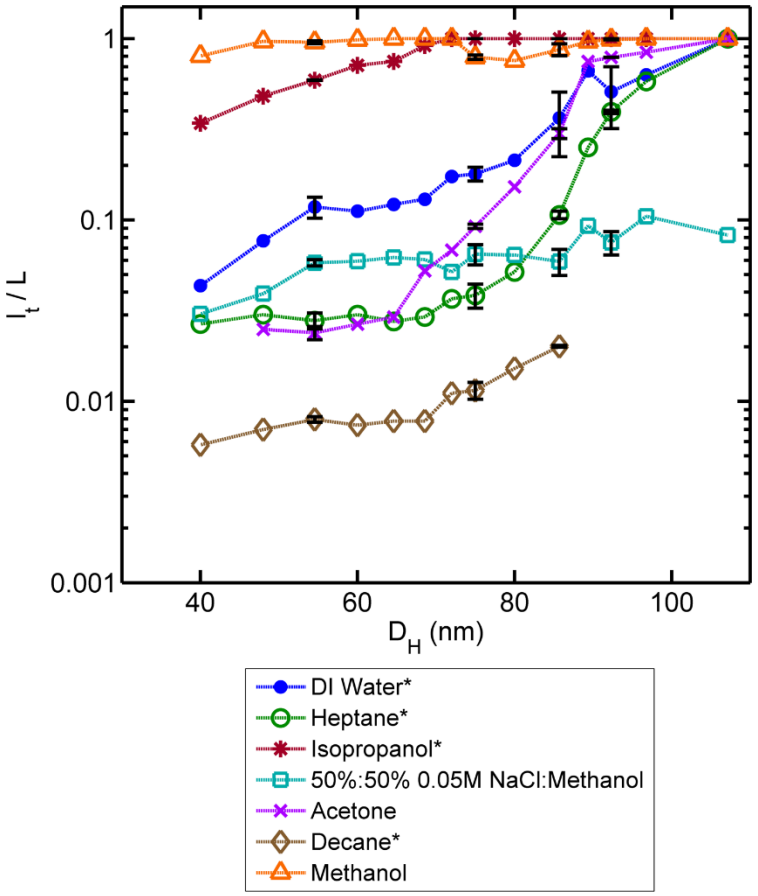

Figure 5.5: Ratio of imbibition termination length (l_t), as detected by Rhodamine B fluorescence, over total length of the nanochannel array (L = 250 μm) versus hydraulic diameter of the nanochannels for the tested fluids. Liquid droplets were administered to a chip inlet and freely imbibed into the nanofluidic chips from that inlet while all other inlets/outlets were left open to the atmosphere. Termination length varied considerably from smallest to largest channel and between different imbibing liquids. Aqueous salt solutions did not readily imbibe into the nanofluidic chip; methanol was added to increase wetting. No data were obtained for decane in the larger nanochannels. Asterisks designate experiments performed on new chips. Error bars are derived from results in duplicates and triplicates of particular channel sizes and display some dispersion for the relatively larger channels.

Figure 5.4.C and D appear to illustrate channel roughness/unevenness as opposed to "smoother" fluorescing profiles in Figure 5.4.A and B. Brighter areas represent either (1) areas of greater fluorophore concentration, or (2) areas of less exposed (photobleached) fluorophores. Hence, the lighter front extents in Figure 5.4.D most likely represent prewetting films or collapsed regions with less liquid volume (and fluorophores) present. The channels are not atomically smooth, but the unevenness perceived with fluorescent imaging in some of the images (i.e. the bottom of Figure 5.4.D) is a non-physical microscopy artifact. Fluorescent microscope settings and fluorophore solubility ranged among experiments and fluids and, thus, should not necessarily be used as a basis of comparison.

The relative transport success of the liquids as a whole into the nanochannel arrays is summarized as a saturation fraction, S_w, for comparison against bulk liquid properties. S_w is the ratio of the total volume of wetting fluid imbibed into the array of 20 nanochannels to the total volume of the nanochannel array; e.g.

$$S_w = \frac{\sum_{i=1}^{20} w_i \left(l_t\right)_i}{L \sum_{i=1}^{20} w_i}, \tag{5.1}$$

where w is the nanochannel cross-sectional width; h, nanochannel depth, cancels out because it is the same for all of the channels. Table 5.1 displays values of S_w and relevant bulk liquid properties for comparison. S_w is not correlated to published bulk values of liquid viscosities, macroscopic silica-liquid contact angles, molecule weight/size, etc. Furthermore, S_w and the imbibition extents are not clearly correlated to combinations of these bulk physical values, such as the dimensionless capillary number (Ca), $\mu V/\gamma$ (where V is the velocity of the fluid). There is also no correlation between the estimated

pressures in the liquids due to viscous losses at the termination lengths and saturated vapor pressures of the liquids at room temperature (at these pressures liquids evaporate). With the exception of DI water, the compared values of surface tension do not significantly vary among the other fluids; a trend between wetting fluid saturation success and decreased surface tension is not present (see S_w and γ values in Table 5.1).

Properties of the experimental fluids and average saturation data

Fluid	S_w†	γ (mN/m)	θ_0* (°)	μ (10^{-3} Pa s)	ρ (kg/m^3)	Mw (g/mol)	P_v (kPa)	μ_D (D)	n	ν_e (10^{15} Hz)	ε	A_{123}** (10^{-20} J)	A_{232}** (10^{-20} J)
Isopropanol	**0.95**	23.8	0	1.96	786.00	60.10	6.02	1.56	1.38	3.1	18.2	-1.04	4.20
Methanol	**0.94**	22.6	0	0.590	791.80	32.04	16.9	1.69	1.33	3	33.1	-1.22	3.68
Acetone	**0.51**	23.7	6	0.308	791.00	58.08	30.6	2.91	1.36	2.9	21	-1.08	4.08
DI Water	**0.48**	72.8	28	1.00	999.97	18.02	3.15	1.85	1.33	3	80	-0.98	4.35
Heptane	**0.15**	20.1	0	0.386	684.00	100.21	6.13	0	1.39	3	1.89	-0.91	4.53
Decane	**0.01**	23.8	0	0.920	730.00	142.29	0.17	0	1.41	3	2	-0.70	5.04

Symbol Key: S_w = saturation of the wetting fluid; γ = surface tension; θ_0 = macroscopic contact angle; μ = viscosity; ρ = density; Mw = molecular weight; P_v = vapor pressure; μ_D = dipole moment (unit = debye); n = index of refraction; ν_e = absorption frequency; ε = dielectric constant; A_{123} = Hamaker constant for the fluid between silica and air; A_{232} = Hamaker constant for air between two layers of the fluid

† [Total volume of wetting fluid imbibed into the nanochannel array] / [total volume of the nanochannel array]

* Macroscopic contact angle on polished quartz (silica) from Ethington (1990) [159]. The contact angles of heptane and decane on quartz were not found in the literature, but were assumed to be zero like the other spreading/wetting fluids. All of the fluids are wetting.

** The Hamaker constant is calculated using the macroscopic Lifshitz calculation. The literature contains experimentally derived values, which can slightly differ from these predictions.

Table 5.1: Properties of the experimental fluids and average saturation data.

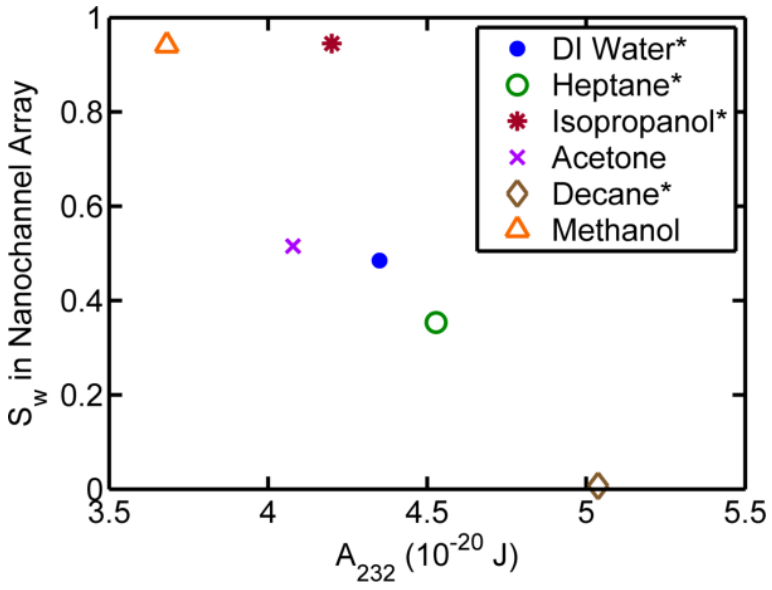

Figure 5.6: The data suggest a trend between imbibition success, summarized by S_w, and calculated Hamaker constants for a system of two films of liquid (fluid 2) interacting across a film of air (fluid 3), A_{232}. The value of A_{232} is always positive, which indicates an attractive force between the like liquid films and a propensity for the enclosed air film to thin. Such attraction may lead to deformation of a nanoconfined meniscus. Note that the data also trend with the absolute value of A_{123}, indicating that precursor film thickness may play a prominent role in nanoscale imbibition. The value for isopropanol is an outlier from both perceived trends (see explanation in the Section 5.1.1). Experimental and calculated values of the Hamaker constant can slightly differ.

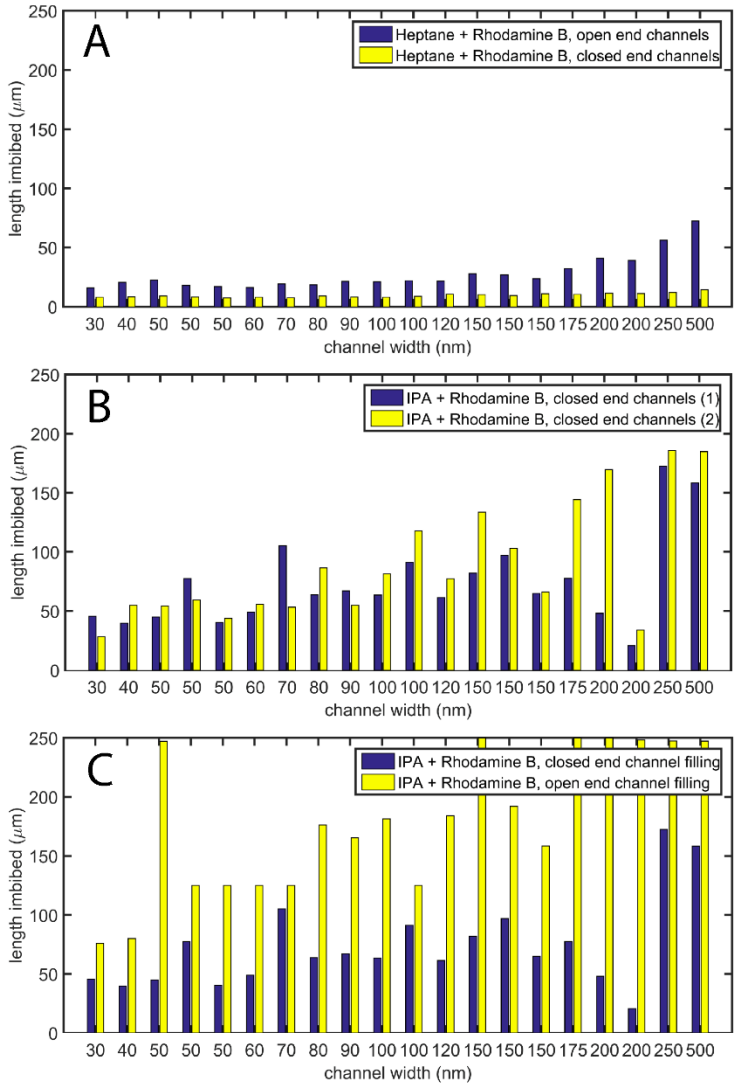

Figure 5.7: Bar plots of imbibition termination lengths in used chips subject to fouling, mainly by the repeated use of Rhodamine B. (A) and (C) Plots show that heptane and IPA are sensitive to closed end conditions (the microchannel/nanochannels juncture opposite of the imbibing front is closed off). (B) The haphazard trend in channel termination lengths and general inconsistency between two IPA imbibition runs in the same chip indicate a "struggling" meniscus that is subject to arrest by pinning mechanisms.

Examination of the properties of the different imbibing liquids at an intermolecular forces level suggests a robust correlation between nanochannel imbibition success and the Hamaker constants of the system, A_{232} and A_{123}. These constants are representative of the strength of van der Waals interaction forces for, respectively, two films of the same liquid acting across a film of air and a solid and air acting across a film of said liquid. Hamaker constants, generally referred to as A_H, allow molecular interactions to be considered from a continuum perspective and are dependent on fluid and material properties; more details on A_H are included in Section 2.3.1. Figure 5.6 displays a cross-plot of the values of A_{232} and S_w for the liquid-air-liquid systems in the nanochannels. The outlier to the trend is isopropanol. The value for isopropanol is most likely an outlier based on its (a) polarity and (b) precursor film thickness. The pore space available for a fluid meniscus and mass flux becomes smaller in the presence of, respectively, relatively thick precursor films and adsorbed layers. Isopropanol has lesser extents of these films and layers compared to methanol, which has a lower A_{232} value, but a very similar S_w results. In more detail,

(a) The surface charge of oxides such as alumina and silica increases in polar liquids [72]. To achieve electroneutrality, a larger amount of molecules may accumulate in boundary layers for surfaces of greater negative interfacial potential or charge density. Isopropanol, followed by methanol, is the least polar of the tested polar fluids and theoretically forms a thinner layer of absorbed molecules than methanol.

(b) The greater the negative value of A_{123}, which corresponds to the van der Waals forces between a solid and gas across a liquid film, the greater the propensity of a precursor film or meniscus edge to thicken. The value of A_{123} for isopropanol is

notably smaller than that of methanol and thus, isopropanol may have smaller precursor films.

Further experimental observations of interest using fluorescent microscopy in the nanochannels are included in Appendix C.

5.1.2 Anomalous dynamic length-versus-time power law trends

Open-end channel imbibition experiments with pure (no tracer) IPA in the 2D silica nanochannels were observed with DIC microscopy. These experiments invariably confirmed that that the imbibition length-versus-time rates were severely slower than the imbibition rates predicted by the Washburn equation. Due to a faster data acquisition frame rate, α-values ("wicking coefficient") and n-values (power-law exponent) were extracted from the DIC microscopy experiments. An example of these results at a frame rate of 39 frames per second is displayed in Figure 5.10.

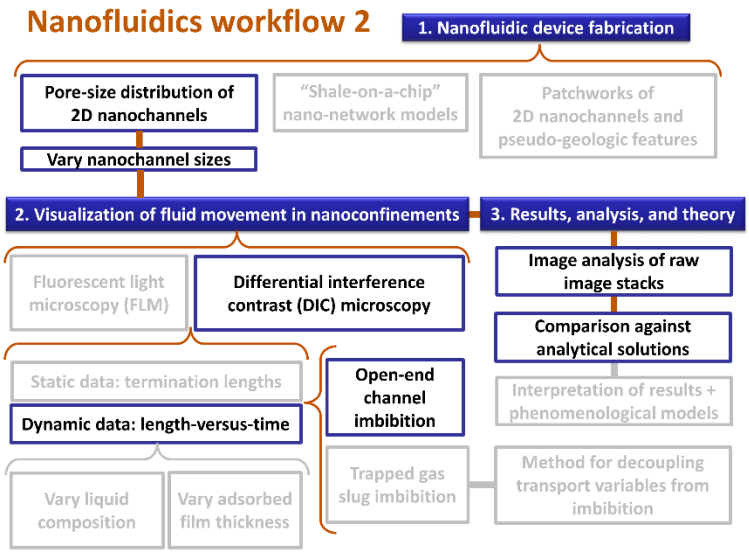

Figure 5.8: Workflow for the dynamic DIC experiments detailed in Section 5.1.2.

For open-end channel imbibition non-diffusive ($n \neq 0.5$) imbibition was observed in two scenarios: 1.) in the larger, more slit-like channels of the array of 2D nanochannels (typically the 200 nm × 60 nm channel and larger) and 2.) in nanochannels with prevalent evaporation-induced adsorbed films, as discussed subsequently in Section 5.3.1. Imbibition length approximately trended with the square root of time in the array's smaller channels (when dry). In the array's larger nanochannels imbibition approached a linear trend ($n = 1$). Figures 5.9 and 5.10 show examples of the near-linear imbibition in the array's largest channels. Figure 5.10 is plotted on a log-log scale to show the difference in imbibition n-values (the slopes of the lines on the log-log plot) between different channel sizes.

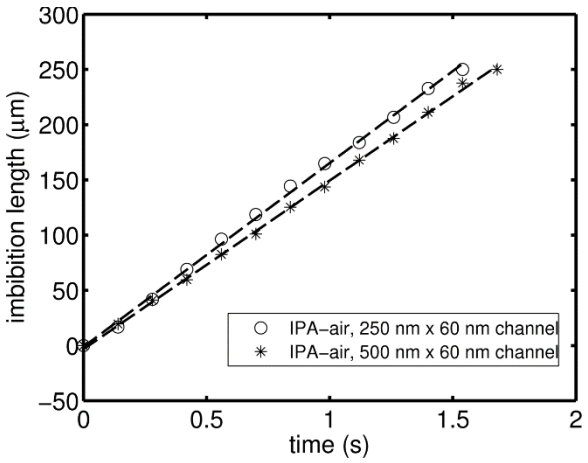

Figure 5.9: An example of IPA imbibition data exhibiting linear trends along the entire length, 250 μm, of the more slit-like nanochannels; such trends are unprecedented and repeatedly observed on these channels.

The trend of α-values with decreasing channel width is lower and steeper than predicted by the Washburn equation. These values are displayed with square markers in Figure 5.13 against the Washburn-prescribed α-values (black line).

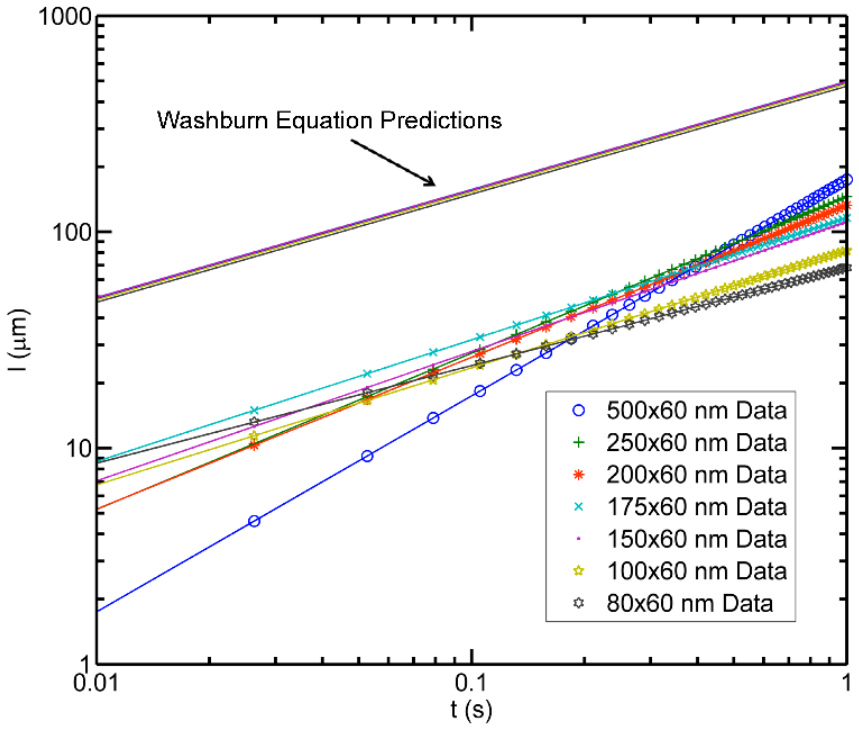

Figure 5.10: Imbibition trends can be viewed conveniently on a log-log plot where $\log(l) = n\log(t) + \log(\alpha)$. Open-end channel imbibition of IPA (captured at 39 frames per second) reveals distinct differences in y-axis intercept values (which correspond to α-values) from the Washburn equation (plotted solid lines) by at least a factor of five. In the larger nanochannels there is a distinct difference in slope (n-value) from the expected 0.5 value. Data are displayed from select channels (the smallest channels of the array were difficult to visualize at faster frame rates) and the same experiment.

An n-value greater than 0.5 indicates that some physical resistive characteristic of the system is decreasing with time. The unique aspects of the larger nanochannels are greater surface areas, mass fluxes, and velocities. Hydrodynamic resistance of the air in front of the imbibing fluid does decrease with time, but this resistance is not a logical explanation as the effect would be greatest in the smallest nanochannels. Fluid evaporation at the meniscus was discounted prior since it is assumed to remain fairly constant during the experiment. It is possible that the channel geometry is not consistent

along the entire channel. However, the imbibition solution for a diverging channel would result in a $t^{0.25}$ relationship [160]. The $n = 1$ result was seen in experiments where fluid originated from either termination point of the nanochannel array, whereby the possibility of converging or diverging geometries is invalidated.

Qualitative arguments for the near-linear imbibition behavior include that the volumetric flux in the larger nanochannels is significant enough to either: (a) deteriorate boundary layers with time; or (b) significantly detach a hypothesized annular quasi-crystalline boundary region from the nanochannel walls. In the first scenario, the velocity will remain fairly constant due to a decrease in resistance with time. In the second scenario, viscous losses are significantly decreased such that the velocity also remains roughly constant. This scenario has potentially profound implications since high viscous losses or hydraulic resistivity is a major barrier in nanofluidics. Continuous filling as a result of liquid recession from channel surfaces has been simulated in hydrophobic carbon nanotubes of much smaller radii [161], but to my knowledge has not been observed in lyophilic nanochannels. It is worth noting that Haneveld et al. [91], who performed imbibition experiments in 1D nanochannels of identical material composition to the ones used in this work, show a slight deviation above $n = 0.5$ with DI water in their data plots of open-end channel imbibition.

5.2 DISPARITIES BETWEEN EFFECTIVE TRANSPORT VARAIBLES IN 2D NANOCHANNELS AND BULK SOLUTION VALUES

Length-versus-time open-end channel experiments alone do not reveal the source of slower than predicted and/or non-diffusive imbibition. The trapped bubbled imbibition experiments and analysis scheme described in Chapter 4 are used to obtain estimates of

the effective values of imbibition relevant transport variables P_c and μ; k_H is also obtained. These values are compared against their bulk predictions or values; respectively, the Young-Laplace equation and the literature value for a liquid's viscosity. As a refresher, Case I, II, and III data categories are described in Section 4.2.

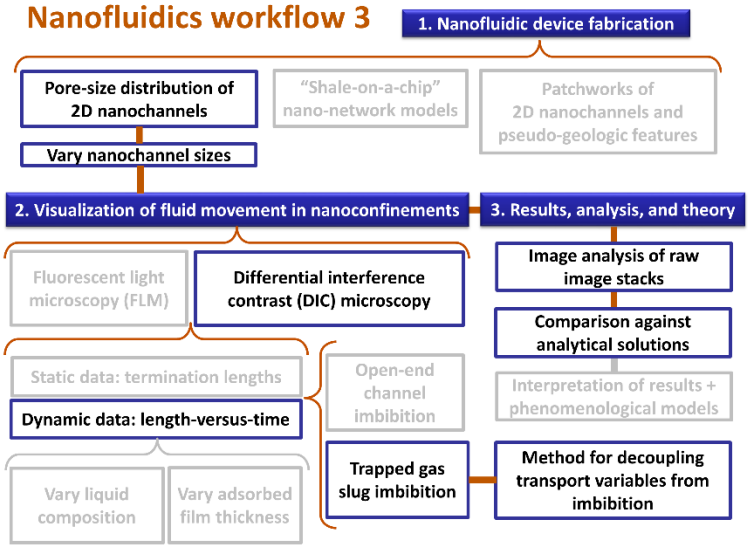

Figure 5.11: Workflow for the dynamic DIC experiments detailed in Section 5.2.

5.2.1 Decoupled effective nanoscale P_c, μ, and k_H values for a perfect wetting fluid

IPA, a perfect wetting fluid, is used for the experiments detailed in this section (Table 5.2 presents a summary of published values for relevant bulk properties of IPA). After experimentation with aqueous solutions, hydrocarbons, ketones, and alcohols in the nanofluidic chips, IPA was found to be ideal for experimentation due to its consistent wetting abilities (i.e. a macroscopic contact angle of approximately zero, which reduces sensitivity to situations of slight contamination and dehdroxylization). Additionally, by

using IPA the formation of electrical double layers can be discounted and any EDL-related effects can be decoupled because, unlike aqueous solutions, IPA is devoid of ions. Data sets from three independent trapped bubble (or gas slug) experiments with IPA and air were analyzed and are labeled accordingly in Figures 5.14-5.16. Figure 5.12 displays examples of raw trapped bubble imbibition profiles from these data sets.

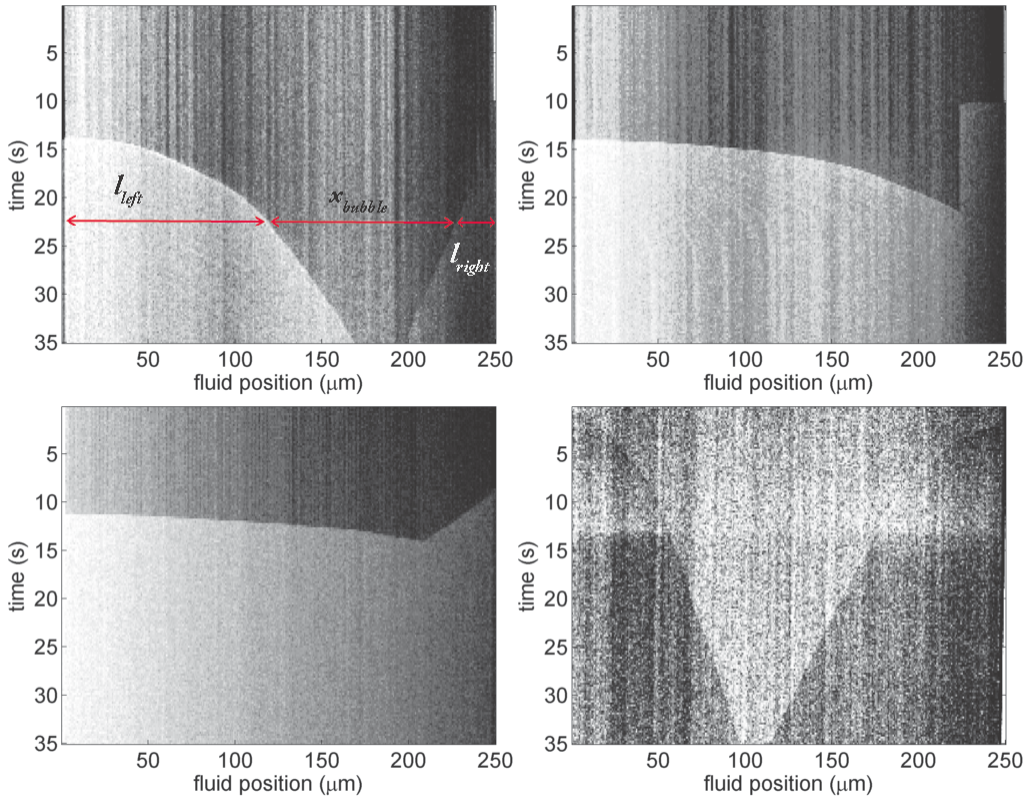

Figure 5.12: IPA-air fluid imbibition profiles obtained by extracting a 2D image of a row of pixels along an image stack in the direction of time (z-direction of the stack); method is described in Section 3.4.2. The selected fluid profiles feature a trapped air bubble between two liquid fronts within (clockwise from top left): a 60 nm × 60 nm channel (from Data Set 1); a 150 nm × 60 nm channel (from Data Set 1; note the trapped liquid plug on the right); a 30 nm × 60 nm channel (from Data Set 2); and a 200 nm × 60 nm channel (from Data Set 3). Note the differences in data quality and imbibition speed with increasing nanochannel width.

Bulk physical values for isopropanol at T=25˚C

Variable	Name	Bulk Value	Source	Notes
μ	Viscosity	1.96 mP.s	*Chemical Properties Handbook* [162]	---
γ_{gl}	Surface tension	21.4 mN/m	*DOW MSDS*	---
θ	Contact angle	0˚	*Janssen et al.* [163]	IPA on SiO_2*
D	Diffusivity	2200 $\mu m^2/s$	*Ferrell and Himmelblau* [164]	Nitrogen and oxygen in water**
k_H	Henry's Law partitioning coefficient	1.56×10^{23} μm^3.Pa/mol	*Wilhelm et al.* [165]	Nitrogen in water**

* The authors reported contact angles of <10°. 0° is the best case scenario.
** Published values for air in IPA were not available, so nitrogen in water was used as an estimate of the appropriate value range.

Table 5.2: Bulk physical values for isopropanol at T = 25˚C

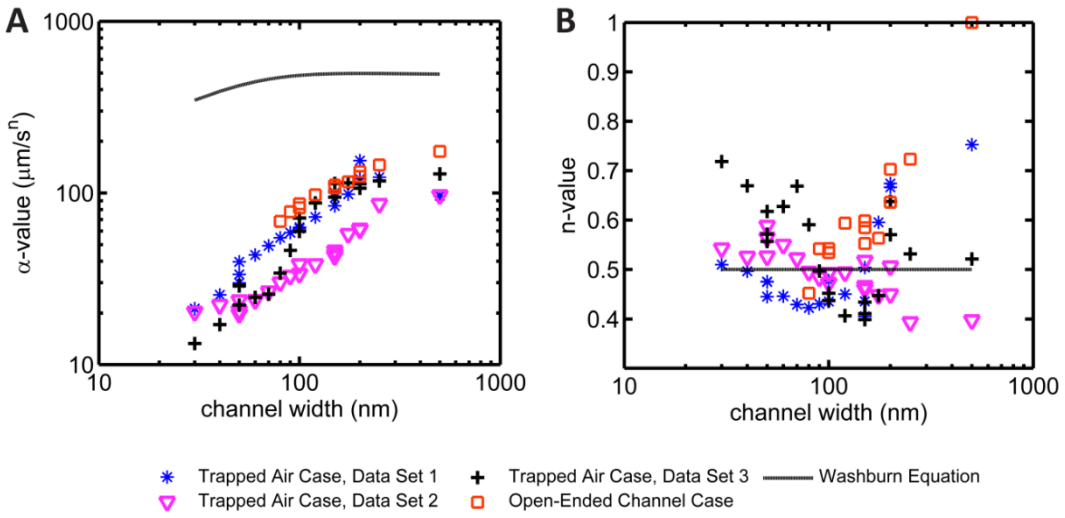

Figure 5.13: (A) α-values from $l=\alpha t^n$ fitted data are significantly smaller than predicted by the Washburn equation and trend steeper with decreasing channel width. For the open-end channel case, captured with the Nikon Eclipse Ti, it is difficult to discern imbibition profiles in nanochannels smaller than 80 nm in width. (B) n-values for the trapped air bubble experiments vary, as expected. However, open-end channel imbibition n-values (square markers) in nanochannels with larger surface areas unexpectedly vary greatly from n = 0.5, the Washburn equation value.

Figure 5.13 compares the α-values and n-values from the $l=\alpha t^n$ power law for each channel size and trapped bubble data set. Data for open-end channel imbibition is plotted as well (these square markers correspond to the dynamic trends in Figure 5.10). The trend of α-values with decreasing channel width adheres to a similar slope to that of the open-end channel case; both trends are lower and steeper than predicted by the Washburn equation.

The trapped bubble imbibition experiments enable independent calculation of P_c, μ, and k_H from Case II and III type data. Figures 5.14 and 5.15 depict, respectively, the ratio of the nanochannel P_c values over the bulk value (Young-Laplace equation) and the ratio of the nanochannel μ–values over the bulk value for IPA versus nanochannel widths. Variability of the results is addressed through the presentation of three independent data sets. Additionally, error bars are displayed for P_c and μ values. These error bars represent three times the standard error of the normally distributed variable estimators of the least-squares analysis, or the 99.7% confidence range of the least-squares value fit. **Nanochannels larger than 200 nm in width were not used in the decoupling procedure because the *n*-values in these channels are unexpectedly greater than 0.5 in the case of open-end channel imbibition.**

Figure 5.14 shows that P_c trends from 40% to near 100% less than the values predicted by the Young-Laplace equation with decreasing channel width. The divergence from Young-Laplace increases with decreasing channel dimensions. Figure 5.15 reveals that μ ranges from around 2 to 70 times higher than the bulk value of IPA in rectangular nanochannels with heights of 60 nm. Some variance among the data sets (indicating high sensitivity to surface and environmental conditions such as wall texture and

humidity/adsorption) and a few outliers are observed in the results, but overall deviation of values from the bulk is apparent.

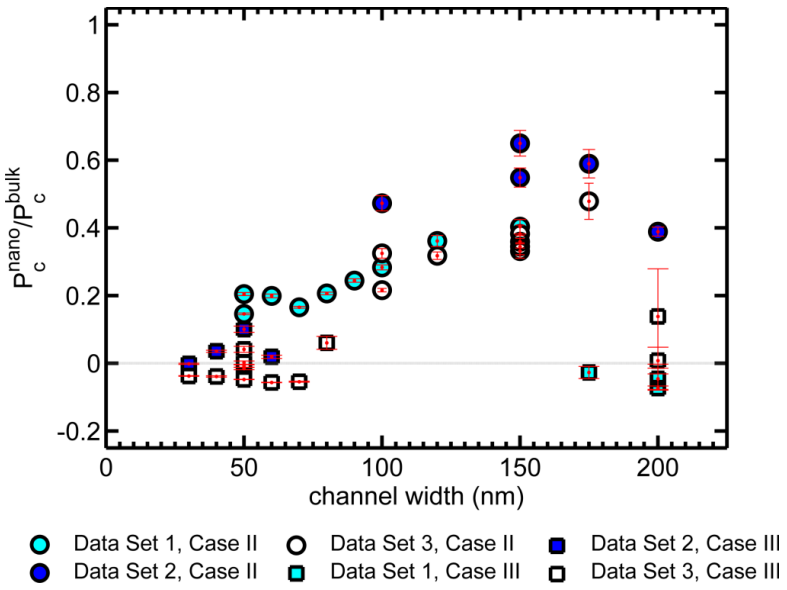

Figure 5.14: Ratios of nanochannel capillary pressure values over bulk values for IPA versus nanochannel width. The nanochannel capillary pressure values correspond to effective contact angles of 60° and greater, far larger than the macroscopic contact angle for IPA on silica. Negative values of capillary pressure, seen exclusively in the Case III data, potentially correspond to dewetting, which occurs when effective contact angles exceed 90°.

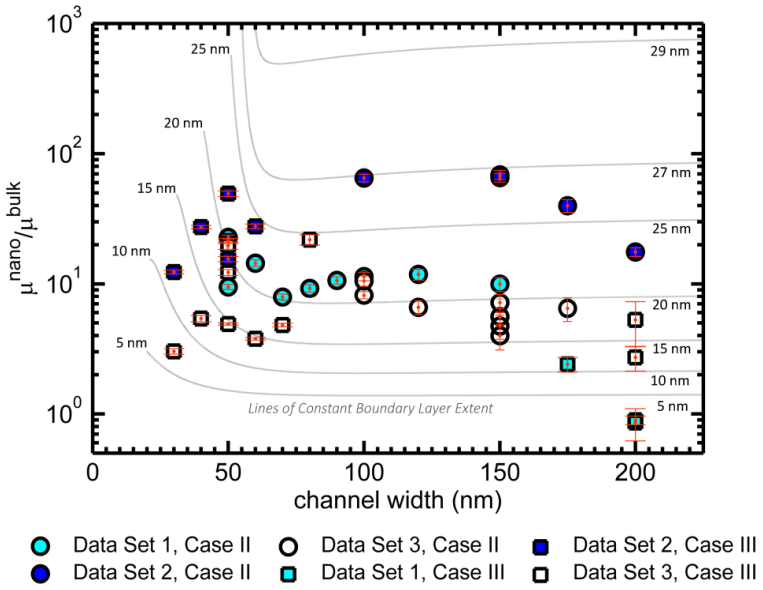

Figure 5.15: Ratios of the nanochannel viscosity values over the bulk value for IPA versus nanochannel width reveal that effective viscosity significantly increases in the nanochannels. Lines corresponding to effective viscosity at different immobile boundary layer lengths are displayed, where the number labels refer to the extent of a boundary zone of structured molecules from each surface of the nanochannel. Overall y-axis positions of the same colored markers shifts slightly between data sets, indicating these boundary layers are very sensitive to experimental conditions.

Effective viscosity values many times larger than the bulk value point to an effective reduction in channel area or the formation of highly structured/viscous boundary layers, since channel permeability is proportional to channel radius squared. Layers of structured molecules can be conceptualized as an annular zone of high viscosity through which the bulk fluid flows. The definition of geometric permeability (Eq. (2.12)) is used to find the equivalent channel dimensions corresponding to the effective nanochannel viscosity values. Assuming a macroscopic viscosity in the bulk region and immobile boundary layers, an estimated boundary layer length is calculated

for each channel. Boundary layer extent should remain roughly constant from channel to channel when it remains only a function of surface interactions. Indeed, the sizes of the estimated boundary layers are around 10-25 nm (see Figure 5.15). However, the extent of the estimated boundary layers is unexpected; in disjoining pressure theory the effect of long range intermolecular surface forces is calculated to become negligible within only a few nanometers or molecular layers from a surface [166]. Benchmarking of the results with the literature revealed that experimental investigations on boundary layers of pure substances fall into two categories: thin boundary layers of several molecular layers and thick boundary layers with a liquid-crystal structure [65] [82] [83] [84] [85] [86] [87]. Further literature review on thin and thick boundary layers and quasi-crystalline structures is introduced in Section 2.4.

Evidence of boundary layer effects is also displayed in interfacial mass transport within the nanochannels. Following Henry's Law (Eq. (4.16)), a higher k_H value corresponds to less gas partitioning. Best-fit values of k_H trend higher with decreasing channel width and, as such, indicate a reduction in area available for gas partitioning that is proportionally greater in the smaller nanochannels. Figure 5.16 displays k_H values versus relative reduction in channel area (i.e. a ratio of "effective area" over geometric area) due to the presence of the estimated immobile boundary layers. For simplicity, a flat interface is assumed in the calculations; k_H values show that smaller relative reductions in channel area correspond to greater gas partitioning. Actual channel dimensions, h and w, were used in the decoupling scheme, whereby the varying k_H values are indicative of the need to use an effective area when computing interfacial flux. This observation indicates that the hypothesized quasi-crystalline boundary layers do not allow significant

partitioning of impinging gas molecules; i.e. have different partitioning and diffusive properties than the bulk value.

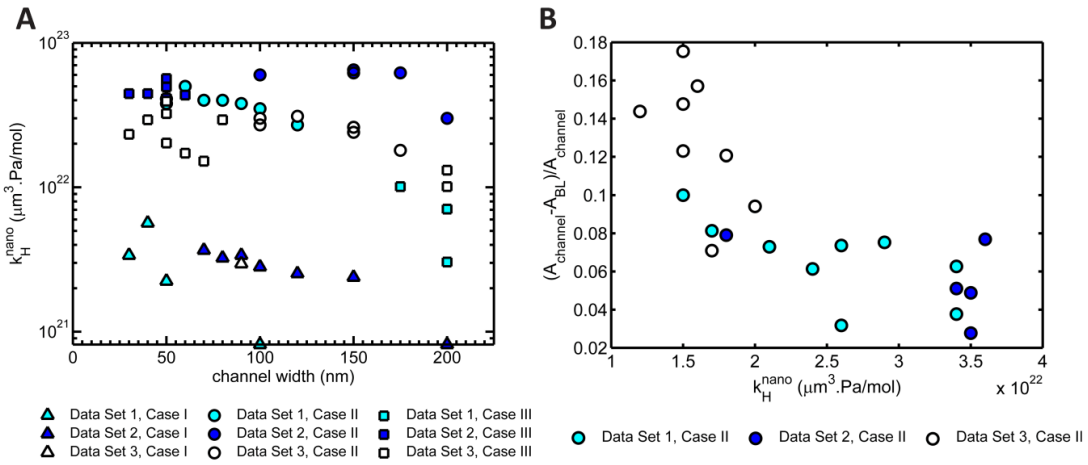

Figure 5.16: (A) k_H values versus nanochannel width display the variance in the partitioning coefficient, which is typically a constant physical value for a particular liquid-gas interface. An increase in k_H, or lower relative interfacial gas transfer, occurs with decreasing channel width. Error ranges on k_H markers are the step size taken in the iteration on the value of k_H , approximately 9.9×10^{20} μm^{3}Pa/mol. (B) Case II data k_H values versus the relative reduction in channel area due to the presence of the estimated immobile boundary layer lengths indicate that boundary layers obstruct partitioning of gas molecules.

The liquid pressures at the IPA menisci in the nanochannels are mathematically negative because P_c is greater than one atmosphere, even at its decoupled value, and both sides of the chip are open to the atmosphere. Negatively pressured liquids are considered thermodynamically metastable and in tension [167]; metastable fluids reach stability by splitting into two or more phases. At very high negative pressures stable and unstable ice-like structures and hydrates are theorized to form in water at a broad range of temperature conditions, including room temperature for some of the structures [168]. In addition to

surface-induced boundary layers, liquid metastability may help further explain the formation and stability of thick quasi-crystalline boundary layers. However, negatively pressured liquids are not a circumstance of all nanoconfinements.

The results imply that the Young-Laplace equation may need modification in nanoconfinements. The conventional Young-Laplace equation curvature does not take into account neither boundary layers nor the transition zone region between the disjoining pressure dominated surface and the bulk curvature. Figure 5.14 indicates that the influence of these regions on capillary pressure increases as the size of the nanoconfinement decreases. Mathematical descriptions of these regions in relation to the bulk include a lubrication approximation solution by de Gennes et al. that describes the interface profile in the transition region for general dynamic wetting [169] and a derivation of the effective contact angle due to the impact of long range intermolecular forces by Derjaguin [166].

For the μ-values decoupled from the IPA data, the most plausible argument for boundary layers on the order of 10 nm or more is a competition between a non-trivial nucleation of structured or quasi-crystalline layers of polar IPA molecules at the negatively charged silica surfaces and the destruction of the structured layers by viscous shearing. Boundary layer growth can also be tapered by thermal motion and surface roughness since the formation of multiple planes of growth can create destructive interference. Additionally, experiments have shown that impurities in solutions limit boundary zone growth [82].

5.2.2 Notes on uncertainty of effective nanoscale P_c, μ, and k_H values

There is always uncertainty associated with raw measurements. In the nanofluidic experiments the only raw data are optical measurements (which are a direct form of data)

and the uncertainties in determination of the meniscus position in the images in terms of pixels (image analysis) are very small (less than $\pm$ 2% error). The results displayed in Figures 5.14-5.16 of this section are the product of analyzing these measurements of imbibition length-versus-time by means of several formulas that result in a least-squares approach. Due to the least-squares analysis approach and the fact that the analysis is contingent upon only one raw measurement type (image data), a propagation of uncertainty or errors method is not adequate for determination of uncertainty bars on the values of P_c, μ, and k_H. Rather, the uncertainty of these values is addressed by finding the standard error of the normally distributed variable estimators of the least-squares analysis. These standard error values multiplied by three, akin to three standard deviations or a 99.7% confidence range, become the error bars for P_c and μ in Figures 5.14 and 5.15, respectively. The error ranges on k_H markers in Figure 5.16 are the step size taken in the iteration on the value of k_H, approximately 9.9×10^{20} μm^3.Pa/mol.

The aspects of the Case II and III data analysis (which is used to solve for variables P_c, μ, and k_H) that are subject to variation are:

- Selection of an accurate value of diffusivity, D
- Room temperature conditions, T=25˚C
- Applicability of the 1D ADE itself in a nanoconfinements
- α- and n-values (not specifically the extraction of their values from image analysis, but the sensitivity of these values to environmental conditions such as humidity, which can slightly differ between experiments)
- Proper assessment of the value of N_i, the excess number of moles/molecules at the meniscus due to interfacial mass transport resistance

I systematically explored each of the aforementioned uncertainties. Sensitivity analysis with D revealed that variable results are barely sensitive to this parameter within $D = 2200 \pm 1000$ μm^2/s. Recall that the Case I data analysis renders that 2200 μm^2/s, the bulk value, is a good estimate of the value of D. Likewise, per sensitivity analysis, reasonable variations in T from assumed $T = 25$˚C make negligible differences in the variable results. Recall that the Case I data is used to validate the 1D ADE by means of obtaining good quality matches between the 1D ADE analytical solution and data curves with realistic values of D, k_H, and N_i. When α and n-value sensitivity analysis is performed marker positions in Figures 5.14-5.16 do change slightly, but the order of magnitude and general trends of the results do not change. The variable results barely differ between the case where N_i is incorporated and the case when it is neglected; thus, sensitivity to this variable is extremely minimal.

In terms of experimental *repeatability*, the stymied imbibition results with IPA (and other liquids) have been consistently observed in the nanofluidic chips constructed for this work beyond the reported data cases. However, the *reproducibility* of the experiments by other researchers with their own batches of 2D nanochannel chips is yet to be determined. The varying nanochannel imbibition results in the literature suggest, as discussed in Section 2.5, that nanoscale transport is extremely sensitive to surface conditions, hence experiment reproducibility is more challenging than it would be in larger conduits.

5.3 OBSERVATIONS OF INHIBITED NANOSCALE IMBIBITION IN RESERVOIR-LIKE LIQUID SCENARIOS

Imbibition conditions in subsurface reservoirs include high pressure and temperature and the presence of in situ liquids in the form of adsorbed films and trapped liquid plugs. In addition, formation water is laden with salt. While it was challenging to control pressure and temperature and simultaneously visualize dynamic fluid flow in the nanofluidic chips with the setup implemented in this work, imbibition in the presence of adsorbed films, trapped gas slugs and liquid plugs, and 0.5 M NaCl salt concentration were observed in the 2D nanochannel arrays.

5.3.1 Presence of adsorbed films

Adsorbed films of varied thickness were generated by complete wetting of the 2D nanochannel arrays followed by isothermal drying for recorded periods of time at either room temperature and pressure conditions or in an vacuum oven (Isotemp Model 281A, Fisher Scientific). Despite seemingly constant experimental conditions and seemingly dry channels (as imaged with DIC microscopy), it was observed that polar fluid imbibition (IPA and mixtures of IPA-water) proceeded much faster in chips that were isothermally dried in the vacuum oven (at conditions of T = 190°C and P = -51 kPa) for over 24 hours as opposed to shorter times and to air drying. Chips subject to very short drying times (< 1 hour) often resulted in termination lengths. Note that chips were stored in Gel-Pak holders or petri dishes within a Desi-Vac (Cole-Parmer) desiccator container (with a bed of silica desiccant beads) to mitigate humidity effects.

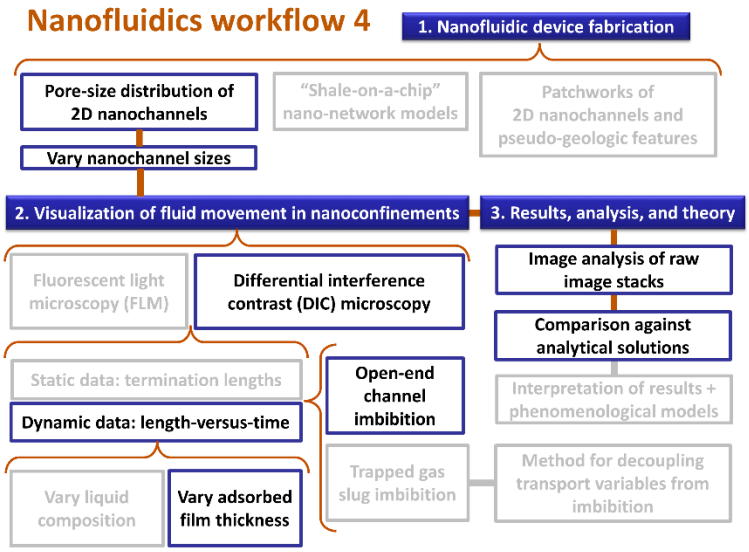

Figure 5.17: Workflow for the dynamic DIC experiments detailed in Section 5.3.1.

As an example, Figure 5.18 displays imbibition of pure IPA in nanochannels subject to 24 hours of air drying for several channel sizes. The chip appeared "dry" (no trapped liquid plugs were evident) with DIC microscopy; the lack of trapped plugs is displayed in the inset raw imbibition profile. This data set was acquired in the same chip as the data from Figure 5.10 after the 24 hours of air drying. As displayed in Figure 5.18, imbibition fronts started out moving swifter than a diffusive trend at early times, but then dramatically slowed down and, in some cases, ceased/became arrested. In these later times, the meniscus appeared to "struggle" in a stick-slip fashion. For t^n power laws, such a trend corresponds to $n < 0.5$; n was found to typically be ~ 0.3 for these scenarios. These $n < 0.5$ trends indicate a physical parameter with unexpected non-constant values decreases the driving force or increases net resistance to imbibition with time. As displayed in Figure 5.18, this dramatic slowdown of the front is even captured in the 500

nm × 60 nm channel, which is markedly different than the linear front captured in this channel size in Figure 5.10; the latter is observed for drier channels.

Because the same chip (thus, the same surface texture) was used, and the same liquid, IPA, was administered between both discussed data sets, it is probable that the $n < 0.5$ trends and late-times stick-slip motions are a product of optically undetectable adsorbed IPA films on the channel walls. These IPA films are potentially non-uniform and discontinuous from the endpoints of the channels to their centers.

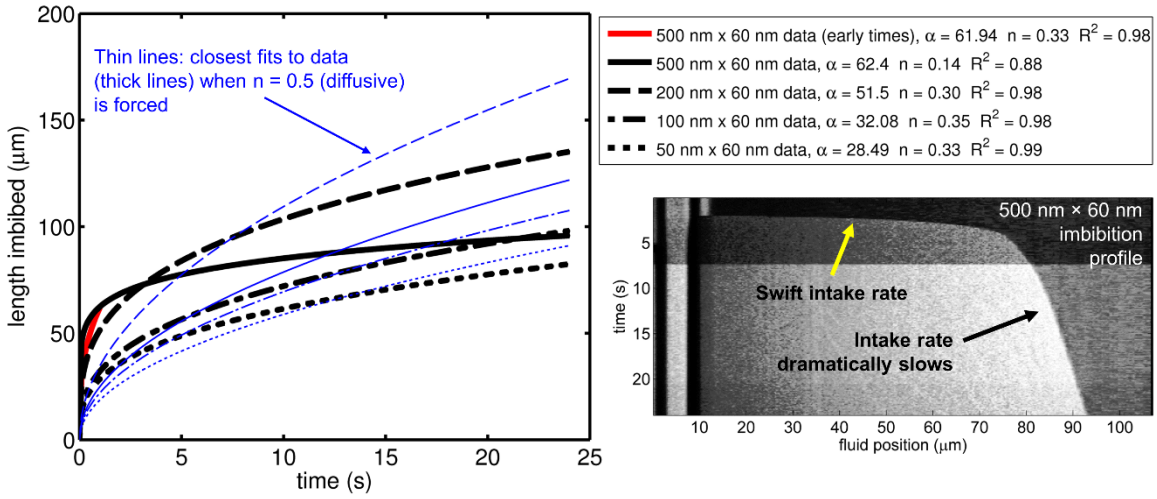

Figure 5.18: IPA imbibition data (captured at 21 frames per second) that exhibits a swift intake rate followed by a dramatic slowdown of flow; i.e. $n < 0.5$. Data α and n fits for several channels are given in the figure key. Thin blue lines represent forced fits of $n = 0.5$ for comparison purposes. The IPA data in this figure does not match the trends of the IPA data in Figure 5.10 (performed in the same chip at a later date), which are much faster and exhibit different power law values. Partially evaporated, discontinuous thin films are ascribed as the most probable explanation for the $n < 0.5$ trends.

5.3.2 Capillary condensation and capillary trapping

In many data sets the presence of trapped liquid plugs were evident with DIC microscopy. Such capillary bound plugs and resultant trapped gas bubbles are commonplace in porous media, and their stability during imbibition in the 2D nanochannels was observed.

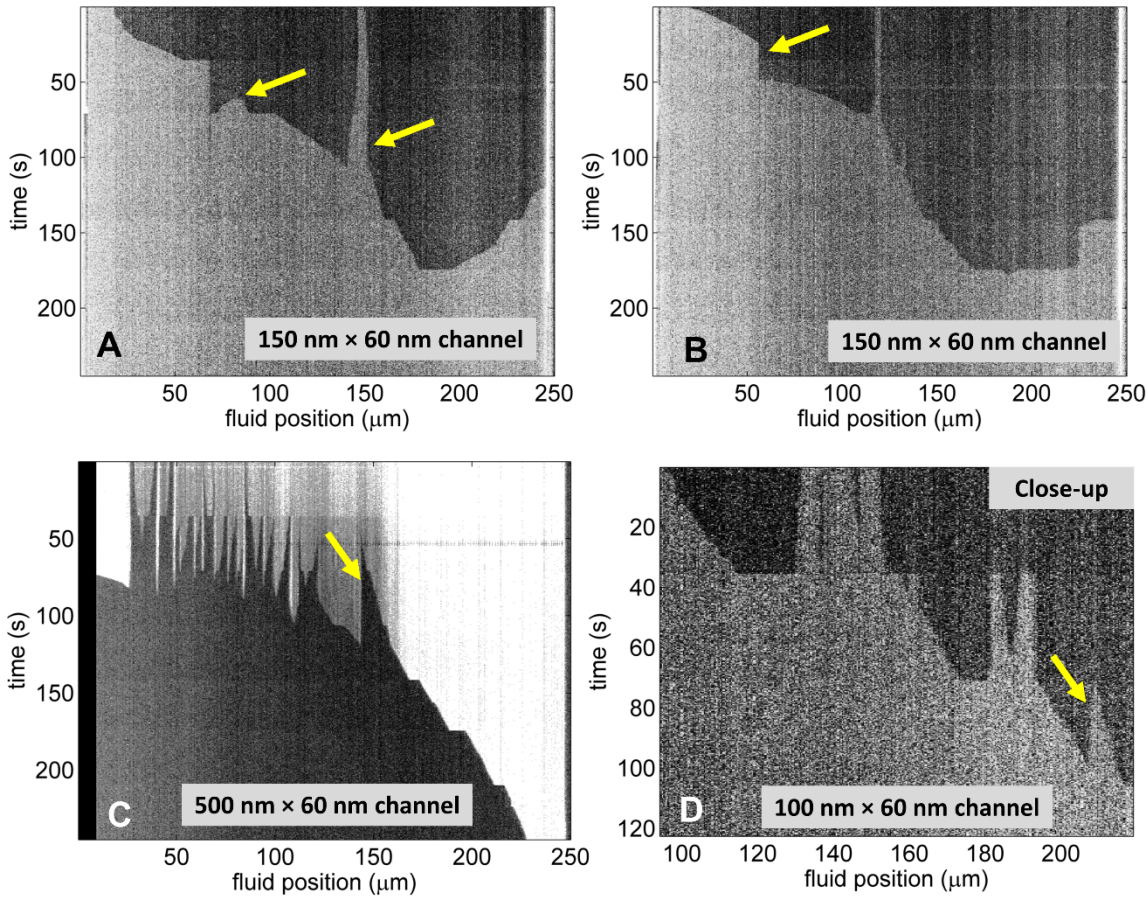

Figure 5.19: Imbibition profiles of degassed IPA in the 2D nanochannels in the presence of capillary trapping. The local imbibition profiles are erratic, but overall and on-average, the data imbibes with a power law trend. Some discontinuities appear in the data every 35 seconds when the capture of a new image stack was initiated. Arrows point to areas where liquid "appeared" ahead of the menisci; i.e., capillary condensation.

IPA was sonicated for ~ 10 min to degas the solution and allowed to imbibe into partially wetted nanochannels (i.e. channels were trapped liquid plugs were visible). Figure 5.19 displays resulting imbibition profiles that are many times slower (refer to the y-axis of the plots in Figure 5.19, which spans over 2 minutes) than open-end channel imbibition (see Figures 5.10 and 5.18 for examples). Assuming the trapped liquid plugs were saturated with gas, the imbibition rate was controlled by the rate of dissolution of gas into the imbibing solution. Thus, imbibition in the presence of capillary trapping occurred the slowest in the largest channels because it is a volume dependent process. Capillary condensation, the formation of trapped plugs from growing films and increasing vapor ahead of the imbibing meniscus, was also observed, as indicated by arrows in the imbibition profiles of Figure 5.19.

5.3.3 High salt concentration

Aqueous solutions with high salt concentrations were introduced into the nanochannels several times. Figure 5.20 displays an example of the imbibition result of a 0.5 M NaCl solution doped with Rhodamine B and captured with FLM; this molarity is lower than the typical salinity of in situ formation water. The results with saline solutions were difficult to compare to the pure liquids of the other sections because the imbibing fronts rapidly evaporated and "salted out/in" during imbibition. Per Raoult's Law, the vapor pressure of a pure solution is lowered when solute is added; hence, the solution is actually less likely to evaporate. Yet, evaporation, like gas dissolution described in previous sections, is a volume dependent process and occurred rapidly in the nanochannels while the microchannels remained saturated. Osmostic flow of water from the nanochannels to the microchannels is possible if the salt concentration in the microchannels is higher than the nanochannels. As displayed in Figure 5.20, evaporation

in the small isolated volumes of the unconnected nanochannels did not permit imbibition as far as 250 μm in even the largest nanochannel. Salting out/in occurs when the solubility of solute molecules (e.g., Rhodamine B) are reduced/increased in a solution of high ionic strength and the molecules precipitate as a function of salt concentration. The ionic strength of the solution is a positive function of salt concentration.

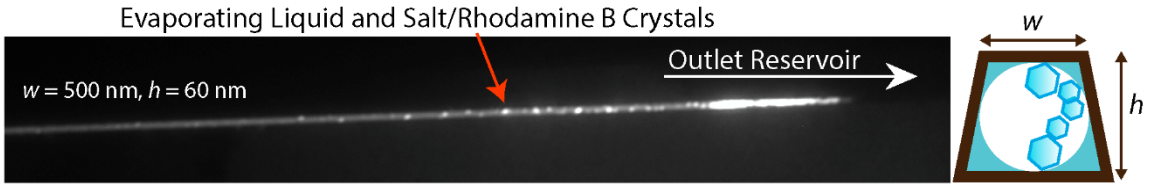

Figure 5.20: FLM image of evaporation and salting out of 0.5 M NaCl solution doped with Rhodamine B within a 500 nm × 60 nm channel.

5.4 ADDITIONAL ATYPICAL NANOFLUIDIC OBSERVATIONS

5.4.1 Longitudinal menisci shapes in nano-slits

The nanofluidic devices described in Section 3.1 include low aspect ratio microchannel pathways that were intended to serve as fluid conduits to the 2D nanochannel arrays in the center of the chips; these pathways also acted as fluid reservoirs. Though the focus of the study was on the 2D nanoconfinements, unusual lateral shapes of the imbibition fronts within these channels prompted ancillary analysis.

The low aspect ratio microchannels leading to the arrays of 2D nanochannels are fundamentally nano-slits. The nano-slits are 1000 nm high, on average, and 80 μm wide and each slit channel is composed of varying material surfaces and channel heights. The structure of the nano-slits allowed an examination of bulk capillary curvature in the

lateral direction, interface stability, and film flow actions in thin apertures of compound surface properties. The top material of the nano-slits is borosilicate glass and from the center to the edges of the channel the bottom materials are: platinum, ~1 μm below the borosilicate glass top; silicon dioxide, 1 μm below the borosilicate glass top; and, after a sharp step, silicon dioxide, 2 μm from the borosilicate glass top. This slit is connected to an adjacent high aspect ratio silicon dioxide microchannel via a 60 nm high aperture which runs along the channel geometry. Revisit Figure 3.3D for a schematic visualization of the compound configuration. The platinum film, originally intended to be an electrode, spans approximately half of the total width of each nano-slit.

In the nano-slit aperture, $w>>h$ and, per the Young-Laplace equation, capillary pressure in the vertical direction dominates over that of the lateral direction. The result of this dominance is nontraditional menisci shapes in the lateral direction. Front speeds and lateral shapes of the menisci within the complex nano-slits differ greatly among the observed liquids; instability and unusual multi-curvatures are observed in many cases. Figure 5.21 displays images of the diverse lateral curvatures for several of the tested fluids. The vertical curvature of the menisci within the 1000 nm high aperture cannot be captured with 2D optical microscopy techniques. Methanol imbibed the swiftest into the nanofluidic chips, completely filling a nano-slit on the order of seconds. On the other hand, water struggled the greatest with imbibition into the nano-slits, moving slowly, on the order of minutes, with an erratic, multi-curvature interface. Interestingly, the lateral menisci of the hydrocarbons heptane and decane were also slow, and the profile was "V"-shaped instead of hemispherical or curved when the front was atop sections with the metal film. The extreme differences in the shapes of lateral menisci and imbibition progression between the different wetting liquids required a phenomenological

explanation. Similar to the data obtained from the 2D nanochannels, the nano-slit imbibition trends do not correlate to the bulk physical properties listed in Table 5.1.

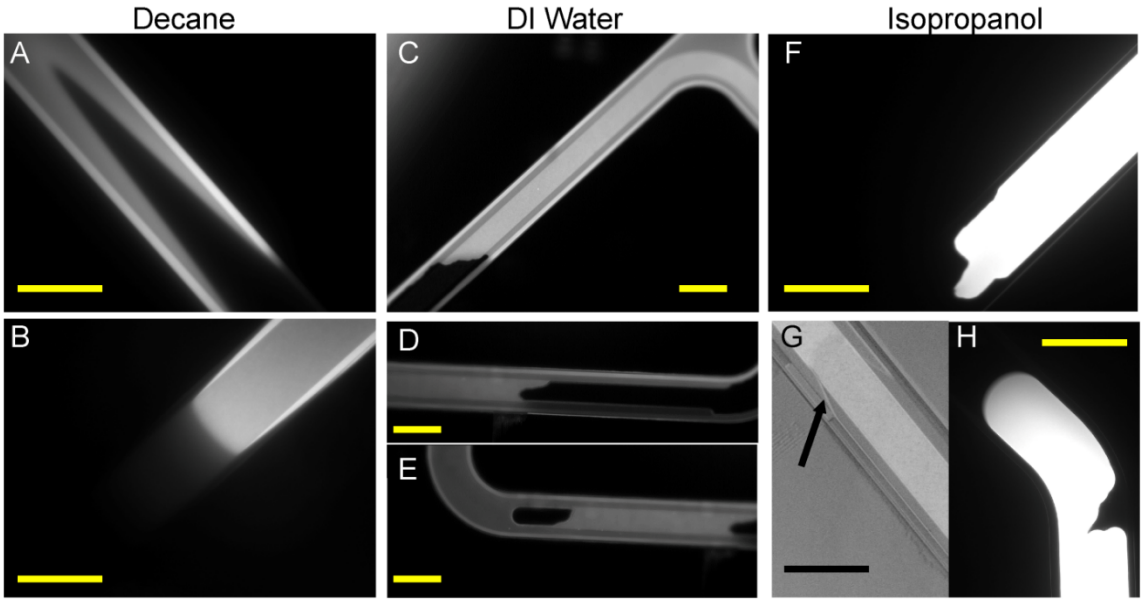

Figure 5.21: Imbibition situations in the nano-slits or low aspect ratio microchannels: (A) Decane imbibition front over a location where platinum is present. (B) Decane imbibition front over a location where no platinum is present (silica is under the front). (C) - (E) DI water forms a wavy, unstable front on all microchannel materials. The upper image is a dynamic meniscus while the lower two are static. (F) Isopropanol imbibition front over a location where no platinum is present. (G)-(H) Isopropanol imbibition front over a location where platinum is present taken with two different types of microscopy. Scale bars are all equal to 80 μm. All fluids are doped with Rhodamine B and images are captured with a Zeiss Axiovert 200M with the exception of Image (G) which features, for comparison, pure isopropanol and was captured with a Zeiss Axioskop 2 MAT.

Again, the unusual and varied lateral menisci in the nano-slits demonstrate the complete domination of capillary pressure in the vertical direction over capillary forces in the horizontal direction along the width of the nano-slits. Thus, local capillary pressure

can be approximated as the curvature between two plates. Regions of higher local capillary pressure move faster than adjacent regions and result in protruding areas of an interface front (for example, the middle of the parabolic isopropanol meniscus profile shown in Panels G and H of Figure 5.21). Liquid pressures behind the menisci in the nano-slits are also mathematically negative, on the order of -50 kPa while no cavitation is observed. Distorted menisci are reported in other works with nano-slits and are proven to be a product of suction due to negative pressure conditions in nano-slits with elastic membranes [170] [171] [172]. The inward deformation of the slits will theoretically lead to higher capillary pressures (in the limit of increased meniscus deformation) and higher imbibition velocities (in the limit of increased hydraulic resistance).

Fronts of isopropanol bound between glass and platinum indicate that capillary pressure is largest in the middle of the nano-slit. Indeed, the middle of an aperture is the location where suction deformation is theoretically largest for ductile materials. Yet, not all of the observed lateral menisci share isopropanol's behavior. For example, the observed capillary pressure of decane and heptane between glass and platinum in the 1000 nm thick aperture is seemingly much less than that of the same liquids between silica and glass in the 2000 nm deep aperture (Panel A of Figure 5.21). Furthermore, the inferred capillary pressure of these hydrocarbons is the smallest in the middle of the slits for those wall compositions. The hydrocarbon meniscus may be subject to deformation at this location and/or the distorted channel (reduced effective diamaters) appreciably increases the resistance to flow. Water, the tested liquid with the highest surface tension, had the most unstable interface, most likely due to pinning and propagation of resulting locally non-constant curvatures; isopropanol is observed to exhibit similar instabilities when bound between glass and silica in a 1000 nm thick aperture. Additionally, the liquid

imbibition speeds negatively correlate with A_{232}, which indicates thinning of the air film enclosed by a meniscus in apertures as thick as 1000 nm high. Indeed, retarded van der Waals forces between various surfaces including glass have been measured out to separations of 1.2 μm [77].

The above observations in the nano-slits further confirm that a complex interplay between metastable liquids, elastocapillary deformation, and long-range intermolecular forces (as well as surface charges) must be considered within the experimental system in addition to conventional hydrodynamic and interface descriptions.

5.4.2 Liquid crystallization in 2D nanochannels and nano-slits

Dendrite ice crystals were found to form on the platinum electrodes in the nano-slits/low aspect ratio microchannels (revisit Figure 3.3D to see the location of platinum in the fluidic design) when the chips are subjected to mild winter temperatures upon transport between experimental facilities (no colder than 2˚C; the absolute minimum temperature for the applicable days of data collection). Dendrite ice crystals are natural fractal patterns that generally only form when air is supersaturated with water vapor and temperatures are within -10˚C to -20˚C [173]. However, some sources report that these fractal patterns can also form in the temperature range of -1˚C to -3˚C and low excess water vapor [174]. Supercooled water vapor may result in the nucleation of ice crystals within a thin film of water saturated in Rhodamine B. As the water freezes the fluorescent solute is excluded from the crystal phase. This mechanism explains the seemingly negative dendrite morphology in Figure 5.22. The platinum electrodes on the chips are assumed to be the site of ice nucleation because metals are superior conductors of heat. If ice only takes the dendrite morphology in the temperature range of -10˚C to -20˚C, the formation of these dendrites in thin water films suggest that the thermodynamic phase

transition properties of the film and chip environment may differ from bulk properties and ambient conditions. Evidence of ice formation in the nanochannels at the 2˚C is also observed (see Figure 5.23). The crystallization occurred in the nanochannels hours before the nano-slits. As displayed in Figure 5.23, such crystallization was strong enough to compromise the structure of the silica nanochannels; this deformation occurred more prominently in the large nanochannels (left of Figure 5.23) than the smaller nanochannels.

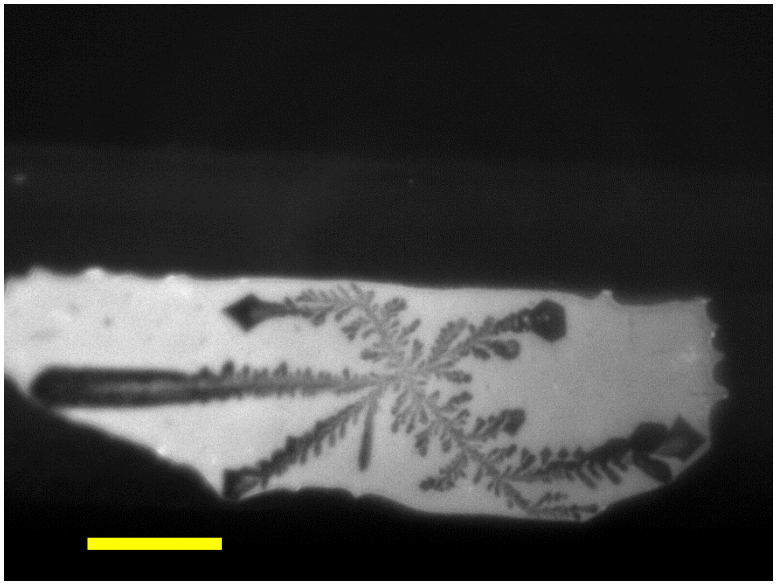

Figure 5.22: An elaborate dendrite crystal formed from DI water and Rhodamine B atop a platinum film in one of the nano-slits; the yellow scale bar is 16 μm.

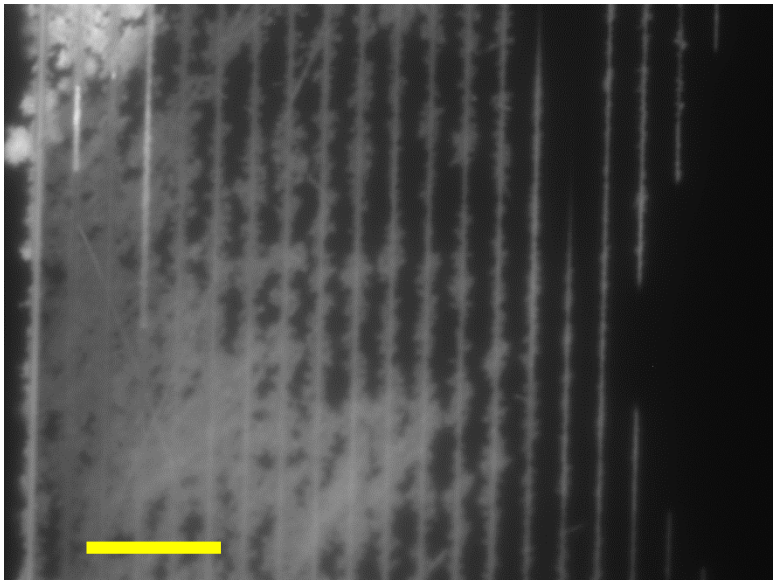

Figure 5.23: Crystallization in the nanochannels in which DI water and Rhodamine B compromised the structure and deteriorated the bond or structure of most of the channels (especially the leftward ones), as revealed by the signal of Rhodamine B; the yellow scale bar is 16 μm.

5.5 EXAMPLES OF FOUNDATIONAL RESULTS IN NANO-NETWORK DEVICES

The bulk of the experimental work presented in this dissertation was performed in the arrays of 2D nanochannels. Figures 5.20 and 5.21 display examples of, respectively, pore collapse with the diffusion of trapped gas and imbibition in the presence of a pseudo-fracture, within PDMS nano-networks composed of patchworks nanochannel and pseudo-shale features.

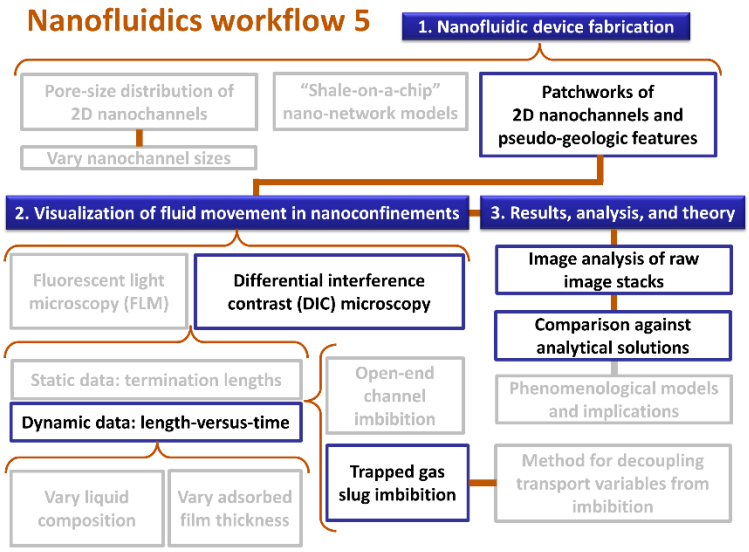

Figure 5.24: Workflow for the dynamic DIC experiments detailed in Section 5.5.

Figure 5.25 displays that there is an almost 50% change in porosity, ϕ, over several minutes in the ductile PDMS nanostructures as trapped air diffuses out of the structures. Per Fick's second law of diffusion and assuming no convection, the general form of the mass flux, N_a, as a function of diffusivity, D, and initial concentration, c_{a0} is

$$N_a = c_{a0}\sqrt{\frac{4Dt}{\pi}}\ , \tag{5.2}$$

such that,

$$\frac{moles}{m^2 s} \propto t^{0.5}\ . \tag{5.3}$$

Therefore, the collapse of the pores is expected to trend proportional to $t^{-0.5}$. However, the data reveals different early and late time trends: at early times the pore space deforms slower than gas pressure diffuses ($\propto t^{-0.2}$) and at later times the pore deformation speeds up to a diffusive trend ($\propto t^{-0.5}$).

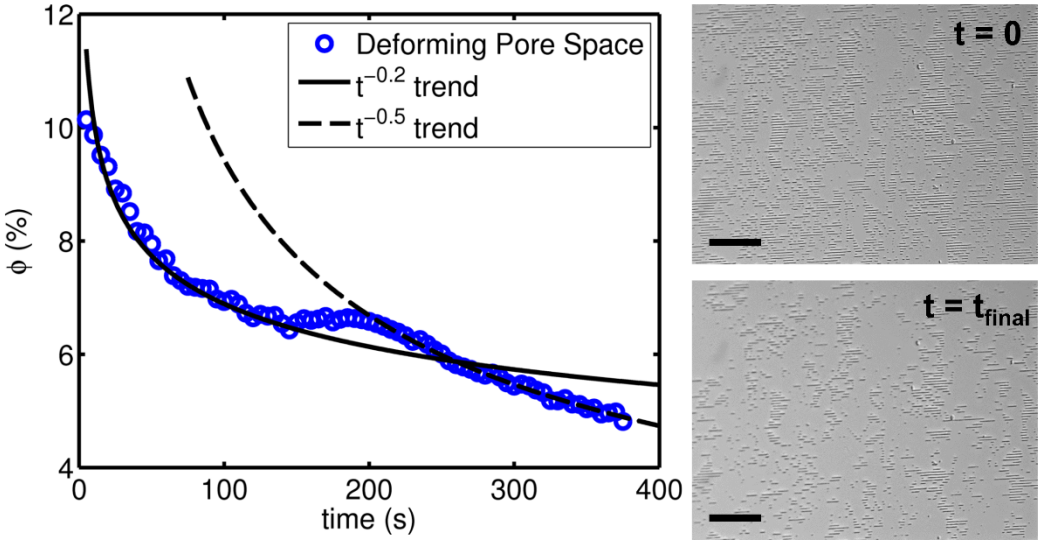

Figure 5.25: Pore collapse in isolated PDMS channel voids or "pores" with the diffusion of trapped gas. Scale bar is 45 μm.

Figure 5.26 displays imbibition of mineral oil into parallel, identical PDMS nanochannels across a pseudo-fracture towards a collapsed region of the device. The results are plotted as saturation of the wetting fluid, S_w, versus time. S_w is related to the Washburn equation for imbibition by

$$S_w = \frac{V_w}{V_p} = \frac{Nwhl}{V_p} = \frac{Nwh\left(\alpha t^{0.5}\right)}{V_p} \quad , \tag{5.4}$$

where N is the number of channels, w and h are the channel cross-sectional dimensions, and V_w and V_p are the volume of wetting fluid and total void space. The data reveals non-diffusive trends both before and after the fluid front, which is not plug-like, reaches the pseudo-fracture. These results may be a product of the limitation of imbibition by partitioning and diffusion of the trapped air mass, as discussed in Chapter 4 and Section 5.1.4.

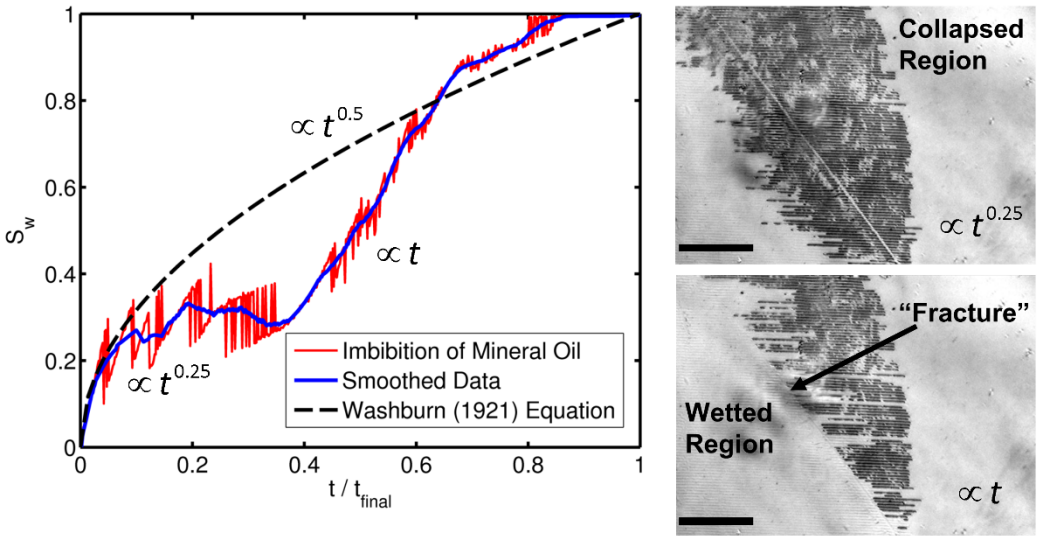

Figure 5.26: Imbibition of mineral oil on large-scale arrangements of PDMS nanochannels in the presence of a synthetic microfracture reveals non-diffusive early and late time trends. Noisiness of the data is due to interface detection uncertainty in the image analysis process. Scale bar is 45 μm.

In sum, when flow trends are not proportional to $t^{0.5}$ there are additional physics are at play not accounted for in the assumed description of the physical situation. When non-diffusive trends are seen in tight media, some authors attribute these trends to highly heterogeneous and ill-connected geometry [175] [176]; however, the emergent physical transport mechanisms, which generate non-diffusive trends in simple nanofluidic geometries, may play a significant role as well. Section 8.3, which addresses future research directions, discusses recommended experiments for nano-network style devices.

5.6 CONCLUSIONS AND RECOMMENDATIONS

How wonderful that I have met with a paradox. Now I have some hope of making progress.

Niels Bohr, Nobel laureate in Physics

It was observed that imbibition of various wetting liquids in an array of different-sized, horizontal, two-dimensional silica nanochannels terminated within the channels as a function of hydraulic diameter and liquid type. This front termination is not predicted by the classic Washburn equation for capillary flow, which establishes diffusive dynamics in horizontal channels. In addition, non-Washburn dynamics ensued due to several inhibitory mechanisms: stick-slip menisci pinning (even of perfectly wetting fluids), capillary trapping, and heightened evaporation due to high salt concentrations.

The experimental method and data analysis process of Chapter 4 (utilizing transient, nanoconfined bubbles) was applied to systematically identify the variables responsible for the inadequacy of the Washburn equation. Decoupled transport variables were presented for the imbibition of IPA in arrays of silica 2D nanochannels. Imbibition of IPA into these nanochannels in ambient conditions was consistently at least five times slower than the Washburn equation prediction. Key findings from the analysis are as follows:

- The extent of IPA's deviation from bulk liquid viscosity values indicates that thick boundary layers, or structured zones of molecules, on the order of ~10-25 nm are organized at room temperature. These boundary layers may be thermodynamically stable due to negative-pressure conditions in the nanochannels. Failure to consider these boundary layers may result in a gross

overestimation of fluid transport efficacy for nano-materials with conditions similar to those of this experiment. An analogous interpretation of these results is deformation/reduction of the cross-sectional area of the channels.

- Contradictory to the Young-Laplace equation, capillary pressures or effective contact angles for IPA in the nanochannels decrease with a reduction in channel width. This trend indicates a local prevalence of boundary zones that do not obey the bulk Laplace curvature and net dewetting in some cases.
- IPA-air interfacial gas partitioning coefficients are not constant between nanochannels and suggest that the theorized solid-liquid boundary zones do not allow significant passage of gas molecules (again, an actual reduction in channel dimensions is possible). This tendency suggests the need to use an effective area, as opposed to a geometric area, when computing interfacial flux across nanoconfined menisci. The results also demonstrate that interfacial resistance to mass transport is a dominant factor in nanoscale transport.
- Imbibition trends during open-end channel imbibition are linear or quasi-linear in the nanochannels with the greatest amount of liquid-solid surface area. This is an unexpected trend warranting further investigation given that high viscous losses, which result in decaying imbibition velocities, are a major flow barrier in liquid nanofluidics.
- Overall, boundary layers on the order of 10 nm plus, as the experimental results suggest, are on the threshold of two contrasting surface chemistry theories, thin bimolecular boundary layers and thick quasi-crystalline boundary layers, and beckon deeper inspection into what controls the extent of boundary layer extent during liquid flow in lyophilic 2D nanoconfinements.

While liquid flow in nanochannels of the dimensions used in these experiments are by the dimensionless Knudsen number definition (see Section 2.2.5) still continuum, potential influences of boundary layers or cross-sectional deformation on effective viscosity must be accounted for when using the Navier-Stokes equation in this domain. A relatively simple model for incorporation of thick boundary layers in nanoscale hydrodynamic descriptions is as follows: consider flow in the boundary layer and bulk regions as the laminar flow of adjacent immiscible fluids of different viscosities, a well-known transport phenomena problem [1]. Others have created more complex descriptions of liquid flow in nanoconfinements where viscosity is a function of position from the wall [177], but such descriptions may not be applicable in the presence of thick boundary layers.

Finally, it is often recommended to repeat the experiments with an identical and scaled-up array of microchannels instead of nanochannels to help probe experimental error. There are several contentions with this notion. First, it is physically unrealistic to upscale this particular nanochannel setup to a microchannel setup on a chip or microscope slide scale since the nanochannel lengths are thousands of times longer than they are wide (recall, the channels span 250 μm in length). Next, the majority of experimental concerns are unique to the nano scale (swifter evaporation, negative pressures, Angstrom scale leakage, clogging/impurities, etc.); thus, moving to a microchannel version of the experiments and potentially obtaining a close match to the Washburn equation prediction would not necessarily logically prove that the nanochannel experiments are error-free/ideal. However, replicating the experiment in sequentially larger nanochannels beyond the ascent in width featured in this work may be very worthwhile for future investigations. Such a method will enable assessment of when

imbibition approached the Washburn equation prediction (and, thus, bulk values) in confinements that are prone to similar nanoscale experimental concerns.

> *In the case of water, achieving purity is virtually impossible because water has a propensity to absorb all kinds of foreign molecules; it's a natural solvent for almost everything. In this sense, contaminants are natural features of water, and their presence in limited quantities does not necessarily imply that any observed feature needs to be reflexively discarded.*
>
> Gerard Pollack, Professor of Bioengineering
> From the book *The Fourth Phase of Water* (2013)

CHAPTER 6: Phenomenological Models for Effective Nanoscale Capillary Pressure, Channel Diameter, and Viscosity†

As I go down in size, there are a number of interesting problems that arise. All things do not simply scale down in proportion. There is the problem that materials stick together by the molecular (van der Waals) attractions. It would be like this: After you have made a [nanoscale] part and you unscrew the nut from a bolt, it isn't going to fall down because the gravity isn't appreciable; it would even be hard to get it off the bolt. It would be like those old movies of a man with his hands full of molasses, trying to get rid of a glass of water. There will be several problems of this nature that I will have to be ready to design for.

Richard Feynman, Nobel laureate in Physics
Challenging others to explore nanotechnology
From his lecture *Plenty of Room at the Bottom* (1959)

The following discussions and presented phenomenological models are based on the anomalous findings presented in Sections 5.1-5.3, which arise from experiments performed in the arrays of parallel nanochannels detailed in Section 3.1.

6.1 EXAMINATION OF THEORIES FOR STYMIED NANOSCALE IMBIBITION DATA

Theories for the varying termination lengths in the nanochannels and the atypical progression of menisci in the nano-slits draw from hydrodynamic, thermodynamic, mechanical, and surface chemistry principles. The compatibility of these theories with the data were reviewed and many of them are discussed and negated subsequently. Overall,

† The models presented in this chapter were published under the following reference, which was completed under the supervision of Carlos Torres-Verdín and Matthew Balhoff.

Kelly S, Torres-Verdin C, Balhoff MT. Anomalous liquid imbibition at the nanoscale: the critical role of interfacial deformations. Nanoscale. 2015; accepted pending minor revisions.

the inability of many of the liquids to completely traverse the majority of the nanochannels are best explained by two concurrent phenomena:

a. The influence of surface forces, specifically van der Waals forces, on a nanoscale meniscus can lead to deformation of the meniscus and an effective P_c value lower than the macroscopic Young-Laplace value.
b. Immobile or liquid crystal (a mesomorphic phase where a liquid possess crystalline structure in one or two dimensions due to long range orientational ordering) boundary layers and possible deformation of these quasi-crystalline zones by elastocapillary effects result in smaller effective channel (or pore) diameters. These quasi-crystalline zones and associated suction-induced shrinkage corresponds to decreases in hydraulic conductivity, potential increases in effective viscosity, and intensification of effect (a).

Phenomenological models for (a) and (b) are presented later in this chapter.

6.1.1 Leakage, fluorophores, and dynamic contact angles

A lack of Rhodamine B fluorescence between parallel nanochannels signifies that leakage of fluid along the silica-borosilicate glass bonding interface is unlikely in the imbibition data examined. However, liquid leakage cannot be detected in possible apertures at the bonding interface that are smaller than 1.7 nm in height, the length of a Rhodamine B molecule [178]. Yet, leakage is improbable because decane, which has a molecular length of approximately 10 Å [179], imbibed the least. Decane molecules can barely fit more than one at a time into an aperture less than 1.7 nm; hence, decane, though displaying minimal imbibition, is the least likely to be prone to leakage in sub-nanometer apertures. Large dynamic contact angles [180] were first suspected to be the cause of imbibition in the nanochannels advancing much slower than predicted by the Washburn

equation. Dynamic contact angles are greater than static contact angles, and their departure from a static contact angle value positively scales with *Ca* or imbibition velocity [181]. However, the termination lengths in the nanochannels do not correlate with *Ca*; it was observed that liquids that imbibed the fastest also imbibed the farthest, indicating that dynamic wetting failure does not explain the results presented herein. It was initially a major concern that the neutral tracer Rhodamine B may have effects on hydrodynamic transport and menisci. However, similar stymied isopropanol imbibition results to that with FLM were achieved using the same nanofluidic chip design and differential interference contrast microscopy (DIC), a tracer-free method [182]. In addition, on several occasions tracer-free fluid was imbibed into the chips and Rhodamine B subsequently injected; the fluorophore diffused to a length within the experimental error of the termination lengths (see error bars in Figure 5.4) observed during imbibition with the fluorophore. Because Rhodamine B is a neutral molecule, it is expected that its effect on surface tension will be less than that of a charged molecule or surfactant, which lower surface tension; however, the effect of Rhodamine B on surface tension in bulk solution was not tested.

6.1.2 Precursor films

Wetting fluids lead to greater imbibition extents, but result in longer and thicker wetting "fingers" (films of liquid that advance beyond the meniscus along the corners of a channel) [183], which can decrease effective nanochannel diameter. These wetting fingers (sometimes referred to under the category of prewetting or precursor films) are aspect ratio dependent and are found to form more prominently in narrow rectangular channels [183] [184], such as 1D nanochannels. The fingers rise faster and farther than the meniscus and follow a different power law trend ($l \sim t^{1/3}$) [185]. In vertical rectangular

micro-tubes the presence of long wetting fingers in front of menisci decreases the vertical equilibrium height of a meniscus to approximately 0.94 of its predicted value [186]. A potential cause of imbibition coming to a stop in nanochannels is the formation of enclosed bubbles when wetting fingers proceed ahead of the meniscus and thicken [170]. However, the likelihood for prewetting film thickening, described by the Hamaker constant for the system of a liquid between silica and air, A_{123}, trends with imbibition success, S_w. Thus, it is surmised that the effect of wetting finger thickening may encourage nanoscale imbibition by preventing film rupture in the presence of surface roughness and other inhomogeneities. Figure 5.3.D (isopropanol, $A_{123} = -1.04 \times 10^{-20}$ J) and Figure 6.1.B (heptane, $A_{123} = -0.91 \times 10^{-20}$ J) show evidence of respectively, intact and ruptured prewetting films.

6.1.3 Metastability and cavitation

The inlets and outlets of the nanofluidic chips were open to the atmosphere, which means that the gas/air pressure in contact with the imbibing liquid, P_0, was atmospheric, 101.325 kPa. Pressure in the imbibed liquid drops linearly and the pressure gradient changes with the length imbibed, given by

$$\frac{\Delta P}{l(t)} = \frac{P_0 - P_c}{l(t)} \quad . \tag{6.1}$$

The theoretical liquid pressure in the 2D nanochannels behind the meniscus per the Young-Laplace equation is approximately -0.7 to -2 MPa (from largest to smallest nanochannel) for all of the liquids. Thus, liquid pressures throughout the nanochannels will likely fall below their saturated vapor pressures and below zero (see Figure 6.2.B). Liquids existing at pressures below the saturated vapor pressure line and negatively pressured liquids are in the metastable region of a substance's thermodynamic phase

diagram. These liquids are theoretically in tension, meaning the liquid molecules exist in a fragile, stretched state [187] [167] [188] and pull on the walls of their confinement [189]. In this state, liquid menisci may also be more subject to deformation by boundary layer effects (long range intermolecular forces) as well as dewetting and pinning. At certain high negative pressures the tensile strength of a molecule is reached and a liquid transitions to vapor; this point is called the spinodal pressure. Negatively pressured liquids in the nanochannels described herein are nowhere near their spinodal pressures (for example, the spinodal pressure of water at room temperature is between -150 and -250 MPa) [190], and, hence, phase transitions due to tensile strength limits (boiling) are not a possibility in the experiments.

A liquid typically experiences cavitation, the formation of vapor bubbles within the liquid, when its pressure, P_l, drops below its saturated vapor pressure, P_{sat}, for a particular temperature. Impurities, seeding, or preexisting bubbles can trigger cavitation. In nanoconfinements this cavitation is not always possible due to the instability of very small bubbles below a critical radius, r_c, (that is, these bubbles collapse), given by [191]

$$r_c = \frac{2\gamma}{P_{sat} - P_l} \ . \tag{6.2}$$

Nanoconfinements whose smallest critical dimension is below r_c have the ability to maintain large negative pressures on the liquid side of a meniscus because bubbles are not energetically sustainable (see inset cartoon in Figure 6.1). The theoretical *maximum* liquid pressures in the nanochannels due to predicted menisci curvatures correspond to critical bubble diameters of approximately 40 nm in the 30 × 60 nm channel and 120 nm in the 500 × 60 nm channel (Eq. (6.2) is fairly insensitive to fluid type when $P_l >> P_{sat}$ and γ values are similar). The proximity of the critical bubble diameters to the cross-sectional

dimensions of the smallest nanochannels in the array indicates that nucleation of bubbles is possible in the realm of a meniscus within these channels, but not certain. While cavitation can stymie the imbibing front, it does not explain the evident difference in termination lengths among the different liquids and in the relatively larger nanochannels.

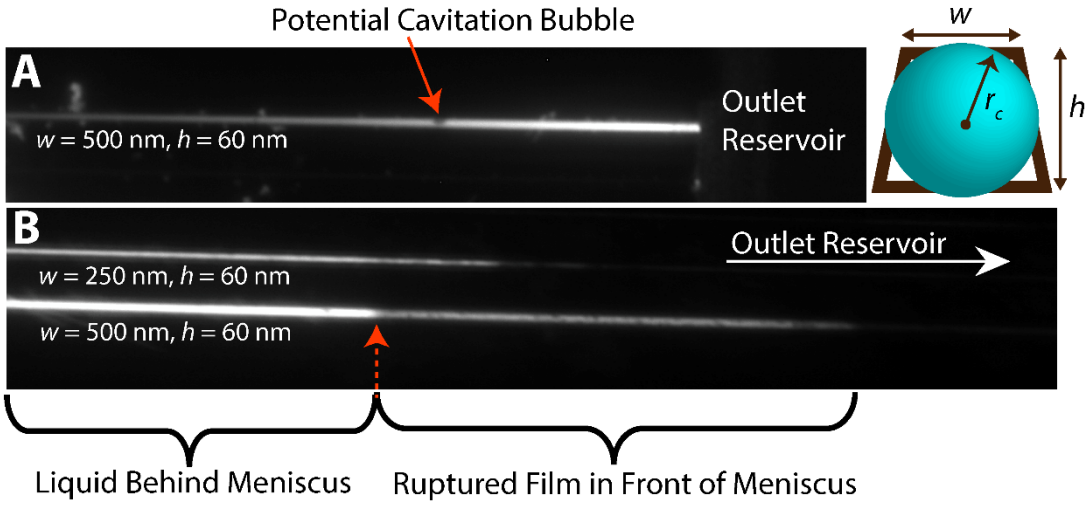

Figure 6.1: (A) Methanol in a 500 nm × 60 nm channel displays a potential cavitation bubble. Methanol readily reaches the channel outlet, but does not enter the outlet reservoir. Fluorophores appear to accumulate at the stopped front. *Inset*: illustration of the case where the critical radius of an energetically stable bubbles (r_c) is larger than a nanochannel's shortest dimensions and, thus, is not expected to form. (B) Heptane in a 500 nm × 60 nm channel displays with a closed outlet reservoir displays an evaporating or ruptured precursor films/wetting fingers. The spacing between parallel nanochannels is 4 μm.

The fluorescent microscopy image data indicate that the presence of large bubbles/gas slugs can be detected within the nanochannels. Figure 6.1.B displays what a front looks like when there are both liquid and gas states present in a front film – either by way of evaporation, precursor film rupture, or even cavitation. This image was taken

of heptane in a 500 nm × 60 nm channel with a 100X objective from an experiment in a previously used chip where one of the reservoirs was blocked. None of the data included in this analysis had such a ruptured/evaporative front. Figure 6.1.A shows an image of the front of imbibed methanol in a 500 nm × 60 nm channel also taken with a 100X objective. In this case, a diffuse ruptured film is not present, but there is evidence of a lone bubble (potentially cavitation). Thus, the optical microscopy data suggests that cavitation is possible, especially in the larger nanochannels of non-uniform cross-sections, but that it is not widely observed. Indeed, Zhang et al. found from simulations that cavitation is more likely in non-uniform nanochannel cross-sections [192]. Figure C.4 of Appendix C also shows examples of how gas slugs appear in the images of the nanochannels. The cavitation observed in 1D nanochannels in the work of Duan et al. resulted in long gas slugs [98]; such slugs would be obvious in the nanochannels examined in this work.

6.1.4 Boundary layer viscosity

The effective increase in liquid viscosity due to attraction of molecules to the walls of the nanochannels through long-range intermolecular forces were also considered. A simple model was employed: Eyring's liquid viscosity theory [59] was modified to account for an addition to the free energy of activation, ΔG_I, for a liquid molecule in the presence of an interface, given by

$$\mu_{nano} = \left(\frac{\delta}{a}\right)^2 \frac{\tilde{N}\hbar}{\tilde{V}} \exp\left(\left(\Delta G_0 + \Delta G_I\right)/k_B T\right), \tag{6.3}$$

where k_B is Boltzmann's constant, δ is the distance between molecular layers, a is length of jump a molecule must make to get to a vacant space, $\tilde{N}$ is Avogadro's number, $\hbar$ is the Planck constant, $\tilde{V}$ is liquid molar volume, R is the gas constant, T is temperature, and

ΔG_0 is the free energy of activation for a molecule to escape from a "cage" of neighbor molecules. The ratio of Eq. (6.3) and the unmodified version of Eyring's equation results in a cancelation of like terms and the expression

$$\frac{\mu_{nano}}{\mu_{bulk}} = \exp\left(\Delta G_I / k_B T\right) . \tag{6.4}$$

ΔG_I is described in terms of the force between a macroscopic body (solid wall) and a molecule, i.e., [69]

$$\Delta G_I = \frac{\pi \rho_s C_{ls}}{6D^3} , \tag{6.5}$$

where D is distance between the molecule and the solid interface, ρ_s is molecular number density of the solid, and C_{ls} is the van der Waals interaction constant in units of J-m^6 between liquid and solid molecules (a system's Hamaker constant is equal to $\pi^2 \rho_l \rho_s C_{ls}$, where ρ_l is molecular number density of the liquid). Thus, viscosity is a function of distance from a channel wall. However, because Eq. (6.4) is an exponentially decaying function, this model only results in notable viscosity increases out to a distance of one or two nanometers from a surface. Consequently, μ_{nano} can theoretically be over an order of magnitude larger than μ_{bulk} in nanopores with diameters around several nanometers and less, but the effect of long-range intermolecular forces on viscosity is not large enough in the investigated nanochannel sizes to account for the observed l_t values. Recall, in the literature review of Section 2.2.3 that Lui and Li (2011) found through molecular dynamics simulations notable variance from the macroscopic value of liquid viscosity in channels of D < 30 nm with increases in fluid-wall binding energy (analogous to ΔG_I) and large divergences when D < 5 nm [60].

6.2 MODEL FOR NANOSCALE MENISCI

A composite film model of a nanoscale meniscus (see Figure 6.2.A) as constructed to theoretically investigate the effect of long-range intermolecular surface forces on menisci in 2D nanochannels. The disjoining pressures across several thin film systems may interact with one another (overlapping force fields) due to their close proximity in a nanoconfinement. Each film or channel material is numerically labeled: material 1 is the silica channel surface, material 5 is either silica or borosilicate glass (respectively, the side walls or the top of the channels), films 2 and 4 are opposing edges and/or precursor films of the liquid meniscus, and film 3 is the air confined within the meniscus curvature and between precursor films. In larger confinements, such as microchannels, the non-wetting fluid would not be considered an interior thin film. Hamaker constants mixing rules for any film (labeled *b*) combined between two other films or solids (labeled *a* and *c*) are as follows [54]:

$$A_{abc} = \left(\sqrt{A_{aa}} - \sqrt{A_{bb}}\right)\left(\sqrt{A_{cc}} - \sqrt{A_{bb}}\right) , \tag{6.6}$$

and

$$A_{abc} \approx \pm\sqrt{A_{aba} A_{cbc}} \quad . \tag{6.7}$$

The adhesion ($A_{abc} > 0$) or repulsion force ($A_{abc} < 0$) per unit area due to van der Waals interactions, Π, across a single medium confined between infinite parallel plates separated by a distance d is the derivative of the free energy per unit area, G [63]:

$$\Pi(d) = \frac{F(d)}{Area} = -\frac{\partial G}{\partial d} = \frac{-A_H}{6\pi d^3} \quad . \tag{6.8}$$

The net van der Waals interaction force per unit area *between* two surfaces for the proposed composite (multilayer) film system, Π_s, is calculated as follows [193] [77]:

$$\Pi_s(d,h_1,h_2)=\frac{-A_{234}}{6\pi d^3}+\frac{\sqrt{A_{121}A_{343}}}{6\pi\left(d+h_1\right)^3}+\frac{\sqrt{A_{545}A_{323}}}{6\pi\left(d+h_2\right)^3}-\frac{\sqrt{A_{121}A_{545}}}{6\pi\left(D\right)^3}\ , \tag{6.9}$$

where D is the total width of an examined cross-section, d is the thickness of the enclosed gas (film 3), and h_1 and h_2 are the thickness of films 2 and 4, respectively. Note that, even in the absence of a meniscus, Π_s can lead to pore wall deformation for very small (near-Angstrom) nanopore spaces when it is on par with the strength of the pore material. The net van der Waals interaction force per unit area acting on film 2 for the proposed composite (multilayer) film system, Π_m, is calculated as follows [73] [77]:

$$\Pi_m(d,h_1,h_2)=\frac{-A_{123}}{6\pi h_1^3}+\frac{A_{234}}{6\pi d^3}-\frac{\sqrt{A_{545}A_{323}}}{6\pi\left(d+h_2\right)^3}\ . \tag{6.10}$$

Only van der Waals forces are considered in this analysis. However, the presence of the EDL can be accounted for in the derivations by incorporating Eq. (2.22) or a similar form (depending on surface charge assumptions) into Eq. (6.10) and following the subsequent derivation procedure.

Up to its midpoint, a 2D meniscus is regarded as a film of varying thickness, and, for mathematical simplicity, the 2D profile is considered to depend on one coordinate, x, such that [26],

$$P_c=\gamma\kappa\approx-\gamma\frac{d^2h}{dx^2}\ , \tag{6.11}$$

where $h(x)$ describes the meniscus profile along a cross-section up to the meniscus midpoint and x runs along the solid channel surface. The axis origin is aligned with the point where the meniscus curvature begins. It is assumed that the meniscus shape does not change during imbibition (a quasi-static or "rigid" meniscus; no dynamic effects). The film system is then considered to be symmetric (material 1 is the same as material 5

and film 2 is the same as film 4) such that $h_1 = h_2 = h$ and $d = D - 2h$ and, given the mixing rules of Eq.'s (6.6) and (6.7),

$$\Pi_m(h,D) = \frac{1}{6\pi}\left(\frac{-A_{123}}{h^3} + \frac{2A_{232}}{(D-2h)^3} - \frac{A_{123}}{(D-h)^3}\right). \tag{6.12}$$

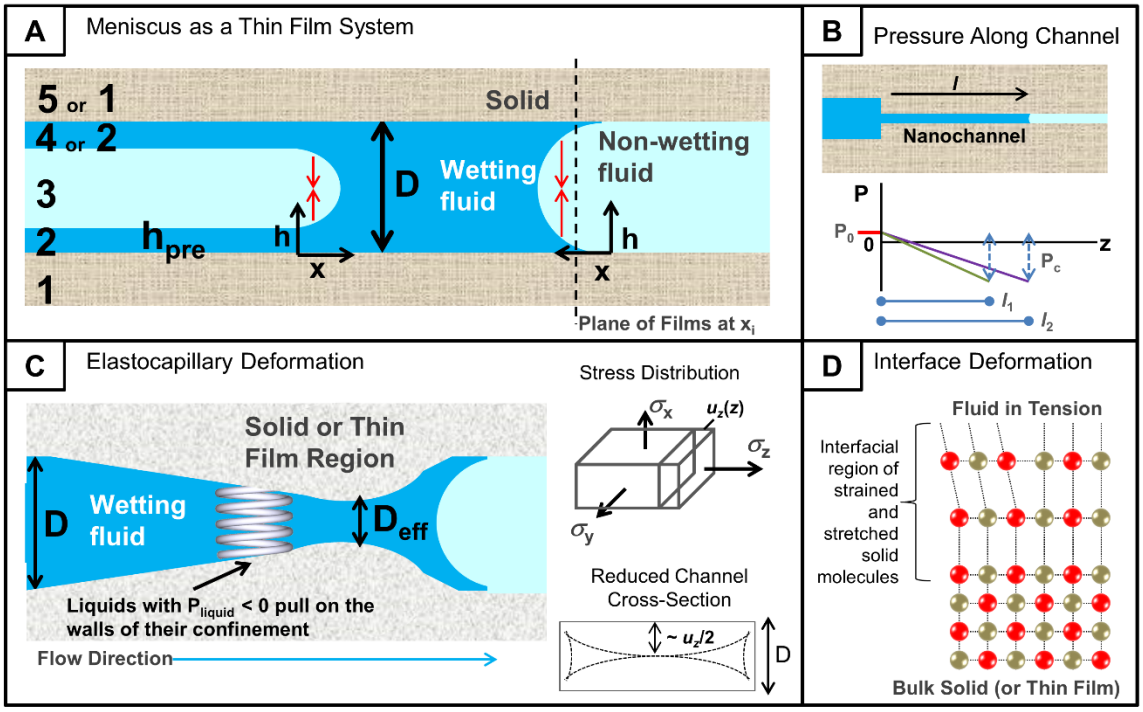

Figure 6.2: (A) Diagram of two possible configurations of a nanoscale meniscus where the meniscus is considered as a system of composite films/materials in a 2D nanopore or nanochannel space of diameter, D. A wetting film of height h_{pre} (shown with the left meniscus) may be present. The thickness of films 2, 3, and 4 vary as a function of x along the meniscus. Height, h, and curvature of the meniscus may vary from the semicircular curves illustrated due to the influence of surface forces (net force is depicted with a red arrow). (B) Pressure drops along a nanochannel are mathematically negative when $P_c >> P_0$. (C) Metastable and negatively pressured liquids generate a suction effect within a pore space; crystalline or quasi-crystalline thin films may be deformed as well. (D) Additional deformations occur at the interfacial zone of a solid (cartoon adapted from Weissmüller and Kramer [2010]) [194].

An equilibrium equation is necessary to solve for the local meniscus curvature due to the presence of surface forces as a function of D and h. In the case of a nanoscale meniscus that is only partially deformed and retains some portions of constant (bulk) curvature, the applicable expression is:

$$P_c^m = \gamma\kappa_n + \Pi_m(D,h) \ , \tag{6.13}$$

and

$$P_c^n = \gamma\kappa_n \ , \tag{6.14}$$

where P_c^m is the macroscopic capillary pressure predicted by Young-Laplace's equation for a planar aperture and the local meniscus curvature, κ_n, and Π_m change along the meniscus with changes in the lengths of h and d; P_c^n is the local nanoscale capillary pressure. From Derjaguin's work on menisci in narrow slits, a symmetric meniscus is in equilibrium with a precursor film of height h_{pre} such that [73],

$$\Pi_f(h_{pre}) = \gamma\kappa_n + \Pi_m(D,h) \ , \tag{6.15}$$

where Π_f is the force per unit area due to van der Waals interactions across the precursor film; Π_f can be set to the same value as P_c^m for a first-hand estimation or can be determined with disjoining pressure isotherms or the Langmuir equation for absorption [77]. The pore space available for a fluid meniscus becomes smaller in the presence of relatively thick adsorbed or precursor films. Overlapping surface force layers can lead to additional widening of thin films in narrow confinements [73]. A_{232} will always be a positive value since like substances or solids attract each other over a thin film rendering such a film prone to thinning. Thus, the meniscus curvature is expected to further deform in narrow pore spaces with increasing positives value of A_{232}, the force across the gas enclosed by the meniscus. Figure 6.3 illustrates the effect of non-retarded and retarded van der Waals surface forces up to the midpoint of a meniscus in apertures of heights D =

2 nm and D = 60 nm (the depth of the nanochannels). Retardation effects occur when confined molecules are relatively far enough apart that their dipole moments become out of phase faster than the electric field interactions between the molecules, which are limited by the finite speed of light [68], and are explained in greater detail in Section B.2 of the Appendix B. For effect, the curves in Figure 6.3 are each compared to the corresponding case where forces from the thinning of the interior gas and opposite side of the meniscus are ignored (blue dotted lines). Values and determination of Hamaker constants for the retarded regime are described in Table B.1 of Appendix B.

Substitution of Eq.'s (6.11) and (6.12) into the relationships in Eq.'s (6.13) and (6.15) results in the following ordinary differential equations (ODE) for, respectively, a meniscus where part of the curvature is constant/bulk and a meniscus where no part of the curvature is constant:

$$\gamma \frac{d^2h}{dx^2} = \frac{\gamma \cos\theta_0}{D} + \frac{1}{6\pi}\left(\frac{-A_{123}}{h^3} + \frac{2A_{232}}{(D-2h)^3} - \frac{A_{123}}{(D-h)^3} \right), \tag{6.16}$$

and

$$\gamma \frac{d^2h}{dx^2} = \frac{A_{123}}{6\pi (h_{pre})^3} + \frac{1}{6\pi}\left(\frac{-A_{123}}{h^3} + \frac{2A_{232}}{(D-2h)^3} - \frac{A_{123}}{(D-h)^3} \right). \tag{6.17}$$

The above ODEs can be solved numerically to ascertain $h(x)$, the profile of a nanoscale meniscus curvature as a function of fluid properties and A_H values, nanochannel cross-sectional aperture, and, in some cases, precursor film thickness. However, it is more practical to obtain the average capillary pressure in a nanoscale aperture, $\overline{P}_c^n$, due to the influence surface forces. In addition, the curvature approximation in Eq. (6.11) is only valid when dh/dx is small; that is, the meniscus/film thickness varies

slowly. This condition is not the case as h approaches $h = 0$ and $h = D/2$, limits which result in an approach toward infinite values of Π_m.

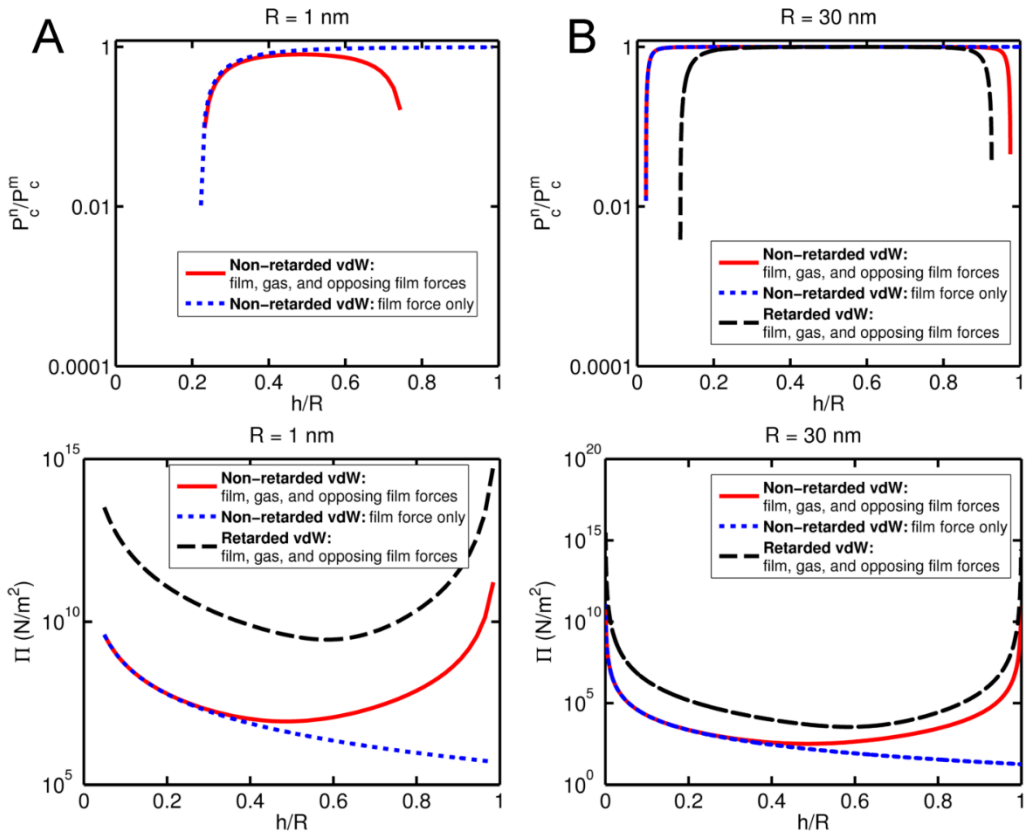

Figure 6.3: Plots of retarded and non-retarded van der Waals (vdW) forces as a function of meniscus height normalized over 2D channel radius (h/R) for channels of (A) $D = 2$ nm and (B) $D = 60$ nm. Plots of the ratio of the local (non-average) capillary pressure considering these surfaces forces to the macroscopic capillary pressure are also shown in an analogous manner. Retarded forces are unlikely in nanochannels less than 10 nm in diameter and hence are not plotted for the capillary pressure ratio in the 2 nm diameter channel; the hypothetical values of the retarded force along a 2 nm diameter channel are plotted in the lower panel.

The average value of surface forces, $\overline{\Pi}_m$, are first approximated by integrating Eq. (6.12) with respect to h from precursor film of height h_{pre} (at $x = 0$) to channel radius, R, minus half of the minimum width of the minimum stable gas film, d_g, and dividing by this interval. Again, $h = 0$ and $h = D/2$ cannot be used as integrands because they result in infinite values of Π_m. h_{pre} and d_g represent the maximum lengths where surface forces dominate over surface tension and are determined by setting the definition of Π in Eq. (6.8) equal to the macroscopic capillary pressure value and solving for d using, respectively, A_{123} and A_{232}.

Because the shape of the meniscus, $h(x)$, is unknown, h is set to increase linearly between the integrands, thus finding the average of all meniscus/film heights possible in the aperture. Consequently, $\overline{\Pi}_m$ is an <u>estimate</u>. Hence, an estimate of $\overline{P}_c^n$ for a symmetric 2D meniscus with regions of constant and non-constant curvature in the presence of an adsorbed or precursor film of height h_{pre} and within a planar channel or pore space of height D is given by

$$\overline{P}_c^n \approx P_c^m - \frac{\int_{h_{pre}}^{R-d_g/2} \Pi_m(h,D)dh}{R-\frac{d_g}{2}-h_{pre}} = P_c^m - \frac{\frac{1}{6\pi}\left[\frac{A_{123}}{2}\left(\frac{1}{h^2}-\frac{1}{(D-h)^2}\right)+\frac{A_{232}}{2(D-2h)^2}\right]\Bigg|_{h_{pre}}^{R-d_g/2}}{R-\frac{d_g}{2}-h_{pre}}. \quad (6.18)$$

An analogous calculation can be performed for extremely small nanochannels (< ~5 nm in diameter) by replacing P_c^m with Π_f in Eq. (6.18). There is no surface tension in the expression resulting from that equation because long-range intermolecular force components dominate over capillary pressure.

The previous expressions assumed a 2D meniscus in a slit aperture. Unlike the Young Laplace equation, a calculation of the mean curvature of the normal curvatures, κ_1 and κ_2, along the normal planes at a point in the nanoscale meniscus is inadequate for

extension of the meniscus analysis to 3D. That method neglects attractive forces at locations other than along the principal cross-sections and will underestimate the degree of meniscus deformation. The Derjaguin approximation [63] is used to extend the 2D analysis of $\overline{P}_c^n$ to a 3D approximation of $\overline{P}_c^n$ in a cylindrical conduit. The Derjaguin approximation states that the *local* disjoining pressure of a curved surface with a certain film system is approximated by the disjoining pressure of a flat surface with the same film system [63]. Some works have used this approximation to determine the shape of a 2D meniscus on a grooved (curved) nanostructured surface [195] [196]. A 3D meniscus in a cylindrical conduit of radius R (D/2) can be considered to be a series of local 2D meniscus film systems whose aperture height, S, changes with the radial distance, r, along the cross-section of the conduit. S is determined by the length of a geometrical chord and the average of the disjoining pressure in the cylindrical conduit renders $\overline{P}_c^{n,3D}$, the average 3D nanoscale capillary pressure, namely,

$$\overline{P}_c^{n,3D} \approx P_c^m - \frac{1}{R-h_{pre}} \int_0^{R-h_{pre}} \left(\frac{\int_{h_{pre}}^{(S-d_g)/2} \Pi_m(h,S)dh}{\frac{S-d_g}{2}-h_{pre}} \right) dr \ , \tag{6.19}$$

with

$$S = 2\sqrt{R^2 - r^2} \ . \tag{6.20}$$

The closed form result of Eq. (6.19) is shown in Section B.1 of Appendix B. In non-circular cross-sections such as rectangles, S should be described such that the integration will occur from the conduit's largest dimension (diagonal length) to the smallest (a corner).

The ratio of $\overline{P}_c^n$ (in the 2D or 3D form) to the macroscopic capillary pressure predicted by Young-Laplace's equation, P_c^m, can conveniently be expressed as an effective contact angle, θ_{eff}, given by

$$\theta_{eff} = \cos^{-1}\left(\frac{\overline{P}_c^n}{P_c^m}\cos\theta_0\right), \tag{6.21}$$

where θ_0 is the macroscopic contact and is equal to zero for perfectly wetting fluids. The effective contact angle convention is useful for practical implementation of nanoscale menisci descriptions because it allows all of the surface force formulations to be encapsulated in a single term and the structure of Young-Laplace's equation remains applicable; i.e. for a cylindrical pore,

$$\overline{P}_c^n = \frac{2\gamma\cos\theta_{eff}}{R}. \tag{6.22}$$

Figure 6.4 displays θ_{eff} for the experimental fluids along the range of applicable nanochannel hydraulic diameters. The plot reveals a steep increase in θ_{eff} with a decrease in pore or channel diameter below ~ 10 nm and a difference in θ_{eff} between different fluids for a particular conduit size. The order of these effective contact angles increase from methanol to the hydrocarbons, indicating that the preceding theory correlates with the relative imbibition successes observed in the nanochannel arrays. An exception to this trend is the curve for water; recall from Table 1 that $\theta_0 = 28^\circ$ for water on silica and water is the only one of the tested liquids with a notable macroscopic contact angle. DI water may still have a trace amount of ions present and the extent of the resultant electrical double layer is inversely proportional to ionic concentration. Thus, the curvature of a water meniscus may be subject to electrical double layer and hydration forces, which were not accounted for in this analysis. Also note that the silanol groups at the channel walls may lead to deprotonation or proton uptake effects during the imbibition of aqueous

solutions [197]. Effective contact angles for D = 60 nm, the depth of all of the nanochannels, are in the arena of ~25-30˚. While considerable, these values are nowhere near high enough for the flow to come to a complete stop in the nanochannels. The imbibition data also suggest that the spread of the different values of θ_{eff} between fluids should be more pronounced than Figure 6.4 indicates. The consideration of elastocapillary deformation in conjunction with meniscus deformation strengthens the explanation of the anomalous imbibition results.

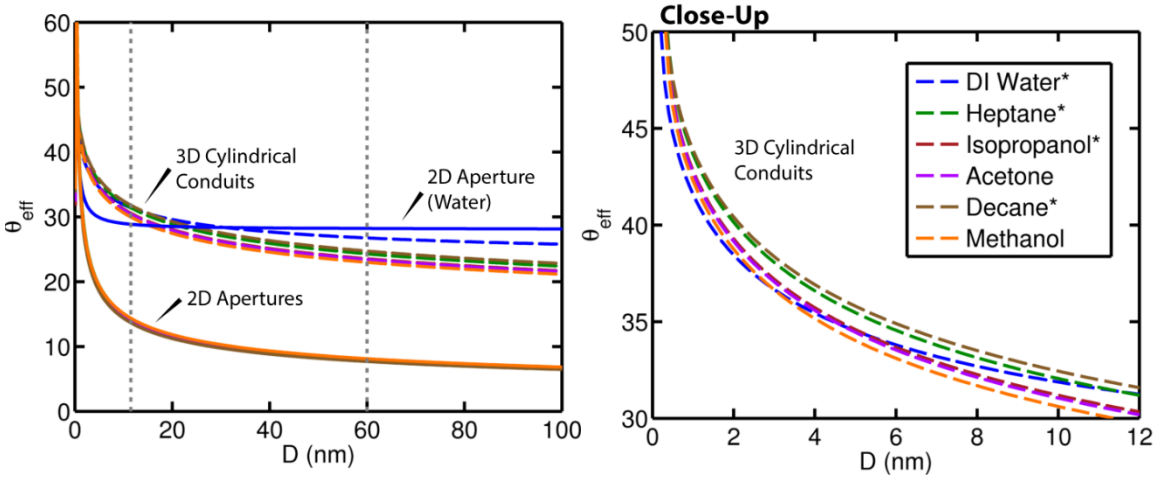

Figure 6.4: *Solid curves*: effective contact angles for the experimental fluids along the range of applicable nanochannel hydraulic diameters using the result of Eq. (6.18) (2D case). *Dashed curves*: effective contact angles using the result of Eq. (6.19) (3D case). θ_{eff} gradually approaches bulk contact angle θ_0 (mainly zero) as hydraulic diameter increases and rises steeply as hydraulic diameter decreases below 10 nm. For example, at D_H = 1 μm, θ_{eff} (3D case) = 14° and θ_{eff} (2D case) = 3° for isopropanol; cos(14°) = 0.970 and cos(3°) = 0.997. Recall that θ_{eff} is not representing an actual contact angle, but a correction due to surface force influences. The right plot is a close up of the region to the left of the leftmost dotted gray line in the left plot. The rightmost dotted gray line indicates the etched depth of the nanochannels.

6.3 MODEL FOR CONFINEMENT DEFORMATION

For a wetting fluid, negative liquid pressures behind an imbibing meniscus result in compressive stresses in the wetted areas of a pore space. The resultant stress jump between the wet and dry regions of the pore space lead to decreases in effective pore diameter through shrinkage, buckling, and sometimes channel collapse. Note that the opposite phenomena, expansion, occurs for non-wetting liquids. Per classic mechanical definitions, solid deformations can occur in both the radial (cross-sectional) and axial/longitudinal (along the capillary) directions depending on the elastic properties of the media, the length of the channel or pore, and the thickness of its walls or distance between local pore spaces; however, radial deformations are often negligible. Thin-walled carbon nanotubes are highly susceptible to elastocapillary deformation [198], and harder materials such as silica also exhibit fluid-induced deformation [199], though typically on the order of Angstroms.

Liquid pressures are constant within a static trapped liquid plug and the maximum deformation occurs in the center of the plug. During imbibition, liquid pressure drops linearly along the imbibed length of channel or z-direction (see Figure 6.2.B), and the longitudinal stress vector on the capillary walls, σ_z, scales with the pressure of the imbibing liquid. Hooke's law relates total stress for a given geometry and strain ($\delta l/l$): $\delta l/l = \delta u_z/\delta z = (\sigma_z - \nu(\sigma_x + \sigma_y))/E$, where $u_z(z)$ denotes the local longitudinal deformation for the length imbibed z [200]. The nature of δl is compressive for wetting fluids and the maximum compressive deformation or wall shrinkage is expected to occur in the vicinity of the meniscus front. Shrinkage in the axial direction along a channel will lead to deformations or buckling in the radial direction. Eventually, at length l_c channel convergence or collapse may occur. Bico et al. (2004) and Kim and Mahadevan (2006)

provide equations for the determination of l_c during imbibition between parallel sheets [31] [32]; however, the nanoconfinements in this work are akin to voids in a solid, not thin-walled tubes or sheets. Love (1929) derived the height deformation in the center of a rectangular area within a semi-infinite solid as a function of pressure [201].

The aforementioned elastocapillary equations take into account *bulk* mechanical effects, assuming that the surface-induced pressure in the solid is the same as the pressure in the liquid. This assumption is acceptable for macro- and microscopic conduits but is technically incorrect [202] [203]. Following the theory of interfacial zones introduced by Gibbs over a century ago [202], Figure 6.2.D depicts how the molecules at a liquid-solid interface are most likely found in a strained and stretched state compared to those of the bulk/interior solid; albeit the effect of stretch is usually on the order of picometers and negligible [204]. In addition, possible liquid crystal boundary layers formed at the liquid-solid interface will have different elastic properties than the solid confining material. Recall that metastable liquids are in tension and pull on the walls of their confinements. Thus, surface stresses at the solid interface must be considered at the nanoscale, just as long-range intermolecular forces were considered in tandem with bulk surface tension forces in the previous section. Weissmüller and Cahn (1996) and Weissmüller (2010) provide a generalized capillary equation for the average pressure in the solid bulk, P_s, as a function of enclosed fluid pressure, P_f, the volume-specific surface area (interfacial area, A_s, per solid volume, V_s) of the pore space, ξ, elastic strain, ε, and average (scalar) surface stress at the interface, f_I (units of N/m) [205] [204]:

$$P_s = P_f + \frac{2}{3}\zeta f_I \ , \tag{6.23}$$

$$f_I = \gamma + \frac{d\gamma}{d\varepsilon} \ , \tag{6.24}$$

and

$$\zeta = \frac{A_{surface}}{V_s} \ . \tag{6.25}$$

Eq. (6.24) is the Shuttleworth equation [206]. The interpretation of the Shuttleworth equation is highly debated and the topic of interfacial surface stresses is generally under-researched. Materials are inclined to have decreased Young's moduli, or "soften", at interfaces because atomic coordination is less at surfaces [207]. Unfortunately, it is challenging to determine f_I without stress-strain data. For reference, values of f_I for metals are usually around 1 N/m [204]. The surface stress term in Eq. (6.23) can play a large role in highly porous nanomaterials or thin-walled nanoconfinements. For a cylindrical void (an approximation of the geometry of the tested nanochannels and a standard throat geometry for pore network models), $\xi = 2r/R^2$, where r is the void radius and R is an appropriate radius for a representative unit cell or the distance between void spaces, a function of porosity, ϕ. In the silica nanofluidic chip configuration (R = 2 μm) $r << R^2$. If potential liquid crystal boundary layers of thickness δ are considered as detached channel walls to the interior liquid, then $\xi = 2(r\text{-}\delta)/(2r\delta\text{-}\delta^2)$ and ξ is much larger than the former case.

Local longitudinal deformation in arrays of channels as a function of distance along the axial direction of an imbibition front, $z(t)$, is described by [204]:

$$u_z = \frac{1}{2}\left(P_f + \frac{2}{3}\zeta \bar{f}_I \right) \frac{1}{K} \frac{1-\nu}{2\nu - 1} z(t) \ , \tag{6.26}$$

and

$$K = \frac{E}{3(1-2\nu)} \ , \tag{6.27}$$

where E is Young's modulus, ν is Poisson's ratio, and x is position along the length of the channel. It is posited that the local solid shrinkage in the longitudinal directional will approximately manifest itself as a decrease in channel cross-sectional area by way of the first order approximation of the Poisson's ratio relationship for the changes in cross-sectional lengths, u_x or u_y, of an axially deformed bar of length l:

$$u_{x,y} \approx u_z \nu \ . \tag{6.28}$$

Thus, u_x or u_y is an estimate of decrease in diameter, and at $z = l_c$, either u_x or u_y is approximately equal to the smallest critical dimension of the channel; this dimension is 60 nm for the majority of the studied nanochannels. The discussed model does not explicitly predict when the imbibition front should stop, but predicts when a channel will collapse in its smallest direction, significantly increasing flow resistance. At this point, for walls (or thin crystalline films) of sufficient ductility, the cross-sectional area may become separated into limited spaces (see Figure 6.2.C). Equations for independent displacement in the radial direction are available as well [204] [208], but their effects are usually small compared to the longitudinal case. In the case of the silica nanochannels where E = 73 GPa and ν = 0.2, silica deformation in the longitudinal direction is also negligible. However, if an adsorbed liquid crystal is considered to be the confining medium and semi-infinite and its Young's modulus is estimated to be two orders of magnitude less than silica (for reference, the Young's modulus of ice is one order of magnitude less than silica) then the confinement deformation depicted in Figure 6.5 is possible. Per Eq. (6.26) ad negligible surface stress effects, Figure 6.5 displays curves of l_c/L (plotted in black) for different values of θ_{eff} against the imbibition termination lengths of the Section 5.1.1 data; recall that L is the length of the nanochannels.

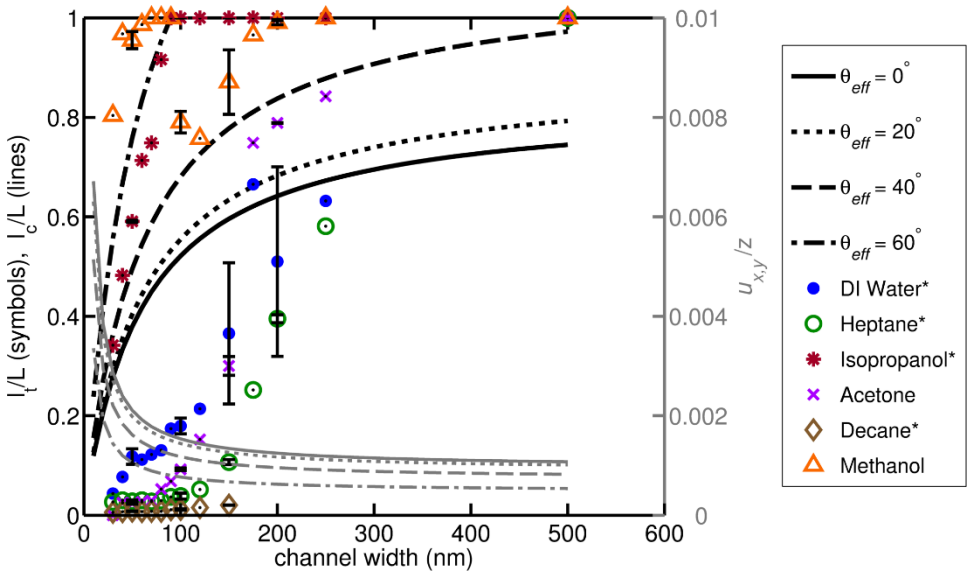

Figure 6.5: Black curves go with the left y-axis while gray curves go with the right y-axis. Curve patterns correspond to θ_{eff} values. When l_t/L data points fall below one of the black curves, the imbibition front is stopped by the combined effect of an increase in hydraulic resistance and decrease in capillary pressure. When l_t/L data points fall above one of these curves, the capillary pressure is lower than predicted, but still strong enough to overcome the corresponding hydraulic resistance. Gray curves describe the amount of deformation experienced by the pore cross-section per the length imbibed; deformation rises dramatically in channels less than 100 nm in critical dimension. Channel deformation is expressed in terms of $u_{x,y}/z$ (the right y-axis), where z is length imbibed, because $u_{x,y}$ scales linearly with z (see Eq. (6.26)) and has a slope dependent on material, channel, and fluid properties: P_f, K, and ν (and sometimes f_1, ξ). Thus, for any channel width, w, and z, $(u_{x,y}/z)*z$ renders $u_{x,y}$; $u_{x,y}$ values are on the order of nanometers when z is on the order of microns. Estimated elastic parameters for a liquid crystal: $E = 7.3$ GPa and $\nu = 0.3$. $\gamma = 0.02$ N/m was used for constructing curves.

Note that in the case of defects or surface roughness an adsorbed liquid crystal film may delaminate at some location over a delamination length, a. For a film of height/thickness h and Young's modulus E_f on a stiff substrate such as silica, the

maximum normal stress, σ_m or P_f, needed to cause buckling of the film (another mechanism for alteration of the cross sectional area available for flow) is [209]

$$\sigma_m = \frac{\pi^2}{12}\left(\frac{h}{a}\right)^2 E_f^2 \ . \tag{6.29}$$

In axially convergent channels, liquid is expected to imbibe *faster* and *beyond* the length and rate predicted by the Washburn equation in the limit of channel collapse and increased viscous dissipation [210] [211]. The termination length data presented herein suggest otherwise; that is, they suggest that the smaller of the observed nanochannels are deformed such that their effective diameter is small enough at the region of the front to reach a threshold of significant meniscus deformation (in Figure 6.4, observe the nature of the curves below ~ D = 10 nm). This compounded deformation of channel and meniscus contributes to the eventual stopping of an imbibing liquid front, possibly before its respective l_c curves in Figure 6.5. Increased μ_{eff}, discussed subsequently, contributes to the premature stoppage as well.

Recall from Section 5.1.2 that the imbibition of isopropanol in arrays of silica nanochannels equivalent to those in this work did not follow a diffusive trend in the array's larger nanochannels [182]. Instead, the imbibition approached a linear trend, even though the velocity was slower than predicted. Theoretically, a converging channel leads to increases in capillary pressure with length imbibed and an exponent of the imbibition time greater than 0.5. This relationship only manifests itself in the largest nanochannels in the array, where channel deformations, viscous losses, and menisci deformations (per the analysis of the preceding section) are predicted to be least. These data points often fall above l_c curves in Figure 6.5.

In some situations (e.g. geological porous media), additional deformations, plastic (permanent) or elastic (temporary), can be caused by external forces [212], but only stresses due to capillary and interfacial effects need to be considered in this work. Additionally, it is possible that some reports of higher effective viscosity in nanoconfinements may be misinterpretations of solid of thin film interface deformation.

6.4 MODELS FOR EFFECTIVE DIAMETER AND LIQUID VISCOSITY

Overall, channel deformations lead to a decrease in effective diameter and, hence a decrease in hydraulic conductivity or permeability (for porous media). When the cross-sectional area of a nanoscale channel or pore is severely decreased, the aforementioned viscosity effects described by Eq.'s (6.3)-(6.5) arise. Effective channel diameter, D_{eff}, due to elastocapillary and surface deformation effects, and effective viscosity, μ_{eff}, the evaluation of Eq. (6.4) at D_{eff}, are defined as:

$$D_{eff} = 2\left(R - \Delta r_{elastic} - \Delta r_{solvation} - \Delta r_{adsorbed}\right) , \tag{6.30}$$

and

$$\frac{\mu_{eff}}{\mu_{bulk}} = \left.\frac{\mu_{nano}}{\mu_{bulk}}\right|_{D_{eff}} , \tag{6.31}$$

where R is the radius or hydraulic radius of a dry channel or pore and $\Delta r_{elastic}$ is equal to u_z and due to both radial (when applicable) and axial deformations (a function of length imbibed); $\Delta r_{solvation}$ describes the layer(s) of fluid molecularly bound to the solid, and $\Delta r_{adsorbed}$ encompasses adsorbed, prewetting, and solute films. Both of these variables are non-constant. Figure 6.6 displays how viscosity theoretically diverges from its bulk value for the tested fluids near solid interfaces per the model in Eq.'s (6.3)-(6.5). Upon deformation and opposite wall contact channel cross-sections drastically narrow and

regions of such enhanced viscosity are possible. Liquid-specific properties are incorporated into the model as follows:

$$\Delta G_1 = \frac{A_{12}}{6\pi D^3 \rho_s} = \frac{\sqrt{A_{11}}\sqrt{A_{22}} M_w}{6\pi D^3 \tilde{N} \rho} \quad , \tag{6.32}$$

where A_{12} is the Hamaker constant for materials/fluids 1 and 2 acting across a vacuum, ρ is fluid density (units of kg/m^3), and M_w is molecular weight. $A_{22} \approx A_{232}$ and for silica A_{11} = 6.53 × 10^{-20} J. A relationship between Hamaker constants and imbibition success by way of increased viscosity at surfaces is evident.

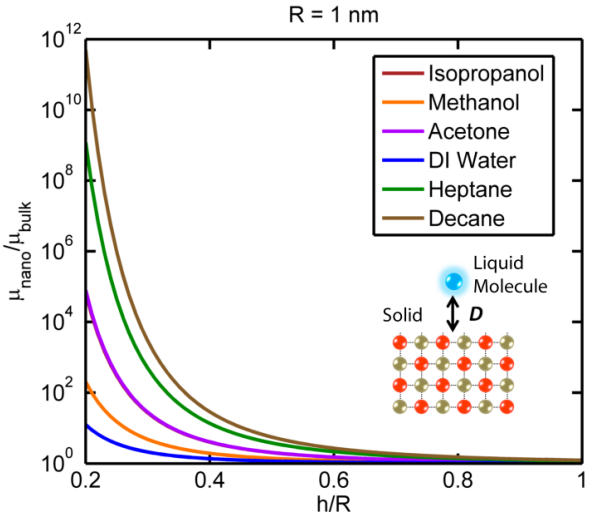

Figure 6.6: Model for divergence of viscosity from its bulk value near a solid interface (at h =0) for the tested fluids. Curves for isopropanol and methanol overlap. The hydrocarbons, especially decane, exhibit the greatest divergence near surfaces; decane also imbibed the least. The diagram refers to the model which the enhanced viscosity is derived from: additional energy on fluid molecules near interfaces due to interactions with solid molecules.

6.5 PROPOSED SCALING OF MODELS

I propose a dimensionless number designated by the Greek letter Λ for the ratio of average surface forces acting over a meniscus (van der Waals, electrostatic, etc.) to bulk capillary forces in a representative conduit or pore size:

$$\Lambda = \frac{\overline{\Pi}_m}{P_c^m} \ . \tag{6.33}$$

When $\Lambda << 1$ the influence of surface forces is insignificant and the classic Young-Laplace equation is sufficient. When $\Lambda \approx 1$, a portion of the meniscus is still dominated by bulk values (constant curvature), but surface forces create non-negligible deformations in regions closer to solid interfaces. The classic Young-Laplace equation is insufficient for proper description of these menisci. Eq. (6.13) is applicable in this range and an effective contact angle can be found such as is presented in this work. Finally, in the case where $\Lambda >> 1$, surface forces are very significant and virtually no part of the meniscus exhibits constant curvature; i.e. the classic Young-Laplace equation fails. Eq. (6.15) is applicable for these channels and an average capillary pressure can be obtained with Eq. (6.19) where P_c^m is replaced by Π_f.

A considerable change in effective channel or pore diameter can occur due to elastocapillary deformation of solid and/or liquid crystal regions as well as adsorbed films. Likewise, an effective liquid viscosity, primarily a product of the decrease in channel area available for unhindered flow and potentially non-constant, must be considered instead of a bulk value when the deformed or initial diameter of nanoconfinements approach the length scale of solvation forces. A simple dimensionless index designated by the Greek letter Γ for assessment of the need to consider D_{eff} and μ_{eff}

is the ratio of the characteristic collapse length to the length of the media or the imbibition length of interest, namely,

$$\Gamma = \frac{l_c}{L} \ . \tag{6.34}$$

When $\Gamma \leq 1$, effective liquid viscosity should be considered. Calculations of l_c will vary between media; however, the equations for deformation along the axial direction have been found to be the same among fiber networks and solids with either spherical or cylindrical pores [204]. Recall that l_c is a function of the (average) pore or conduit size, specific surface area, fluid pressure, surface stress, and the bulk elastic properties of a media. Eq. (6.26) can also be used for dimensionless scaling of pore deformation effects when both sides of the equation are divided by $z(t)$.

Γ should be assessed first and if $\Gamma \leq 1$, then Λ be assessed at an effective pore diameter. Figure 6.7 shows a visual diagram of the dimensionless numbers and deformation regimes. Overall, $\overline{\Pi}_m$ and l_c are derived from available mineral and fluid properties: E, ν, ε, n, etc.

Ideally, if the transport of nanoscale liquids and menisci are governed by interfacial forces, reliable estimates of permeability to the liquid phase are a function of these influences. Thus, estimates can be achieved with knowledge of bulk media properties such as material composition or mineralogy, in situ or imbibing fluids, and average pore diameter, regardless of the specific local pore-network topology (such as that given by FIB-SEM, discussed in Chapter 7). Table B.2 of Appendix B displays diffusive and non-diffusive power law imbibition trends, extracted from literature data, in different nanoporous materials for various imbibing liquids and pore sizes.

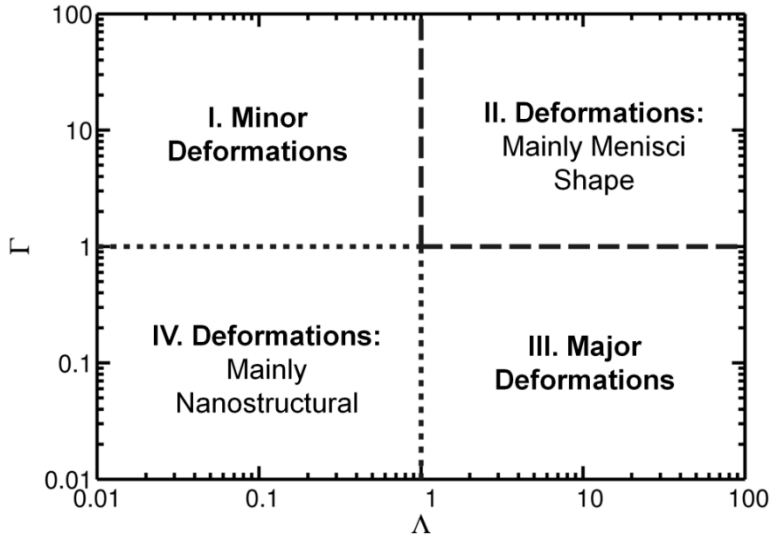

Figure 6.7. Conceptual diagram of the significance of the dimensionless numbers Λ and Γ. Researchers are encouraged to calculate estimates of Λ and Γ for their nanoporous media of interest. If the values fall in region I then menisci and elastocapillary deformations are minor or even negligible and conventional imbibition and multi-phase flow predictions should not falter. If the values fall in region II then the material is strong enough or relevant length of fluid travel is small enough that elastocapillary effects are small, but the effects of surface forces (depending on the solid and fluid types and pore sizes) on meniscus shape are significant. Likewise, if the values fall in region IV, nanostructural deformations are prevalent. In both of these regions some deviation from conventional imbibition and multi-phase flow predictions is anticipated. In region III major nanostructural and menisci deformations converge leading to a severe deviation from conventional imbibition and multi-phase flow predictions (such as seen in the data presented in this paper). These region-wise descriptions hold best the farther values are from the borders of a region.

6.6 CASE STUDY: ELASTOCAPILLARITY IN NANOPOROUS AGAROSE DISCS

Small agarose discs, 5 mm in diameter and 1 mm thick, were generated to demonstrate elastocapillarity in a three-dimensional (3D) nanoporous media. Agarose is a polysaccharide polymer gel that forms a nanoporous structure of relatively consistent

nanopore size upon gelation and is commonly used in DNA electrophoresis in the biomedical sciences due to the selectivity of this pore structure. The hydrogel's average pore size, d_{pore}, is directly related to the concentration of agarose powder, C, prepared in water and can be described by the following empirical equation [213]:

$$\bar{d}_{pore} = 140.7C^{-0.7} \ , \tag{6.35}$$

such that higher concentrations yield lower average pore diameters. Likewise, the porosity, ϕ, can be calculated by [214],

$$\phi = 1 - \frac{C}{\rho_{agarose}\omega_{agarose}} \ , \tag{6.36}$$

where $\rho_{agarose}$ is the dry agarose density and $\omega_{agarose}$ is the mass fraction of agarose in a network fiber. Agarose is highly porous; in this regard, agarose is not representative of shale. However, the consistent and tunable pore size distribution of agarose allows control of the geometric aspect of the experiments, a control not applicable with heterogeneous rock samples such as locally heterogeneous shale (complex geometry renders additional unknowns). Figure 6.8 displays an example of the 3D network geometries of agarose achieved by drying the sample with a critical point drier (CPD).

The 3D agarose structure is held together with hydrogen bonds and is hydrophilic and negatively charged (like shale/clay). Water, the wetting fluid, is held inside the agarose by capillary forces; however, the agarose will dehydrate as a function of time per storage conditions. An example of imbibition of sub-microliter surface droplets into hydrated agarose is displayed in Figure 6.9.

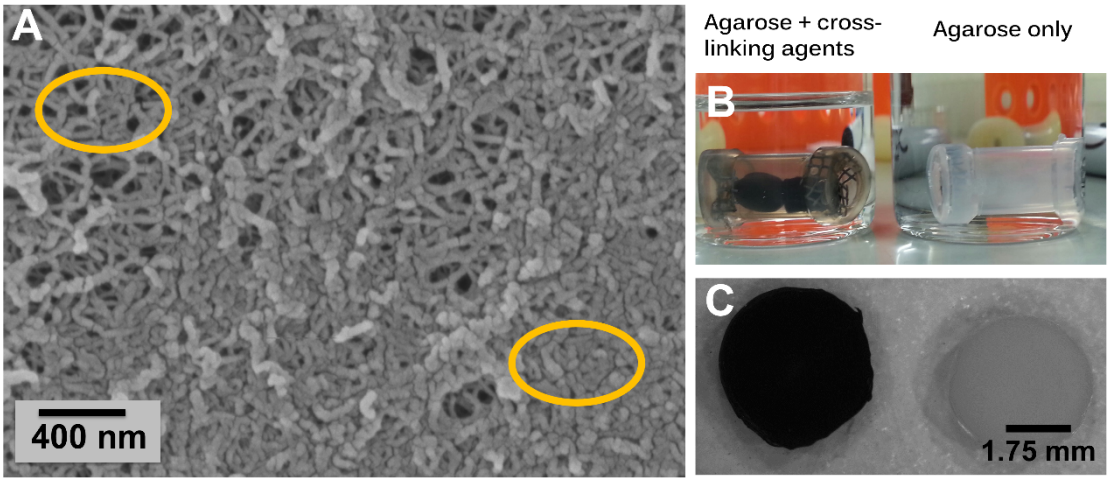

Figure 6.8: (A) High magnification SEM image (Detector = SE, AV = 5 kV, WD = 9.3 mm) of one of the agarose disks after critical point drying (CPD). Circles point out porous and collapsed regions. (B) Agarose disks, ~5 mm in diameter in their original state, are dehydrated in a series of ethanol treatments prior to CPD. Black discs were fixed with tannic acid and other additions to further crosslink the agarose (strengthen its structure). (C) Agarose discs after CPD demonstrate shrinkage.

In a small case study, 15 agarose disc samples were subjected to a series of standard ethanol dehydration treatments (to exchange the water in the samples with ethanol) followed by an exchange of the ethanol with liquid CO_2 in a Tousimis Samdri 790 CPD. The 5 mm discs were made of 2% agarose, corresponding to an average pore diameter of ~90 nm. Around half of the discs were fixed with tannic acid and other additions to further crosslink the agarose (strengthen its structure), and the remaining discs were left as plain agarose controls. After several liquid CO_2 flushes the sample chamber was raised to the pressure and temperature conditions of the CO_2 critical point and, ideally, the nanoconfined liquids transitioned from a liquid to a gas without the formation of menisci. A lack of menisci formation is desired to prevent elastocapillary collapse in the highly porous agarose. However, after CPD, the 15 agarose discs still

experienced a mean radial decrease of 27.58 +/- 2.23 % for the further fixed samples and 33.45 +/- 2.23 % for the plain agarose samples. In normal evaporation (air drying) conditions, the agarose completely collapsed and CPD-dried agarose collapsed upon imbibition. Such deformation is expected in a hydrogel, but bring up the question of the change in nanopore structure within relatively softer materials in shales such as clays and kerogen when samples are brought from the subsurface to ambient conditions; furthermore, shale samples imaged in SEMs are dehydrated and may reveal a different structure than their in situ topology.

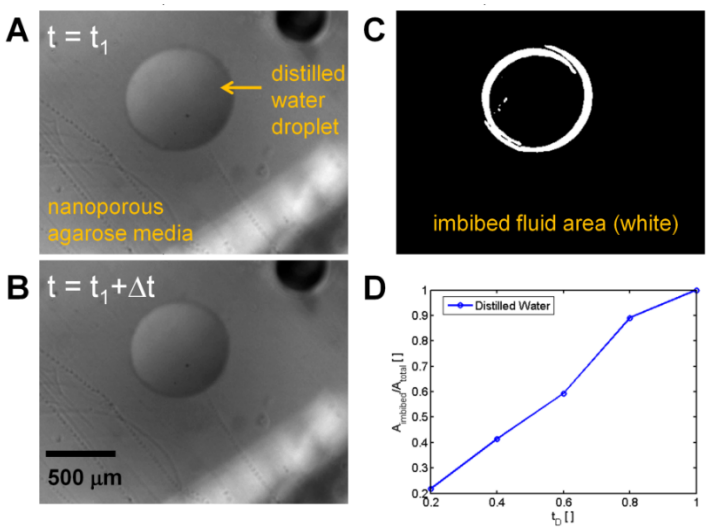

Figure 6.9: Example of imbibition of sub-microliter droplets into saturated agarose for distilled water. (A) One image in a series of droplet imbibition images. (B) The sequential image (Δt = 1 second). (C) The decrease in droplet area between the two images is computed with image analysis codes. (D) The change in droplet area with time (captured at 1 fps) translates to imbibition and is roughly linear in the case of a small droplet and highly porous material. The data example is presented on a normalized scale where $t_D = t/t_{final}$.

6.7 CONCLUSIONS AND RECOMMENDATIONS

An investigation into the mechanisms behind anomalous imbibition of various liquids in lyophilic 2D nanochannels revealed the need to consider the "deformation" of fluids and solids at interfaces. The major conclusions and contributions of the work are as follows:

- Macroscopic descriptions of imbibition are insufficient in fully nanoscale (2D) confinements because they do not consider menisci deformation due to long-range intermolecular forces and effective pore diameter due to pore space deformation by elastocapillarity and surface stresses and/or viscous films/layers. These effects were most prominent in the smallest nanochannels observed (30 nm × 60 nm).
- Liquids with low A_{232} and high absolute values of A_{123} imbibed the most effectively in the 2D nanochannels. The latter indicates that despite decreasing the effective channel diameter, precursor films may have a positive effect on nanoscale imbibition in such confinements.
- Phenomenological models for effective contact angle, effective diameter, and effective viscosity explain the nanofluidic data of this work and potentially the nanofluidic works of others.
- It was demonstrated that the Young-Laplace equation breaks down as a function of several parameters: channel diameter, Hamaker constants, the height of a prewetting film, and surface tension. The derivations are based on surface-force theories (the works of Derjaguin, Israelachvili, Langbein, Hamaker, Lifshitz, etc., all referenced herein), which conveniently enable molecular interactions to be described from a continuum perspective.

- The dimensionless ratio Λ, introduced herein, can be used to determine when the Young-Laplace equation is reliable, when a modified version of the Young-Laplace equation is required, or when the Young-Laplace equation is no longer applicable.
- Longitudinal elastocapillary deformations of a confinement are functions of channel or pore size, capillary and liquid pressure, specific surface area, position, and the bulk elastic properties of a media. A dimensionless ratio of the length of pore collapse to the length of interest of the media can be used to determine when elastocapillary effects are prominent and D_{eff} and μ_{eff} necessary.
- Overall, meniscus deformation and increases in effective viscosity are exacerbated by elastocapillary deformation, while elastocapillary deformation is exacerbated by negatively pressured and metastable liquids. These phenomena converge in the studied nanochannels to stymie imbibition and are likely in other nanoscale media.

We are all agreed that your theory is crazy. The question that divides us is whether it is crazy enough to have a chance of being correct.

Niels Bohr to Wolfgang Pauli, both Nobel laureates in Physics

CHAPTER 7: Nanoscale Digital Rock Physics with FIB-SEM – a Useful Complementary Approach to Nanofluidics?‡

…These electrons are focused down in size by the electron microscope lenses to impinge directly upon the surface of the metal. Will such a beam etch away the metal if it is run long enough? I don't know.

Richard Feynman, Nobel laureate in Physics
Hypothesizing nanolithography/milling techniques
a decade before their inception.
From his lecture *Plenty of Room at the Bottom* (1959)

Thus far in this dissertation nanoscale fluid flow has been studied experimentally with optical microscopy as a means to better understanding transport in shale. This chapter presents an independent but parallel study which investigates the usefulness of investigating nanoscale fluid flow in shale with digital rock physics (simulations) informed by slices of electron microscopy images from the FIB-SEM technique, which was introduced in Chapters 1 (Section 1.2) and Chapter 2 (Section 2.1).

Image-informed pore-scale models are useful tools for studying porous media: a debated question in shale pore-scale petrophysics is whether there is a representative elementary volume (REV) for shale models? Furthermore, if an REV exists, how does it differ among petrophysical properties? In this work three dimensional (3D) models of the topology of microscale shale volumes were obtained from image analysis of focused ion

‡ The material in this chapter was published under the following reference, which was completed under the supervision of Hesham El-Sobky, Carlos Torres-Verdín, and Matthew Balhoff. The FIB-SEM data was provided by ConocoPhillps and Sandia National Labs.

Kelly S, El-Sobky H, Torres-Verdín C, Balhoff MT. Assessing the Utility of FIB-SEM Images for Shale Digital Rock Physics. Advances in Water Resources. 2015. doi:10.1016/j.advwatres.2015.06.010.

beam-scanning electron microscope (FIB-SEM) image stacks. The utility of these models as a potential REV for shale is investigated in this chapter. The scope of data used in this study includes multiple local groups of neighboring FIB-SEM images of different microscale sizes, corresponding core-scale (milli- and centimeters) laboratory data, and, for comparison, series of two-dimensional (2D) cross-section SEM images, which capture a larger microscale field of view than the FIB-SEM images; this array of data is larger than the majority of investigations with FIB-SEM-derived microscale models of shale. Properties such as porosity, organic matter content, and pore connectivity are extracted from each model. Assessments of permeability with single phase, pressure-driven flow simulations are performed in the connected pore space of the models using the lattice-Boltzmann method. Calculated petrophysical properties are compared to those of neighboring FIB-SEM images and to core-scale measurements of the sample associated with the FIB-SEM sites.

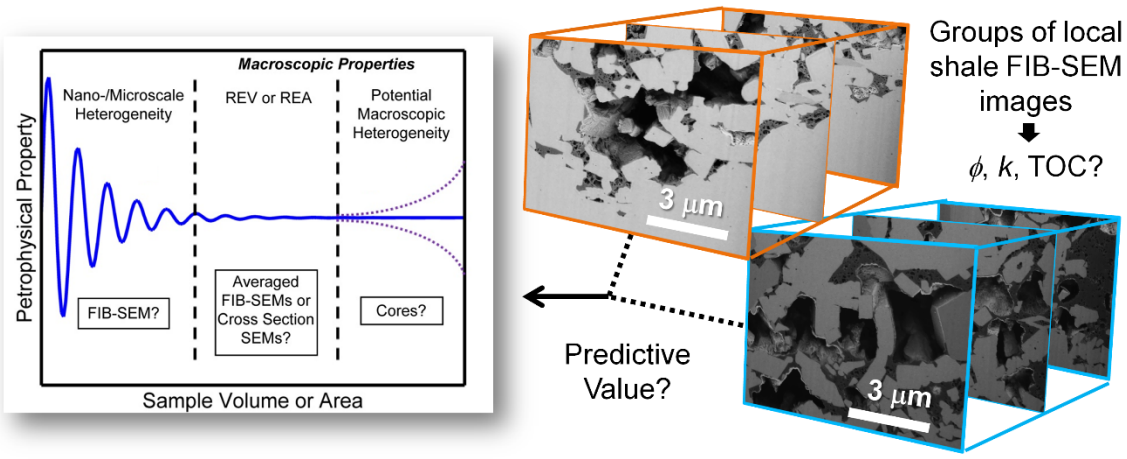

Figure 7.1: Depiction of the REV question for shale.

7.1 STUDY OBJECTIVES

This chapter seeks to address the following contentions to help determine whether or not FIB-SEM images are a suitable REV for quantitative study of shale:

- How do calculated petrophysical properties vary among groups of locally collected FIB-SEM images?
- How do the calculated petrophysical properties compare to core data from corresponding macroscopic samples?
- Do calculated petrophysical properties better converge among groups of locally collected FIB-SEM images of larger overall volume? How does the convergence of petrophysical properties among groups of BIB-SEM images, a 2D method, compare to that of FIB-SEM, a 3D method?
- There are many image analysis methods available for a pore, grain, and kerogen segmentation workflow. How sensitive are calculated petrophysical properties to the selection of a segmentation methodology?
- Which pores constitute the major connected pathways through the extracted pore-networks? What does this tell us about relevant transport mechanisms?
- Do some petrophysical properties (namely porosity and permeability) differ from core values because the volume of the 3D image is not suitable or because there are an abundance of pores below the resolution of SEM (Angstrom-size pores) that are not considered in the analysis?

7.2 OVERVIEW OF THE AVAILABLE DATA

The large amount of data uniformly analyzed at the microscale (at several local sites per sample) and core-scale for this study differentiates the analysis from many

investigations of shale FIB-SEM images (see a literature review in Section 2.1) and enables a basis of comparison for local heterogeneity and upscaling potential.

7.2.1 FIB-SEM data and corresponding core-scale data

Table 7.1 summarizes the FIB-SEM data used in this study and Figure 7.2 gives an example of an image slice from each image stack. Specific sample names and geologic formations of origin will remain anonymous. Instead, the nomenclature for the sample aliases is a letter followed by a number; for example, "A1". Image stacks sharing the same alphabetic label such as "A" come from the same local region of a sample. The numeric component of the labels corresponds to the selected FIB-SEM sites in the local region. Local in this context is defined as a distance within approximately 1 mm (see Figure D.4 in Appendix D for an example of image locality). Groups A and B come from the same well, identified as Formation 1/Shale Well 1, and are from samples approximately 30 meters apart in depth. Each of these groups contains 3-4 high quality, neighboring image stacks and the individual stacks each represent around 115 μm^3 of volume. Group D also comes from Formation 1, but from a different well, and Group C comes from a different formation and well altogether. The image stacks in Groups C and D cover approximately 5000 μm^3 of volume, a much larger microscale domain. Additionally, the images in Groups A and B capture a higher resolution microscopic shale volume than the images in Groups C and D, which were obtained with a different FIB-SEM instrument. Note that sample D1 is the only sample in Group D, but is comprehensively analyzed because it was the highest quality of the domains with larger microscale volumes, where each stack contained 2000 images.

The images for Groups A and B were acquired with an FEI Company Helios NanoLab dual beam FIB-SEM, an instrument with the potential for sub-nanometer

resolution. The acquisition parameters included high vacuum mode, an accelerating voltage of ~1 kV, a working distance of ~3 mm, and an ion beam current of ~400 pA for precision milling. The images for Groups C and D were acquired with an older model FEI Company dual beam FIB-SEM. The acquisition parameters included high vacuum mode, an accelerating voltage of ~2 kV, a working distance of ~4 mm, and an ion beam current of ~40-80 pA (much lower than that of Groups A and B). The Everhart-Thornley detector (ETD) was used for Groups C and D, while a circular backscatter detector (CBS) was used for Groups A and B. A brief discussion on the difference between SEM detectors is provided in Appendix D. All stacks were acquired with an automatic "slice and view" package and a sample tilt of 52˚ and milled with Gallium ions.

Standard core analysis data were acquired from each core associated with a group of FIB-SEM images. The relevant core data available for Groups A-D include Gas Research Institute (GRI), X-ray diffraction (XRD) data, LECO TOC, and Rock Eval Pyrolysis. GRI data includes: "as received" bulk density, matrix permeability, gas-filled porosity, and gas saturation; and dry and Dean Stark (extracted conditions) grain density, matrix permeability, porosity, oil saturation, and water saturation. XRD identifies and quantifies the crystalline components of a (powdered) shale sample on a relative percentage basis and thus is not helpful for evaluating organic matter, which is non-crystalline. The LECO TOC method, named after the LECO brand carbon analyzer, provides a reliable value of TOC by measuring the amount of carbon produced upon combustion of a powdered, dry sample. Results are delivered in weight percent as the weight of combusted carbon over the original weight of the dry sample. Values of organic matter (or kerogen) density and the mass fraction of carbon in kerogen are needed to convert to volume percent; a kerogen density of 1.3 g/cc and a carbon mass

fraction of 0.80 (a typical value for mature kerogen) are assumed throughout this analysis. Rock Eval Pyrolysis was used to measure the maturity of the organic matter and yields the normalized amounts of free hydrocarbons in the sample (S_1), hydrocarbons formed by pyrolysis of kerogen (thermal cracking) (S_2), and CO_2 released during breakdown of kerogen (S_3), as well as the temperature at which the maximum thermal cracking occurs (T_{max}). In addition to these standard core measurements, ultraviolet (UV) and fluorescent microscopy mapping of a thin section impregnated with Rhodamine B dyed epoxy were performed for the Group C sample. The core data is summarized in tabular form in Tables 7.2 and 7.3; permeability is presented in the unit of milliDarcy (mD), as is commonly used for porous media applications. One mD is equal to 9.87×10^{-6} m^2.

Overview of analyzed FIB-SEM images.

Group	Formation identifier	Well identifier	Alias	Image size: x, y, z (pixels)[a]	Resolution x, y, z (nm/pixel)	Image quality description	Cropped domain size: x, y, z (pixels)[b]
A	Formation 1	Shale Well 1	A1	1989 × 1313 × 350	5, 5, 7	Excellent	1989 × 1313 × 350
A	Formation 1	Shale Well 1	A2	1795 × 1310 × 349	5, 5, 7	Excellent	1750 × 799 × 349
A	Formation 1	Shale Well 1	A3	1996 × 1406 × 348	5, 5, 7	Excellent	1996 × 1364 × 348
B	Formation 1	Shale Well 1	B1	2016 × 1401 × 347	5, 4, 5	Excellent	1952 × 1389 × 347
B	Formation 1	Shale Well 1	B2	2096 × 1310 × 288	4, 4, 5	Excellent	1745 × 748 × 288
B	Formation 1	Shale Well 1	B3	2001 × 1312 × 328	4, 4, 5.5	Excellent	1655 × 990 × 328
B	Formation 1	Shale Well 1	B4	1961 × 1337 × 285	4, 4, 4	Excellent	893 × 649 × 285
C	Formation 2	Shale Well 2	C1	940 × 820 × 2000	15.6, 15.6, 10	Good; some pore edge effects	877 × 411 × 2000
C	Formation 2	Shale Well 2	C2	854 × 780 × 2000	15.6, 15.6, 10	Acceptable; lighting/contrast issues, charging	853 × 665 × 1502
C	Formation 2	Shale Well 2	C3	978 × 820 × 2000	15.6, 15.6, 10	Acceptable; lighting/contrast issues, charging	978 × 596 × 2000
C	Formation 2	Shale Well 2	C4	926 × 790 × 2000	15.6, 15.6, 10	Acceptable/poor; very dark images makes kerogen/pore differentiation challenging	558 × 631 × 2000
D	Formation 1	Shale Well 3	D1	885 × 581 × 2000	15.6, 15.6, 10	Very good	427 × 581 × 1047

[a] After image alignment and alignment-based cropping steps.
[b] Stacks are further cropped to enclose the largest connected network(s) in the x, y, and z directions prior to LBM simulations.

Table 7.1: Overview of analyzed FIB-SEM images.

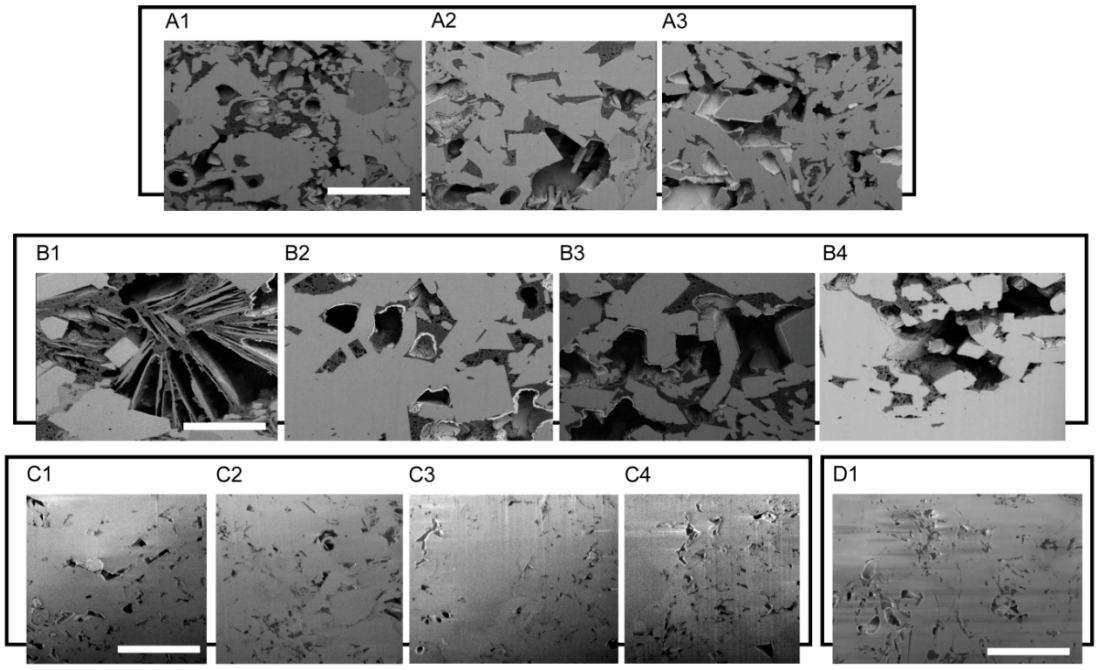

Figure 7.2: Examples of single images from each analyzed FIB-SEM stack. Scale bars for each group are as follows (the scale is approximately the same from stack to stack within a group): A = 3.3 μm, B = 2.9 μm, C = 5.9 μm, and D = 4.8 μm. Note that images from Groups A and B are of superior quality, but that images from Groups C and D offer a larger field of view. Group C and D image stacks were provided by Sandia National Labs (Albuquerque, NM) and the other images were provided by ConocoPhillips.

GRI core data corresponding to FIB-SEM images.

Group/ sample	As received core			
	Bulk density (g/cm^3)	Matrix permeability (mD)	Gas-filled porosity (%)	Gas saturation (%)
A	2.381	5.04E−06	6.42	58.1
B	2.354	4.34E−05	10.86	83.5
C	2.61	1.50E−04[a]	4.30	40.5
D	2.381	1.20E−05[a]	5.15	46.5

Dry core (Dean–Stark extraction)				
Grain density (g/cm^3)	Matrix permeability (mD)	Porosity (%)	Oil saturation (%)	Water saturation (%)
2.629	9.36E−04	11.05	18.8	23.0
2.682	1.04E−04	13.01	5.1	11.4
2.69	–	7.9	41.3	18.2
2.620	–	11.07	35.2	18.3

[a] Pressure transient tests were performed on whole cores plugs (not crushed plugs) for these samples.

Table 7.2: GRI core data corresponding to FIB-SEM images.

TOC core data corresponding to FIB-SEM images.

Group/sample	LECO TOC (wt.%)	S1 (mg/g)[a]	S2 (mg/g)	S3 (mg/g)	T_{max} (°C)
A	4.768	7.11	3.57	0.8	469
B	0.839	1.27	0.36	0.28	463
C	1.29	3.20	5.12	1.13	436
D	3.46	13.85	5.91	0.51	460

[a] mg of hydrocarbon/g of rock.

Table 7.3: TOC core data corresponding to FIB-SEM images.

7.2.2 BIB-SEM data and corresponding core-scale data

High resolution 2D microscale images covering a field of view area over ten times larger than a FIB-SEM image slice were acquired with Broad ion beam SEM images (BIB-SEM) for samples from 9 different depths in Formation 1/Shale Well 1, labeled Groups E-M. Specifically, 10 2D images of areas approximately ~770 μm^2 were obtained for each sample, resulting in almost 8000 μm^2 of shale area coverage per BIB-smoothed sample face. The variation in geometric petrophysical properties for these images were assessed to compare their utility to that of FIB-SEM images. The BIB-SEM images were taken with a Zeiss SEM with both ETD and backscattered electron (BSE) detectors and acquisition parameters included high vacuum mode, an accelerating voltage of ~1 kV, and a working distance of ~4-5 mm. Argon ions were used in a separate milling process performed prior to imaging, as opposed to Gallium ions used *in situ* during FIB-SEM imaging. Details on the BIB-SEM preparation procedure are available in the literature [11], [45], [215], and [216]. Tables 7.4-7.6 present descriptions of the 2D cross-section SEM images and their corresponding core data, which was acquired in a similar manner as the core data corresponding to the FIB-SEM images. Figure 7.9 shows examples of some of the BIB-SEM images.

Overview of analyzed 2D BIB-SEM cross-section images.

Group/sample	Formation identifier	Well identifier	Aliases	Image sizes x, y, z (pixels)[a]	Resolution x, y (nm/pixel)	Image quality description
E	Formation 1	Shale Well 1	E1–E10	3072 × 3502 × 1	10, 10	Excellent
F	Formation 1	Shale Well 1	F1–F10	3072 × 3502 × 1	10, 10	Excellent
G	Formation 1	Shale Well 1	G1–G10	3072 × 3502 × 1	10, 10	Excellent
H	Formation 1	Shale Well 1	H1–H10	3072 × 3502 × 1	10, 10	Excellent
I	Formation 1	Shale Well 1	I1–I10	3072 × 3502 × 1	10, 10	Excellent
J	Formation 1	Shale Well 1	J1–J10	3072 × 3502 × 1	10, 10	Excellent
K	Formation 1	Shale Well 1	K1–K10	3072 × 3502 × 1	10, 10	Excellent
L	Formation 1	Shale Well 1	L1–L10	3072 × 3502 × 1	10, 10	Excellent
M	Formation 1	Shale Well 1	M1–M10	3072 × 3502 × 1	10, 10	Excellent

[a] After image alignment and cropping steps.

Table 7.4: Overview of analyzed 2D BIB-SEM cross-section images.

GRI core data corresponding to 2D BIB-SEM cross section images.

Group/ sample	As received core			
	Bulk density (g/cm^3)	Matrix permeability (mD)	Gas-filled porosity (%)	Gas saturation (%)
E	2.427	5.96E−06	5.87	51.2
F	2.446	5.27E−06	5.11	54.1
G	2.409	7.35E−06	6.25	52.1
H	2.301	6.35E−06	7.71	54.1
I	2.645	9.26E−10	0.69	23.0
J	2.540	9.59E−07	3.46	59.8
K	2.485	1.92E−07	4.27	55.5
L	2.482	1.13E−07	1.77	23.5
M	2.421	3.88E−06	6.21	56.7

Dry core (Dean–Stark extraction)				
Grain density (g/cm^3)	Matrix permeability (mD)	Porosity (%)	Oil saturation (%)	Water saturation (%)
2.682	5.86E−04	11.48	18.7	30.2
2.659	1.71E−04	9.43	26.2	19.7
2.675	6.63E−04	11.99	15.4	32.5
2.617	1.32E−03	14.25	29.6	16.3
2.703	2.68E−06	2.99	9.1	67.9
2.673	5.33E−06	5.78	12.5	27.7
2.661	1.97E−05	7.70	36.4	8.2
2.629	2.80E−04	7.55	43.5	33.0
2.667	2.06E−03	10.95	8.0	35.3

Table 7.5: GRI core data corresponding to 2D BIB-SEM cross-section images.

TOC core data corresponding to 2D BIB-SEM cross section images.

Group/sample	LECO TOC (wt.%)	S1 (mg/g)[a]	S2 (mg/g)	S3 (mg/g)	T_{max} (°C)
E	2.888	4.98	3.14	0.37	413
F	3.037	5.06	2.32	0.53	463
G	4.175	6.020992	3.89	0.66	462
H	4.886	9.96	5.78	0.86	452
I	0.383	0.733668	0.27	0.45	367
J	1.634	3.401163	1.06	0.58	451
K	2.231	4.657676	1.49	0.73	452
L	4.412	8.979187	3.93	0.7	467
M	4.043	7.490119	3.42	0.71	468

[a] mg of hydrocarbon/g of rock.

Table 7.6: TOC core data corresponding to 2D BIB-SEM cross-section images

7.2.3 Core-scale data acquisition procedures

Even though core data are used as a basis of comparison in this study, it should be noted that there are errors intrinsic to any sample analysis method and propagation of errors when a value is based on several measured quantities; i.e., porosity. Additionally, remnants of water, carbonate, and sulfur compounds not properly removed prior to LECO TOC analysis can lead to exaggerated TOC values. Standard core analysis protocols were followed for laboratory analysis of the core samples described herein. "As received" samples were stored in airtight vials and ambient exposure time was kept at a minimum during sample preparation. Samples were considered "dry" when they reached an equilibrium weight after being subjected to an oven at 110 ˚C for at least a week after fluid extraction (Dean-Stark method). Permeability on both "as received" and dry samples was determined with a transient pressure decay test performed on a crushed and

sieved sample of shale or a whole core plug, 1 inch in diameter and 1.5 inches in length (permeability measurements for Samples C and D were made on core plugs). Porosity was indirectly determined by measuring grain volume of the sample after fluid extraction with the Boyle's Law method (with helium), the weight of the sample before fluid extraction, and the bulk volume of the sample before fluid extraction with mercury intrusion.

7.2.4 Image artifacts

Image artifacts present challenges in the image analysis process. Potential physical artifacts associated with FIB-SEM shale images are due to the influence of the ion beam on the sample. In heterogeneous materials, different materials will mill at slightly different rates, leading to potential unevenness of the imaged surface. Furthermore, the possible creation (opening) or destruction (smoothing) of smaller pores on account of the intense ion beam remains an open question. Non-physical artifacts associated with SEM shale images, including FIB-SEM and BIB-SEM, include topography-induced contrast and charging. Pore edges and the edges of raised or depressed regions are non-planar surfaces and give off a greater electron signal than planar areas of the imaged face. As such, these areas will result in brighter pixels. A similar concept applies when the milled shale face is slanted. Charging occurs when electrons accumulate on the sample due to lack of a conductive path and is evident by nonphysical streaks, extremely bright areas, and warping of the image. Another major challenge inherent to shale SEM image analysis is proper identification of pores from kerogen ("kerogen" is synonymous with "organic matter") and in some cases, even the grain material. Relatively smaller pores, mainly in the organic matter and on the order of tens of nanometers and less, correspond to pixels of a variety of darker shades which

depend on the amount of electron signal the pore generates; shallow pores in the kerogen pores can still generate electron signal. Larger micron-sized pores reveal their interior surfaces such that they become 3D cavernous features on a 2D surface that is intended to be interpreted as a 2D slice. Additionally, these pore interiors are composed of an array of different pixel tones, which makes pore differentiation based on simple grayscale value histogram thresholding techniques insufficient.

Figure 7.3 displays examples of the aforementioned artifacts from the image data used herein. In panel A Pore edges (lower arrow) appear brighter than the surrounding grains and kerogen. This artifact makes it difficult for a computer program to distinguish what material borders a pore. The top two arrows point to a kerogen patch (left) and shallow pore (right). These distinctions can be made with the human brain but a computer will most likely interpret the dark kerogen patch as a pore. Panel B displays "Curtaining," a physical artifact due to the ion beam. Panel C shows image warping and streaks due to electron charging. Panel D features an ion-milled surface (top square) in contrast to a mechanically milled one; how are pores and throats affected by the beam? Panel E shows an example of a complex pore (in the square) made out of clay-platelets. Because the pores between the clay are an array of different grayscale values typical thresholding is not sufficient. From left to right, the first arrow points out an area of electron beam damage due to focusing and the second arrow shows an example of BSE brightness in a pyrite framboid due to atomic number contrast. Finally, panel F displays another example of a complex 3D pore, composed of many grayscale tones. In the same 2D plane there are pores that are nearly black (thus, 2D); these pores are easily identified. The higher the image magnification the greater the visibility of organic matter pores (for example, many kerogen pores are visible in the square region).

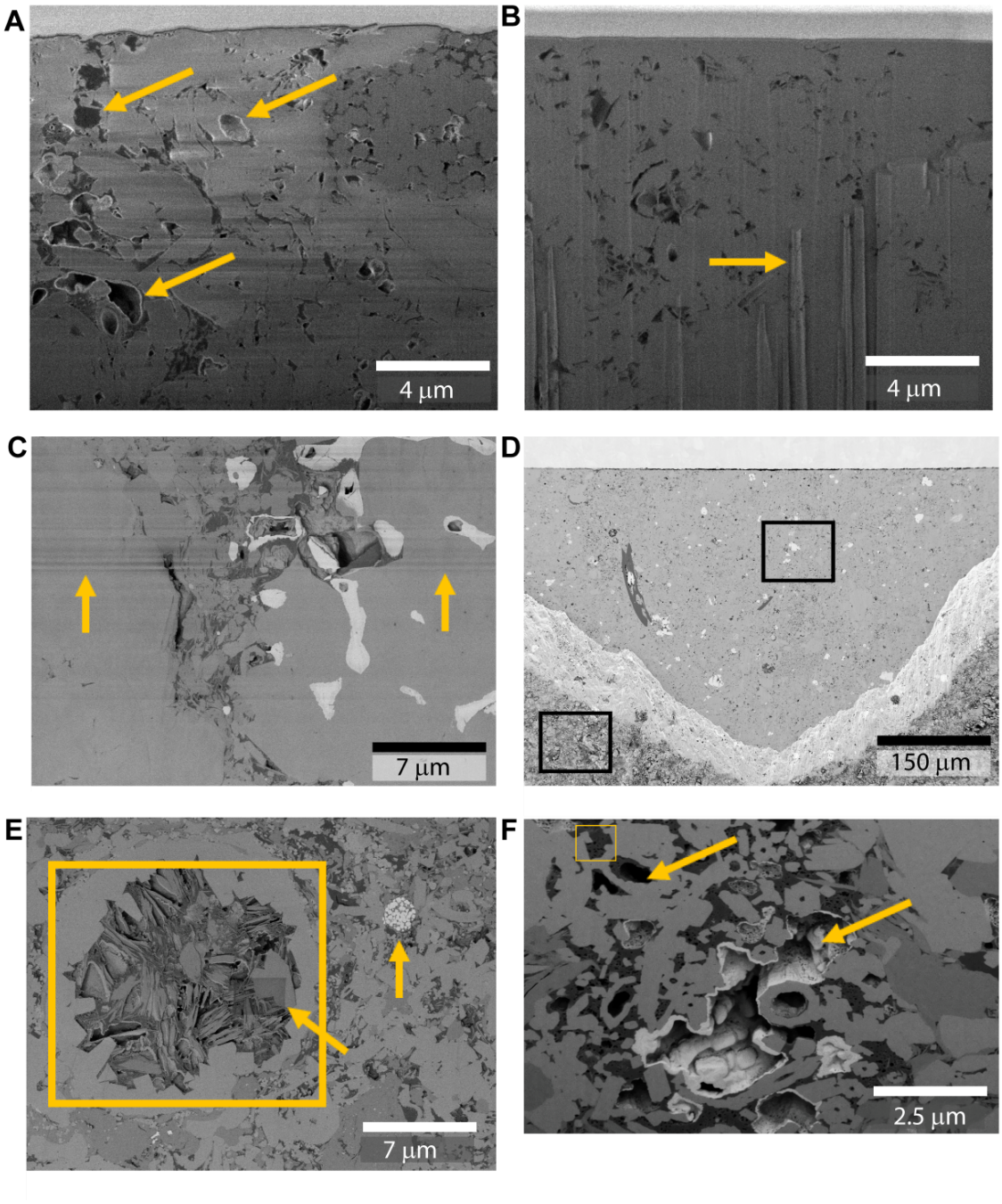

Figure 7.3: Examples of physical and non-physical image artifacts in SEM images. Images were provided by Sandia National Labs (Albuquerque, NM) and ConocoPhillips.

7.3 IMAGE PROCESSING METHODS

Due to the aforementioned image artifacts and the spectrum of grayscale values associated with large pore features, the image analysis process of shale FIB-SEM images is nontrivial, even for high quality FIB-SEM images. Rigorous image processing was employed to calculate the 3D shale images' porosity, kerogen, and crystalline-matrix volumes and the respective relative pore surface areas of these components.

7.3.1 Workflow

The FIB-SEM image analysis was performed with a combination of the open-source image processing program ImageJ/Fiji (National Institutes of Health) for pre-processing and MATLAB scripts for segmentation and post-processing. A Linux machine with 12 cores (2.9 GHz), 25 GB of RAM, and a Quadro 4000 graphics card was used for the image analysis. The processing time required was, on average, 5 hours per single FIB-SEM image stack: around 1 hour in ImageJ and around 4 hours in MATLAB. The main pre-processing steps performed in ImageJ include, in sequential order: linear stack alignment with an affine Scale Invariant Feature Transform (SIFT) algorithm [217]; cropping of the aligned stack; noise reduction (smoothing) with a 3D median filter (note that a 3D nonlinear means filter also works well); and streak removal and background normalization with the application of a bandpass Finite Fourier Transform (FFT) filter. The same pre-processing workflow was uniformly applied to each stack of images, with the exception of the bandpass FFT filter, which was only applied to image stacks from Groups C and D (due to uneven contrast and streaks). Subsequently, a fuzzy logic, c-means centroid search "soft thresholding" (membership-function based) was implemented in MATLAB for image segmentation (identification of pores, kerogen, and crystalline matrix) [218]. The soft thresholding segmentation process was uniformly

applied to each stack of images. However, another segmentation method was explored for comparison: histogram-based thresholding with implementation of level set method contours to capture large multi-colored pores [219]. After segmentation, the resulting 3D matrix was composed of three numbers which represent whether the voxel represents pore, kerogen, or crystalline space. An "edge-finder" script was then applied using MATLAB which assigns the surface area of the pore as either a "kerogen-pore" or "matrix-pore" boundary; the respective boundary voxels are assigned unique numbers as well. A speckle filter was also applied to remove void spaces 1 pixel in volume, which are generally isolated and meaningless in LBM simulations. Pore-boundary identifications are useful for identification of the percentage of kerogen and crystalline pore surfaces and for specification of specific pore wall boundary conditions during LBM flow simulations, especially in multi-phase flow where wettability considerations must be made. Finally, our MATLAB code calculates the 3D image's porosity, kerogen and matrix volumes and their relative pore surface areas (that is, "grain pores" versus "kerogen pores"), the pore-size distribution (see Figure D.2 in Appendix D for an example), and the number of independently connected pore mini-networks.

The 3D image was then "cropped" such that there was connected pore space along all three rectangular coordinate directions (see Table 7.1 for the difference between pre-processed and cropped images). First, the 3D volume was binarized into pore space and non-pore space to determine the cropped volume. Then the number of connected objects (independent pore networks) in 3D and their locations and connected lengths in the x, y, and z directions are found with the functions *bwconncomp* and *regionprops* from MATLAB's Image Processing Toolbox. The excerpt of our image analysis script that applies to this method is provided in Appendix D. The FIB-SEM volume was cropped to

the longest of the identified pore space lengths in x, y, and z directions and it was ensured that cropping in one direction does not cut off the connected pathway of another direction by finding the connected objects after each subsequent cropping step. The nature of this method ensures connectivity along all three rectangular coordinates, but does not stipulate the robustness of the connectivity (i.e. the connected path can potentially be as small as one pore-voxel at any location including the boundary planes) or that the connected paths are the same three dimensional object. Figure 7.5 displays examples of the cropped FIB-SEM images. The rectangular volume housing the largest connected network(s) was then written as a data file in the input structure necessary for subsequent fluid flow simulations. The size of the data file for each processed and cropped data set was 1-2 GB. Figure 7.4 displays an overview of the image analysis workflow. The entire stack of image slices and their corresponding segmentation results are visually compared at the end of the image analysis process for quality assessment and control. Note that the BIB-SEM images were analyzed independently by the vendor that acquired the images, but were also subject to a uniform application of an image analysis workflow and quality assessment and control.

7.3.2 Sensitivity to segmentation methods

Table 7.7 compares the results of two segmentation methods, histogram thresholding with level set method and soft thresholding, within FIB-SEM stack D1. Based on this comparison, the image analysis process is most variable in terms of distinguishing between kerogen and pores and identifying whether a pore boundary is organic or crystalline. The level set contours, as implemented in this example, successfully captured complex pores, but caused the boundaries of many kerogen pores to grow beyond their physical boundaries until they touched crystalline material. Both

methods render smaller porosity values than the core data and limited pore connectivity. However, the soft thresholding method provided larger pore connectivity than the histogram thresholding and level set contours. Kerogen connectivity extends across the entire domain in both cases. Following inspection of the resulting segmented image stacks from each method it was selected to use soft-thresholding for image segmentation in the FIB-SEM groups.

Comparison of image analysis methods performed on FIB-SEM location D1[a].

Property	*Option A*: histogram thresholding + level set method	*Option B*: soft thresholding	Core data
Total porosity (%)	3.53	2.51	5.15[b], 11.7[c]
Kerogen (vol.%)	4.55	6.66	6.97[d]
Crystalline (vol.%)	91.92	90.83	87.88
Kerogen pore surface area (% of total surface area)	25.46	81.55	–
Crystalline pore surface area (% of total surface area)	74.54	18.45	–
Pore surface area to volume ratio	0.828	0.875	–
No. of independently connected objects	24,823	19,907	–
Largest *pore* connectivity in *X*-dir	581 voxels	581 voxels	–
Largest *pore* connectivity in *Y*-dir	209 voxels	426 voxels	–
Largest *pore* connectivity in *Z*-dir	734 voxels	1046 voxels	–
Largest *kerogen* connectivity in *X*-dir	581 voxels	581 voxels	–
Largest *kerogen* connectivity in *Y*-dir	855 voxels	855 voxels	–
Largest *kerogen* connectivity in *Z*-dir	1967 voxels	1997 voxels	–

[a] Matrix size: 581 × 855 × 1997 pixels (992,019,735 voxels).
[b] "As received" core.
[c] Dry core.
[d] From LECO TOC.

Table 7.7: Comparison of image analysis methods performed on FIB-SEM location D1*.

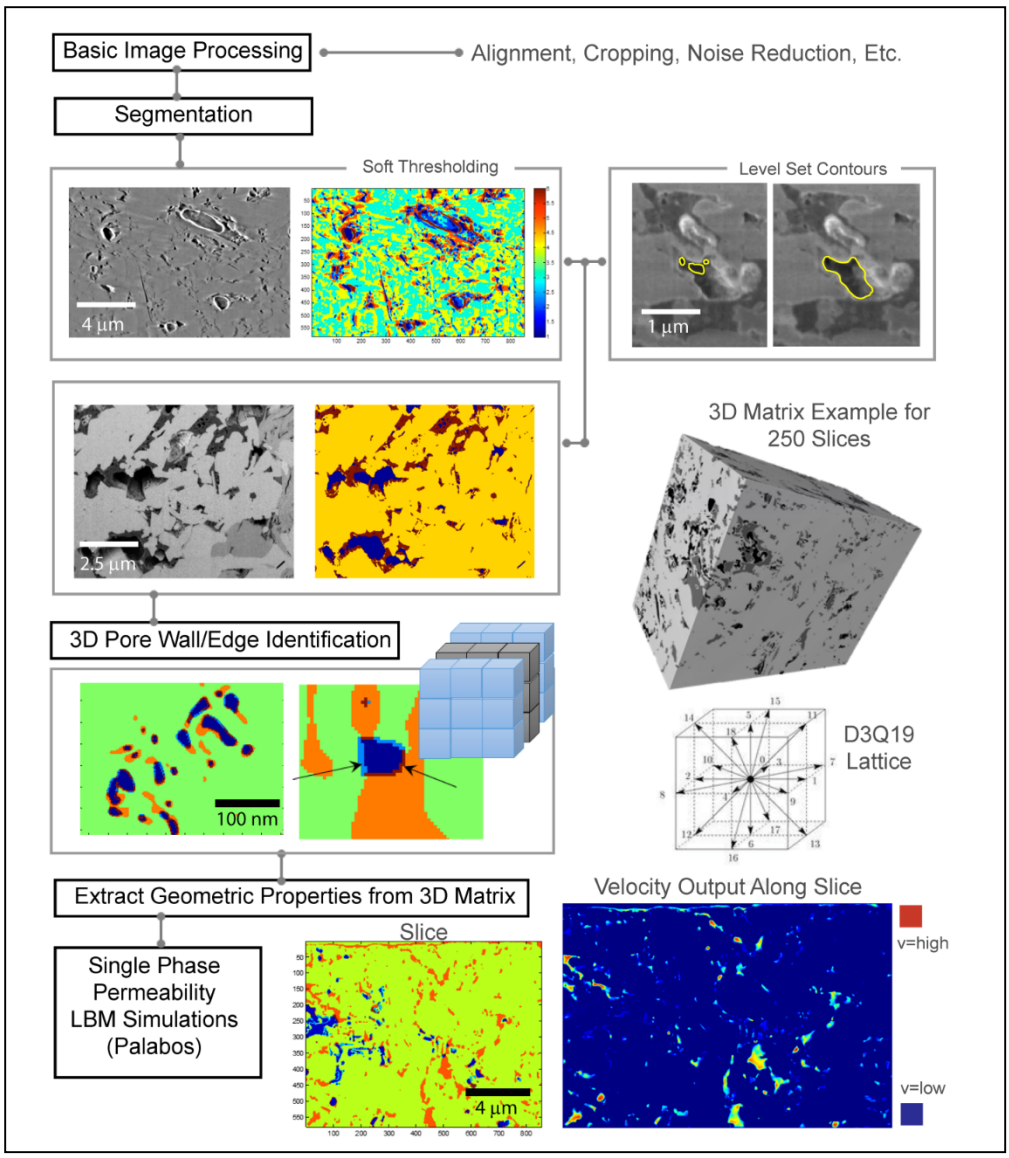

Figure 7.4: Major components of the image analysis workflow. In the segmentation process, 6 feature types, from darkest to lightest tones, are identified with soft thresholding, but features 3+ are all considered to be crystalline matrix (feature 1 is considered to be pores and feature 2 is considered to be kerogen). Level set method contours are an option used to capture complex pores. In the pore-boundary identifications, dark blue voxels are pores, light blue voxels are pore-crystalline boundaries, and red voxels are pore-organic boundaries. In the example LBM velocity output slice the kerogen and pore space were both designated as flow paths for visualization purposes only.

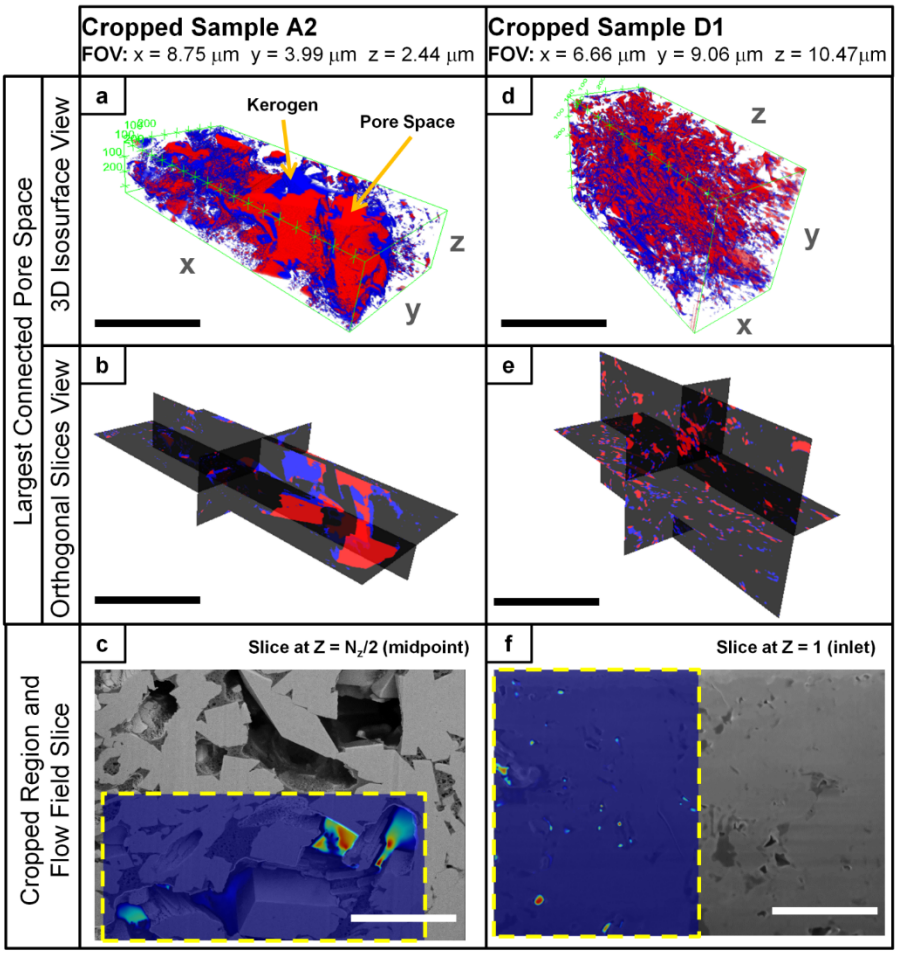

Figure 7.5: Examples of cropped domains whose pore networks are connected along the *x*, *y*, and *z* directions for samples at different fields of view (FOV): A2 and D1. The 3D isosurface views are crowded, but give a sense of the spatial distribution of pores (red) and kerogen (blue) at different FOVs. The orthogonal slices give a sense of the limited connectivity along single planes: connectivity appears mainly in isolated clusters and only a few large pores dominate the connected paths for Sample A2. The bottom panels show the cropped regions for the two samples in the *x*-*y* plane against the size of the image after pre-processing. The LBM *z*-direction velocity field (pressure drop in the *z*-direction) is superimposed against the images; the speed of the flow field is represented by color intensity where the dark blue equates to no flow and the bright red equates to the fastest velocities. Many of the kerogen pores are very small and/or isolated from the prime flow paths and, thus, show little or no flow. Scale bars: (a) 3.9 μm, (b) 7.5 μm, (c) 3.9 μm, (d) 7.5 μm, (e) 3.3 μm, (f) 4.5 μm.

7.4 FLUID FLOW SIMULATIONS WITH THE LATTICE-BOLTZMANN METHOD

The lattice-Boltzmann method (LBM) was implemented to simulate fluid transport in the extracted shale pore space and estimate permeability. An overview of LBM and an explanation of why it is appropriate for FIB-SEM fluid flow simulations are included in Appendix D. Single phase, single component (SPSC) LBM flow simulations on a D3Q19 lattice were applied on the largest connected pore space extent using the open-source LBM library Palabos, [220] which is written in C++. A bounce-back boundary condition was applied at the pore walls and fixed pressure gradient, Δp, was held between the inlet and outlet planes. The velocity field was initially zero and particles are actuated via a linear pressure drop between the inlet to outlet [221]. Open boundaries are padded with walls (non-periodic) and a single relaxation time of $\tau = 1$ was used. The simulation was determined to be at steady-state when the standard deviation of the average energy over 1000 timesteps falls below a dimensionless value of 10^{-4} [221]. Once the simulation reaches steady state, permeability, k, was determined with Darcy's equation,

$$k = \overline{u}\frac{\mu L}{\Delta p} \tag{7.1}$$

where μ is fluid viscosity, L is the length of the 3D volume along the direction of the pressure drop, and $\overline{u}$ is the average of the velocity in the pore space voxels, using the velocity component in the direction of the pressure drop. Figure D.1 of Appendix D displays a verification of the implemented LBM code by comparison of the simulation results for the velocity field in a rectangular conduit of dimensions $w \times h \times L$ against the corresponding Poiseuille analytical solution.

Verification in a simple geometry infers that the LBM code correctly simulates viscous, pressure-driven fluid flow, but does not necessarily imply that the LBM code

correctly captures the single phase permeability of the interpreted FIB-SEM images. There are many chemical and physical phenomena at play during single phase flow of liquids and gases at the nanoscale including, but not limited to: chemi- and physisorption, electrostatic effects, disjoining pressure, diffusion (Fickian and Knudsen), thin wetting films, slip (for lyophobic surfaces), and boundary layers (for lyophilic surfaces). The permeability obtained with LBM simulations performed herein is *geometric* permeability, meaning that only the geometry of the identified pore space itself influences the fluid flow. The dimensionless Knudsen number, *Kn*, for the average organic matter pore diameters in the FIB-SEM images, around 20 nm - 500 nm, ranges from 0.35 - 0.01 when calculated for helium at a temperature of 25˚C and a pressure of 200 psig (GRI permeability fluid and measurement conditions). These *Kn* numbers translate to, respectively, transition diffusion between Knudsen diffusion and slippage (but still viscous) flow regimes [222]. Many of the pores which constituted the connected flow pathways in the analyzed FIB-SEM datasets were intercrystalline or intergranular pores (often adjacent to kerogen) on the order of a micron. When a temperature of 100˚C and a pressure of 4000 psi, shale reservoir-like conditions, are considered for methane, *Kn* ranges from 0.02 - 0.0006 for pore diameters from 20 nm - 500 nm and there are, theoretically, less non-Darcy effects for gas flow in the pore-space; *Kn* numbers for liquids in the range of nanopores theoretically fall in the Darcy flow regime under all conditions since the mean free path of the liquid molecules is on the order of their tight intermolecular spacing.

It is expected that the geometric permeability value may underestimate gas permeability at low pressure conditions (i.e. GRI permeability acquisition) because it does not take into account slip flow and Knudsen (and Fickian) diffusion through the

pore space and kerogen [223], [44], and [224]; however, it is expected that the geometric permeability may overestimate liquid permeability because liquid flow can be stymied by boundary layer effects [182] and matrix swelling.

The fluid properties of methane ($\rho = 0.66$ kg/m^3, $\mu = 2 \times 10^{-6}$ kg/(m·s)) and small pressure drops of the order of 10^{-1} bar were used for the LBM simulations featured herein. It is often necessary to use small pressures in LBM simulations because LBM works best at lower velocities [225]; this restriction is inherent because the expansion of LBM's equilibrium distribution function is based on the assumption of small Mach numbers (less than 1). Simulations usually took several thousand dimensionless time steps to reach steady-state, which, corresponds to a fraction of a second when converted to real units with the physical parameters of the domain.

LBM fluid flow simulations are computationally expensive: a 900 million voxel 3D matrix, the smaller of the image matrices analyzed herein (without cropping), can equate to a four dimensional matrix of around 17 billion data points because each voxel has 19 nodes in LBM's D3Q19 lattice. However, Palabos is written to run efficiently with large datasets and in a parallel computing environment via a multi-block structure [220]. Time-memory requirements render it virtually impossible to run LBM fluid flow simulations for such large 3D matrices on a single core CPU without considerable grid coarsening. When coarsening interpreted 3D images to aid in computer memory issues one must be aware of the fact that many of the smaller pores captured are on the order of several pixels and can be lost during grid coarsening. No grid coarsening was performed in this analysis; the fluid flow simulations were executed in parallel on a Linux computer cluster environment. Regarding time-memory requirements, on 288 cores (24 nodes, 48 GB/node) a single phase fluid flow simulation in one of the FIB-SEM images typically

reached steady-state in around 45 minutes or less and took around 3.5 hours to reach steady-state on a single node (12 cores). Spurious velocity results on account of small pores with too few grids to capture the relevant physics were avoided by eliminating such "speck"-like pores during image processing. It was also confirmed that the LBM code renders the same geometric permeability output for pressure drops of different magnitudes; see Figure D.3 of Appendix D. SPSC permeability measurements were achieved in the *x*, *y*, and *z* directions (anisotropy assessments) for each image stack in Groups A and B and the lone stack in Group D. Within the scope of this work additional physics were not incorporated into the simulations (for example, multi-phase flow and, as a result, relative permeability and capillary pressure curves). It was prudent to first assess whether the microscale FIB-SEM domains are reliable for basic petrophysical assessments such as porosity and geometric single phase permeability in the connected pore-space.

7.5 STUDY RESULTS AND DISCUSSION

Figure 7.6 compares the values of extracted porosity and organic matter between FIB-SEM stacks belonging to the same group and a comparison to the relevant core data from the corresponding sample plug. Crystalline porosity and organic matter porosity are distinguished and group averages are shown as well. The results show large variations in porosity and kerogen volume between these local FIB-SEM image stacks and also from the corresponding core data; the relative change of these variations is often on the order of several tens of percent difference. The notion of inter-stack averaging of geometric properties is appealing; in Group A, the *average* values of porosity and organic matter among the stacks are right on par with the "as received" GRI porosity (*not* the dry

porosity) and the LECO TOC (vol %) value. On the other hand, average values of the volume percent of organic matter in Groups B and C are at least double the LECO TOC (vol %) data.

Kerogen can sometimes be falsely identified as pores and vice versa in a FIB-SEM image analysis process due to similar grayscale pixel values. The extracted kerogen and pore space volume percent values are presented in a stacked bar plot format in Figure 7.6; this stacked manner shows that the sum of the kerogen and pore volumes also changes considerably from stack to stack and variability is not an consequence of the image analysis process but the physical domains themselves. There is less inter-stack variability in Group C, the FIB-SEMs taken over the larger volumetric domains of 5000 μm^3.

Figure 7.7 shows the results of the geometric SPSC LBM permeability simulations in Groups A and B and cross-plots of select petrophysical properties. High permeability anisotropy within 3D images and large permeability differences between neighbor 3D images are clearly observed. Specifically, permeability in one geometric direction varies as much as three orders of magnitude between local images and is on average at least an order of magnitude greater than the corresponding GRI permeability measurements on "as received" core-scale samples (where *in situ* fluids are still present in the sample). The GRI permeability measurement on dried Sample A is closer in magnitude to the average of the simulated permeability values, but this is not the case for dried Sample B. SPSC permeability simulations performed in the extracted pore network from FIB-SEM D1, a domain over 30 times larger than those of Groups A and B in terms of microscale volume (but similar in voxel volume), also rendered permeability anisotropy across several orders of magnitude. Figure D.5 of Appendix D relates

directional permeability to percolation path length in FIB-SEM D1; however, this trend in anisotropy is not seen in Groups A and B.

When simulations are performed in a suitable REV of a homogenous media a plot of permeability (*x*-axis) versus domain volume (*y*-axis) would display a roughly vertical trend at a given permeability value. The bottom panel of Figure 7.7 reveals that there is no such vertical trend between the simulated permeability and cropped FIB-SEM volumes for Groups A and B; the horizontal and inclined orientation of the trends suggests extreme heterogeneity, a volume below the REV, or both. However, correlations between extracted FIB-SEM porosity and permeability are seen (Figure 7.7, panel C). In conventional porous media, these types of porosity-permeability trends on semi-log plots are emblematic of rock types, where the media's porosity and permeability are related through the Carman-Kozeny equation derived from a bundle of tortuous tubes. Thus, the main percolation pathways captured in the FIB-SEM images are akin to tortuous tubes rather than extensive interconnected networks; this is confirmed with simulation visualizations (see Figure 7.5). Furthermore, many branches of the pore networks within the investigated volumes are isolated/unconnected; Figure 7.7, panel D shows that the number of independent pore networks within a 3D image positively scales with percentage of organic matter. There is an overall trend between porosity and kerogen volume (Figure 7.7, panel E), but it is not distinct in Group A.

Figure 7.8 compares the high resolution 2D cross-section SEM images (Groups E-M) in a manner analogous to that of Figure 7.6. Similar to the geometric results with FIB-SEM, there is high variation between local images and associated core data. Yet, overall, the sums of the average values of porosity and organic matter in the 2D cross-section SEM images (recall, 10 images per group) are comparable to the sums of the LECO TOC

(vol %) and the "as received" GRI porosity (*not* the dry porosity) with the exception of Group G. In regard to petrophysical trends, the trend between total porosity and organic matter in the 2D cross-section SEM images is not particularly strong; the R^2 value is 0.34. Groups E-M capture larger fields of view, which may explain why they contain larger amounts of interpreted crystalline porosity than the FIB-SEM images.

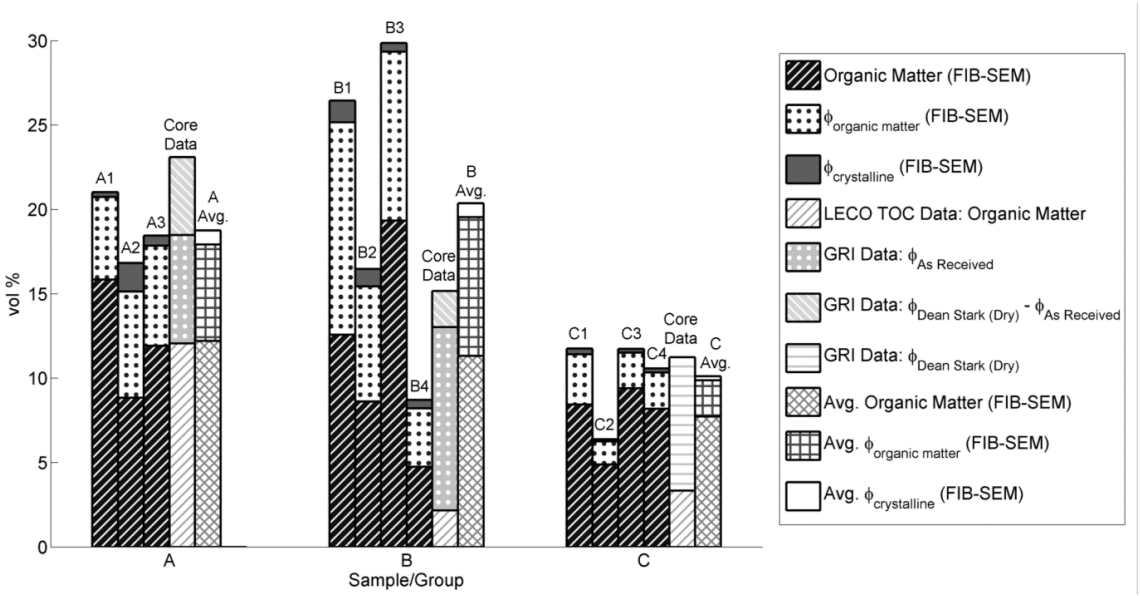

Figure 7.6: Comparison of the extracted pore-space and organic matter volumes within local groups of 3D FIB-SEM images and to the groups' respective core data. The LECO TOC value is presented in vol% and, thus, is slightly variable since it is dependent on the kerogen density and a carbon mass fraction used to convert from wt%; 1.3 g/cc and 0.80 were used, respectively.

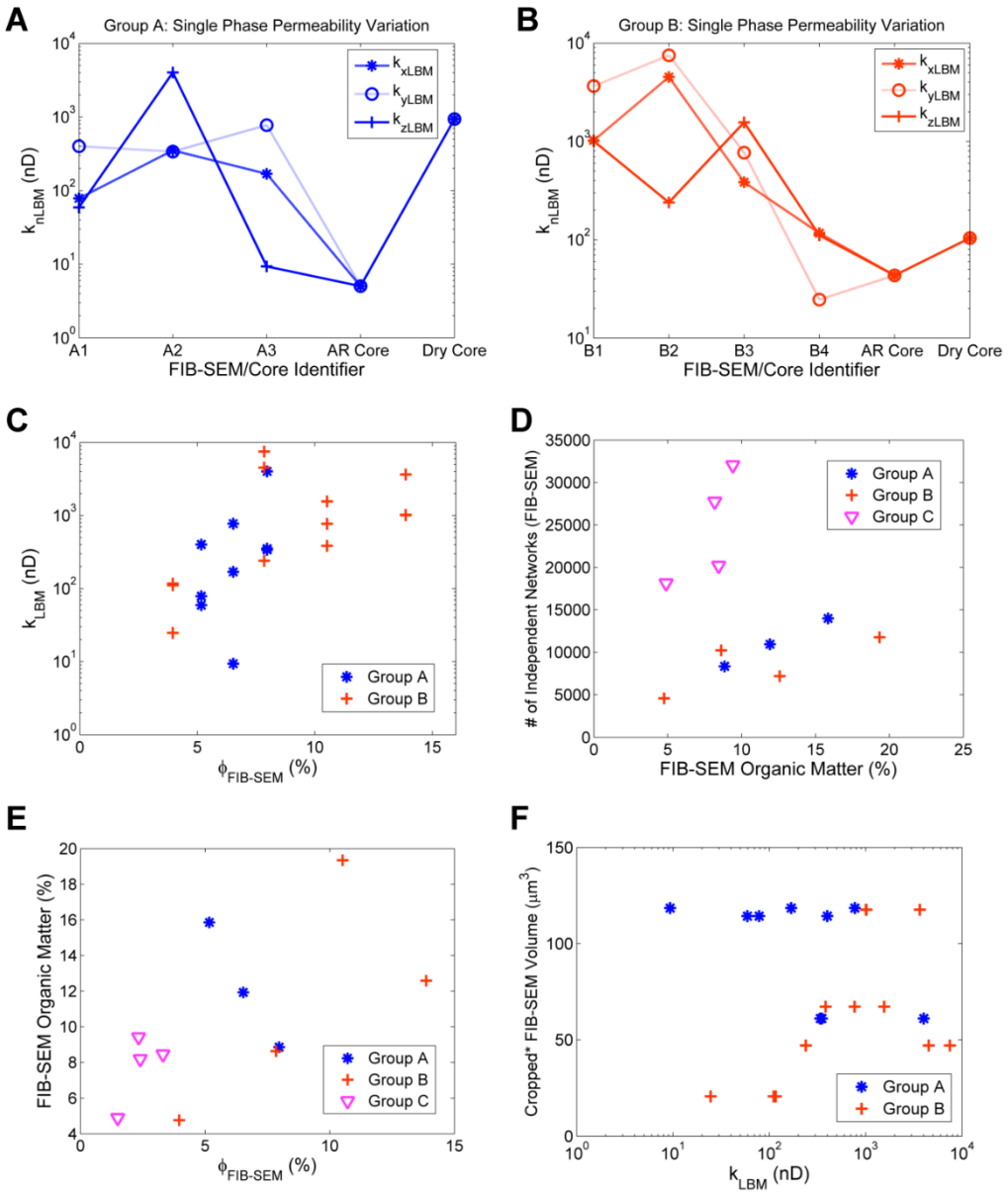

Figure 7.7: Panels of relevant petrophysical assessments from the FIB-SEM image stacks, including: (A)-(B) variations in single phase permeability among neighboring samples and core data and (C)-(F) cross-plot relationships. Note that the relationship between permeability and porosity (panel C) can perhaps be ascribed to percolation pathways. *Processed image stacks are cropped to the largest connected pore pathway in potentially all three Cartesian directions following the extraction of geometric properties and prior to fluid flow simulations.

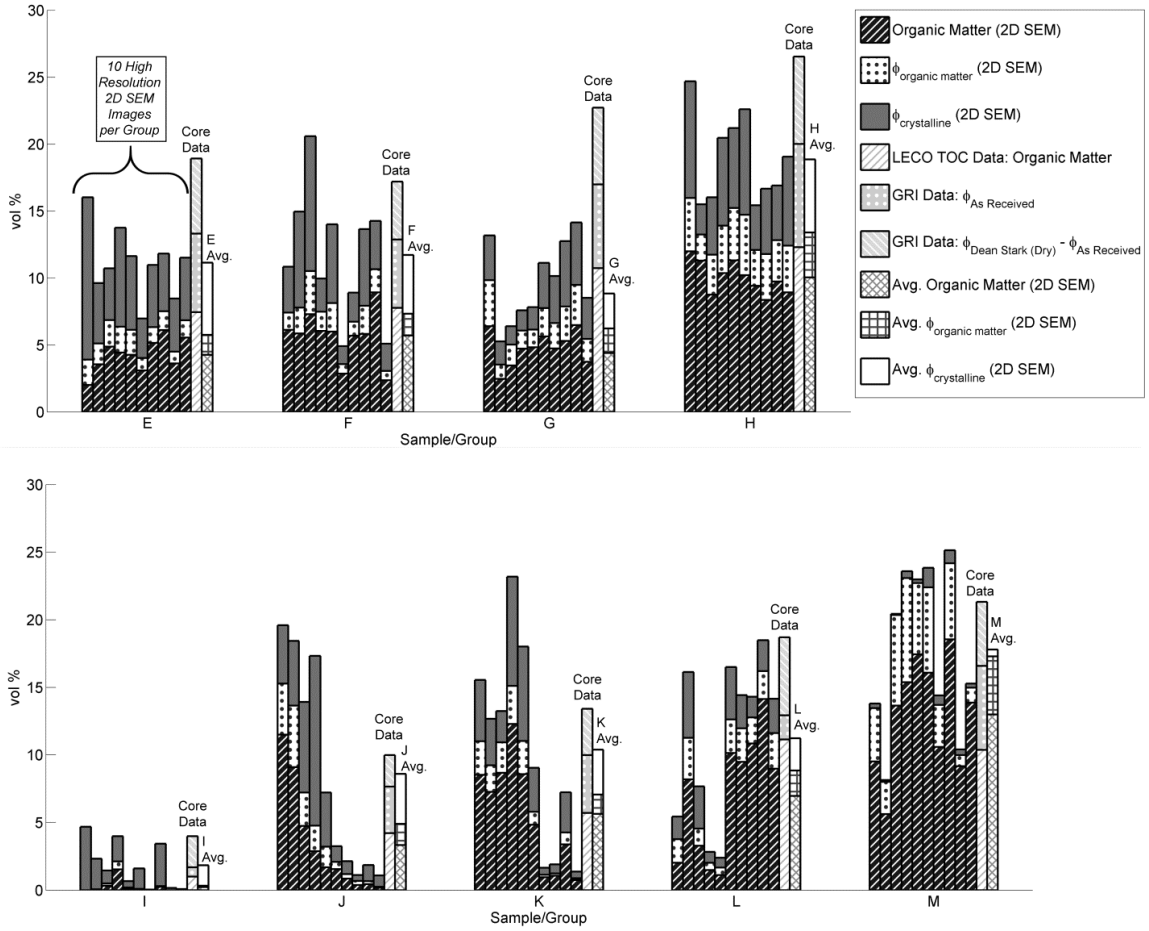

Figure 7.8: Comparison of the pore-space and organic matter volumes within local groups of 2D cross-section SEMs (acquired from BIB-SEM) and to the groups' respective core data. The LECO TOC value is presented in vol% and, thus, is slightly variable since it is dependent on the kerogen density and a carbon mass fraction used to convert from wt%; 1.3 g/cc and 0.80 were used, respectively.

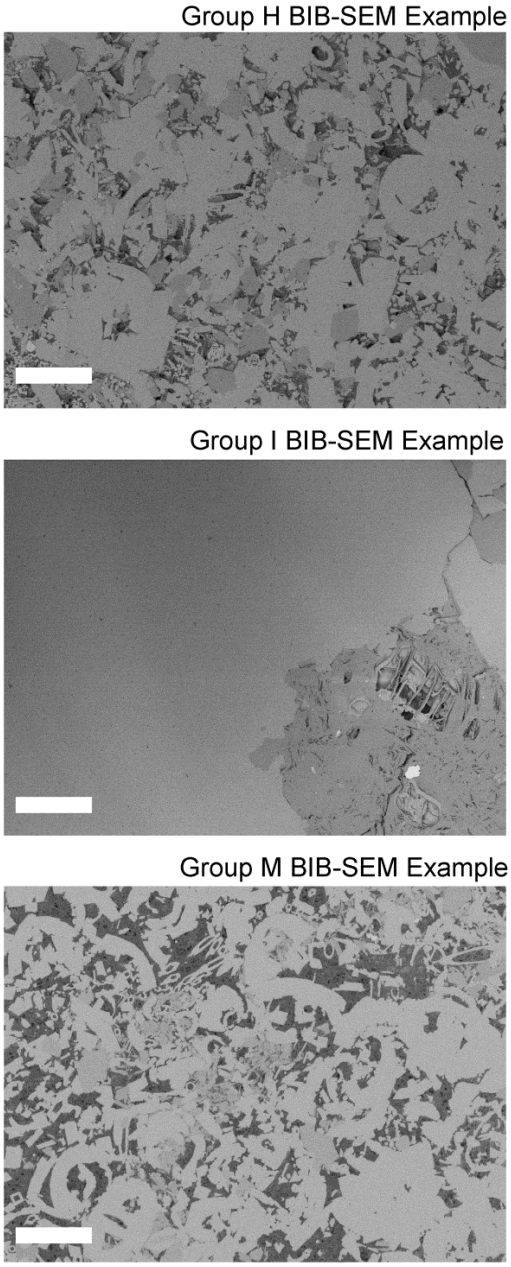

Figure 7.9: Examples of 2D cross-section SEM images that illustrate the variation in composition and pore-space between samples/groups; the scale bars are 5 μm. The core corresponding to Group I clearly has the lowest porosity and organic matter of the samples, per the GRI and LECO TOC measurements; this predominance of grains is reflected in the Group I images. The reverse applies for Groups H and M, which had the highest porosity and organic matter content of the samples.

Analysis of the FIB-SEM images was performed without *a priori* knowledge of the bulk properties of the samples. The image analysis and simulation processes were examined *a posteriori* to determine what steps are necessary to achieve a better match between extracted FIB-SEM properties and the available core data, a reliable indicator of the samples' bulk properties. Unfortunately, there is no consistent solution across Groups A - D for porosity agreement. By examining the average values of each group of stacks, it is noted that the following practical measures are necessary for close agreement with core: in Groups A and D compare to the "as received" porosity (gas-filled porosity) value only; in Group B a greater number of FIB-SEM images is needed to offset two unreasonably high outlier values (stacks B1 and B3); and in Group C the quality of the images need to be enhanced (at time of acquisition) to obtain a clearer distinction between kerogen and pore features. Simulated permeability values are generally *higher* than GRI measurements (with the exception of the dry core permeability of Sample A) where the fluid used is helium. In low pressure conditions, the addition of diffusion through pores (Fickian and Knudsen diffusion) and kerogen (Fickian diffusion), slip flow, and other phenomena associated with gas transport in shales into simulations will further *increase* the total mass flux and apparent permeability [223]. However, simulations performed in a nanotube show that at high pressure conditions the apparent permeability of a flowing gas converges with Poiseuille flow or Darcy permeability [226]. Note that the incorporation of diffusion through kerogen may lead to a convergence of mass flux and apparent permeability between neighboring FIB-SEM stacks, since the kerogen is ubiquitously better connected than the pore-space. The LBM code framework used herein for fluid flow simulations can be used to solve a diffusion problem as well with some adjustments. In pure diffusion the probability

density function would become the diffusion scalar, velocity components would be omitted from the code, pressure drop would become concentration drop, and viscosity would be exchanged with the diffusivity constant. Incorporating both advection and diffusion should be explored in future works.

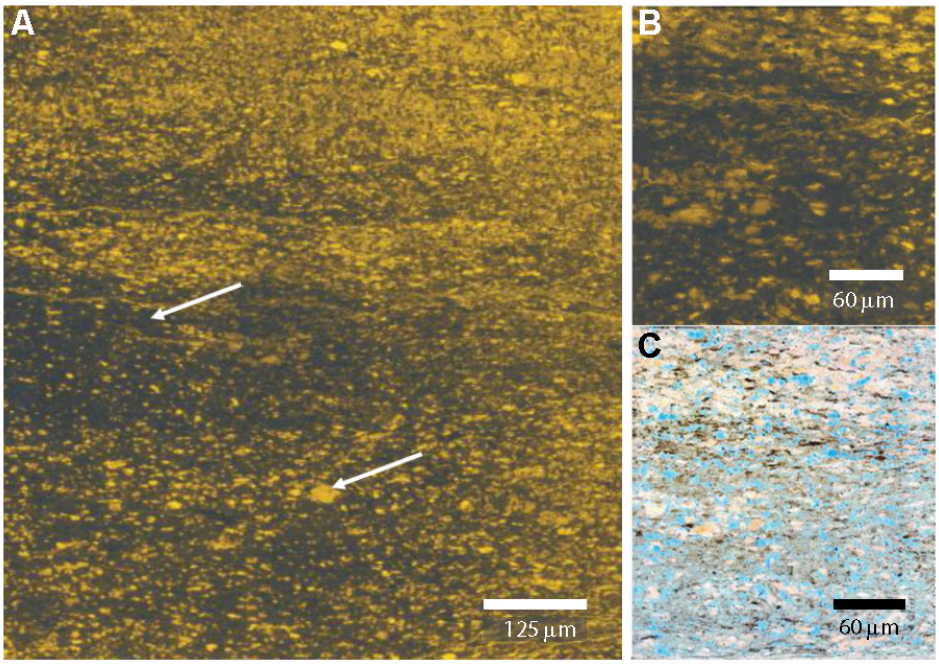

Figure 7.10: (A) A large-scale view of fluorescent mapping of a low viscosity epoxy dyed with Rhodamine B, a neutrally charged fluorescent tracer, and vacuum-pulled through a thin section of the Group C sample. The mapping is enabled by stitching together (mosaic style) 154 20X images captured with a Zeiss 510 laser scanning confocal microscope (Sandia National Labs). The arrows point out regions of potentially high porosity and connectivity (evidenced by high fluorophore content) and areas that did not experience liquid contact. (B) Close-up of fluorescent mapping. (C) Corresponding close-up of UV-fluorescent mapping, where carbonate fossils show up blue in color. Images were provided by Sandia National Labs (Albuquerque, NM).

In this work and others, [39] and [40] pore connectivity is generally not observed throughout raw FIB-SEM domains and cropping of the domain in at least one direction is usually required. This cropping in itself suggests that the domain is not representative, as fluids, including liquids (which do not diffuse through kerogen), do percolate through shale as a whole. Figure 7.10 displays an example of fluorescent mapping of a low viscosity epoxy vacuum-pulled through a thin section made from the Group C sample; this thin section displays a myriad of widespread fluorescent paths, evidencing macroscopic connectivity and percolation. Upon cropping of the FIB-SEM images, note that a series of larger, tenuously connected pores provide the predominant flow path(s) in the simulations. Some of the pathways meandered to such a degree with little connectivity that a large portion of the velocity vectors pointed against the pressure gradient at steady state conditions. These isolated path(s) between the pressure inlet and outlet planes may be figments of a limited field of view (i.e. only capturing random portions of a larger network of flow paths), which is further evidenced by the random nature of the permeability anisotropy. In a departure from conventional terms, Zou introduces conceptualizing fluid transport through shale in terms of "connection rate" of pores rather than permeability [34]. Indeed, in Figure 7.10, there are regions of the sample not illuminated by fluorophores or occupied by carbonate fossils (which are detected with UV light), which suggests that these areas have extremely low connectivity or isolated pore networks. Investigators expect and seek connectivity in 3D images of conventional porous media; the fact that complete connectivity in shale FIB-SEM images is rarely captured may not be an indicator that connectivity is below the resolution of SEM or is destroyed by the ion beam, but that a considerable fraction of the millions of nanoscale pore networks in a shale sample are simply not connected in the first place.

This consideration has been posed before: for example, upon a mismatch between standard laboratory analysis of shale samples and observations with SEM and TEM, Bennett et al. [227] suggested that either a large number of pores are shale not connected or that core measurement techniques were insufficient. Hu et al. suggest that poor pore-connectivity is the cause of many anomalous transport observations in tight media including atypical imbibition and diffusion trends [176].

7.6 CONCLUSIONS AND RECOMMENDATIONS

Analysis of the variability of geometric properties between local FIB-SEM images of shale and core-measurements reveals that *individual* FIB-SEM stacks intended for high spatial resolution may not be representative of local or macroscopic geometric properties. High resolution FIB-SEM image stacks of volumes less than 200 μm^3 display substantial variations in porosity and kerogen volume between neighboring (local) stacks and from the associated core data (macroscopic properties). Specifically, calculated values of porosity and kerogen volume varied by far greater than 5% in several cases, which is on the order of porosity values themselves for low porosity samples such as shale. In FIB-SEM images taken over larger domains, approximately 5000 μm^3, greater local continuity of geometric properties was found; however, the image resolution is generally lower in these domains. Averaging of several local FIB-SEM image stacks can yield suitable values of porosity and the volume percent of organic matter, but this outcome is not always guaranteed. Furthermore, the assessment of basic geometric properties does not require a 3D domain; therefore, an imaging alternative to FIB-SEM images for evaluation of geometric properties is BIB-SEM-generated 2D cross-section SEM images. Averages of the geometric properties calculated from these 2D cross-

section SEM images are comparable with core-scale measurements when "as received" porosity is used.

The results of connectivity assessment and geometric permeability simulations imply that FIB-SEM stacks are not suitable domains for representative 3D pore network models of shale and permeability simulations in the connected pore space. SPSC LBM simulations performed in the 3D pore-structures rendered permeability anisotropy within both relatively small and large FIB-SEM image volumes. Permeability varied as much as three orders of magnitude between local FIB-SEM images and, on a FIB-SEM group basis, did not match up to the corresponding core GRI permeability measurements. Additionally, the shale FIB-SEM images display poor overall connectivity and the domains almost always required cropping (including the larger 5000 μm^3 domains); a single FIB-SEM domain contains thousands of independent networks or pores, but typically only a few key percolation pathways. These pathways were tortuous and irregularly connected.

Even though FIB-SEM images are useful for obtaining qualitative knowledge about shale morphology (e.g., the relative abundance of porosity in the kerogen and the orientation of clays and kerogen in relation to grains), it is concluded that they are not a practical REV for shale digital rock physics. The main impetus of a 3D imaging technique such as FIB-SEM is to capture the relevant pore-structure or network of a medium. This objective is highly challenging in shale: connectivity is either extremely tortuous or isolated in clusters at microscale fields of view, but the majority of the nanoscale pore space is altogether lost at larger fields of view. Hence, this work does not critique the FIB-SEM technique itself, which has successfully captured suitable REVs in more locally homogenous nanoporous materials and tissues, but the application of FIB-

SEM in shale. I look forward to further studies on the qualitative and possibly overlooked quantitative uses of FIB-SEM images for shale and other geologic nanoporous media, but advise that researchers be cautious concerning local heterogeneity and domain size in the study of a single FIB-SEM stack.

Overall, a viable alternative to FIB-SEM images are the BIB-SEM-generated 2D cross-section SEM images examined herein. These images balance high resolution and large fields of view, but their potential for fluid flow simulations is limited due to their 2D nature. However, methods to integrate a BIB-scale ion polisher into an SEM allowing collection of consecutive image slices (3D) at a larger field of view are reported and under development [216]. It is recommend that researchers pursue this method as a possible means of obtaining a representative pore network model of the shale layer they are studying, though analysis of the resulting 3D images will be extremely memory intensive. Other methods to approach the shale REV challenge with are: nano-CT images; integration of new analytical techniques such as Small Angle Neutron Scattering (SANS) [228] and nitrogen sorption hysteresis [229] for large-scale pore structure information; courser, but larger REVs such as high resolution micro-CT where high resolution details are artificially populated; and synthetic 3D models inspired by large-scale and local SEM images for probing of physical phenomena. TEM investigations into the potential Angstrom-sized pore-structure of shale below the resolution of SEM are also beneficial for (mainly) qualitative purposes; these sub- 5 nm pores would barely contribute to viscous flow but can contribute to overall mass transport through diffusion. A comparison of shale pore structure following different sample storage and preparation techniques (especially sample drying methods) may address the reality or sensitivity of the images captured under high vacuum with SEM. Creative utilization of an

environmental SEM (ESEM), which allows hydrated samples and gas or water vapor in the microscope chamber, some pressure and temperature control, and condensed water droplets on the sample will also help in identifying the role of environmental variables on the imaged pore structure.

Based on the work presented herein, I pose the following recommendation: while pursuing the aforementioned and other new approaches to pore-scale experiments, imaging, and simulations of shale, researchers should be mindful of whether their domain size is on the scale of local heterogeneity and ask whether it is worthwhile to capture the organic matter pore-structure of shale at the expense of a larger field of view.

To answer the answer posed by the title of this chapter, digital rock physics in local shale 3D images, plagued by the issue of an appropriate REV, is not a suitable complement to nanofluidics for shale transport studies. More appropriate complementary investigations are identified in Sections 8.3.2.3-4 (future work tasks).

Nature's imagination far surpasses our own.

Richard Feynman, Nobel laureate in Physics

CHAPTER 8: Conclusions and Future Directions

The more I learn, the more I realize [how much] I don't know.

Albert Einstein, Nobel laureate in Physics

This dissertation addressed how nanofluidics can be used to investigate a fluid transport-related hypothesis for tight porous media. The prime hypothesis explored herein was that the properties and surface chemistry of interfaces between confining walls and confined fluids need to be accounted for in transport equations describing flow through nanoscale domains.

8.1 PREVAILING CONCLUSIONS OF THE RESEARCH

The following prevailing conclusions delineate primary contributions and findings that were not established prior to this work or are further confirmed by this work. Specific conclusions and recommendations are found at the ends of Chapters 3-7 of this dissertation.

Main contributions:

- Nanofluidic chips that contain an array of twenty parallel nearly rectangular 2D nanochannels (30 nm - 500 nm in width and all 60 nm in depth) were constructed to mimic the types of cross-sectional areas seen in flow-enabling shale pores; associated chip fabrication methods were documented as well. This simple channel geometry enabled comparison against bulk analytical transport solutions,

a comparison generally only shown for 1D nanochannels in the currently existing nanofluidics literature.

- This work reports the first construction of "reservoir-on-a-chip" versions of shale. Such synthetic representations of shale enable a novel branch of experimental investigations into nanopore-scale fluid transport physics that are intended to supplement conventional shale core analysis techniques. The documented two-step fabrication scheme for a master pattern is relatively simple, robust, and cost-effective. Investigations with these chips are relegated for future work (Sections 8.3.2.4-5).
- A second simple methodology for large-scale shale-like "reservoir-on-a-chip" devices that feature patchworks of nanochannels and pseudo-geologic features was reported in this work. This scheme utilizes premade diffraction gratings as master patterns and implements fouling mechanisms to the advantage of the researcher, a factor that renders a reservoir-on-a-chip construction process without the need of a cleanroom facility. This approach was demonstrated with imperfect diffraction gratings and preliminary results in resultant chips were shown in Section 5.5. The repurposing of consumer-grade compact or blu-ray discs as diffraction gratings for this method further enhances its simplicity and economics.
- This work introduced a method that enables quantification of the effects of fully sub-micron nano-confinement on imbibition, capillary pressure, viscosity, and interfacial mass transfer within a nanochannel geometry; i.e., the decoupling of these variables from nanochannel imbibition data with trapped air bubbles.
- Quantification of gas partitioning across a meniscus and diffusion in solution was necessary for the aforementioned decoupling method (detailed in Section 4.2).

Hence, a closed-form solution to the 1D advection diffusion equation (ADE) was derived to describe diffusion across a meniscus interface and within an imbibing liquid in a long conduit. This derivation accounts for the following nontrivial conditions: a time dependent liquid velocity, $u_x(t)$, moving boundary (meniscus), and one time dependent boundary condition (i.e., the pressure of the bubble and, thus, the concentration of air molecules at the interface can either remain constant, increase, or decrease with time).

- This work presented an image acquisition and analysis method that allows extraction of the position of liquid as a function of time within silica nanochannels as small as 30 nm in width from amidst noise for differential interference contrast microscopy image stacks data. The "dynamic" image analysis method revealed pixelated temporal "profiles" of nanoconfined liquids and gases.
- Local phenomenological models for effective contact angle, effective diameter, and effective viscosity were developed to explain the anomalous nanofluidic data of this work. Specifically,
    - It was demonstrated that the Young-Laplace equation breaks down as a function of several parameters: channel diameter, Hamaker constants, the height of a prewetting film, and surface tension. The derivations are based on surface-force theories (the works of Derjaguin, Israelachvili, Langbein, Hamaker, Lifshitz, etc., all referenced herein), which conveniently enable molecular interactions to be described from a continuum perspective.
    - The dimensionless ratio Λ, introduced herein, can be used to determine when the Young-Laplace equation is reliable, when a modified version of

the Young-Laplace equation is required, or when the Young-Laplace equation is no longer applicable.

- Longitudinal elastocapillary deformations of a confinement or quasi-crystalline thin films are functions of channel or pore size, capillary and liquid pressure, specific surface area, position, and the bulk elastic properties of a media. A dimensionless ratio of the length of pore collapse to the length of interest of the media, Γ, can be used to determine when elastocapillary effects are prominent and effective diameter and effective viscosity necessary.

In addition to the results presented in this thesis, these models can potentially describe the nanofluidic and nanoporous materials imbibition works of others.

- A consistent image processing workflow for shale FIB-SEM analysis and subsequent digital rock physics was detailed in Chapter 7. Image analysis of FIB-SEM microscopy data is beleaguered by image artifacts and topographical complexity (as described in Section 7.2.4).

Primary findings:

- It was observed that imbibition of various wetting liquids in an array of different-sized, horizontal, 2D silica nanochannels terminated within the channels as a function of hydraulic diameter and liquid type. This front termination is not predicted by the classic Washburn equation for capillary flow, which establishes diffusive dynamics in horizontal channels. Results did not correlate with bulk fluid properties, but correlated with the van der Waals properties of thin films described by system-specific Hamaker constants: liquids with low A_{232} and high absolute values of A_{123} imbibed the most effectively in the 2D nanochannels.

- The captured speeds and power law dynamics of the nanoscale imbibing fronts were also anomalous. Fluids imbibed slower than the Washburn equation prediction and in some cases the $t^{0.5}$ diffusive trend broke down even when the imbibing liquids were subject to atmospheric pressure at both the inlet and outlet of the setup. Two atypical scenarios consistently observed were:
    - Fronts started out moving swifter than a diffusive trend, but then dramatically slowed down or ceased/became arrested. For t^n power laws, such a trend corresponds to $n < 0.5$; n was usually found to be around 0.3 for these scenarios. These data indicate a physical parameter with unexpected non-constant values decreases driving forces or increases net resistance to imbibition with time.
    - Near linear filling ($l \propto t$) was observed in the 2D nanochannels with the most narrow cross-sectional areas (particularly in the 500 nm × 60 nm slit-like geometry). These data indicate a physical parameter with unexpected non-constant values increases driving forces or decreases net resistance to imbibition with time.
- In addition, non-Washburn dynamics were found to ensue due to several inhibitory mechanisms: menisci struggling and arrest in the presence of adsorbed thin films (even for perfectly wetting fluids), capillary trapping and capillary condensation, and evaporation and salting out/in of saline solutions.
- The likelihood for prewetting film thickening, described by the Hamaker constant for the system of a liquid between silica and air, A_{123}, trends with imbibition success, S_w. Thus, it is surmised that the effect of precursor film thickening, despite decreasing the effective channel diameter, may encourage nanoscale

imbibition by preventing film rupture in the presence of surface roughness and other inhomogeneities. The likelihood for attraction of two identical fluid films across an aperture of air, described by the system Hamaker constant A_{123}, also trends with imbibition success, S_w. Therefore, menisci deformation in the central zone of a meniscus may reduce effective capillary pressure. Deformation of menisci enhances sensitivity to rugosity or asperities, artifacts potentially introduced by the employed fabrication methods.

- When the presented method to quantify the effects of nanoconfinement on effective transport values was implemented with the perfectly wetting liquid isopropanol, results indicated that in 2D silica nanochannels there is a significant departure from isopropanol's bulk transport properties. Specifically, the findings included effective capillary pressures at least 40% less than the value predicted by the Young-Laplace equation, a decrease in effective capillary pressure with a decrease in nanochannel size, an on average tenfold increase in effective viscosity from the bulk viscosity, and non-constant interfacial mass transfer coefficients [182].
- An effective decrease in channel diameter is required to explain the anomalous nanofluidic results. The possible mechanisms are relatively thick film formation and highly viscous (almost immobile or quasi-crystalline) boundary layers and, potentially, solid deformation; these effects are potentially concurrent. The increased effective viscosity values for isopropanol correspond to an effective decrease in channel diameter extending as thick as 10 - 25 nm from silica surfaces [182].

- The nanofluidic findings, in sum, demonstrated that nanoscale transport is not just limited by channel depth (60 nm in this case) as 1D nanofluidic works explore. The addition of a second nanoscale dimension to nanochannel cross-sectional proportions (i.e., 2D nanochannels) revealed different imbibition trends from 1D nanofluidics and resulted in substantial anomalies as a function of channel cross-sectional area.
- A thorough study of groups of neighboring FIB-SEM image sites revealed these high resolution, 3D microscopy images are not a suitable compliment to nanofluidics nor a practical REV for quantitative shale digital rock physics. Rather, FIB-SEM images are useful for obtaining *qualitative* knowledge about local shale microfabric.

Overall, macroscopic descriptions of imbibition are insufficient in fully nanoscale (2D) confinements because they do not consider menisci deformation due to long-range intermolecular forces and effective pore space deformation due to elastocapillarity, surface stresses, adsorbed/precursor thin films, and/or viscous boundary layers. These effects were most prominent in the smallest nanochannels observed (smallest fabricated: 30 nm × 60 nm) and, hence, stem from an increase in surface area to volume ratio. Experimental results were extremely sensitive to fluid and environmental conditions (including surface asperities), such that departure from ideal conditions (e.g., an atomically flat tube, spectroscopically pure liquid, and no relative humidity) furthers the divergence from macroscopic solutions. This divergence threshold from textbook transport solutions is far higher in microscale conduits, such that those equations remain mostly applicable for conventional porous media. However, for unconventional or

nanoporous media, emergent interfacial fluid and solid deformations must be captured through the use of effective values and scaling laws stemming from phenomenological models.

8.2 IMPLICATIONS AND APPLICATIONS

Determination of the net effects of interfaces and surface chemistry on hydrodynamic transport is critical to describing and enhancing the success of liquid transport from a source into an adjacent nanoscale domain. Nanofluidics is not a panacea for this complex problem, but can assist in identifying emergent nanoscale properties that may scale to influence larger transport trends.

8.2.1 Unconventional core and reservoir scale implications

Liquid flows in shale nanopores have been wholly less subject to investigation than gas flows. Yet, the study of liquid and multi-phase component flows at the nanoscale is very important for understanding the interaction of free and bound water with hydrocarbons in shale systems, liquid driven core analysis methods, and the fate of injected liquids (such as “fracking fluids”) into the reservoir. The findings of this work revealed that there is a divergence from conventional equations and a change in effective pore diameter in the presence of nanoscale menisci; menisci are common occurrences in core samples and reservoirs during imbibition/drainage, multi-phase flow, and capillary condensation. In addition, potential nanopore deformation should be taken into account during liquid evaporation and oven drying of samples, common petrophysics lab practices.

The possibility of deformed menisci at the nanoscale may counter the premise of using MICP at high pressures for pore size distribution estimates based on meniscus

curvature alone. Additionally, capillary condensation measurements are only indicative of pore size distribution to the extent the vapor-liquid meniscus interface adheres to Kelvin's equation, an equation based on meniscus curvature. The discussed θ_{eff} convention (Chapter 6) can be practically implemented because it allows complex surface force formulations to be encapsulated in a single term and fits in the structure of the Young-Laplace equation. Additionally, a dimensionless index, Λ, was proposed for the ratio of average surface forces per unit area over a meniscus to bulk capillary pressure, P_c^m, in an average or representative pore size: $\Lambda = <\Pi_m>/P_c^m$. The dimensionless ratio of the pore collapse length to the length of the media or the imbibition length of interest, namely, $\Gamma = l_c/L$, can indicate whether nanostructural deformations should be taken into account. See Sections 6.5-6.6 for more details. Overall, $<\Pi_m>$ and l_c are derived from readily available mineral and fluid properties: E, ν, ε, n, etc. It is anticipated that using Λ, Γ, and other emergent scaling laws (to be established) one can more accurately predict the timescale of imbibition/drainage from fractures to/from matrix. Overall, the key implications are summarized as follows:

- Descriptions of shale transport should take into account (and advantage of) the discussed emergent nanoscale phenomena.
- The models provided herein can be further scaled to enhance understanding of shale two-phase flow and production trends.
- Furthermore, production trends can potentially be enhanced through control of surface forces.

8.2.2 Applications of the nanofluidic devices

Analogous to the use of micromodel experiments as a benchmark for fluid transport models in conventional media, "nanomodels" (as presented in Sections 3.2-3.3)

can potentially serve as such a benchmark for unconventional media, including shale [230]. The nanofluidics scheme performed in this work enables the ability to do in situ fluid analysis by comparing the nanofluidic differences among tested fluids. With the array-style and shale-inspired nanofluidic chips described herein, researchers can test pore-scale transport hypotheses with direct visualization of both the network geometry and in situ fluid movement. In addition to the position of fluid interfaces, the location of molecular fluorophores and tracers can be captured within the optically transparent chips. Furthermore, such nanofluidic experiments help establish whether nanoscale transport is governed by interfacial, viscous, or diffusive forces for varying solid-liquid and solid-liquid-gas conditions. Further details on these applications are discussed within Section 8.3.2.

8.2.3 Broader applications

Interest in fluid and interfacial behavior and controlling transport within nanoconfinements spans many disciplines. Nanoporous materials can be geological, biological, and synthetic. In addition to subsurface reservoirs, discussed thoroughly in Chapters 1 and 2, other nanoconfinement-based research areas include filtration and adsorption in nanoporous membranes [9], lab-on-a-chip drug delivery systems and sensor/function-based nanofluidic devices [230], and intracellular transport in plants [167]. Biological nanoporous media include the brain (see Figure 8.1.D) and porins in a cellular membrane. Interstitial fluid, composed of water and a medley of solutes including salt ions, sugars, and hormones, navigates through the brain along perivascular pathways and axon tracts [231]. Vycor “thirsty” or filtration glass is used for desalination of sea water and chemical separation. In addition, nanofluidic devices are a means to molecule isolation (especially DNA [232]) and fluid analysis.

The study of naturally occurring nanoporous media is particularly challenging because researchers are limited in their control or modification of the solid properties; however, the properties of injected wetting liquids (i.e., solute and solute concentration, pH, gas concentration) can be tailored. Tuning of a system's Hamaker constant by such fluid solvent and solute selection can potentially enhance or decrease fluid imbibition and drainage effects as needed. Changes in the dimensions of a nanoporous media or conduit can potentially be used to characterize either the intrinsic capillary forces or mechanical properties of the solid. Specifically, elastocapillarity can be externally controlled with methods such as electric fields [233], and implemented as a diagnostic method for investigating the internal structure of complex nanoporous media.

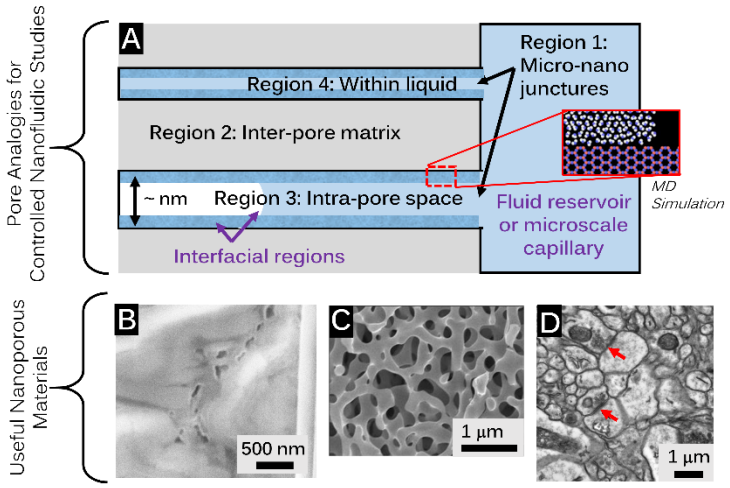

Figure 8.1: (A) Diagram of the regions of interest in nanoporous materials studies (B) Close-up of sub-500 nm pores in organic matter between grains in a focused ion beam - scanning electron microscope (FIB-SEM) image of a nanoporous rock sample. (C) Scanning electron microscope (SEM) image of Schott's CoralPor glass (image from Schott Glass website [234]). (D) Transmission electron microscope (TEM) image of brain tissue (image from Duke University School of Medicine website [235]); arrows point to examples of synaptic pathways.

8. 3 OPEN PROBLEMS AND FUTURE RESEARCH DIRECTIONS

This dissertation established anomalous nanofluidic trends, experimental methods, and explanations, but additional study into the role of interfacial phenomena in nanoconfinements is required to further verify the proposed models and properly apply them to nanoporous media. The objective of future research directions is to further understand, quantify, and control how interfacial phenomena, specifically van der Waals forces and the electrical double layer, and osmosis and diffusion affect liquid transport in nanoporous materials. Nanofluidic experiments and phenomenological model development similar to the approach taken in this dissertation, as well as and molecular dynamics simulations should be used to further investigate these interfacial phenomena at the nanoscale and compare to existing theories for microscale transport. The scientific findings can then be used to control (enhance or impede) flow in nanochannels and nanoporous materials.

Thus far, mainly ideal wetting liquids were used in the nanofluidic experiments. Similar experiments with reservoir-applicable fluids can also be performed. Because nanoscale transport is highly sensitive to specific surface-liquid-gas combinations, it is recommended that the trapped bubble experimental method presented herein (Chapter 4) be used in the assessment of the adequacy of bulk solutions and properties for various liquids and nanoconfinement conditions. The latter includes different channel shapes, lengths, and materials and/or surface coatings (recall that charged surfaces can induce an EDL in aqueous environments). Parallel nanochannels are ideal for this method and the straightforward fabrication schemes outlined in Chapter 3 for obtaining large-scale nanochannel patterns with diffraction gratings and Blu-Ray discs are suitable for constructing batches of such configurations.

Water, ubiquitous and vital to the aforementioned broader impacts (e.g., interstitial fluid in biological nanoporous materials is water with a host of biological solutes, and water of various salinities and solutes is injected into subsurface reservoirs for production), is the liquid of focus in the suggested future work plan. This plan seeks to achieve enhanced control of aqueous solution transport efficacy by means of the informed selection and order of injected solute concentrations based on potentials at interfaces and in situ solute concentrations. Such solute gradient-driven and surface chemistry-driven actuation methods can be especially useful in situations where the application of external pressure or electrical gradients is impractical or harmful. In addition osmosis, diffusion, and evaporation may greatly impact viscous transport efficiency at the nanoscale due to the inherent low volumes of nanoconfined liquid and gases. Osmosis is the movement of water up the concentration gradient (water moves from the low solute concentration region to the high solute concentration region) and diffusion is the movement of a solute species down the concentration gradient. In small volumes these processes occur rapidly.

8.3.1 Emergent hypotheses from this dissertation

The main hypothesis established in this work are that liquid, multi-phase, and solute transport in nanoconfinements are dominated by interfacial physical and chemical phenomena and concentration gradients. For nanoconfined aqueous solutions, these governing phenomena can be understood and controlled by varying the salt concentration, pH, and dissolved gas concentration of the incoming solution. Specifically, the hypotheses are:

1. van der Waals forces alter effective values of capillary pressure, viscosity, and effective pore diameter as a function of liquid and gas properties and nanoconfinement size.
2. The presence of the electrical double layer alters effective values of capillary pressure, viscosity, and effective pore diameter and generates an ionic sieve as a function of water and gas properties and nanoconfinement size.
3. Due to inherently small volumes of confined liquid, osmotic and diffusion potentials dominate the stability of gas bubbles (capillary trapping) and overall movement of, respectively, water and gas/solute in nanoconfinements as a function of concentration gradients. These movements are spontaneous and are hypothesized to affect or govern pressure-driven viscous flow in nanoconfinements. Osmotic pressure, Π_o, is the pressure required to prevent osmotic flow and is potentially influenced by Π_{EDL} and Π_{vdW}.

8.3.2 Suggested plan of future work

To understand, quantify and control how interfacial phenomena, specifically van der Waals forces, the electrical double layer, and osmosis and diffusion, affect anomalous liquid transport in nanoporous materials, the following 4 research tasks, most of them entire projects in themselves, are recommended:

1. **Continue probing liquid and multi-phase transport using nanofluidic experiments.** Nanochannel array style nanofluidic devices can be used to obtain controlled and observable geometries and direct observation of enclosed water movement with fluorescent and differential interference contrast (DIC) microscopy imaging. The sensitivity and interdependence of the hypotheses can be addressed with the following nanofluidic experiments: imbibition/drainage

with variations in salt and solute concentration and type, pH, and pre-treatment wetting films; trapped bubble experiments to decouple transport variables [182]; and application of reservoir-controlled solute concentration gradients for both imbibition (multi-phase) and single-phase flow.

2. **Continue the derivation of scalable phenomenological models to describe anomalous nanoscale transport.** Using the outcomes of experiments in Task 1, one can achieve enhanced estimates of the effective nanoscale values of P_c, effective channel diameter, d_{eff}, μ, and h_{pre} as a function of mainly: the **Hypotheses 1 variables of** channel diameter, d, and liquid, solid, and gas system ε_i and n_i properties (thus tuning Hamaker constant, A_H, values); and the **Hypotheses 2 variables** of d, liquid ε_w, N_i^0 , z_i, and Ψ. Nanoscale variation in mass flux J and concentration of the resident fluid, c_s^r, as a function of **Hypotheses 3 variables** solute concentration of the injected fluid/reservoir, c_s^i, k_H, D, and μ can also be formulated. These analytic or semi-analytic models can be rigorously derived from physical principles, using appropriate assumptions so that the models are scalable and practically implementable.
3. **Perform and validate molecular dynamics simulations.** The experimental work and resulting phenomenological models and theories can be complemented with molecular dynamics (MD) simulations using the Large-scale Atomic/Molecular Massively Parallel Simulator (LAMMPS, Sandia National Labs). Salt and solute concentration and type, pre-treatment wetting films, pH, and surface roughness can be varied and P_c, μ, d_{eff}, h_{pre} , J, and c_s can be simulated and compared with experimental results. Once the simulations and experiments match, the developed MD models can be used to explore conditions that are experimentally

difficult/unfeasible (for example, an exact control on surface roughness and charge).

4. **Utilize emergent nanoscale surface phenomena (the hypotheses) for enhanced flow control in nanoconfinements.** Using nanochannel array and nano-network patterned nanofluidic devices, the derived theoretical models of Task 2 can be used in experiments that tune a system's interfacial potentials and administer concentration gradients by fluid solvent and solute selection. The effect of this tuning on the aforementioned transport variables and resultant enhancement or decrease of liquid and multi-phase (trapped gas) transport efficacy can be evaluated; a selective sieving mechanism due to the EDL can also be evaluated. Further theory validation experiments can then be performed on controlled pore glass.

These research branches can generate the synergy depicted in Figure 8.2 and detailed subsequently.

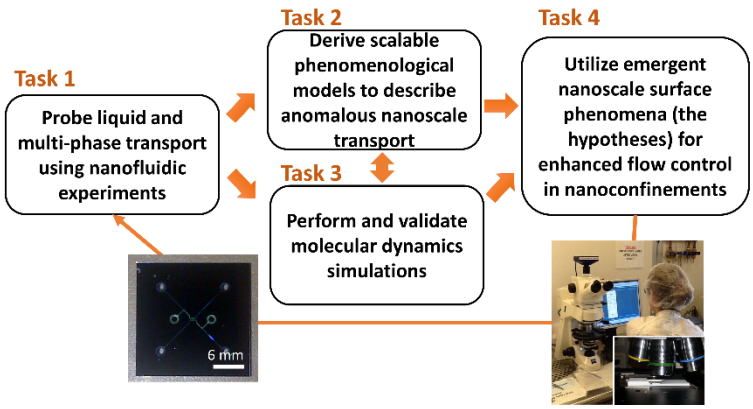

Figure 8.2: Diagram of the research tasks with photos of one of the nanofluidic chips used in this work and the Zeiss Axioskop 2 MAT microscope.

8.3.2.1 Task 1. Nanofluidic experiments probing water

A. *Water imbibition/drainage with variation in solute and material properties*

Hypotheses 1 and 2 can be tested by imbibition and drainage experiments of various electrolyte salt solutions to render front length-versus-time data as a function of nanoconfinement size; the tested nanochannel sizes should range from ~ 30 nm - 1μm in diameter. Monovalent (i.e. NaCl) and bivalent (i.e. $CaCl_2$) salt concentrations from 10^{-4} M - 1 M (which correspond to approximately 30 nm - 0.2 nm Debye screening lengths for NaCl) should be used. The surface charge (zeta potential) of the nanochannels can be varied by lowering or raising (lowering in the case of silica) pH from neutral to the isoelectric point of the confining materials. Nanochannel surface properties can be adjusted during chip fabrication by wafer and polymer substrate selection as well as uniform and non-uniform surface coatings and the introduction of bound liquid films. An indicator of experimental success will be a coherence to the data as a function of fluid properties and nanoconfinement size.

Imbibition spontaneously occurs, making it a simple actuation mechanism for experimentation. Drainage, pulling of a wetting liquid out of pore-space or fluidic geometry, can be achieved using a vacuum pump connected via a tube to a fluidic port; the interfacing setup necessary for drainage may present challenges in maintaining an unobstructed path between microscope objective and the thin roof of the channels (usually a glass coverslip) as well as preventing chip movement (loss of focus plane) during experiments. Relative humidity of a chip-containing chamber can be monitored. In addition, the surface chemistry of the entire chips, including inlet reservoirs, can be hydrophilic to support aqueous fluid studies.

B. *Water imbibition with trapped air slugs*

Hypotheses 1, 2, and 3 can be tested by evaluating and decoupling effective nanoscale values of P_c, μ, D, and k_H and comparing their divergence from respective bulk values. The cases where divergence is non-negligible will indicate a strong influence of surface forces on transport (to be better understood in Task 2).

Nanoscale transport is highly sensitive to specific surface-liquid-gas combinations; therefore, the trapped bubble or air slug experimental method presented in Chapter 4 can be implemented. Parallel nanochannels are ideal for this method, as liquid imbibes from two opposing reservoirs giving rise to a trapped air slug. The concentration of dissolved gas in the experimental liquids can be controlled with aeration or degassing by means of sonication and a vacuum. To minimize variables, only two salt concentrations, low (10^{-4} M) and high (1 M), should be tested when gas concentration is varied. In other experiments, the concentration of gas can be kept constant (high gas saturation actually simplifies the problem) and the fluid properties varied as they were in Task 1.A. The experimental results can allow an assessment of the adequacy of bulk solutions properties for various aqueous liquids and nano-confinement conditions. An indicator of experimental success will be a coherence of the data as a function of fluid properties and nanoconfinement size. The trapped gas initially tested should initially be air due to experimental constraints with interfacing other gases. Such interfacing and fluid introduction can be challenging, but microscope-specific incubation modules for temperature control and gas introduction and perfusion chambers for fluid introduction are common in the biological sciences and may be of use. Note that a major obstacle of these chambers and interfacing mediums, encountered during this work, is maintaining an unobstructed path between microscope objective and the thin roof (usually a glass coverslip) of the channels.

C. *Flow actuation by solute concentration gradients*

Hypotheses 3 can be tested by comparing imbibition speeds in the presence of solute concentration gradients to Task 1.A. If imbibition is slower in this case (all other conditions being the same), then osmosis plays an important role in nanoscale liquid actuation. If fluorophore diffusion varies with salt concentration, then the presence of the EDL leads to restricted diffusion.

Implementation of concentration gradients is relatively simple; it requires filling the nanochannels and adding a solute species to one inlet/reservoir that is less than the resident concentration in the nanochannels. Salt concentration gradients can be implemented during imbibition by immediately following the addition of a low salt concentration or deionized solution with a higher salt concentration solution. The same range of salt concentrations used in Tasks 1.A-B can be tested and length-versus-time data can be recorded. For completely filled nanochannels (single-phase flow), fluorophores can be used to observe motion down and up concentration gradients; i.e., diffusion and osmosis. Testing with neutral (e.g., Rhodamine B), positive (e.g., Rhodamine 6G), and negatively charged (e.g., Fluorescein) fluorophore molecules is advised. During this work, it was found that quantum dot nanoparticles (Cytodiagnostics; 2 nm in diameter) were observable and useful tracers. Gas concentrations can be varied in this scheme as well to probe the effect of the EDL on diffusive properties (i.e. restricted diffusion).

8.3.2.2 Task 2: Advance the derived phenomenological models and their scalability

A. *Continued formulation of the effects of van der Waals forces and the EDL on transport*

Chapter 6 presented preliminary phenomenological models for liquid menisci and effective diameter, among other variables, are derived based on results in 2D

nanochannels. The implications of emergent nanoscale phenomena differ from some popular conceptions of nanoscale transport (e.g., slip flow). However, further development and validation of these models and their scalability is necessary. In particular, non-aqueous fluids were mainly used within the previous work and the effect of the EDL on transport was left relatively unexplored. In addition, 3D derivations are typically necessary in nanopores and the errors associated with approximations such as the Derjaguin Approximation [236], used to reach relatively concise solutions, should be examined. Descriptions of effective transport variables informed by available macroscopic or continuum fluid and solid properties should be sought to enable scalable relations. A summary of such variable dependencies is depicted in Figure 8.3.

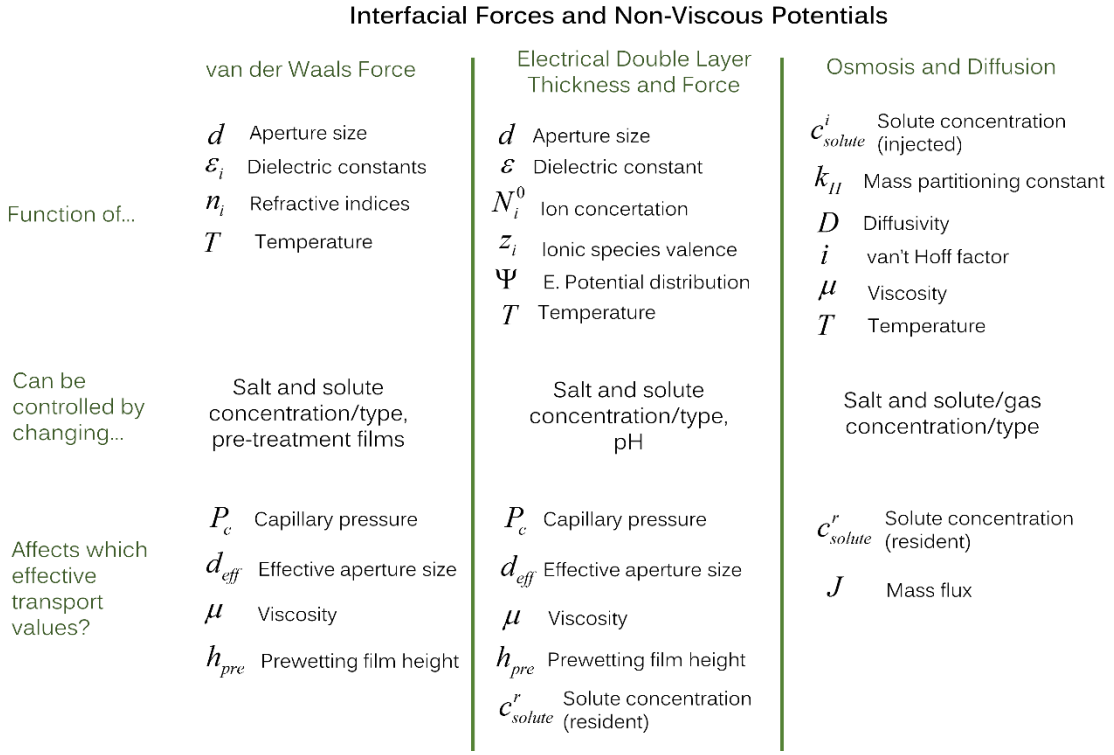

Figure 8.3: Roadmap of the variable relationships between liquid/solute properties, surface forces and gradients, and relevant transport parameters.

B. *Nanoscale Transport Models for Hypothesis 3: Dominance of concentration gradients*

Hypothesis 3 can be theoretically verified by achieving estimates of the variation in mass flux J and csr as a function of csi, solute concentration of the injected fluid/reservoir, k_H, D, and μ by changing salt and solute concentration and type. Osmosis is well established as the movement of water across a semi-permeable membrane to achieve concentration equilibrium. Osmotic pressure for low concentration solutions can be described by the Morse equation, $\Pi_0 = ic_a RT$, where i is the van't Hoff factor and R is the ideal gas constant. These gradients may dominate over viscous flow as an actuation and transport mechanism; an appropriate dimensionless number can be derived to access dominance. Nanochannels or nanoporous materials are the semi-permeable membranes of the studied systems and derivations (using momentum and mass balances across control volumes) of the impact of osmotic pressure on imbibing fluid can be sought. In addition, models can be developed to honor the possible hindrance of solute movement (osmotic or diffusive) by the presence of structured boundary zones at solid-liquid interfaces and EDL zones.

8.3.2.3 Task 3: Validate models with molecular dynamics simulations

The experimental work and phenomenological models should be complemented with molecular dynamics (MD) simulations. Substantial computational times and the memory-intensive nature of MD simulations render them an impractical method for models requiring more than a localized study and/or simulated times longer than several pico- or nano-seconds; these limitations must be taken into account in planned configurations.

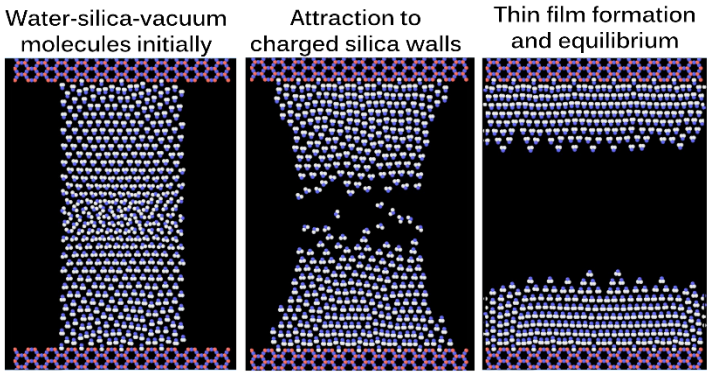

Figure 8.4: Preliminary MD simulations with silica and deionized water. For reference, the established diameter of a water molecule is approximately 2.8 Å.

The open-source MD code Large-scale Atomic/Molecular Massively Parallel Simulator (LAMMPS, Sandia National Labs) can be used to help further elucidate how surface effects, such as adsorption, potentials, and roughness, govern transport in nanopores and allow the examination of configurations, fluids, and boundary conditions not feasible with the nanofluidic investigations. LAMMPS is advocated for MD investigations due to its strong parallel performance, relative ease in code modification, comprehensive built-in library of intermolecular potentials, and its ability to conveniently produce simulation movies/visuals. Access to a supercomputing center will greatly assist this investigation.

A. *Code development: simulate a meniscus region and extract variables of interest*

Hypotheses 1 and 2 can be explored through the simulation of a meniscus zone, which can allow solid-liquid and solid-liquid-gas interfaces to be simultaneously studied. **Hypotheses 2 and 3** can be explored through the simulation of a reservoir to nanochannel juncture, which allows the investigation of selective sieving by the EDL and osmotic flux over a reliable control volume. The first setup can be a nanoscale aperture (2D) or nanochannel (3D) between two fluid reservoirs, one gas molecules and the other

water molecules; there can be moving walls on the reservoirs to introduce a piston-like control of pressure. The second setup can be similar to the former with the exception of only one moving wall/piston and a periodic boundary condition on the other end of the nanochannel. The TIP3P model can be used for water and the solid molecules can be silica or polymer (depending on the chip type used in the experiments to be matched). As long-range electrostatic effects are expected to be important, we can use potentials employing Ewald summation. Figure 8.4 displays a preliminary 2D model of water in a silica nanoconfinements. As described below, 2D simulations can be used to explore the qualitative mechanisms underlying anomalous nanoscale fluid transport. Once the qualitative concepts are settled, one can perform larger 3D simulations using supercomputing resources to provide more realistic comparison with experiment. Note however that even for nanoscale channels it can be impossible to match the length and particularly the time scales reached in experiments. Thus, simulations should be run at steady-state conditions for small spatial regions of the system (i.e., "snapshots" during the imbibition process) that can then be extrapolated to experimental conditions.

B. *Match simulations and experiments and fine tune phenomenological models*

Experiments in the nanofluidic systems have a duration on the scale of seconds to minutes, while molecular dynamics simulations cannot follow times larger than a nanosecond. Thus, a theoretical framework is required to bridge the space and time scale gaps between molecular simulation and experimental conditions. An example of how this sort of bridging can be done is given by molecular dynamics simulations of fracture that were directly compared against experiment [237]. For imbibition the appropriate framework may be simulation velocity.

C. *Vary parameters not feasible or easily controllable with nanofluidic investigations*

Surface roughness, surface charges and conditions (e.g. dangling oxygens or silanols [238]), and temperature are challenging to precisely regulate with the experimental setup described in Chapter 3, and, thus, can be explored with the MD simulations once the models and experiments are in agreement. By varying these parameters, the simulations can enable testing of the robustness of the derived phenomenological models.

A particularly intriguing feature of anomalous transport on the nanoscale is the deviation of flow properties from the Washburn equation as time progresses. The flow slows more than the continuum theory predicts, and eventually almost completely stops. An important goal is to understand the qualitative basis for this phenomenon; the MD simulations can help delineate what mechanisms are responsible and allow investigations of previously unexplored possibilities such as pinning phenomenon in which the fluid interacts with the walls of the channel and contact angle hysteresis. Various possible mechanisms, including channel roughness and strong interactions of charged species can also be investigated.

Another in-depth modeling approach is the development of "hybrid models" which model the bulk fluid as continuum and the boundary layers with molecular dynamics, linking the two together in an overlap region [239]. Considering that the smallest dimensions of the nanochannels in the experimental setup are currently 30 nm it is a fair assumption that modified LBM simulations, which incorporate the distribution of forces from the interfacial boundaries, may be a suitable and computationally realistic modeling method for comparison with the experimental results.

8.3.2.4 Task 4: Utilize emergent nanoscale phenomena for enhanced flow control in nanoconfinements

The above nanoscale investigations are designed to study the influence of interfacial interactions and concentration gradients on nanoscale fluid imbibition/two-phase flow and single phase flow. The next step will be to validate these models and demonstrate the hypotheses can be engineered for practical advantage.

A. Predict/control transport in nanofluidic devices as a function of fluid properties

This dissertation provided the foundation for facile construction of nano-network chips (Chapter 3), but experimental work in these configurations was limited. Both the array-style and nano-network nanofluidic devices described in Chapter 3 can be used in the validation experiments. In situ fluid analysis can be performed in these chips using the methodologies described in Task 1 (imbibition/drainage, orchestrated trapped air slugs, and applied concentration gradients). However, a broader range of solute concentrations and nanochannel materials/coatings can be used to test the validity of the derived phenomenological models (Task 2). For the nano-network devices, mapping of the spatial distributions and overall saturations of multiphase fluids within the nano-networks can be captured over time. Accurate prediction of imbibition rates and fluorescent solute movement in the nanofluidic configurations (within practical experimental errors) can provide model validation. The fluid testing methods are designed to be relatively simple in that they only require filling one of more of the chip reservoirs with the tested fluids, therefore a potential challenge is that the experiments are only limited by nanofabrication and microscopy resolution. The nano-network experiments can aid in assessing the scalability of the proposed models. A fundamental question uniquely addressed by experiments in nano-network chips is the role of network

geometry at the nanoscale and how anomalous transport trends observed in nanoporous media are a function of media geometry (pore connectivity, tortuosity, etc.) in addition to breakdowns in continuum transport [176].

B. *Predict/control transport in controlled pore glass as a function of fluid properties*

Controlled pore glass (CPG) such as Vycor 7930 or Schott CoralPor (see Figure 8.1.C), zeolites, nanoporous metals (e.g. gold), and hydrogels such as agarose are examples of obtainable and practical nanoporous material for fluid flow experiments [240] [241]. However, for opaque nanoporous materials, visualization is a challenge and indirect data methods must be used, which introduces more variables. Thus, sheets of Vycor or CoralPor CPG can be obtained and cut into microscope slide sizes (25 mm × 75 mm) and then thermally fused to nanoporous glass coverslips (to construct impermeable boundaries) and sealed at the sides. CPGs are water wet and the flow methodologies described in Task 1 (imbibition/drainage, orchestrated trapped air slugs, and applied concentration gradients) can be applied to these nanoporous material chips. CPGs range in average pore size from ~ 4 - 400 nm [242] and have successfully been used in water imbibition experiments [243]. Fluorescent and DIC microscopy can be used for capture of new liquid fronts. Accurate prediction of imbibition rates and fluorescent solute movement in the CPGs (within practical experimental errors) can provide model validation. The CPG experiments can aid in assessing the scalability of the proposed models. If the scaled phenomenological models do not give accurate predictions then the role of network geometry can have to be revisited in Task 4.A.

For large-scale nanoporous networks such as in CPGs, the use of a trapped bubble or air mass to introduce an additional force may not induce an appreciable force on the fluid until late times (the size of the trapped air mass can depend on the size of the sample

and the concentration of gas in the incoming liquid). Thus, another source of significant pressure, $P_{ext}(t)$ can be implemented for bulk samples in place of the bubble pressure used in the nanofluidic devices. $P_{ext}(t)$ variations are discussed in Section 4.4.

C. *Selective sieving mechanism*

Hypothesis 2 implications can be tested by controlling the EDL thickness and passing charged molecules through the sample. Recall that the EDL thickness is controlled by the ion concentration of the fluid in that it is inversely proportional to that concentration. The EDL thickness can be fine-tuned in consecutive trials such that its thickness (which can reach around 100 nm for very low ionic concentration fluids) equals a specific pore throat radius. If EDL regions from two walls of a pore overlap the conduit can serve as a *nanofluidic diode*, allowing only the passage of primarily counter-ions and counter-charged molecules.

Selective sieving experiments can be performed in both nanofluidic devices and the CPG chip-style configuration described in Task 4.B. In the various chips the response of positive (e.g., Rhodamine 6G) and negatively charged (e.g., Fluorescein) fluorophore molecules or tracers to the EDL can be observed. Parameters to control in these experiments include salt concentration and fluorescent tracer molecule concentration. Note that an electric field can be applied across the sample to provide a bias potential for the fluid and molecular tracers, but that tracer diffusion from a chip fluid reservoir (a simple mechanism) is expected to be sufficient for the experiments. If both salt and tracer particles (such as fluorescent quantum dots) are used, a lower spectrum of salt concentrations can be used to promote larger EDL extents and prevent particle clustering (by maintaining a repulsive EDL force between particles as calculated by DLVO theory [77]). The fluorophore used for the initial experiments can be neutral and driven by fluid

flow alone. In the next experiment, a positively charged fluorophore mixed in an aqueous solution of very low salt concentration can be introduced across the sample in a similar fashion. Salt concentration can be progressively increased and the progression of tracer molecules observed. This same procedure can be repeated for decreasing salt concentration (dilution) as well. In theory, positively charged tracers cannot enter nanochannels of radii smaller than the EDL thickness corresponding to the salt concentration. For the CPGs, this threshold can correspond to the average pore size. Thus, the ability for tracer molecules to diffuse through a channel or CPG medium can reveal EDL thickness and allow comparison against theory.

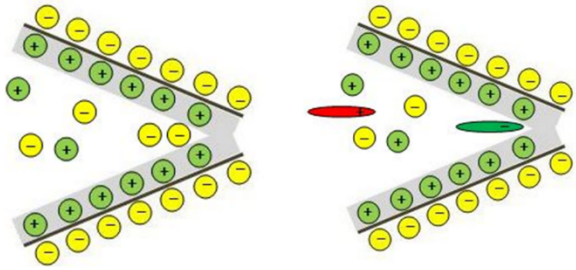

Figure 8.5: Cartoon illustrating how the EDL creates a nanofluidic diode for oppositely charged ions and molecules in a pore-like constriction. Illustration inspired by Abgrall and Nguyen [58].

8.3.2.5 Additional ensuing research tasks

A. *Nanofluidics experiments with potentials variation*

Application of electric potential, chemical potential, thermal, concentration, and pressure gradients across the chips through interfacing equipment will enable a study of the effects of these gradients on fluids and tracers. Due to the very shallow depth of the

nano-networks, movement of the chips must be avoided during external equipment interfacing and fluidic observation, lest the focus plane may be lost. Electric potential gradients can be applied with integrated electrodes and an applied voltage difference. Thermal gradients may be achieved with the integration of miniature Peltier stages strategically placed on certain chip locations; note; however, that the necessity of sufficient heat sinks may be a spatial obstacle for this method. Pressure gradients were found to be best controlled by initiating a vacuum at the chip outlets; syringe pumping worked well for wetting fluids only. Chemical potential can be adjusted during chip fabrication by uniform and non-uniform surface coatings, as well as by the introduction of liquid films. Concentration gradients, perhaps the simplest to implement of the discussed methods, require adding a certain species to one inlet/reservoir.

A more specific example of a thermodynamic nanofluidic approach is inserting fluids of interest into the chips and sealing off the device's inlets/outlets, trapping those fluids within the inner channels or networks. Placing the device on a Peltier stage or in a microscope incubation chamber and varying the system temperature can induce phase changes. Preliminary phase diagrams for nanoconfined fluids can potentially be obtained with this scheme. Relative humidity of a chip-containing chamber may be a parameter that can also be readily tuned.

Proposed experiments/analysis in the network style nanofluidic devices in addition to imbibition/drainage tests include, but are not limited to:

- Mapping of the spatial distributions of multicomponent and multiphase fluids within the nano-networks over time. This temporal mapping can be achieved by inserting two liquids doped with different fluorescent dyes, such as water and oil,

from different chip inlets and initially trapping air or a pure gas (if it can be interfaced) in-between.

- Investigation of the time scales of communication between the dual-porosity features of the chips, the minor (matrix) and major (microfracture) patterns.

B. *Investigations with electron microscopy imaging techniques*

Beyond optical microscopy (necessary for dynamic measurements) and FIB-SEM (useful for 3D nanoscale sample characterization), an Environmental-SEM (with Peltier temperature and low pressure control options) can be used for ancillary nanofluidic flow experiments and sample characterization. The sample holder of an ESEM Peltier stage is typically around 10 mm in diameter. This instrument enables nanoscale observations of condensed water on shale samples prepared to this size (mounted on a small metal disc) as well as on synthetic nanoscale configurations such as TEM grids with lacey and holey carbon support films and small pieces of Blu-Ray discs. It is possible that SEM images of nanoscale menisci as a function of pressure and temperature can be captured with this method as well.

C. *Thin water films as motors*

Extensions of this research may focus on utilizing interfacial and thin film properties as a means of fluid transport. Investigators can take advantage of the naturally occurring and relatively large EDL present in nanoconfinements with electric field driven actuation rather than pressure-driven flow. Conlisk et al. found that voltage driven volumetric flow in 1D nanochannels varied linearly with nanochannel height; this dependence is opposed to pressure driven flow, which varies with height cubed, indicating that voltage driven actuation is a more effective mechanism for driving flow in nanoporous media than applying very large pressure drops [244]. In Chapter 6, the

positive effect of thick precursor films on imbibition were discussed in terms of preventing rupture and pinning. In addition, it is hypothesized that at certain conditions these thin films can serve as motors for flow, actuating confined fluids by means of shear. Assessment of the response of aqueous fluids and assemblages of thin film systems (e.g. hydrocarbon between water films) to electric field actuation in nanofluidic configurations is needed. Imbibition into an already wetted domain and single phase flow can be pursued for these experiments.

D. *Selective sieving in shale samples for novel core analysis*

The selective sieving phenomenon which can be made into a novel shale sample analysis technique that estimates connectivity, permeability, and pore size distribution by controlling the EDL thickness and passing charged molecules through the sample. In fact, most surfaces have an induced charge when in contact with an aqueous fluid, organic matter included, and thus have the capacity for EDL formation. The EDL thickness can be fine-tuned in consecutive trials such that its thickness (which can reach around 100 nm for very low ionic concentration fluids) equals that of a specific pore throat radius. If EDL regions from two walls of a pore overlap the conduit will serve as a nanofluidic diode, allowing, upon flow, the passage of primarily counter-ions and counter-charged molecules. Figure 8.5 illustrates the concept of certain charges having greater mobility within a pore constriction due to electrostatic effects.

To assess initial permeability of the sample to molecular tracers a high salinity solution can be first used. This high concentration can reduce the EDL size and minimize clay swelling. Outlet measurements across the small sample can produce a reading of fluorescent intensity versus time (fluorescent intensity is indicative of concentration). The fluorophore used for the initial trial can be neutral and driven by fluid flow alone. Next, a

positively charged fluorophore mixed in an electrolyte of lesser salt concentration can be introduced across the sample in a similar fashion. Approximately, this tracer cannot enter throats of radii smaller than the corresponding EDL thickness for that concentration and can accumulate in pores where this threshold exists. Via its unique absorption and excitation wavelengths, the fluorescent intensity/concentration of this specific fluorophore can be measured over time at the outlet. This same procedure can be repeated many times for decreasing salt concentrations and unique fluorophores. Between trials the sample can be thoroughly flushed out with high salinity, fluorophore-free water by means of electroosmotic flow. Since the use/control of the EDL as an electrostatic sieve may determine the minimum pore size through which fluorophores can pass comparison of the various tracer concentration profiles can help elucidate the connection between pore size distribution and connectivity in shale. For example, when the EDL is very large, if not much tracer makes it to the outlet this would suggest that a certain pore size threshold lower than that EDL threshold is crucial to the permeable network. Overall, the concept takes advantage of a naturally occurring phenomenon unique to nanoconfinements. The details of the experimental setup for selective sieving tests may be challenging; however, one possible approach to the set-up is integrating small samples such as loose chips of core or cuttings into microfluidic chips most probably made of PDMS.

> *There is nothing like looking, if you want to find something. You certainly usually find something, if you look, but it is not always quite the something you were after.*
>
> J.R.R. Tolkien, *The Hobbit* (1937)

Appendices

APPENDIX A: FURTHER DETAILS ON "SHALE-ON-A-CHIP" FABRICATION

A.1 Pictures from the Shale-on-a-Chip Fabrication Workflow

These following compilation of photos from our fabrication process are intended to aid those replicating the process.

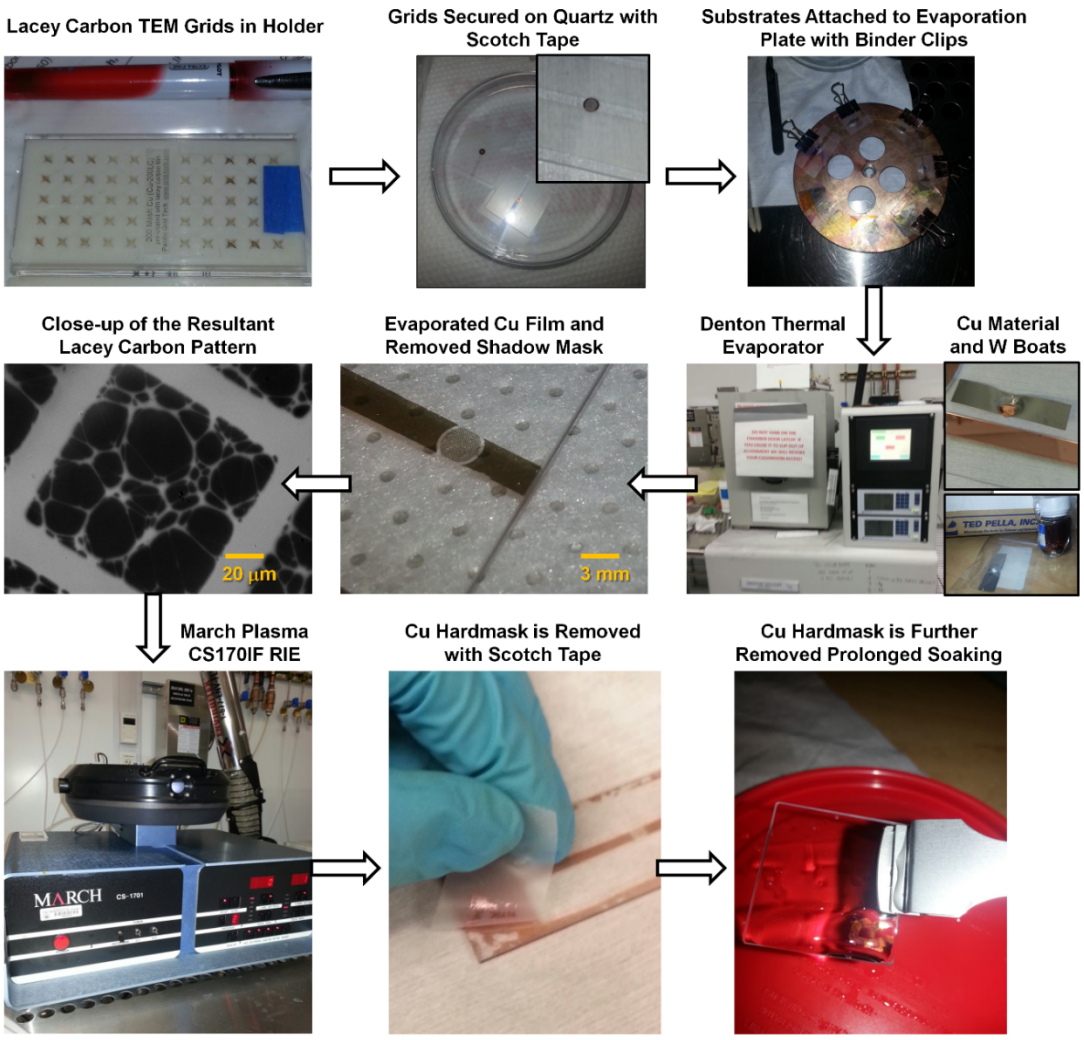

Figure A.1: Photos of the main steps of the reservoir/shale-on-a-chip fabrication process.

A.2 Reactive Ion Etch Recipe Tuning

Reactive ion etch (RIE) recipe tuning with the March Plasma CS170IF revealed that higher radio frequency (RF) power and longer chamber times resulted in better quality etching.

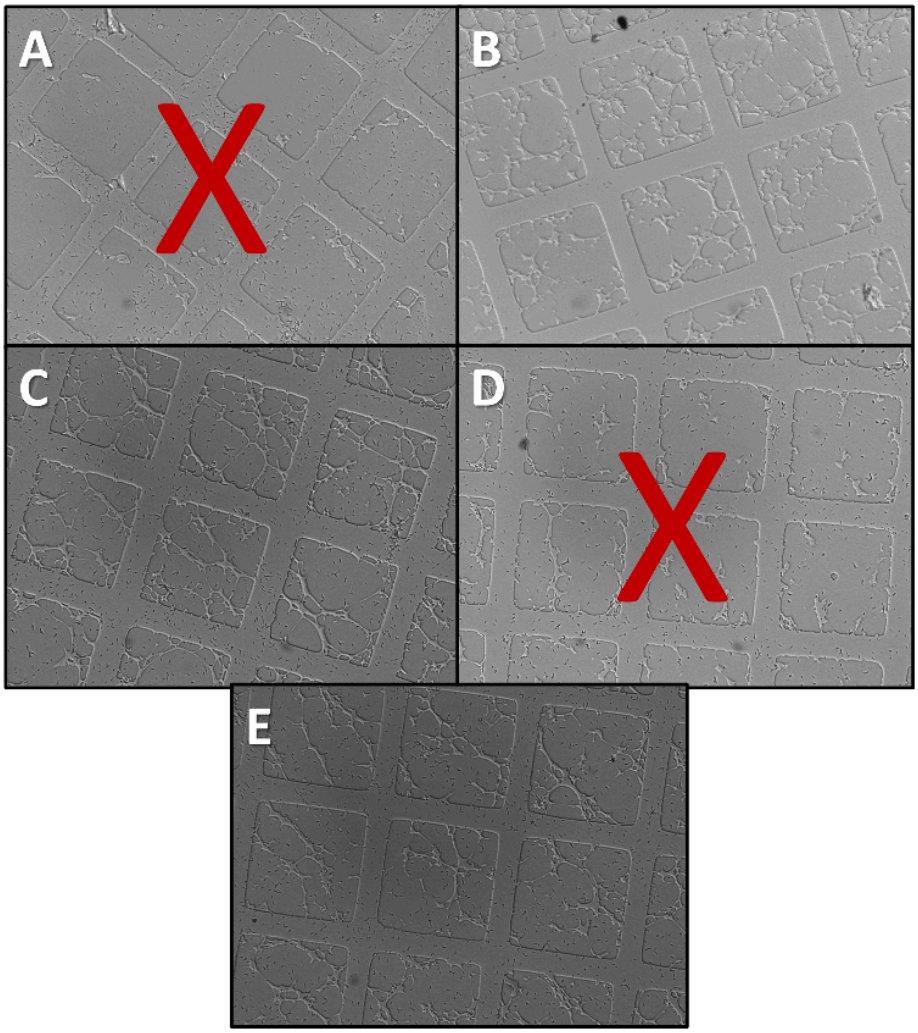

Figure A.2: Results of different RIE etching formulas as indicated in Table A.1. Letters correspond to the Trial IDs.

CF_4 Reactive Ion Etch Recipe Results with a March Plasma CS170IF

Trial ID	t (s)	CF_4 Flow Rate (sccm)	Base Pressure (mTorr)	RF Power (W)	Etch Quality
A	**120**	10.5	80	**200**	Poor
B	**120**	10.5	80	**250**	Good
C	**120**	10.5	80	**300**	Good
D	**240**	10.5	80	**150**	Poor
E	**240**	10.5	80	**200**	Good

Table A.1: CF_4 reactive ion etch recipe results with a March Plasma CS170IF

A.3 Scanning Electron Microscope Imaging Parameters

The scanning electron microscopes (SEMs) used were a JEOL SEM JSM-6490 and a FEI XL30 Environmental-SEM. The former was used in high vacuum mode only and the latter was used in both high vacuum and low vacuum (at a pressure of ~ 0.1-0.3 torr) modes. The detectors used in high vacuum mode were the Everhart-Thornley and the BSE detectors and the GSED was used in low vacuum mode. When viewing in high vacuum mode a thin layer of gold was deposited on the samples with a Denton Gold Sputter unit. The sputter time for the gold film ranged from 15-60 s among the samples; I conjectured that a thinner layer of gold may be best since the thickness of the deposited gold layer is on a similar order of thickness to that of the nano-structures. For the low vacuum mode no ancillary sample preparation was needed.

In regard to imaging settings I viewed the samples at a range of accelerating voltages (5-30 kV) and spot sizes (30 - 90 nm) and found, to our initial surprise, that visualization of the sample was extremely difficult at high accelerating voltages and small spot sizes, settings characteristic of high resolution imaging. This may be because the investigation volume of incident electrons increases with stronger beam energy or

accelerating voltage. A larger depth of investigation potentially equates to less signal from the thin surface features which are ~ 20 nm high features in this case. A smaller spot size can equate to gaps between dwell points where signal is not generated (perceived graininess). This graininess was especially pronounced with the thin film nano-structures. Indeed, looking into the literature, most papers featuring thin film type SEM images use accelerating voltages on the order of 5 kV and very small working distances [245]. Likewise, I found images improved at shorter working distances, but I were limited in this parameter when desiring to tilt the sample. The maximum tilt I were able to achieve was 45˚ (in the JEOL). It was hoped semi cross-sections of some of the nanochannel networks could be gleamed in tilted views, but due to the shallowness of the structures, there was only moderate success with this goal. I found the optimum parameters for imaging the thin film nano-structures to be an accelerating voltage of ~10 kV, a spot size of 60 nm +, and a working distance of 10 mm or less. Additional techniques that improved the image quality were the use of Aperture 1, the smallest aperture, in the JEOL and using a cleaner pole piece in the frequently used FEI.

APPENDIX B: 3D NANOSCALE CAPILLARY PRESSURE

B.1 Approximation of Nanoscale Capillary Pressure in 3D

A 3D meniscus in a cylindrical pore of radius R (D/2) can be considered to be a series of local 2D meniscus film systems whose aperture height, S, changes with the radial distance, r, along the pore. S is determined by the length of a geometrical chord and the average of the disjoining pressure in the cylindrical pore renders $\overline{P}_c^{n,3D}$, the average 3D nanoscale capillary pressure, namely,

$$\overline{P}_c^{n,3D} \approx P_c^m - \frac{1}{R-h_{pre}} \int_0^{R-h_{pre}} \left(\frac{\int_{h_{pre}}^{(S-d_g)/2} \Pi_m(h,S)dh}{\frac{S-d_g}{2}-h_{pre}} \right) dr \ , \tag{B.1}$$

with

$$S = 2\sqrt{R^2 - r^2} \ . \tag{B.2}$$

Per the Derjaguin approximation [71], the local disjoining pressure of a curved surface with a certain film system and thickness is approximated by the disjoining pressure of a flat surface with the same film system. Using this approximation I integrate along the geometrical cords of the circular area. An estimate of $\overline{P}_c^n$ for a symmetric 3D meniscus with regions of constant and non-constant curvature in the presence of an adsorbed or precursor film of height h_{pre} and within a planar channel or pore space of height D is given by:

$$\overline{\Pi}_m = \frac{\mathrm{A}+\mathrm{B}}{6\pi\left(R-h_{pre}\right)} \tag{B.3}$$

$$\mathrm{A} = \left[\left(\frac{-A_{123}}{2a^2} + \frac{A_{123}}{8(a-2)^2} + \frac{-A_{232}}{2(a-1)^2} \right) * \right.$$

$$\left. \left(\frac{R\left(\tan^{-1}\left(\frac{h_{pre} r}{\sqrt{h_{pre}^2 - R^2}\sqrt{R^2 - r^2}} \right) + \tan^{-1}\left(\frac{r}{\sqrt{h_{pre}^2 - R^2}} \right) \right) + \sqrt{h_{pre}^2 - R^2}\, \tanh^{-1}\left(\frac{r}{R} \right)}{h_{pre} R \sqrt{h_{pre}^2 - R^2}} \right) \right]_{r=0}^{r=R-h_{pre}}$$

(B.4)

$$\mathrm{B} \approx \left[\left(\frac{-A_{123}}{2} \right) \left(\frac{\sqrt{h_{pre}^2 - R^2}\left(\tan^{-1}\left(\frac{r}{\sqrt{R^2 - r^2}} \right) \right)}{h_{pre}^2 \sqrt{h_{pre}^2 - R^2}} + \right. \right.$$

$$\left. \left. \frac{h_{pre} \tan^{-1}\left(\frac{h_{pre} r}{\sqrt{R^2 - r^2}\sqrt{h_{pre}^2 - R^2}} \right) - h_{pre} \tanh^{-1}\left(\frac{r}{\sqrt{h_{pre}^2 - R^2}} \right)}{h_{pre}^2 \sqrt{h_{pre}^2 - R^2}} \right) \right]_{r=0}^{r=R-h_{pre}}, \qquad \text{(B.5)}$$

where a = 1 - d_g/S. The term B is approximate because I assume $h_{pre} << R$ for simplification purposes, a reasonable assumption for nano-confinements greater than 10 nm in diameter. Without this assumption the solution to the ODE is tediously long (that is, the above form is comparatively concise), but can be solved and displayed with a software such as Wolfram *Mathematica*.

B.2 Determination of Hamaker Constants for Retarded van der Waals Forces

Hamaker constants in the retarded regime differ from those in the non-retarded regime, are often denoted by B_H, and are calculated by [68]:

$$B_H = \hbar c \frac{\pi^2}{240}\left(\frac{\varepsilon_0 - 1}{\varepsilon_0 + 1}\right)^2 \phi(\varepsilon_0) \ , \tag{B.6}$$

where $\hbar$ is the reduced Planck constant, c is the speed of light, ε_0 is a medium's dielectric constant, and $\phi(\varepsilon_0)$ is a function whose value lies between 0 and 1 and is commonly taken to be $69/(2\pi^4)$.

Retarded Hamaker constants for the experimental fluids

Fluid or Solid	B_{22} (10^{-28} J)	B_{123}(10^{-28} J)	B_{232} (10^{-28} J)
heptane	2.74	-1.92	2.74
methanol	25.64	11.37	25.64
decane	3.21	-1.84	3.21
isopropanol	23.23	9.65	23.23
Water	27.52	12.74	27.52
Acetone	23.91	10.13	23.91
Silica	7.94	---	---

Table B.1: Retarded Hamaker constants for the experimental fluids

B.3 Diffusive and Non-Diffusive Imbibition Trends in Nanoporous Materials

Imbibition power law trends for various liquids and nanoporous materials

Liquid	Nanoporous material	r_{avg} (nm)	Data type	Fitted *n*-value	R^2	Ref
liquid helium	silica aerogel (90% porosity)	10	length vs. time	0.51	0.999	[246]
1 M KOH	nanoporous gold	45	mass vs. time	0.41	0.885	[241]
DI water	Vycor	5	mass vs. time	0.49	0.998	[247]
C_{16} aliphatic hydrocarbon	Vycor	5	mass vs. time	0.44	0.999	[247]
liquid crystal (8OCB)	Vycor	5	mass vs. time	0.47	0.995	[247]
7:3 water/ethanol mixture	polystyrene microbead assemblages	150	length vs. time	0.65	0.999	[248]
3:7 water/ethanol mixture	polystyrene microbead assemblages	150	length vs. time	1.13	0.999	[248]
brine	zeolites	0.4	mass vs. time	0.34	0.999	[249]
DI water	carbon molecular sieves	< 1	displaced gas recovery vs. time	0.40	0.933	[250]
DI water	Barnett shale	ranges	mass vs. time	0.26	0.999	[175]

Table B.2: Imbibition power law trends (*n*-values) for various liquids and nanoporous materials extracted from data sets from the literature. Most experiments were run near standard ambient temperature and pressure conditions, with the exception of the liquid helium experiment (run at 2.5 K).

APPENDIX C: ADDITIONAL EXPERIMENTAL IMAGES OF INTEREST

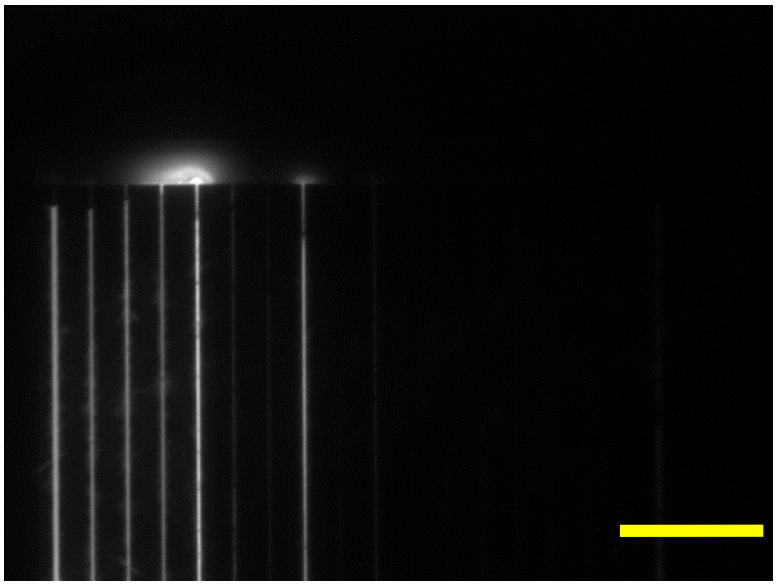

Figure C.1: A fan-like discharge of IPA emanates from some mid-sized nanochannels ($\geq$ 100 nm × 60 nm) while in others captured in this photo the meniscus front stops just short of the channel outlet; the yellow scale bar is 16 μm.

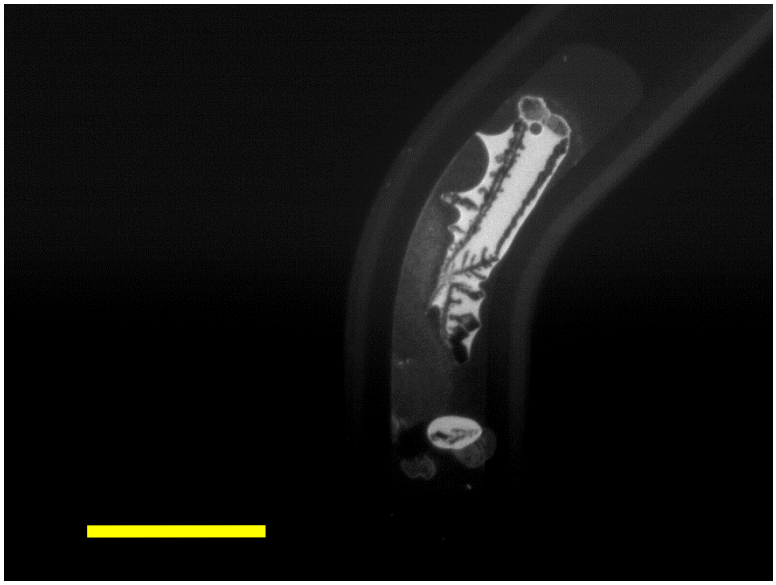

Figure C.2: A dendrite crystal formed from DI water and Rhodamine B atop a platinum film in a nano-slit; the yellow scale bar is 80 μm.

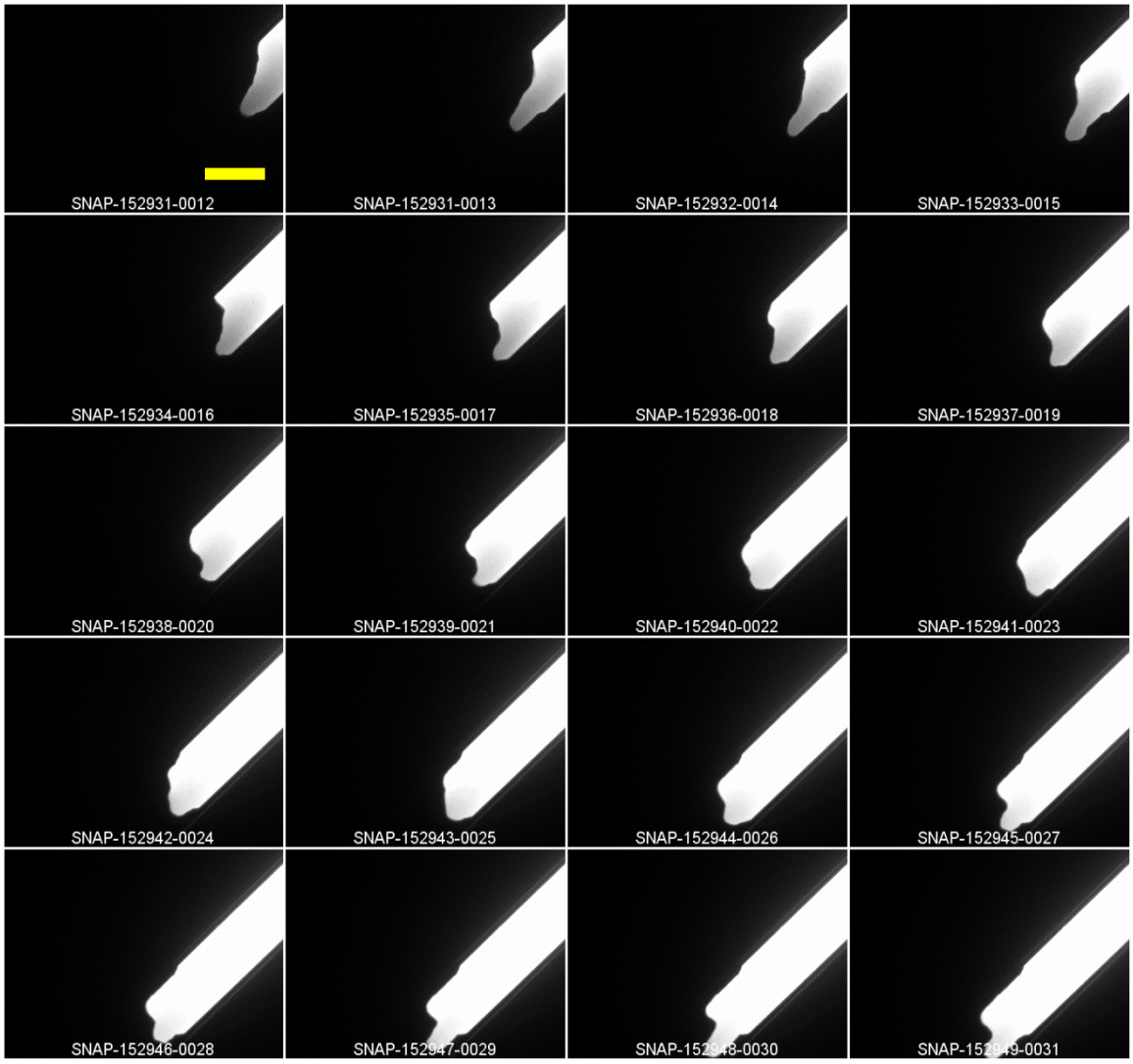

Figure C.3: Dynamic visualization of a lateral isopropanol meniscus imbibing over silica in one of the nano-slits (low aspect microchannels); the yellow scale bar is 80 μm. The snapshots are presented in order from left to right and row by row, as indicated by the numbers at the end of the image names following the timecodes. The front is very unstable, but was stable on the platinum portions of the nano-slits (see Figure 5.17).

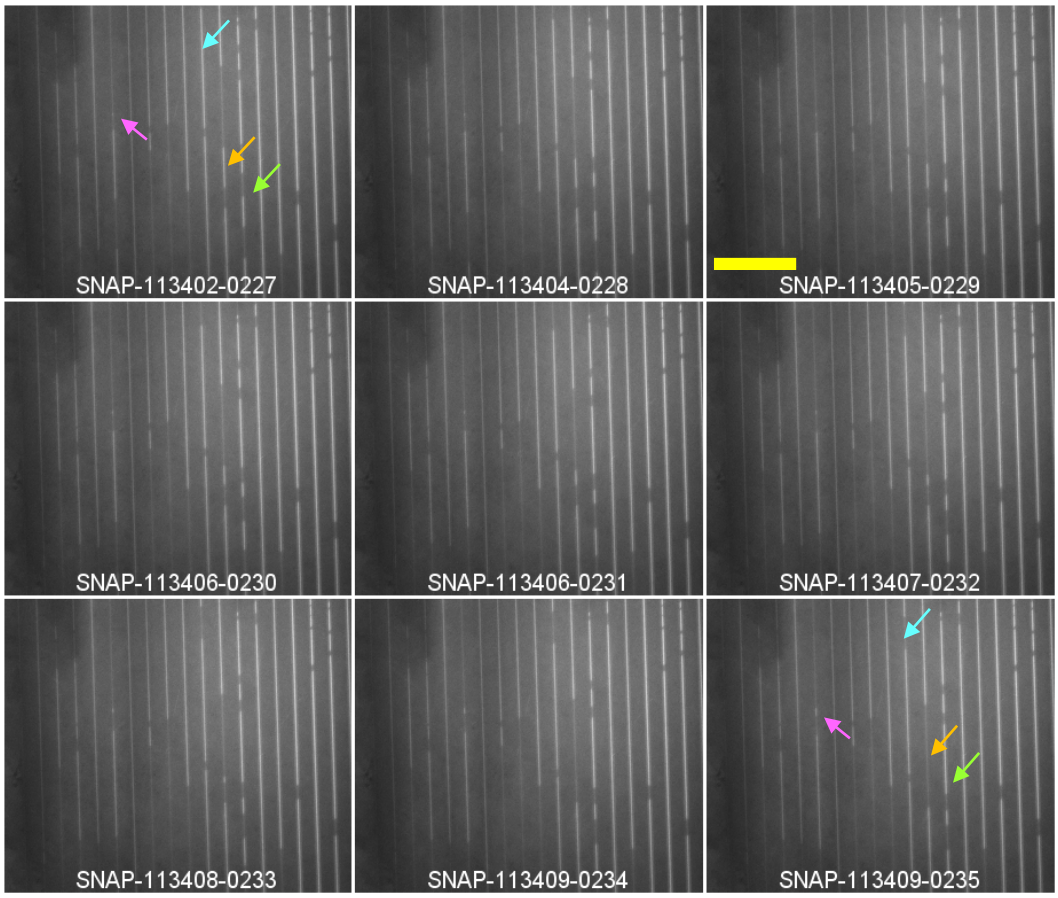

Figure C.4: Images of gas slug movement in a compromised nanofluidic chip (compromised due to leakage between channels in very narrow apertures, as indicated by the faint background fluorescent signal); the yellow scale bar is 18 μm. The snapshots (part of a longer sequence of images) are presented in order from left to right and row by row, as indicated by the numbers at the end of the image names following the timecodes. Colored arrows indicate some areas of major changes in liquid/gas position between the first and last image. The movement and fairly constant (with time) shape of the gas slugs indicates that the liquid (isopropanol) is too saturated in gas (and tracer) for noticeable gas diffusion to occur. Also, the gas does not appear to flow in and out of the nearby apertures but the liquids do, indicating the apertures are mostly saturated in liquid. The arrows indicate areas where the nearby apertures source or extract liquid to and from the nanochannels (liquid plugs appear to "disappear" and "reappear"). An alternative interpretation to this interesting image stack is capillary condensation.

APPENDIX D: FIB-SEM AND LBM SUPPLEMENTARY INFORMATION

D.1 Background: Acquisition of Shale FIB-SEM Images

The preliminary step in acquisition of 3D shale FIB-SEM images is milling an isolated microscale plateau of shale material into the surface of a mechanically milled shale sample with a coarse focused ion beam (FIB). The sample stage is positioned so that the FIB is oriented normal to the shale surface. The FIB is then set to mill an edge of the plateau at a finer current, destroying one sliver of the shale at a time (this microscopic process is analogous to a cheese slicer thinly slicing a block of cheese). An electron beam, positioned 52˚ from the FIB, images the exposed shale surface. This "slice and view" process is typically automated and slices can be as thin as a few nanometers. In the imaging process impinging electrons either elastically scatter from the sample at relatively high energies or displace lower energy electrons from the sample surface via inelastic collisions. The high energy electrons or backscattered electrons (BSE) and low energy electrons or secondary electrons (SE) are captured by separate detectors, aptly named the BSE and SE (or Everhart-Thornley) detectors. Elastic scattering of electrons positively correlates with atomic number; therefore, resulting grayscale BSE-SEM images clearly display material contrast in heterogeneous shale. Relatively heavier elements and their corresponding materials such as iron-rich pyrite, calcium-rich calcite, and silicon-rich quartz will translate to far brighter image pixels than kerogen, which is predominantly composed of carbon, hydrogen, and oxygen, all relatively lighter elements. SE-SEM signal is best for capturing surface morphology and texture and high resolution imaging. Some material contrast is seen with SE-SEM, but it is not as strong as that of BSE-SEM. Some SEM software offer a feature that allows images to have a combination of BSE and SE signals, thus optimizing material contrast and resolution.

D.2 Background: Fluid Flow Simulations with the Lattice-Boltzmann Method

The theoretical basis of LBM is the Boltzmann equation (1872), which states that the probability density function, or probability that a certain number of fluid molecules or particles will be found in a particular volume for a particular time and particle momentum, is a function of external forces and particle diffusion and collision. The Bhatnager-Gross-Krook (BGK) Approximation (1954) allows the Boltzmann equation to be applied in a computationally efficient manner, especially when compared to molecular dynamics simulations. In the BGK Approximation the density distribution of particles within a particular volume (e.g. a block within a gridded domain) are described by the probability that a certain fraction of the particles will be in different regions of the block. These regions are predefined by a lattice, which emanates from the center of each block and, instead of random molecular diffusion, values of the probability density function stream and collide along this lattice over a relaxation time. The amount of blocks or lattice units (lu) in a domain must be large enough for the approximation to capture the relevant physics; that is, a pore that is only a few lattice units wide may produce spurious results. Viscous hydrodynamic flow between parallel plates is found to be accurately captured down to a plate separation of 5 lattice units [251]. Further details on the theoretical background behind LBM, the development of the method, and verifications can be found in the literature [251] and [225].

LBM simulations are performed in a gridded or voxelized domain, which eliminates the need to construct meshes of the pore-space from 3D images. Thus, LBM is often touted as being an excellent method for flow domains with complex solid boundary properties and textures, such as porous media. A common lattice assigned to each voxel for 3D simulations is D3Q19, which is a label indicating a 3D simulation where each

voxel has 19 nodes. Another constructive feature of LBM is its ability to incorporate various boundary conditions and external forces into a simulation with relative ease. Various equations of state, including Shan-Chen, van der Waals, Peng-Robinson, Redlich-Kwong, Soave-Redlich-Kwong, and Carnahan-Starling can be implemented in LBM through an interaction potential (often called effective mass), which emerges in a force term between streaming particles [252]. Consequently, multiphase and multicomponent flows can be simulated using LBM with greater facility than many other computational fluid dynamics (CFD) methods. A drawback of LBM simulations is that they can be very time consuming when the simulation domain is large. However, the method is highly parallelizable, an advantage which helps offset long simulation times.

D.3 Verification of the LBM code

The LBM code is written using the open source C++ library Palabos [220] and [221]. A verification of the LBM code implemented in the FIB-SEM images is made by comparison of the simulation results for the velocity field in a rectangular conduit of dimensions $w \times h \times L$ against the corresponding Poiseuille analytical solution [253],

$$u_x(y,z) = \frac{4h^2 \Delta p}{\pi^3 \mu L} \sum_{n,odd}^{\infty} \frac{1}{n^3} \left[1 - \frac{\cosh\left(n\pi \frac{y}{h} \right)}{\cosh\left(n\pi \frac{w}{2h} \right)} \right] \sin\left(n\pi \frac{z}{h} \right) . \tag{B.7}$$

μ is fluid viscosity, L is the length of the 3D volume along the direction of the pressure drop, and $\overline{u}$ is the average of the velocity in the pore space voxels, using the velocity component in the direction of the pressure drop.

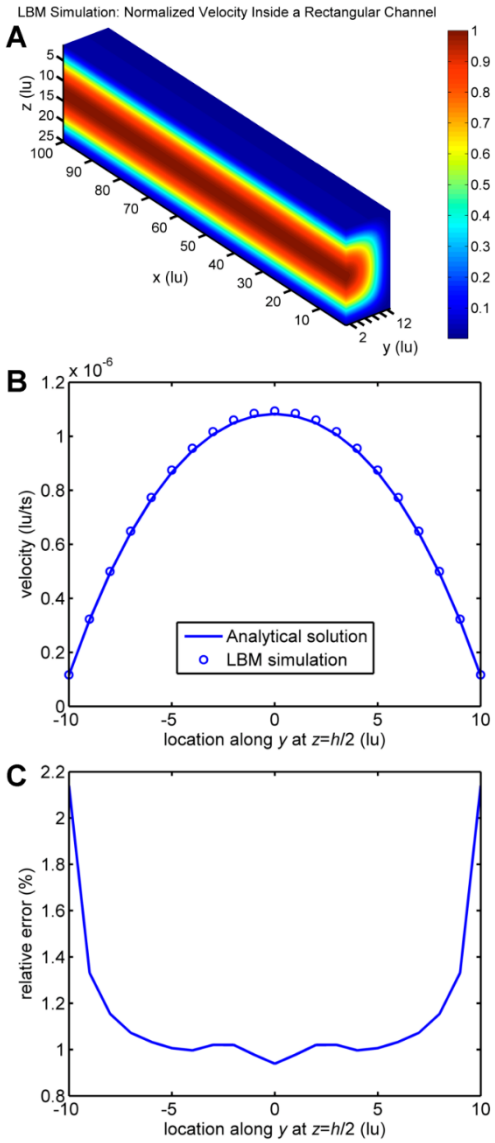

Figure D.1: Verification of the single phase, single component LBM code for the parabolic velocity field in a rectangular channel of dimensions 100×25×25 pixels (or lu). The outermost pixels are designated as solid (channel walls) and the pressure drop is applied in the x-direction. Relative errors ($|1 - u_{LBM}/u_{Poiseuille}|$) are small and decrease with grid-refinement. The velocity at the walls ($u = 0$) is not plotted.

D.4 Domain Cropping Script (Simplified Version)

The following script excerpt is written in MATLAB and requires MATLAB's Image Processing Toolbox. To determine the cropped volume I first binarize the 3D volume into pore space and non-pore space (variable DATA_ID represents the binarized 3D domain). Then the number of connected objects (independent pore space networks) in 3D and their locations and connected lengths in the *x*, *y*, and *z* directions are found with the functions *bwconncomp* and *regionprops* from MATLAB's Image Processing Toolbox.

```
**************************************************************************
%% Calculate Pore Connectivity Information

CC = bwconncomp(DATA_ID);
Number_of_objects = CC.NumObjects
stats = regionprops(CC, 'PixelIdxList');
s = [x,y,z];

for i=1:numel(stats) % loop through the identified independent networks
    [X,Y,Z] = ind2sub(s,stats(i).PixelIdxList); % index list for
network i
    conny(i,1) = max(Y) - min(Y); % connected length in y
    connx(i,1) = max(X) - min(X); % connected length in x
    connz(i,1) = max(Z) - min(Z); % connected length in z
end

Zmax_pore = max(connz)
Ymax_pore = max(conny)
Xmax_pore = max(connx)

**************************************************************************
```

D.5 Additional Figures

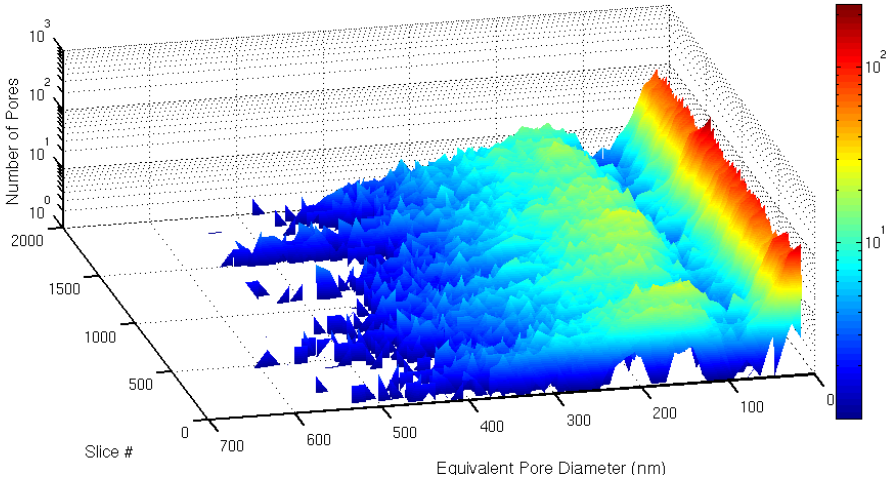

Figure D.2: 3D representation of image slice histograms reveal a bimodal pore size distribution in sample D1. The color bar represents the number of pores (the same as the z-axis). Presumably the first peak (smaller equivalent pore diameter) represents organic matter pores and the second peak represents intergranular and intercrystalline pores.

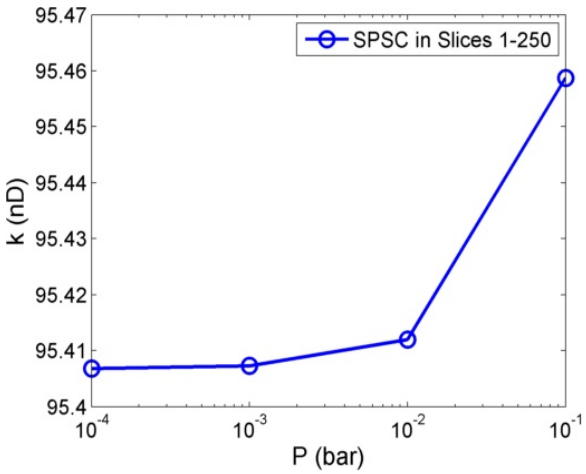

Figure D.3: Single phase, single component (SPSC) permeability simulations in the first 250 slices (out of 2000) of sample D1 reveal that permeability remains almost constant (see the y-axis values) over varying magnitudes of pressure drops (see the x-axis values). The values only vary in the hundredths place decimal point.

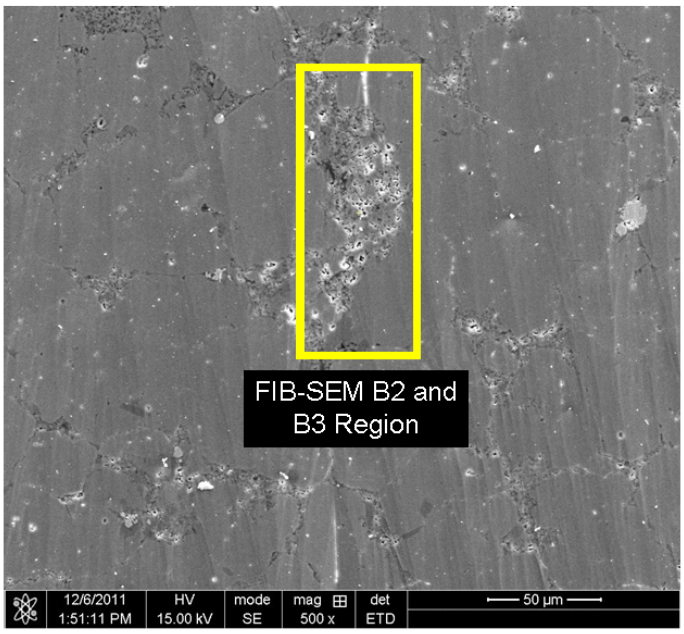

Figure D.4: Example of the locality of FIB-SEM images from the region designated for the selection of B2 and B3 FIB-SEM sites. Although not all local FIB-SEM image stacks were taken as locally as B2 and B3, they were always within several hundred micrometers of each other. Note that despite the locality, there was great variability between the extracted porosity and organic matter values for FIB-SEM sites B2 and B3 (see Fig. 6 of manuscript).

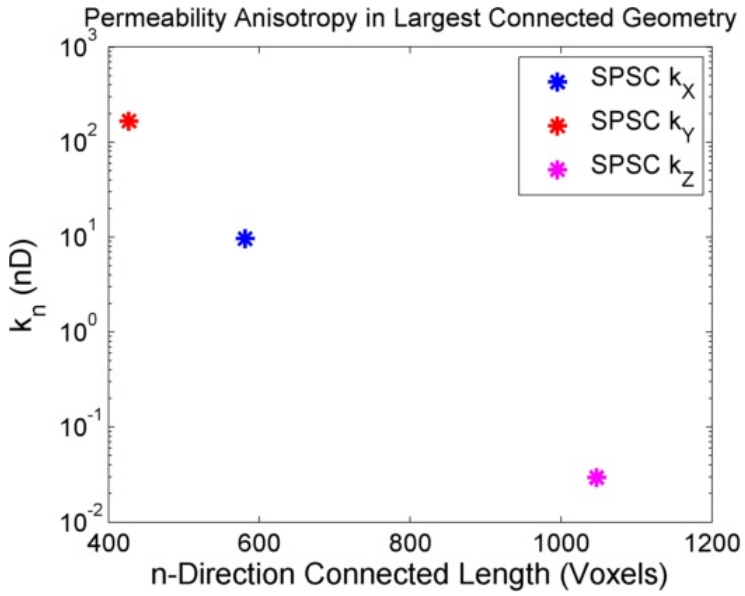

Figure D.5: FIB-SEM D1 maintained the largest connected domain after image processing and cropping to the largest connected network. When directional permeability values for pressure gradients along the different Cartesian coordinates are plotted against the length of the domain along the pressure gradient I see a trend in the values. This trend suggests that permeability is dependent upon a few tortuous paths where the opportunity for increased tortuosity increases with domain length. The permeability of the Sample D core sample was 12 nD; simulated permeability in the *x*-direction is close to this value, but the other geometric directions are not.

References

[1] R. B. Bird, W. E. Stewart, and E. N. Lightfoot, *Transport Phenomena*. John Wiley & Sons, 2007.

[2] M. Tyagi, T. Gimmi, and S. V. Churakov, "Multi-scale micro-structure generation strategy for up-scaling transport in clays," *Advances in Water Resources*, vol. 59, pp. 181–195, Sep. 2013.

[3] R. M. Allen-King, P. Grathwohl, and W. P. Ball, "New modeling paradigms for the sorption of hydrophobic organic chemicals to heterogeneous carbonaceous matter in soils, sediments, and rocks," *Advances in Water Resources*, vol. 25, no. 8–12, pp. 985–1016, Aug. 2002.

[4] R. Juanes and H. Class, "Special issue on computational methods in geologic CO2 sequestration," *Advances in Water Resources*, vol. 62, Part C, pp. 353–355, Dec. 2013.

[5] A. P. S. Selvadurai, "Fluid leakage through fractures in an impervious caprock embedded between two geologic aquifers," *Advances in Water Resources*, vol. 41, pp. 76–83, Jun. 2012.

[6] H. Dehghanpour, H. A. Zubair, A. Chhabra, and A. Ullah, "Liquid Intake of Organic Shales," *Energy Fuels*, vol. 26, no. 9, pp. 5750–5758, Sep. 2012.

[7] W. S. Han and B. McPherson, "Comparison of two different equations of state for application of carbon dioxide sequestration," *Advances in Water Resources*, vol. 31, no. 6, pp. 877–890, Jun. 2008.

[8] B. Berkowitz, "Characterizing flow and transport in fractured geological media: A review," *Advances in Water Resources*, vol. 25, no. 8–12, pp. 861–884, Aug. 2002.

[9] M. M. Khin, A. S. Nair, V. J. Babu, R. Murugan, and S. Ramakrishna, "A review on nanomaterials for environmental remediation," *Energy Environ. Sci.*, vol. 5, no. 8, pp. 8075–8109, Jul. 2012.

[10] G. T. Gillies, J. H. Smith, J. A. C. Humphrey, and W. C. Broaddus, "Positive pressure infusion of therapeutic agents into brain tissues: Mathematical and experimental simulations," *Technology and Health Care*, vol. 13, no. 4, pp. 235–243, Jan. 2005.

[11] R. G. Loucks, R. M. Reed, S. C. Ruppel, and D. M. Jarvie, "Morphology, Genesis, and Distribution of Nanometer-Scale Pores in Siliceous Mudstones of the Mississippian Barnett Shale." [Online]. Available: http://jsedres.geoscienceworld.org. [Accessed: 01-Feb-2015].

[12] Carl H. Sondergeld, Kent Edward Newsham, Joseph Thomas Comisky, Morgan Craig Rice, and Chandra Shekhar Rai, "Petrophysical Considerations in Evaluating

and Producing Shale Gas Resources," presented at the SPE Unconventional Gas Conference, Pittsburgh, Pennsylvania, USA, 2010.

[13] Q. H. Hu, X. G. Liu, S. Dultz, R. P. Ewing, and H. D. Rowe, "Fracture-Matrix Interaction and Gas Recovery in the Barnett Shale.," presented at the AAPG/SEG/SPE Hedberg Conference "Critical Assessment of Shale Resource Plays," Austin, TX, 2010.

[14] H. Fadaei, J. M. Shaw, and D. Sinton, "Bitumen–Toluene Mutual Diffusion Coefficients Using Microfluidics," *Energy Fuels*, vol. 27, no. 4, pp. 2042–2048, Apr. 2013.

[15] D. A. Handwerger, J. Keller, and K. Vaughn, "Improved Petrophysical Core Measurements on Tight Shale Reservoirs Using Retort and Crushed Samples," 2011.

[16] J. Bear, *Dynamics of Fluids In Porous Media*. American Elsevier Publishing Company, 1972.

[17] P.-E. Øren and S. Bakke, "Process Based Reconstruction of Sandstones and Prediction of Transport Properties," *Transport in Porous Media*, vol. 46, no. 2–3, pp. 311–343, Feb. 2002.

[18] M. J. Blunt, B. Bijeljic, H. Dong, O. Gharbi, S. Iglauer, P. Mostaghimi, A. Paluszny, and C. Pentland, "Pore-scale imaging and modelling," *Advances in Water Resources*, vol. 51, pp. 197–216, Jan. 2013.

[19] J. Bear, C.-F. Tsang, and G. D. Marsily, *Flow and Contaminant Transport in Fractured Rock*. Academic Press, 2012.

[20] A. J. VandenBygaart and R. Protz, "The representative elementary area (REA) in studies of quantitative soil micromorphology," *Geoderma*, vol. 89, no. 3–4, pp. 333–346, May 1999.

[21] E. W. Washburn, "The Dynamics of Capillary Flow," *Phys. Rev.*, vol. 17, no. 3, pp. 273–283, Mar. 1921.

[22] M. R. Stukan, P. Ligneul, J. P. Crawshaw, and E. S. Boek, "Spontaneous Imbibition in Nanopores of Different Roughness and Wettability," *Langmuir*, vol. 26, no. 16, pp. 13342–13352, Aug. 2010.

[23] M. Rauscher and S. Dietrich, "Wetting Phenomena in Nanofluidics," *Annual Review of Materials Research*, vol. 38, no. 1, pp. 143–172, 2008.

[24] N. V. Churaev, "Wetting films and wetting," *Revue de Physique Appliquée*, vol. 23, no. 6, pp. 975–987, 1988.

[25] P. G. de Gennes, "Wetting: statics and dynamics," *Rev. Mod. Phys.*, vol. 57, no. 3, pp. 827–863, Jul. 1985.

[26] K. Chaudhury, P. V. Acharya, and S. Chakraborty, “Influence of disjoining pressure on the dynamics of steadily moving long bubbles inside narrow cylindrical capillaries,” *Phys. Rev. E*, vol. 89, no. 5, p. 053002, May 2014.

[27] B. V. Derjaguin, N. V. Churaev, and V. M. Muller, “Forces Near Interfaces,” in *Surface Forces*, Springer US, 1987, pp. 1–23.

[28] F. M. Etzler and D. M. Fagundus, “The extent of vicinal water: Implications from the density of water in silica pores,” *Journal of Colloid and Interface Science*, vol. 115, no. 2, pp. 513–519, Feb. 1987.

[29] G. Peschel and K. H. Adlfinger, “Viscosity anomalies in liquid surface zones: IV. The apparent viscosity of water in thin layers adjacent to hydroxylated fused silica surfaces,” *Journal of Colloid and Interface Science*, vol. 34, no. 4, pp. 505–510, Dec. 1970.

[30] G. H. Pollack, *The Fourth Phase of Water: Beyond Solid, Liquid, and Vapor*. Ebner & Sons, 2013.

[31] J. Bico, B. Roman, L. Moulin, and A. Boudaoud, “Adhesion: Elastocapillary coalescence in wet hair,” *Nature*, vol. 432, no. 7018, pp. 690–690, Dec. 2004.

[32] H.-Y. Kim and L. Mahadevan, “Capillary rise between elastic sheets,” *Journal of Fluid Mechanics*, vol. 548, pp. 141–150, Feb. 2006.

[33] B. Roman and J. Bico, “Elasto-capillarity: deforming an elastic structure with a liquid droplet,” *J. Phys.: Condens. Matter*, vol. 22, no. 49, p. 493101, Dec. 2010.

[34] C. Zou, Ed., “Unconventional Petroleum Geology,” in *Unconventional Petroleum Geology*, Boston: Elsevier, 2013, p. ii.

[35] S. Kelly, H. El-Sobky, C. Torres-Verdín, and M. T. Balhoff, “Assessing the Utility of FIB-SEM Images for Shale Digital Rock Physics,” *Advances in Water Resources*, 2015.

[36] J. Klaver, S. Hemes, M. Houben, G. Desbois, Z. Radi, and J. L. Urai, “The connectivity of pore space in mudstones: insights from high-pressure Wood’s metal injection, BIB-SEM imaging, and mercury intrusion porosimetry,” *Geofluids*, p. n/a–n/a, 2015.

[37] K. L. Milliken, M. Rudnicki, D. N. Awwiller, and T. Zhang, “Organic matter–hosted pore system, Marcellus Formation (Devonian), Pennsylvania.” [Online]. Available: http://aapgbull.geoscienceworld.org. [Accessed: 01-Feb-2015].

[38] H. Yoon and T. A. Dewers, “Nanopore structures, statistically representative elementary volumes, and transport properties of chalk,” *Geophys. Res. Lett.*, vol. 40, no. 16, pp. 4294–4298, 2013.

[39] M. E. Curtis, C. H. Sondergeld, R. J. Ambrose, and C. S. Rai, "Microstructural investigation of gas shales in two and three dimensions using nanometer-scale resolution imaging," *AAPG Bulletin*, vol. 96, no. 4, pp. 665–677, Apr. 2012.

[40] B. Bai, M. Elgmati, H. Zhang, and M. Wei, "Rock characterization of Fayetteville shale gas plays," *Fuel*, vol. 105, pp. 645–652, Mar. 2013.

[41] V. Shabro, S. Kelly, C. Torres-Verdín, K. Sepehrnoori, and A. Revil, "Pore-scale modeling of electrical resistivity and permeability in FIB-SEM images of organic mudrock," *GEOPHYSICS*, vol. 79, no. 5, pp. D289–D299, Sep. 2014.

[42] B. W. Ward, J. A. Notte, and N. P. Economou, "Helium ion microscope: A new tool for nanoscale microscopy and metrology," *Journal of Vacuum Science & Technology B*, vol. 24, no. 6, pp. 2871–2874, Nov. 2006.

[43] T. Cavanaugh, "Multi-Resolution Imaging of Shales Using Electron and Ion Microscopy," 2015.

[44] F. Javadpour, "Nanopores and Apparent Permeability of Gas Flow in Mudrocks (Shales and Siltstone)," *Journal of Canadian Petroleum Science*, vol. 48, no. 8, pp. 16–21, Aug. 2009.

[45] J. Klaver, G. Desbois, J. L. Urai, and R. Littke, "BIB-SEM study of the pore space morphology in early mature Posidonia Shale from the Hils area, Germany," *International Journal of Coal Geology*, vol. 103, pp. 12–25, Dec. 2012.

[46] N. S. Kumar Gunda, B. Bera, N. K. Karadimitriou, S. K. Mitra, and S. M. Hassanizadeh, "Reservoir-on-a-Chip (ROC): A new paradigm in reservoir engineering," *Lab on a Chip*, vol. 11, no. 22, p. 3785, 2011.

[47] M. Wu, F. Xiao, R. M. Johnson-Paben, S. T. Retterer, X. Yin, and K. B. Neeves, "Single- and two-phase flow in microfluidic porous media analogs based on Voronoi tessellation," *Lab Chip*, vol. 12, no. 2, pp. 253–261, 2012.

[48] M. Oostrom, Y. Mehmani, P. Romero-Gomez, Y. Tang, H. Liu, H. Yoon, Q. Kang, V. Joekar-Niasar, M. T. Balhoff, T. Dewers, G. D. Tartakovsky, E. A. Leist, N. J. Hess, W. A. Perkins, C. L. Rakowski, M. C. Richmond, J. A. Serkowski, C. J. Werth, A. J. Valocchi, T. W. Wietsma, and C. Zhang, "Pore-scale and continuum simulations of solute transport micromodel benchmark experiments," *Comput Geosci*, pp. 1–23, Jun. 2014.

[49] N. K. Karadimitriou and S. M. Hassanizadeh, "A Review of Micromodels and Their Use in Two-Phase Flow Studies," *Vadose Zone Journal*, vol. 11, no. 3, p. 0, 2012.

[50] K. He, L. Xu, Y. Gao, K. B. Neeves, X. Yin, B. Bai, Y. Ma, and J. Smith, "Validating Surfactant Performance in the Eagle Ford Shale: A Correlation

between the Reservoir-on-a-Chip Approach and Enhanced Well Productivity," 2014.

[51] E. Parsa, Y. Gao, X. Yin, K. Neeves, L. Wang, and E. Ozkan, "Experimental Study and Modeling of the Effect of Pore Size Distribution on Hydrocarbon Phase Behavior in Nanopores," 2014.

[52] Q. Wu, J. T. Ok, Y. Sun, S. T. Retterer, K. B. Neeves, X. Yin, B. Bai, and Y. Ma, "Optic imaging of single and two-phase pressure-driven flows in nano-scale channels," *Lab on a Chip*, vol. 13, no. 6, p. 1165, 2013.

[53] K. He, F. Babaye Khorasani, S. T. Retterer, D. K. Thomas, J. C. Conrad, and R. Krishnamoorti, "Diffusive Dynamics of Nanoparticles in Arrays of Nanoposts," *ACS Nano*, vol. 7, no. 6, pp. 5122–5130, Jun. 2013.

[54] J. C. Berg, *An Introduction to Interfaces & Colloids: The Bridge to Nanoscience*. World Scientific, 2010.

[55] W. van der Wijngaart, "Capillary pumps with constant flow rate," *Microfluid Nanofluid*, vol. 16, no. 5, pp. 829–837, May 2014.

[56] P. F. Man, C. H. Mastrangelo, M. . Burns, and D. T. Burke, "Microfabricated capillarity-driven stop valve and sample injector," in *, The Eleventh Annual International Workshop on Micro Electro Mechanical Systems, 1998. MEMS 98. Proceedings*, 1998, pp. 45–50.

[57] E. W. Washburn, "The Dynamics of Capillary Flow," *Phys. Rev.*, vol. 17, no. 3, pp. 273–283, Mar. 1921.

[58] P. Abgrall, *Nanofluidics*. Boston: Artech House, 2009.

[59] R. B. Bird, W. E. Stewart, and E. N. Lightfoot, *Transport Phenomena*. John Wiley & Sons, 2007.

[60] C. Liu and Z. Li, "On the validity of the Navier-Stokes equations for nanoscale liquid flows: The role of channel size," *AIP Advances*, vol. 1, no. 3, p. 032108, Sep. 2011.

[61] S. Murad and I. K. Puri, "Dynamics of nanoscale jet formation and impingement on flat surfaces," *Physics of Fluids (1994-present)*, vol. 19, no. 12, p. 128102, Dec. 2007.

[62] H.-J. Butt, K. Graf, and M. Kappl, *Physics and Chemistry of Interfaces*. John Wiley & Sons, 2006.

[63] B. V. Derjaguin, N. V. Churaev, and V. M. Muller, "Disjoining Pressure," in *Surface Forces*, Springer US, 1987, pp. 25–52.

[64] M. Majumder, N. Chopra, R. Andrews, and B. J. Hinds, "Nanoscale hydrodynamics: Enhanced flow in carbon nanotubes," *Nature*, vol. 438, no. 7064, pp. 44–44, Nov. 2005.

[65] N. V. Churaev, *Liquid and Vapour Flows in Porous Bodies: Surface Phenomena*. CRC Press, 2000.

[66] H. B. G. Casimir and D. Polder, "The Influence of Retardation on the London-van der Waals Forces," *Phys. Rev.*, vol. 73, no. 4, pp. 360–372, Feb. 1948.

[67] R. L. Jaffe, "Casimir effect and the quantum vacuum," *Phys. Rev. D*, vol. 72, no. 2, p. 021301, Jul. 2005.

[68] J. N. Israelachvili and D. Tabor, "The Measurement of Van Der Waals Dispersion Forces in the Range 1.5 to 130 nm," *Proceedings of the Royal Society of London A: Mathematical, Physical and Engineering Sciences*, vol. 331, no. 1584, pp. 19–38, Nov. 1972.

[69] H.-J. Butt, K. Graf, and M. Kappl, *Physics and Chemistry of Interfaces*. John Wiley & Sons, 2006.

[70] M. Boström, B. E. Sernelius, I. Brevik, and B. W. Ninham, "Retardation turns the van der Waals attraction into a Casimir repulsion as close as 3 nm," *Phys. Rev. A*, vol. 85, no. 1, p. 010701, Jan. 2012.

[71] B. V. Derjaguin, N. V. Churaev, and V. M. Muller, "Dispersion Forces in Thin Interlayers and Films," in *Surface Forces*, Springer US, 1987, pp. 85–149.

[72] K. S. Birdi, *Handbook of Surface and Colloid Chemistry, Third Edition*. CRC Press, 2008.

[73] B. V. Derjaguin and N. V. Churaev, "Polymolecular adsorption and capillary condensation in narrow slit pores," *Journal of Colloid and Interface Science*, vol. 54, no. 2, pp. 157–175, Feb. 1976.

[74] V. Tandon, S. K. Bhagavatula, W. C. Nelson, and B. J. Kirby, "Zeta potential and electroosmotic mobility in microfluidic devices fabricated from hydrophobic polymers: 1. The origins of charge," *Electrophoresis*, vol. 29, no. 5, pp. 1092–1101, Mar. 2008.

[75] W. H. Briscoe and R. G. Horn, "Electrical double layer interactions in a non-polar liquid measured with a modified surface force apparatus," in *Trends in Colloid and Interface Science XVI*, M. Miguel and H. D. Burrows, Eds. Springer Berlin Heidelberg, 2004, pp. 147–151.

[76] A. Revil and M. Pessel, "Electroosmotic flow and the validity of the classical Darcy equation in silty shales," *Geophys. Res. Lett.*, vol. 29, no. 9, pp. 14–1, May 2002.

[77] J. N. Israelachvili, *Intermolecular and Surface Forces: Revised Third Edition*. Academic Press, 2011.

[78] U. Raviv, P. Laurat, and J. Klein, "Fluidity of water confined to subnanometre films," *Nature*, vol. 413, no. 6851, pp. 51–54, Sep. 2001.

[79] D. B. Asay and S. H. Kim, "Effects of adsorbed water layer structure on adhesion force of silicon oxide nanoasperity contact in humid ambient," *The Journal of Chemical Physics*, vol. 124, no. 17, p. 174712, May 2006.

[80] J. Klein and E. Kumacheva, "Simple liquids confined to molecularly thin layers. I. Confinement-induced liquid-to-solid phase transitions," *The Journal of Chemical Physics*, vol. 108, no. 16, pp. 6996–7009, Apr. 1998.

[81] R. C. Major, J. E. Houston, M. J. McGrath, J. I. Siepmann, and X.-Y. Zhu, "Viscous Water Meniscus under Nanoconfinement," *Phys. Rev. Lett.*, vol. 96, no. 17, p. 177803, May 2006.

[82] G. Pollack, *The Fourth Phase of Water: Beyond Solid, Liquid, and Vapor*. Ebner and Sons Publishers, 2014.

[83] P. G. de Gennes and J. Prost, *The Physics of Liquid Crystals*, Second Edition. Clarendon Press | International Series of Monographs on Physics 83, 1995.

[84] G. H. Pollack and J. Clegg, "Unexpected Linkage Between Unstirred Layers, Exclusion Zones, and Water," in *Phase Transitions in Cell Biology*, G. H. Pollack and W.-C. Chin, Eds. Springer Netherlands, 2008, pp. 143–152.

[85] H. Yoo, R. Paranji, and G. H. Pollack, "Impact of Hydrophilic Surfaces on Interfacial Water Dynamics Probed with NMR Spectroscopy," *J Phys Chem Lett*, vol. 2, no. 6, pp. 532–536, Feb. 2011.

[86] A. Yu, P. Carlson, and G. H. Pollack, "Unexpected axial flow through hydrophilic tubes: Implications for energetics of water," *Eur. Phys. J. Spec. Top.*, vol. 223, no. 5, pp. 947–958, Apr. 2014.

[87] B. Chai and G. H. Pollack, "Solute-Free Interfacial Zones in Polar Liquids," *J Phys Chem B*, vol. 114, no. 16, pp. 5371–5375, Apr. 2010.

[88] B. V. Derjaguin, N. V. Churaev, and V. M. Muller, "The Structure of Boundary Layers of Liquids and the Structural Component of Disjoining Pressure," in *Surface Forces*, Springer US, 1987, pp. 231–291.

[89] R. M. Pashley and J. A. Kitchener, "Surface forces in adsorbed multilayers of water on quartz," *Journal of Colloid and Interface Science*, vol. 71, no. 3, pp. 491–500, Oct. 1979.

[90] N. Ichikawa, K. Hosokawa, and R. Maeda, “Interface motion of capillary-driven flow in rectangular microchannel,” *Journal of Colloid and Interface Science*, vol. 280, no. 1, pp. 155–164, Dec. 2004.

[91] J. Haneveld, N. R. Tas, N. Brunets, H. V. Jansen, and M. Elwenspoek, “Capillary filling of sub-10nm nanochannels,” *Journal of Applied Physics*, vol. 104, no. 1, p. 014309, Jul. 2008.

[92] V. N. Phan, N.-T. Nguyen, C. Yang, P. Joseph, L. Djeghlaf, D. Bourrier, and A.-M. Gue, “Capillary filling in closed end nanochannels,” *Langmuir*, vol. 26, no. 16, pp. 13251–13255, Aug. 2010.

[93] A. Han, G. Mondin, N. G. Hegelbach, N. F. de Rooij, and U. Staufer, “Filling kinetics of liquids in nanochannels as narrow as 27 nm by capillary force,” *J Colloid Interface Sci*, vol. 293, no. 1, pp. 151–157, Jan. 2006.

[94] A. Hibara, T. Saito, H.-B. Kim, M. Tokeshi, T. Ooi, M. Nakao, and T. Kitamori, “Nanochannels on a Fused-Silica Microchip and Liquid Properties Investigation by Time-Resolved Fluorescence Measurements,” *Anal. Chem.*, vol. 74, no. 24, pp. 6170–6176, Dec. 2002.

[95] M. N. Hamblin, A. R. Hawkins, D. Murray, D. Maynes, M. L. Lee, A. T. Woolley, and H. D. Tolley, “Capillary flow in sacrificially etched nanochannels,” *Biomicrofluidics*, vol. 5, no. 2, Jun. 2011.

[96] J. Lee, T. Laoui, and R. Karnik, “Nanofluidic transport governed by the liquid/vapour interface,” *Nat Nano*, vol. 9, no. 4, pp. 317–323, Apr. 2014.

[97] F. Chauvet, S. Geoffroy, A. Hamouni, M. Prat, A.-M. Gué, and P. Joseph, “Nanobubbles and gas dynamics during capillary filling of nanochannels,” presented at the The 16th International Conference on Miniaturized Systems for Chemistry and Life Sciences, 2012.

[98] C. Duan, R. Karnik, M.-C. Lu, and A. Majumdar, “Evaporation-induced cavitation in nanofluidic channels,” *Proc Natl Acad Sci U S A*, vol. 109, no. 10, pp. 3688–3693, Mar. 2012.

[99] P. Kim, H.-Y. Kim, J. K. Kim, G. Reiter, and K. Y. Suh, “Multi-curvature liquid meniscus in a nanochannel: evidence of interplay between intermolecular and surface forces,” *Lab Chip*, vol. 9, no. 22, pp. 3255–3260, Nov. 2009.

[100] J. W. van Honschoten, N. Brunets, and N. R. Tas, “Capillarity at the nanoscale,” *Chem. Soc. Rev.*, vol. 39, no. 3, pp. 1096–1114, Feb. 2010.

[101] M. P. Rossi, H. Ye, Y. Gogotsi, S. Babu, P. Ndungu, and J.-C. Bradley, “Environmental Scanning Electron Microscopy Study of Water in Carbon Nanopipes,” *Nano Lett.*, vol. 4, no. 5, pp. 989–993, May 2004.

[102] E. Tamaki, A. Hibara, H.-B. Kim, M. Tokeshi, and T. Kitamori, "Pressure-driven flow control system for nanofluidic chemical process," *Journal of Chromatography A*, vol. 1137, no. 2, pp. 256–262, Dec. 2006.

[103] M. Whitby, L. Cagnon, M. Thanou, and N. Quirke, "Enhanced Fluid Flow through Nanoscale Carbon Pipes," *Nano Lett.*, vol. 8, no. 9, pp. 2632–2637, Sep. 2008.

[104] L. Joly, "Capillary filling with giant liquid/solid slip: Dynamics of water uptake by carbon nanotubes," *The Journal of Chemical Physics*, vol. 135, no. 21, p. 214705, Dec. 2011.

[105] S. Cheng and M. O. Robbins, "Capillary adhesion at the nanometer scale," *Phys. Rev. E*, vol. 89, no. 6, p. 062402, Jun. 2014.

[106] H. Hu, C. R. Weinberger, and Y. Sun, "Model of Meniscus Shape and Disjoining Pressure of Thin Liquid Films on Nanostructured Surfaces with Electrostatic Interactions," *J. Phys. Chem. C*, vol. 119, no. 21, pp. 11777–11785, May 2015.

[107] J. T. Mannion, C. H. Reccius, J. D. Cross, and H. G. Craighead, "Conformational Analysis of Single DNA Molecules Undergoing Entropically Induced Motion in Nanochannels," *Biophysical Journal*, vol. 90, no. 12, pp. 4538–4545, Jun. 2006.

[108] J. T. Mannion, C. H. Reccius, J. D. Cross, and H. G. Craighead, "Conformational Analysis of Single DNA Molecules Undergoing Entropically Induced Motion in Nanochannels," *Biophysical Journal*, vol. 90, no. 12, pp. 4538–4545, Jun. 2006.

[109] A. S. Aloy, A. V. Trofimenko, T. I. Kol'tsova, and M. V. Nikandrova, "Formation of surface layers in leaching of borosilicate glasses incorporating different amounts of simulated HLW," *Radiochemistry*, vol. 54, no. 3, pp. 291–297, May 2012.

[110] A. Ledieu, F. Devreux, P. Barboux, L. Sicard, and O. Spalla, "Leaching of borosilicate glasses. I. Experiments," *Journal of Non-Crystalline Solids*, vol. 343, no. 1–3, pp. 3–12, Sep. 2004.

[111] M. M. Visser, S. T. Moe, and A. B. Hanneborg, "Diffusion at anodically bonded interfaces," *J. Micromech. Microeng.*, vol. 11, no. 4, p. 376, Jul. 2001.

[112] I. Sadaba, C. H. J. Fox, and S. McWilliam, "An Investigation of Residual Stress Effects due to the Anodic Bonding of Glass and Silicon in MEMS Fabrication," *Applied Mechanics and Materials*, vol. 5–6, pp. 501–508, 2006.

[113] L. Gitlin, P. Schulze, and D. Belder, "Rapid replication of master structures by double casting with PDMS," *Lab Chip*, vol. 9, no. 20, pp. 3000–3002, Oct. 2009.

[114] Y. Xia and G. M. Whitesides, "Soft Lithography," *Annual Review of Materials Science*, vol. 28, no. 1, pp. 153–184, 1998.

[115] G. Karlsson, "Thickness measurements of lacey carbon films," *J Microsc*, vol. 203, no. Pt 3, pp. 326–328, Sep. 2001.

[116] H. Dehghanpour and M. Shirdel, “A Triple Porosity Model for Shale Gas Reservoirs,” 2011.

[117] H. J. Fan, F. Fleischer, W. Lee, K. Nielsch, R. Scholz, M. Zacharias, U. Gösele, A. Dadgar, and A. Krost, “Patterned growth of aligned ZnO nanowire arrays on sapphire and GaN layers,” *Superlattices and Microstructures*, vol. 36, no. 1–3, pp. 95–105, Jul. 2004.

[118] G. Villanueva, O. Vazquez-Mena, M. A. F. van den Boogaart, K. Sidler, K. Pataky, V. Savu, and J. Brugger, “Etching of sub-micrometer structures through Stencil,” *Microelectronic Engineering*, vol. 85, no. 5–6, pp. 1010–1014, May 2008.

[119] G. C. Schwartz and P. M. Schaible, “Reactive Ion Etching of Copper Films,” *J. Electrochem. Soc.*, vol. 130, no. 8, pp. 1777–1779, Aug. 1983.

[120] D. A. Zeze, R. D. Forrest, J. D. Carey, D. C. Cox, I. D. Robertson, B. L. Weiss, and S. R. P. Silva, “Reactive ion etching of quartz and Pyrex for microelectronic applications,” *Journal of Applied Physics*, vol. 92, no. 7, pp. 3624–3629, Oct. 2002.

[121] E. Thiénot, F. Domingo, E. Cambril, and C. Gosse, “Reactive ion etching of glass for biochip applications: Composition effects and surface damages,” *Microelectronic Engineering*, vol. 83, no. 4–9, pp. 1155–1158, Apr. 2006.

[122] “Optimal protocol for moulding PDMS with a PDMS master « Chips and Tips.” .

[123] G. Shao, J. Wu, Z. Cai, and W. Wang, “Fabrication of elastomeric high-aspect-ratio microstructures using polydimethylsiloxane (PDMS) double casting technique,” *Sensors and Actuators A: Physical*, vol. 178, pp. 230–236, May 2012.

[124] K. Ziółkowska, K. Żukowski, M. Chudy, A. Dybko, and Z. Brzózka, “Enhancing efficiency of double casting prototyping by thermal aging of poly (dimethylsiloxane),” in *Proc. MicroTAS*, Seattle, WA, 2011, pp. 1164–1166.

[125] Z.-J. Jia, Q. Fang, and Z.-L. Fang, “Bonding of Glass Microfluidic Chips at Room Temperatures,” *Anal. Chem.*, vol. 76, no. 18, pp. 5597–5602, Sep. 2004.

[126] Y. Temiz, R. D. Lovchik, G. V. Kaigala, and E. Delamarche, “Lab-on-a-chip devices: How to close and plug the lab?,” *Microelectronic Engineering*, vol. 132, pp. 156–175, Jan. 2015.

[127] J. N. Lee, C. Park, and G. M. Whitesides, “Solvent Compatibility of Poly(dimethylsiloxane)-Based Microfluidic Devices,” *Anal. Chem.*, vol. 75, no. 23, pp. 6544–6554, Dec. 2003.

[128] M. J. Jang and Y. Nam, “Agarose-Assisted Micro-Contact Printing for High-Quality Biomolecular Micro-Patterns,” *Macromol. Biosci.*, vol. 15, no. 5, pp. 613–621, May 2015.

[129] E. P. Dupont, R. Luisier, and M. A. M. Gijs, "NOA 63 as a UV-curable material for fabrication of microfluidic channels with native hydrophilicity," *Microelectronic Engineering*, vol. 87, no. 5–8, pp. 1253–1255, May 2010.

[130] J. Steigert, S. Haeberle, T. Brenner, C. Müller, C. P. Steinert, P. Koltay, N. Gottschlich, H. Reinecke, J. Rühe, R. Zengerle, and J. Ducrée, "Rapid prototyping of microfluidic chips in COC," *J. Micromech. Microeng.*, vol. 17, no. 2, p. 333, Feb. 2007.

[131] A. Klukowska, A. Kolander, I. Bergmair, M. Mühlberger, H. Leichtfried, F. Reuther, G. Grützner, and R. Schöftner, "Novel transparent hybrid polymer working stamp for UV-imprinting," *Microelectronic Engineering*, vol. 86, no. 4–6, pp. 697–699, Apr. 2009.

[132] R. M. Capuano, "Evidence of Fluid Flow in Microfractures in Geopressured Shales," *AAPG Bulletin*, vol. 77, no. 8, pp. 1303–1314, 1993.

[133] T. C. Merkel, V. I. Bondar, K. Nagai, B. D. Freeman, and I. Pinnau, "Gas sorption, diffusion, and permeation in poly(dimethylsiloxane)," *J. Polym. Sci. B Polym. Phys.*, vol. 38, no. 3, pp. 415–434, Feb. 2000.

[134] D. Leythaeuser, R. G. Schaefer, and A. Yukler, "Role of Diffusion in Primary Migration of Hydrocarbons," *AAPG Bulletin*, vol. 66, no. 4, pp. 408–429, 1982.

[135] S. R. Etminan, F. Javadpour, B. B. Maini, and Z. Chen, "Measurement of gas storage processes in shale and of the molecular diffusion coefficient in kerogen," *International Journal of Coal Geology*, vol. 123, pp. 10–19, Mar. 2014.

[136] D. A. Markov, E. M. Lillie, S. P. Garbett, and L. J. McCawley, "Variation in diffusion of gases through PDMS due to plasma surface treatment and storage conditions," *Biomed Microdevices*, vol. 16, no. 1, pp. 91–96, Feb. 2014.

[137] R. L. Anderson, I. Ratcliffe, H. C. Greenwell, P. A. Williams, S. Cliffe, and P. V. Coveney, "Clay swelling — A challenge in the oilfield," *Earth-Science Reviews*, vol. 98, no. 3–4, pp. 201–216, Feb. 2010.

[138] P. J. M. Monteiro, C. H. Rycroft, and G. I. Barenblatt, "A mathematical model of fluid and gas flow in nanoporous media," *PNAS*, vol. 109, no. 50, pp. 20309–20313, Dec. 2012.

[139] A. Rabbani, S. Jamshidi, and S. Salehi, "An automated simple algorithm for realistic pore network extraction from micro-tomography images," *Journal of Petroleum Science and Engineering*, vol. 123, pp. 164–171, Nov. 2014.

[140] R. M. Bustin, A. M. M. Bustin, A. Cui, D. Ross, and V. M. Pathi, "Impact of Shale Properties on Pore Structure and Storage Characteristics," 2008.

[141] *Microelectronics Failure Analysis: Desk Reference*. ASM International, 2004.

[142] P. C. H. Li, *Microfluidic Lab-on-a-Chip for Chemical and Biological Analysis and Discovery*. CRC Press, 2005.

[143] S. Park, Y. S. Huh, H. G. Craighead, and D. Erickson, "A method for nanofluidic device prototyping using elastomeric collapse," *PNAS*, vol. 106, no. 37, pp. 15549–15554, Sep. 2009.

[144] X. Zhang and Z. Liu, "Superlenses to overcome the diffraction limit," *Nat Mater*, vol. 7, no. 6, pp. 435–441, Jun. 2008.

[145] S. Lee, L. Li, Y. Ben-Aryeh, Z. Wang, and W. Guo, "Overcoming the diffraction limit induced by microsphere optical nanoscopy," *Journal of Optics*, vol. 15, no. 12, p. 125710, Dec. 2013.

[146] R. Danz and P. Gretscher, "C–DIC: a new microscopy method for rational study of phase structures in incident light arrangement," *Thin Solid Films*, vol. 462–463, pp. 257–262, Sep. 2004.

[147] A. J. Smith, C. Wang, D. Guo, C. Sun, and J. Huang, "Repurposing Blu-ray movie discs as quasi-random nanoimprinting templates for photon management," *Nat Commun*, vol. 5, Nov. 2014.

[148] N. Fries and M. Dreyer, "The transition from inertial to viscous flow in capillary rise," *Journal of Colloid and Interface Science*, vol. 327, no. 1, pp. 125–128, Nov. 2008.

[149] D. I. Dimitrov, A. Milchev, and K. Binder, "Forced imbibition—a tool for separate determination of Laplace pressure and drag force in capillary filling experiments," *Phys. Chem. Chem. Phys.*, vol. 10, no. 14, pp. 1867–1869, Mar. 2008.

[150] W. B. Krantz, *Scaling Analysis in Modeling Transport and Reaction Processes: A Systematic Approach to Model Building and the Art of Approximation*. John Wiley & Sons, 2007.

[151] E. Doebelin, *System Dynamics: Modeling, Analysis, Simulation, Design*. CRC Press, 1998.

[152] D. K. Jaiswal, "Analytical Solution to the One-Dimensional Advection-Diffusion Equation with Temporally Dependent Coefficients," *Journal of Water Resource and Protection*, vol. 03, no. 01, pp. 76–84, 2011.

[153] M. A. Mariño, "Longitudinal Dispersion in Saturated Porous Media," *Journal of the Hydraulics Division*, vol. 100, no. 1, pp. 151–157, Jan. 1974.

[154] M. T. van Genuchten and W. J. Alves, "Analytical Solutions of the One-Dimensional Convective-Dispersive Solute Transport Equation," United States Department of Agriculture, Economic Research Service, Technical Bulletins 157268, 1982.

[155] Ira N. Levine, *Physical Chemistry*, 2nd ed. McGraw-Hill Book Company, 1983.

[156] K. Li and R. N. Horne, "Characterization of Spontaneous Water Imbibition Into Gas-Saturated Rocks," *SPE Journal*, vol. 6, no. 04, pp. 375–384, Dec. 2001.

[157] L. L. Handy, "Determination of Effective Capillary Pressures for Porous Media from Imbibition Data," Jan. 1960.

[158] M. L. Gee, T. W. Healy, and L. R. White, "Hydrophobicity effects in the condensation of water films on quartz," *Journal of Colloid and Interface Science*, vol. 140, no. 2, pp. 450–465, Dec. 1990.

[159] Edgar F. Ethington, *Interfacial Contact Angle Measurements of Water, Mercury, and 20 Organic Liquids on Quartz, Calcite, Biotite, and Ca-montmorillonite Substrates*, vol. 90. U.S. Geological Survey, 1990.

[160] M. Reyssat, L. Courbin, E. Reyssat, and H. A. Stone, "Imbibition in geometries with axial variations," *Journal of Fluid Mechanics*, vol. 615, pp. 335–344, 2008.

[161] G. Hummer, J. C. Rasaiah, and J. P. Noworyta, "Water conduction through the hydrophobic channel of a carbon nanotube," *Nature*, vol. 414, no. 6860, pp. 188–190, Nov. 2001.

[162] C. Yaws, *Chemical Properties Handbook: Physical, Thermodynamics, Environmental Transport, Safety & Health Related Properties for Organic &*. McGraw-Hill Education, 1999.

[163] D. Janssen, R. De Palma, S. Verlaak, P. Heremans, and W. Dehaen, "Static solvent contact angle measurements, surface free energy and wettability determination of various self-assembled monolayers on silicon dioxide," *Thin Solid Films*, vol. 515, no. 4, pp. 1433–1438, Dec. 2006.

[164] R. T. Ferrell and D. M. Himmelblau, "Diffusion coefficients of nitrogen and oxygen in water," *J. Chem. Eng. Data*, vol. 12, no. 1, pp. 111–115, Jan. 1967.

[165] E. Wilhelm, R. Battino, and R. J. Wilcock, "Low-pressure solubility of gases in liquid water," *Chem. Rev.*, vol. 77, no. 2, pp. 219–262, Apr. 1977.

[166] B. V. Derjaguin and N. V. Churaev, "Polymolecular adsorption and capillary condensation in narrow slit pores," *Journal of Colloid and Interface Science*, vol. 54, no. 2, pp. 157–175, Feb. 1976.

[167] T. D. Wheeler and A. D. Stroock, "The transpiration of water at negative pressures in a synthetic tree," *Nature*, vol. 455, no. 7210, pp. 208–212, Sep. 2008.

[168] M. M. Conde, C. Vega, G. A. Tribello, and B. Slater, "The phase diagram of water at negative pressures: Virtual ices," *The Journal of Chemical Physics*, vol. 131, no. 3, p. 034510, Jul. 2009.

[169] P. G. D. Gennes, X. Hua, and P. Levinson, “Dynamics of wetting: local contact angles,” *Journal of Fluid Mechanics*, vol. 212, pp. 55–63, 1990.

[170] L. H. Thamdrup, F. Persson, H. Bruus, A. Kristensen, and H. Flyvbjerg, “Experimental investigation of bubble formation during capillary filling of SiO2 nanoslits,” *Applied Physics Letters*, vol. 91, no. 16, p. 163505, Oct. 2007.

[171] N. R. Tas, M. Escalante, J. W. van Honschoten, H. V. Jansen, and M. Elwenspoek, “Capillary Negative Pressure Measured by Nanochannel Collapse,” *Langmuir*, vol. 26, no. 3, pp. 1473–1476, Feb. 2010.

[172] J. W. van Honschoten, M. Escalante, N. R. Tas, and M. Elwenspoek, “Formation of liquid menisci in flexible nanochannels,” *Journal of Colloid and Interface Science*, vol. 329, no. 1, pp. 133–139, Jan. 2009.

[173] N. H. Fletcher, “Dendritic growth of ice crystals,” *Journal of Crystal Growth*, vol. 20, no. 4, pp. 268–272, Nov. 1973.

[174] P. V. Hobbs, *Ice Physics*. Clarendon Press, 1974.

[175] H.-H. Liu, B. Lai, and J. Chen, “Unconventional Spontaneous Imbibition into Shale Matrix: Theory and a Methodology to Determine Relevant Parameters,” *Transp Porous Med*, pp. 1–17, Sep. 2015.

[176] Q. Hu, R. P. Ewing, and S. Dultz, “Low pore connectivity in natural rock,” *Journal of Contaminant Hydrology*, vol. 133, pp. 76–83, May 2012.

[177] M. Garajeu, H. Gouin, and G. Saccomandi, “Scaling Navier-Stokes Equation in Nanotubes,” *Physics of Fluids*, vol. 25, no. 8, p. 082003, 2013.

[178] R. Holyst, A. Bielejewska, J. Szymański, A. Wilk, A. Patkowski, J. Gapiński, A. Żywociński, T. Kalwarczyk, E. Kalwarczyk, M. Tabaka, N. Ziębacz, and S. A. Wieczorek, “Scaling form of viscosity at all length-scales in poly(ethylene glycol) solutions studied by fluorescence correlation spectroscopy and capillary electrophoresis,” *Physical Chemistry Chemical Physics*, vol. 11, no. 40, p. 9025, 2009.

[179] S. S. Jang, S.-T. Lin, P. K. Maiti, M. Blanco, W. A. Goddard, P. Shuler, and Y. Tang, “Molecular Dynamics Study of a Surfactant-Mediated Decane−Water Interface: Effect of Molecular Architecture of Alkyl Benzene Sulfonate,” *J. Phys. Chem. B*, vol. 108, no. 32, pp. 12130–12140, Aug. 2004.

[180] E. Vandre, M. S. Carvalho, and S. Kumar, “Delaying the onset of dynamic wetting failure through meniscus confinement,” *Journal of Fluid Mechanics*, vol. 707, pp. 496–520, Sep. 2012.

[181] A. Siebold, M. Nardin, J. Schultz, A. Walliser, and M. Oppliger, “Effect of dynamic contact angle on capillary rise phenomena,” *Colloids and Surfaces A: Physicochemical and Engineering Aspects*, vol. 161, no. 1, pp. 81–87, Jan. 2000.

[182] S. A. Kelly, M. T. Balhoff, and C. Torres-Verdin, “Quantification of Bulk Solution Limits for Liquid and Interfacial Transport in Nano-Confinements,” *Langmuir*, 2015.

[183] F. F. Ouali, G. McHale, H. Javed, C. Trabi, N. J. Shirtcliffe, and M. I. Newton, “Wetting considerations in capillary rise and imbibition in closed square tubes and open rectangular cross-section channels,” *Microfluid Nanofluid*, vol. 15, no. 3, pp. 309–326, Feb. 2013.

[184] R. Seemann, M. Brinkmann, E. J. Kramer, F. F. Lange, and R. Lipowsky, “Wetting morphologies at microstructured surfaces,” *PNAS*, vol. 102, no. 6, pp. 1848–1852, Feb. 2005.

[185] A. Ponomarenko, D. Quéré, and C. Clanet, “A universal law for capillary rise in corners,” *Journal of Fluid Mechanics*, vol. 666, pp. 146–154, Jan. 2011.

[186] J. Bico and D. Quéré, “Precursors of impregnation,” *Europhysics Letters (EPL)*, vol. 61, no. 3, pp. 348–353, Feb. 2003.

[187] A. R. Imre, H. J. Maris, and P. R. Williams, *Liquids Under Negative Pressure: Proceedings of the NATO Advanced Research Workshop of Liquids Under Negative Pressure Budapest, Hungary 23-25 February 2002*. Springer Science & Business Media, 2002.

[188] S. C. Maroo and J. N. Chung, “Negative pressure characteristics of an evaporating meniscus at nanoscale,” *Nanoscale Res Lett*, vol. 6, no. 1, pp. 1–7, Jan. 2011.

[189] P. G. Debenedetti, “Physics of water: Stretched to the limit,” *Nat Phys*, vol. 9, no. 1, pp. 7–8, Jan. 2013.

[190] B. Bhushan, *Scanning Probe Microscopy in Nanoscience and Nanotechnology 2*. Springer Science & Business Media, 2010.

[191] C. E. Brennen, *Cavitation and Bubble Dynamics*. Cambridge University Press, 2013.

[192] R. Zhang, Y. Ikoma, and T. Motooka, “Negative capillary-pressure-induced cavitation probability in nanochannels,” *Nanotechnology*, vol. 21, no. 10, p. 105706, Mar. 2010.

[193] D. Langbein, “Van der Waals Attraction in Multilayer Structures,” *The Journal of Adhesion*, vol. 3, no. 3, pp. 213–235, Jan. 1972.

[194] J. Weissmüller and D. Kramer, “Balance of Force at Curved Solid Metal−Liquid Electrolyte Interfaces,” *Langmuir*, vol. 21, no. 10, pp. 4592–4603, May 2005.

[195] H. Hu, C. R. Weinberger, and Y. Sun, “Effect of Nanostructures on the Meniscus Shape and Disjoining Pressure of Ultrathin Liquid Film,” *Nano Lett.*, vol. 14, no. 12, pp. 7131–7137, Dec. 2014.

[196] M. O. Robbins, D. Andelman, and J. F. Joanny, “Thin liquid films on rough or heterogeneous solids,” *Phys. Rev., A*, vol. 43, no. 8, pp. 4344–4354, Apr. 1991.

[197] K. G. H. Janssen, H. T. Hoang, J. Floris, J. de Vries, N. R. Tas, J. C. T. Eijkel, and T. Hankemeier, “Solution Titration by Wall Deprotonation during Capillary Filling of Silicon Oxide Nanochannels,” *Anal. Chem.*, vol. 80, no. 21, pp. 8095–8101, Nov. 2008.

[198] M. P. Rossi, Y. Gogotsi, and K. G. Kornev, “Deformation of Carbon Nanotubes by Exposure to Water Vapor,” *Langmuir*, vol. 25, no. 5, pp. 2804–2810, Mar. 2009.

[199] G. Günther, J. Prass, O. Paris, and M. Schoen, “Novel Insights into Nanopore Deformation Caused by Capillary Condensation,” *Phys. Rev. Lett.*, vol. 101, no. 8, p. 086104, Aug. 2008.

[200] Daria Monaenkova, “Elasto-Capillarity in Fibrous Materials,” Clemson University, 2012.

[201] A. E. H. Love, “The Stress Produced in a Semi-Infinite Solid by Pressure on Part of the Boundary,” *Philosophical Transactions of the Royal Society of London. Series A, Containing Papers of a Mathematical or Physical Character*, vol. 228, pp. 377–420, Jan. 1929.

[202] H. L. Duan, J. Wang, Z. P. Huang, and B. L. Karihaloo, “Eshelby formalism for nano-inhomogeneities,” *Proceedings of the Royal Society of London A: Mathematical, Physical and Engineering Sciences*, vol. 461, no. 2062, pp. 3335–3353, Oct. 2005.

[203] Y. Z. Povstenko, “Theoretical investigation of phenomena caused by heterogeneous surface tension in solids,” *Journal of the Mechanics and Physics of Solids*, vol. 41, no. 9, pp. 1499–1514, Sep. 1993.

[204] J. Weissmüller, H.-L. Duan, and D. Farkas, “Deformation of solids with nanoscale pores by the action of capillary forces,” *Acta Materialia*, vol. 58, no. 1, pp. 1–13, Jan. 2010.

[205] J. Weissmüller and J. W. Cahn, “Mean stresses in microstructures due to interface stresses: A generalization of a capillary equation for solids,” *Acta Materialia*, vol. 45, no. 5, pp. 1899–1906, May 1997.

[206] R. Shuttleworth, “The Surface Tension of Solids,” *Proc. Phys. Soc. A*, vol. 63, no. 5, p. 444, May 1950.

[207] L. G. Zhou and H. Huang, “Are surfaces elastically softer or stiffer?,” *Applied Physics Letters*, vol. 84, no. 11, pp. 1940–1942, Mar. 2004.

[208] T. B. Hoberg, E. Verneuil, and A. E. Hosoi, “Elastocapillary flows in flexible tubes,” *Physics of Fluids (1994-present)*, vol. 26, no. 12, p. 122103, Dec. 2014.

[209] L. B. Freund and S. Suresh, *Thin Film Materials: Stress, Defect Formation and Surface Evolution*. Cambridge University Press, 2004.

[210] J. M. Aristoff, C. Duprat, and H. A. Stone, "Elastocapillary imbibition," *International Journal of Non-Linear Mechanics*, vol. 46, no. 4, pp. 648–656, May 2011.

[211] T. Cambau, J. Bico, and E. Reyssat, "Capillary rise between flexible walls," *EPL*, vol. 96, no. 2, p. 24001, Oct. 2011.

[212] C. G. Eggers, M. Berli, M. L. Accorsi, and D. Or, "Deformation and permeability of aggregated soft earth materials," *J. Geophys. Res.*, vol. 111, no. B10, p. B10204, Oct. 2006.

[213] P. G. Righetti, B. C. W. Brost, and R. S. Snyder, "On the limiting pore size of hydrophilic gels for electrophoresis and isoelectric focussing," *Journal of Biochemical and Biophysical Methods*, vol. 4, no. 5–6, pp. 347–363, Jun. 1981.

[214] A. Pluen, P. A. Netti, R. K. Jain, and D. A. Berk, "Diffusion of macromolecules in agarose gels: comparison of linear and globular configurations.," *Biophys J*, vol. 77, no. 1, pp. 542–552, Jul. 1999.

[215] G. Desbois, J. L. Urai, P. A. Kukla, J. Konstanty, and C. Baerle, "High-resolution 3D fabric and porosity model in a tight gas sandstone reservoir:A new approach to investigate microstructures from mm- to nm-scale combining argon beam cross-sectioning and SEM imaging," *Journal of Petroleum Science and Engineering*, vol. 78, no. 2, pp. 243–257, Aug. 2011.

[216] G. Desbois, J. L. Urai, F. Pérez-Willard, Z. Radi, S. Offern, I. Burkart, P. A. Kukla, and U. Wollenberg, "Argon broad ion beam tomography in a cryogenic scanning electron microscope: a novel tool for the investigation of representative microstructures in sedimentary rocks containing pore fluid," *J Microsc*, vol. 249, no. 3, pp. 215–235, Mar. 2013.

[217] D. G. Lowe, "Distinctive Image Features from Scale-Invariant Keypoints," *International Journal of Computer Vision*, vol. 60, no. 2, pp. 91–110, Nov. 2004.

[218] S. Aja-Fernández, G. Vegas-Sanchez-Ferrero, and M. A. Martin Fernandez, "Soft thresholding for medical image segmentation," in *2010 Annual International Conference of the IEEE Engineering in Medicine and Biology Society (EMBC)*, 2010, pp. 4752–4755.

[219] C. Li, C. Xu, C. Gui, and M. D. Fox, "Distance Regularized Level Set Evolution and Its Application to Image Segmentation," *IEEE Transactions on Image Processing*, vol. 19, no. 12, pp. 3243–3254, Dec. 2010.

[220] J. Latt, *Palabos, parallel lattice Boltzmann solver*. 2009.

[221] W. Degruyter, A. Burgisser, O. Bachmann, and O. Malaspinas, "Synchrotron X-ray microtomography and lattice Boltzmann simulations of gas flow through volcanic pumices," *Geosphere*, vol. 6, no. 5, pp. 470–481, Oct. 2010.

[222] Rui Wang, Ningsheng Zhang, Xiaojuan Liu, and Xinmin Wu, "Characterization of Gas Flow Ability and Contribution of Diffusion to Total Mass Flux in the Shale," *Research Journal of Applied Sciences, Engineering and Technology*, vol. 6, no. 9, pp. 1663–1668, 2013.

[223] F. Javadpour, D. Fisher, and M. Unsworth, "Nanoscale Gas Flow in Shale Gas Sediments," *Journal of Canadian Petroleum Technology*, vol. 46, no. 10, pp. 55–61, 2007.

[224] I. Lunati and S. H. Lee, "A dual-tube model for gas dynamics in fractured nanoporous shale formations," *Journal of Fluid Mechanics*, vol. 757, pp. 943–971, Oct. 2014.

[225] S. Succi, *The Lattice Boltzmann Equation: For Fluid Dynamics and Beyond*. OUP Oxford, 2013.

[226] X. Zhang, L. Xiao, X. Shan, and L. Guo, "Lattice Boltzmann Simulation of Shale Gas Transport in Organic Nano-Pores," *Sci. Rep.*, vol. 4, May 2014.

[227] R. H. Bennett, W. R. Bryant, and M. H. Hulbert, *Microstructure of Fine-Grained Sediments: From Mud to Shale*. Springer Science & Business Media, 1991.

[228] X. Gu, D. R. Cole, G. Rother, D. F. R. Mildner, and S. L. Brantley, "Pores in Marcellus Shale: A Neutron Scattering and FIB-SEM Study," *Energy Fuels*, 2015.

[229] A. Mehmani and M. Prodanović, "The application of sorption hysteresis in nano-petrophysics using multiscale multiphysics network models," *International Journal of Coal Geology*, vol. 128–129, pp. 96–108, Aug. 2014.

[230] L. Bocquet and P. Tabeling, "Physics and technological aspects of nanofluidics," *Lab Chip*, vol. 14, no. 17, pp. 3143–3158, Jul. 2014.

[231] N. J. Abbott, "Evidence for bulk flow of brain interstitial fluid: significance for physiology and pathology," *Neurochem. Int.*, vol. 45, no. 4, pp. 545–552, Sep. 2004.

[232] J. Fu, R. B. Schoch, A. L. Stevens, S. R. Tannenbaum, and J. Han, "A patterned anisotropic nanofluidic sieving structure for continuous-flow separation of DNA and proteins," *Nat Nano*, vol. 2, no. 2, pp. 121–128, Feb. 2007.

[233] M. Piñeirua, J. Bico, and B. Roman, "Capillary origami controlled by an electric field," *Soft Matter*, vol. 6, no. 18, pp. 4491–4496, Sep. 2010.

[234] "SCHOTT Announces Availability of CoralPor™ Porous Glass Products," *SCHOTT*, 2012. [Online]. Available: http://www.us.schott.com/english/news/press.html?NID=us457.

[235] "Research EM Gallery," *Duke Pathology, Duke University School of Medicine*, 2015. [Online]. Available: http://pathology.duke.edu/experimental-pathology/research-electron-microscopy/res-em-gallery.

[236] B. V. Derjaguin, N. V. Churaev, and V. M. Muller, "The Electrostatic Component of Disjoining Pressure," in *Surface Forces*, Springer US, 1987, pp. 173–230.

[237] J. A. Hauch, D. Holland, M. P. Marder, and H. L. Swinney, "Dynamic Fracture in Single Crystal Silicon," *Phys. Rev. Lett.*, vol. 82, no. 19, pp. 3823–3826, May 1999.

[238] E. R. Cruz-Chu, A. Aksimentiev, and K. Schulten, "Water−Silica Force Field for Simulating Nanodevices," *J. Phys. Chem. B*, vol. 110, no. 43, pp. 21497–21508, Nov. 2006.

[239] I. K. Puri and S. Murad, "A Multiscale Methodology to Approach Nanoscale Thermal Transport," in *Trends in Computational Nanomechanics*, T. Dumitrica, Ed. Springer Netherlands, 2010, pp. 135–150.

[240] S. Gruener and P. Huber, "Spontaneous Imbibition Dynamics of an n-Alkane in Nanopores: Evidence of Meniscus Freezing and Monolayer Sticking," *Phys. Rev. Lett.*, vol. 103, no. 17, p. 174501, Oct. 2009.

[241] Y. Xue, J. Markmann, H. Duan, J. Weissmüller, and P. Huber, "Switchable imbibition in nanoporous gold," *Nat Commun*, vol. 5, Jul. 2014.

[242] L. D. Gelb and K. E. Gubbins, "Characterization of Porous Glasses: Simulation Models, Adsorption Isotherms, and the Brunauer−Emmett−Teller Analysis Method," *Langmuir*, vol. 14, no. 8, pp. 2097–2111, Apr. 1998.

[243] S. Gruener, T. Hofmann, D. Wallacher, A. V. Kityk, and P. Huber, "Capillary rise of water in hydrophilic nanopores," *Phys. Rev. E*, vol. 79, no. 6, p. 067301, Jun. 2009.

[244] A. T. Conlisk, J. McFerran, Z. Zheng, and D. Hansford, "Mass Transfer and Flow in Electrically Charged Micro- and Nanochannels," *Anal. Chem.*, vol. 74, no. 9, pp. 2139–2150, May 2002.

[245] Z. Y. Banyamin, P. J. Kelly, G. West, and J. Boardman, "Electrical and Optical Properties of Fluorine Doped Tin Oxide Thin Films Prepared by Magnetron Sputtering," *Coatings*, vol. 4, no. 4, pp. 732–746, Oct. 2014.

[246] P. Spathis, A. Delga, C. Malheiro, and P. E. Wolf, "Imbibition of Liquid Helium in Aerogels," *J Low Temp Phys*, vol. 171, no. 5–6, pp. 693–698, Oct. 2012.

[247] P. Huber, K. Knorr, and A. V. Kityk, “Spontaneous Imbibition of Liquids into Nanopores,” in *Symposium N – Dynamics in Small Confining Systems VIII*, 2005, vol. 899.

[248] D. Ben Jazia, L. Vonna, G. Schrodj, H. Bonnet, Y. Holl, and H. Haidara, “Imbibing drops of ethanol/water mixtures in model nanoporous networks with tunable pore structure: Deviation from square root to linear time regime imbibition kinetics,” *Colloids and Surfaces A: Physicochemical and Engineering Aspects*, vol. 384, no. 1–3, pp. 643–652, Jul. 2011.

[249] R. M. Barrer and A. J. Walker, “Imbibition of electrolytes by porous crystals,” *Trans. Faraday Soc.*, vol. 60, no. 0, pp. 171–184, Jan. 1964.

[250] Y. Su, S. Xu, J. Wang, and R. Xiao, “Spontaneous liquid–gas imbibition for characterization of carbon molecular sieves,” *Journal of Colloid and Interface Science*, vol. 377, no. 1, pp. 416–420, Jul. 2012.

[251] M. C. Sukop and D. T. Thorne, *Lattice Boltzmann Modeling: An Introduction for Geoscientists and Engineers*. Springer Science & Business Media, 2007.

[252] P. Yuan and L. Schaefer, “Equations of state in a lattice Boltzmann model,” *Physics of Fluids (1994-present)*, vol. 18, no. 4, p. 042101, Apr. 2006.

[253] H. Bruus, *Theoretical Microfluidics*. OUP Oxford, 2008.